Journal of
Mechanics of
Materials and Structures

JOURNAL OF MECHANICS OF MATERIALS AND STRUCTURES

jomms.org

Cover design: Alex Scorpan   Cover photo: Mando Gomez, www.mandolux.com

TURTLE SHELL AND MAMMAL SKULL RESISTANCE TO FRACTURE DUE TO PREDATOR BITES AND GROUND IMPACT

DAVID L. HU, KELLY SIELERT AND MICHAEL GORDON

We investigate the relation between the thickness and diameter of naturally occurring shells, such as the carapaces of turtles and the skulls of mammals. We hypothesize that shells used for different protective functions (for example, protection against headbutting or falling on the ground) will exhibit different power-law trends for shell thickness and diameter. To test this hypothesis, we examine over 600 shells from museum collections with diameters between 1 and 100 cm. Our measurements indicate that eggs, turtle shells, and mammalian skulls exhibit clear and distinct allometric trends. We use a theoretical scaling analysis based on elastic thin shell theory to show that the trends observed are consistent with the corresponding protective functions hypothesized. We thus provide theoretical evidence that shells can be classified by their protective function.

1. Introduction

While the study of safety factors of leg bones during locomotion has a long history [McMahon and Bonner 1985; Currey 1988; Biewener 1990; Biewener 2003; Vogel 2003], less work has been done on shells and armor. Over millions of years, shell-based armor has evolved in a variety of organisms, and has manifested in diverse forms such as eggshells, mollusk shells, skulls, nuts, fingernails, and gourds. Some of these champion protectors, such as the abalone shell, have inspired material science advances such as new forms of bullet-proof armor [Jackson et al. 1988; Menig et al. 2000]. Others, such as the Macadamia nut shell, still require ingenious methods (for example, lasers [Jennings and Macmillan 1986]) to fracture without crushing their fragile contents. One significant obstacle in predicting the strength of natural shells is understanding their complex material properties [Currey 2002]. As a result, existing mechanical shell theories must be applied exceedingly carefully.

The study of man-made shells is a well-developed subject in architectural and mechanical engineering. A physical description of shells used in architecture is provided by [Heyman 1995]; mathematical treatments of shells are provided by [Flügge 1973; Heyman 1977; Steele 1989]. In this study, we consider a spherical shell with a thickness t much less than its diameter L, as in the inset of Figure 1. If its material properties are homogeneous and isotropic, we may apply a relation from linear elastic shell theory [Steele 1989] to determine the shell's strength. As shown in the Appendix, the maximum force F that a shell can resist, when loaded between two plates, is

$$F = A\sigma_f t^2,$$ (1)

where t is the shell thickness, σ_f is the ultimate tensile stress of the material, and $A = \pi$. This relation shows that for spherical shells, breaking force depends exclusively on shell thickness. It is noteworthy
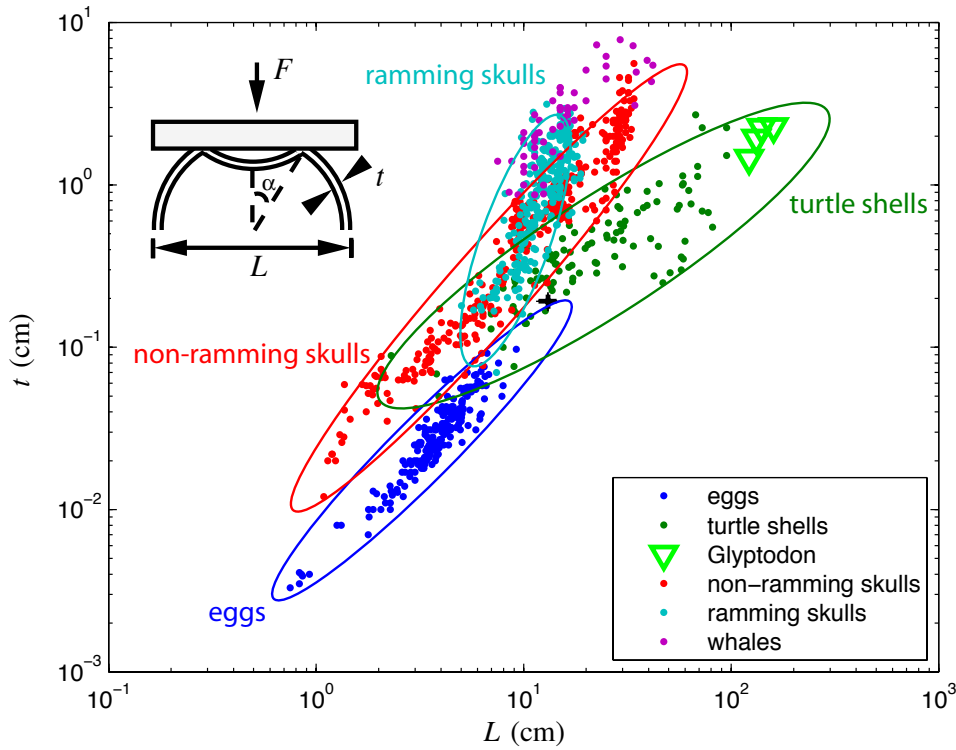
Figure 1. Relation between diameter L and thickness t for turtles, skulls, and eggshells (reprinted from [Schönwetter 1960]). The ovals indicate the range of thicknesses found for each shell type. Inset: schematic of a spherical shell of thickness t and diameter L subject to an applied force F by a flat plate. The load dimples the shell, inducing high stresses at points along a circular region at an angle α to the vertical.

that the derivation (in the Appendix) relies upon the elastic energy of the shell and so implicitly takes into account the work *to* fracture. Consideration of the work *of* fracture is beyond the scope of this study.

   While the assumptions surrounding the derivation of (1) are numerous, extensive experiments by Ar et al. [1979] have shown that (1) provides excellent predictions for egg-breaking. They tested the following hypothesis:

H0. *Birds evolved eggs of sufficient thickness to support the mother's weight during incubation.*

To test this hypothesis, the authors measured the force to break hundreds of eggs, ranging in mass between 0.86 and 1460 g, collecting the data summarized in Figure 2. They found that (1) provides an excellent estimate of breaking strength over a large range of egg sizes and shapes. Specifically, their measurements of breaking force show that $F = 1.7t^{2.0}$ (Figure 1, with $r = 0.98$, t in cm, and F in kgf). Using (1) to infer the value of σ_f yields that the tensile strength of eggshells is $\sigma_f \approx 53.6$ MPa, a value that is within the range given for mollusk and eggshells [Biggs et al. 1976]. Next, [Ar et al. 1979; Pritchard 1993] use scaling arguments involving (1) to make a biologically meaningful statement about constraints on eggshells. They showed that in order for eggs to support the weight of their mother during incubation, the egg thickness must scale with egg diameter L according to $t \sim L^{3/2}$. The work on eggshells represents
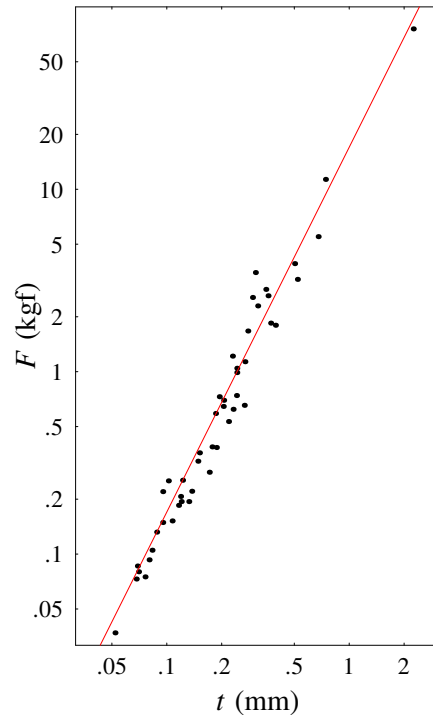
Figure 2. The relation between breaking force F and egg thickness t. The best fit (red line) is given by (1). Adapted from [Ar et al. 1979].

the most precise work on natural shells performed thus far. As we review here, there is much evidence that other kinds of shells have also evolved to resist specific types of loads.

Currey [1988] extensively studied the strength of mollusk shells, giving compelling evidence that they evolved to resist the attacks of predators. He examined the stomachs of fishes, finding that only fish above a certain size had the remains of mollusk shells in their stomachs; this evidence suggests that fish must grow to a critical size before mustering sufficient jaw strength to break mollusk shells. By examining populations of dog whelks exposed to crab predation, Currey found that in areas of intense predation, shells were stronger, weight for weight, than in areas with less predation. Currey also found that the maximum load of a shell varies according to thickness to the 1.7 power, in rough accordance with the trend found for eggs by Ar et al. Zuschin and Stanton [2001] also confirmed that mollusk shells increase in strength primarily by thickening rather than changing their material properties.

Substantial work has been done on the allometry of skulls and is summarized by Emerson and Bramble [1993]. The skull is divided into two parts: the cerebral skull, consisting of the braincase and the eye and ear capsules, and the facial skull, consisting of the jaw and associated musculature. Of particular interest to previous investigators has been the scaling of braincase size to body size. Another topic receiving attention has been how the scaling of predator jaws affects prey consumption [Radinsky 1981]. One example reviewed by Emerson and Bramble shows the importance of jaw size: an examination of the stomach contents of Southeast Asian frogs finds that only frogs above a certain size can eat crabs, presumably because of their jaw strength. It is noteworthy that among these studies, braincase thickness

has not been systematically measured. As we will show here, thickness is the most important variable governing the strength of the cerebral skull.

Ramming animals such as those of the family Bovidae have skulls that must resist the impact forces of head-to-head strikes. Generally, such skulls are covered by one of a variety of horns, whose utility for wrestling, fencing and ramming are discussed by Lundrigan [1996]. Schaffer [1968] estimates the impact forces resulting from ramming goats and sheep. He shows that the neck musculature of sheep is sufficient to prevent the neck from excessive skull rotation upon impact. Other authors, such as Alvarez [1990], have investigated the design of the horns, showing in particular that the horn's wide base of attachment with the skull helps minimize stress during impact. Very few of these authors have examined the skull thickness of ramming animals.

Zangerl [1969] gives a comprehensive overview of turtle shell anatomy and development. It has been suggested that the success of the turtle family is owed to the strength of the turtle's shell; however, biomechanical evidence for this has yet to be found. The shell mass of a turtle is reported to be a significant fraction (25–30%) of body mass [Bramble 1974; Iverson 1984]. This fraction remains constant across a range of turtles sizes: specifically, shell mass scales with the 1.2 power of body mass, or nearly isometrically. In contrast, the plastron is not isometric with body mass, but scales with body mass to the 0.5 power, indicating that larger turtles have thicker plastron than suggested by isometry. The mechanical rationale for these trends remains unknown.

In this study, we will test three hypotheses:

H1. *Turtles evolved shells to resist the bites of predators.*

H2. *Nonramming mammals evolved skulls to resist impact in accidental falls.*

H3. *Ramming mammals evolved skulls to resist headbutting impacts.*

Studies on ramming impacts [Jaslow and Biewener 1995] have used destructive testing and high-speed imagery to make quantitative measurements of stress and strain in shells under impact. In this study, we will use an approach based on nondestructive measurements and scaling. Central to our approach is the assumption that animals evolved shells of the minimum thickness necessary to satisfy their functionality [Alexander 1996].

Our approach is to compare the thickness of shells across a broad range of species. Such measurements do not provide a complete description of shell strength, but provide at least a first-order description, and a simple metric by which to compare different shells. Our methods and results on shell measurements are presented in Sections 2 and 3, respectively. In Section 4, we present scaling arguments intended to provide physical insight into the geometric trends observed. In Section 5, we discuss the implications of our work and future avenues for research.

2. Methods

We measured the geometries of 111 turtle carapaces, 341 hornless mammalian skulls, 264 horned mammalian skulls, and 4 glyptodon fossils, courtesy of the Smithsonian and American Museums of Natural History. Rulers, calipers, and ball-micrometers were used to take these measurements in the same relative position for each type of shell. Turtle carapace thickness was measured at the intersection of the first pleural scute and its adjoining marginal scute. glyptodon shell thicknesses were measured at their anterior

edge. Skulls were measured at the pharyngeal tubercle, accessed at the brainstem opening. An ordinary least squares (OLS) regression, implemented in MATLAB, was used to find the best fits to the data, standard errors of fitting, and closeness of fit (R^2). Best fits are given using one significant digit.

In our study, we assume shells are spherical. The shell "diameter" L reported is defined as twice the shell's maximum radius of curvature. In turtle shells, the maximum radius of curvature was measured directly with rulers placed inside the open half of the shell. Animal skulls were generally not available in cross section. Thus, the diameter was measured by placing measuring tools inside the skull through the brainstem opening.

Before presenting our results, we briefly comment on our assumption of sphericity. Firstly, we observed that many shells (especially brain cases) were indeed nearly spherical, in part because spheres minimize the material required to grow the shell. To demonstrate this statement quantitatively, cross-sections of the shells would have to be measured, by either destructive methods or by using an X-ray machine, all of which is beyond the scope of this study. Examples of clearly nonspherical shells include aquatic shells (turtles, mollusks) that appeared hydrodynamically streamlined. Secondly, we speculate that deviations from sphericity will have a second-order effect on strength compared to changes in thickness. For example, in egg-breaking studies [Ar et al. 1979], no effort was made to choose specimens that were spherical; however, the authors found that the main relation used in this work, (1), was still an excellent predictor of strength for eggs of nearly all shapes and sizes. Based on the success of the methods employed in [Ar et al. 1979], we continue with our study, assuming the shells are generally spherical.

3. Results

Figure 1 shows the relation between shell thickness t and diameter L for the shells studied; tabulated values are given in the Electronic Supplement. Clearly, each shell type (turtles, ramming skulls, and non-ramming skulls) exhibits a different power-law trend, as shown by the ellipses in Figure 1. Best power-law fits for the data were found using the method of least squares and are presented in Table 1. In the next section, we propose scaling arguments to account for the scaling exponents observed.

	OLS		Lower 95%		Upper 95%		R^2	N	L (cm)	Rationale
	a	b	a	b	a	b			range	
Eggs	0.004	1.4	0.004	1.3	0.005	1.5	0.90	201	0.7–13	incubation
Turtle shells	0.03	0.8	0.03	0.7	0.05	0.9	0.71	111	2.3–95	bite resistance
Hornless skulls	0.02	1.5	0.01	1.4	0.02	1.5	0.93	341	10–16	falling
Horned skulls	0.0026	2.3	0.0015	2.1	0.0044	2.6	0.64	264	10–20	ramming
Whales	1.3	0.2	0.7	0.1	2.3	0.2	0.61	60	10–40	NA

Table 1. Best fits for shell thickness as a function of shell length, given in terms of coefficients a and b, where the shell thickness t and length L vary according to $t = bL^a$. Fitting coefficients are given using the OLS method, which provides the best fit coefficients and closeness of fit R^2. The upper and lower bounds for the 95th-percentile confidence interval estimates for a and b are given. N shells were measured by ourselves and by previous workers [Ar et al. 1979].

4. Model

We propose simple models to account for the shell geometry trends observed in Section 3.

4.1. _Turtles._ The armored shell of the turtle has long been assumed to protect turtles from predation [Zangerl 1969; Gibbons 1987]. The shell protects the legs and head, which, for many species, can be retracted into the shell. However, a few animals use their teeth to nibble at the edges of the shell, or poke into soft or thin parts of the shell or carapace. This includes ravens, raccoons, and coyotes [Gibbons 1987; Boarman 2003]. Other very large predators dispatch turtles by biting through their shells with great force. Alligators and crocodiles have been observed eating turtles by biting through their shells [Carpenter and Lindsey 1980; Pérez-Higareda et al. 1989]. Sharks, especially tiger sharks, are known to bite through sea turtle shells of all sizes [Stancyk 1981]. Given this biological evidence, we hypothesize that turtle shells evolved to resist the bites of predators.

To test this hypothesis, we determine whether our measurements of turtle shells (Figure 3a) are consistent with resisting the attacks of predators. For a turtle shell to resist the bite force F_{pred} of a predator, we require the breaking force of the shell F to satisfy

$$F > F_{\text{pred}}. \tag{2}$$

The scaling of F_{pred} in (2) is estimated using measurements [Meers 2003; Wroe et al. 2005] of predator bite force and weight W_{pred}, for which

$$F_{\text{pred}} \sim W_{\text{pred}}^{0.6}, \tag{3}$$

where $R^2 = 0.76$. This relation is consistent with the view that the maximum force exerted by animals scales as the cross-sectional area of the animal's muscles [Alexander 1985; McMahon and Bonner 1985]. The measurements by Wroe et al. [2005] also provide a relation between the weight of the predators and the weight W of their largest prey

$$W_{\text{pred}} = 1.5W^{0.9}, \tag{4}$$

where weights are expressed in newtons and $R^2 = 0.82$. The weight W of turtle shells is modeled as a hemisphere with the density ρ of water: $W = \frac{1}{12}\pi\rho g L^3$, where g is the acceleration of gravity. Combining relations (1)–(4) yields the result that turtle shells should be nearly isometric to resist predation equally among all turtle sizes: $t \sim L^{0.8}$. Our predictions are close to the trends given by our measurements, as shown by the points in Figure 3b, whose best fit gives $t \sim L^{0.8}$ with $R^2 = 0.68$. Comparing turtle shells from over two orders of magnitude in length scale, as in Figure 3a, one finds little visible difference in their thickness-length aspect ratios, as predicted by our model.

Figure 3c shows two relations: filled symbols relate the breaking force and weight W of turtle shells (whose best fit is $F \sim W^{0.5}$); open symbols relate the bite force of predators to the weight of their largest prey (whose best fit is $F_{\text{pred}} \sim W^{0.6}$). It is noteworthy that while trends for shell strength F and bite force F_{pred} were found using three independent sources (our study, [Meers 2003], and [Wroe et al. 2005]), nevertheless F and F_{pred} are found to have similar power-law exponents (_a_ values of 0.5 and 0.6). This similarity suggests that shell thickness and bite force evolved in parallel. Using a _t_-test, we find that there is only a 0.05% probability that the power-law exponents are identical [Zar 2007].

In this section, we hypothesized that predators are capable of breaking turtle shells. We now examine the reasonableness of this assumption by examining which animals in Figure 3c can successfully bite
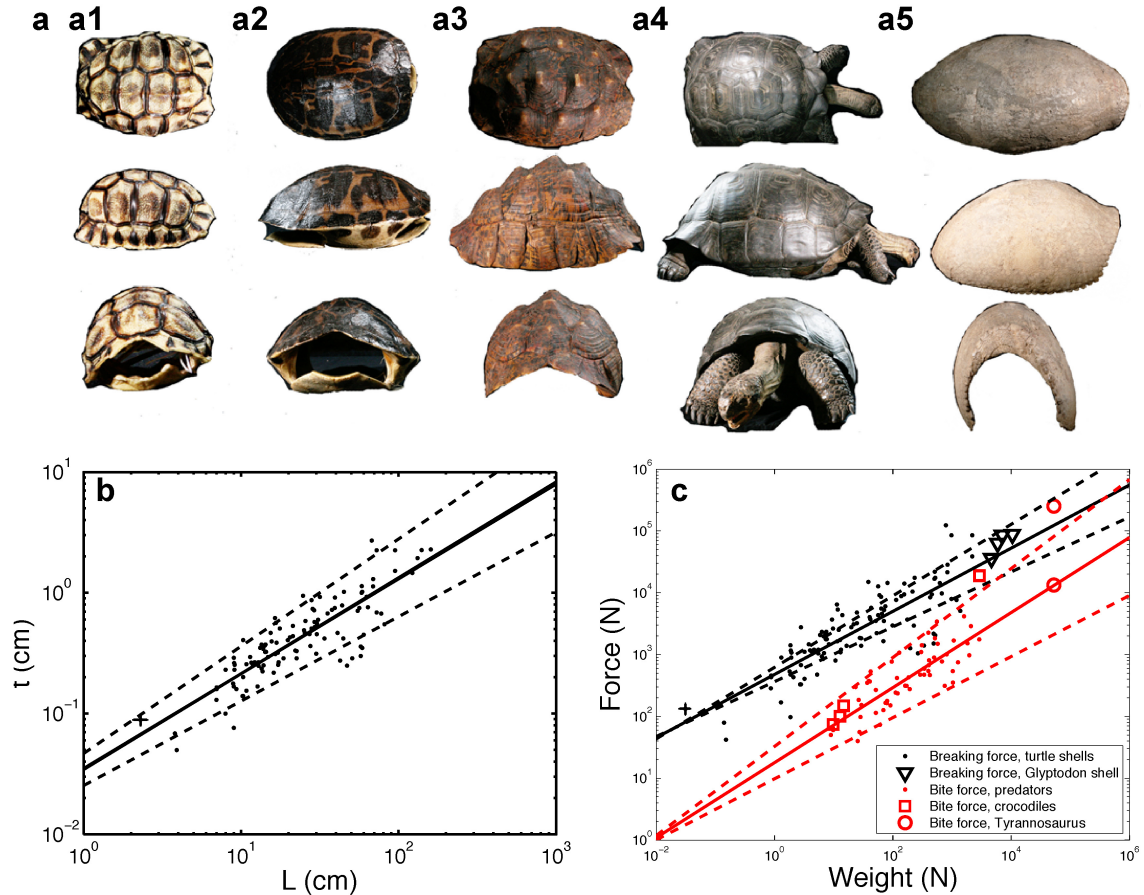
Figure 3. (a) Turtle shells from 3–100 cm in diameter, here magnified to the same size, highlighting the similarity of their proportions. (a1) Angulate tortoise (*Chersina angulata*), $L = 3.9$ cm. (a2) Florida redbelly turtle (*Pseudemys nelsoni*), $L = 28.5$ cm. (a3) Leopard tortoise (*Geochelone pardalis*), $L = 29.1$ cm. (a4) Galapagos giant tortoise (*Geochelone nigra*), $L = 58.8$ cm. (a5) Shell of glyptodon, a prehistoric armored mammal, $L = 130$ cm. (b) The relation between turtle shell thickness t and length L. Solid lines indicate the best fit ($t = 0.04L^{0.8}$); dashed lines indicate the 95% confidence intervals for this fit. Characteristic errors of measurement are shown. (c) Bite force F_{pred} of predators (red) and bite resistance F of turtle shells (black) as a function of their body weights W. Solid lines indicate the best fits: $F_{\text{pred}} = 20W^{0.6}$, $F = 470W^{0.5}$; dashed lines indicate the 95% confidence intervals for this fit.

through a turtle shell. Suppose that predators would like to prey on animals of their same weight. Then the vertical distance between the curves in Figure 3c shows that the average breaking force of turtle shells is approximately 40 times the average bite force of same-weight predators: specifically $F_b \approx SF_p$ with a constant safety factor $S = 40$. Clearly, turtles can resist the bite force of predators of the same weight.

Conversely, by drawing horizontal lines in Figure 3c, we predict that predators 200 times the weight of turtles can succeed in their attack. Thus, juvenile turtles (or turtles with masses on the order of grams)

may be eaten by numerous predators. Moreover, we predict that a 360 kg adult alligator is sufficiently strong to bite through the shell of a 2 kg turtle. Weaknesses such as thinner areas in the shell will allow predators to attack even larger turtles. As turtles grow larger, they will have fewer predators. The so-called "size refuge" of turtles, the size at which they have grown too large to have their shells broken by any predators, is $M^* = 100$ kg, which corresponds to the weights of the Galapagos turtles. Our predictions seem physically reasonable, and give credibility to our scaling argument.

We also include in Figure 3c the predicted shell strength of the armadillo-like glyptodon (Figure 3a5) and the bite force of the predator *Tyrannosaurus rex* [Erickson et al. 2003; Meers 2003]. While the glyptodon has little shared genetics with the turtles, its shell length and thickness follow the trends predicted for turtles (Figure 1), suggesting a universality in shell thickness trends among mammals and reptiles.

In this part of our investigation, our goal was to rationalize the measured scaling for turtle shell thickness. Using previously collected predator bite force data, we found that the scaling exponents for shell thickness are consistent with turtles resisting predator bites. A future approach might take into consideration the measured breaking force of the shell and the energetics of the turtle's bearing of their shell.

4.2. *Nonramming skulls.* Creatures that are taller and faster than turtles must survive the impacts of accidental falls. We hypothesize that mammalian skulls (Figure 4a) are designed to survive impacts from either falling from a stand or from head-to-head ramming. We consider the mechanics of each of these impacts in turn.

One design requirement for a skull is that it should resist breaking due to impact with the ground during locomotion. For the animal to survive such a fall, the breaking force F of the skull must be in excess of this impact force F_{impact}:

$$F > F_{\text{impact}}. \tag{5}$$

The impact force F_{impact} results entirely from the transfer of gravitational energy into kinetic and finally into elastic deformation energy of the skull. At the moment of impact, the speed U of a skull of mass M falling from a height H is $U = \sqrt{2gH}$, where H is the maximum height of the skull during locomotion. The impact force is simply the momentum of this impact divided by the impact time τ:

$$F_{\text{impact}} = MU/\tau = M\sqrt{2gH}/\tau. \tag{6}$$

We simplify (6) by making some further assumptions. First, since we have assumed the shell is spherical, we can write the weight of the shell as $M \sim \rho L^3$. Second, we must make an assumption about the contact duration τ during impact with the ground. Impact mechanics is a complex subject [Chaudhri et al. 1981; Stronge and Stronge 2000; Goldsmith 2001]. For an elastic sphere of diameter L striking a rigid plane surface, the contact time is given by

$$\tau = \frac{\pi}{2}\sqrt{\frac{M}{\pi H_d L}}, \tag{7}$$

where H_d is the dynamic hardness of the sphere, a material property. Assuming H_d is a constant yields that $\tau \sim L$. Thus, $F_{\text{impact}} \sim H^{1/2}L^2$. Combining (6) with (1) yields

$$t \sim H^{1/4}L. \tag{8}$$
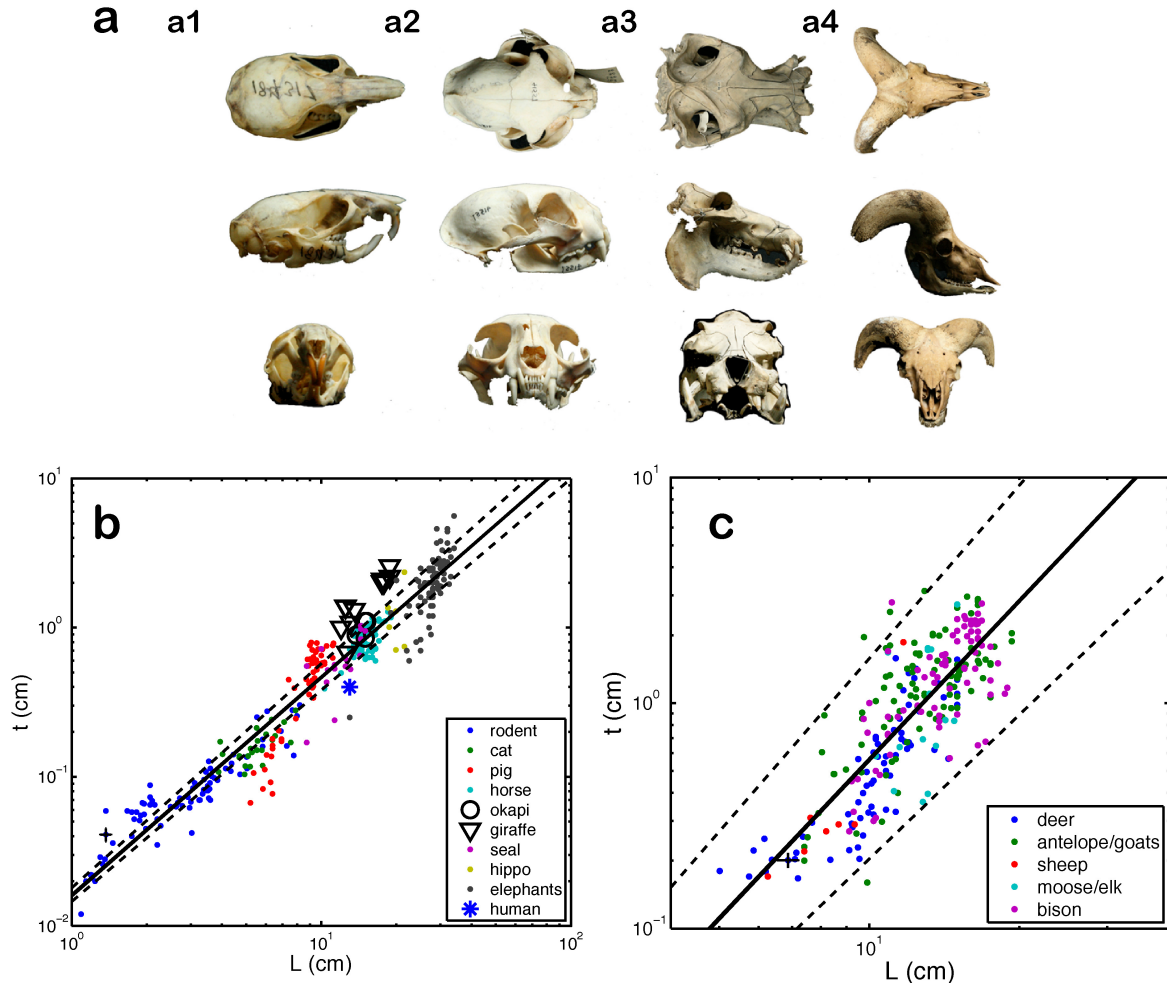
Figure 4. (a) Some mammalian skulls measured in this study. Measurements of characteristic skull thickness were performed at the skull's opening to the brainstem. (a1) Rat (*Rattus rattus*). (a2) Cat (*Felis catus*). (a3) Hippopotamus (*Hippopotamus amphibius*). (a4) Bighorn sheep (*Ovis ammon*). (b) The relation between diameter L and shell thickness t for hornless mammalian skulls. The solid line indicates best fit $t = 0.02L^{1.5}$, dashed lines the 95% confidence intervals for this fit. (c) Relation between diameter L and shell thickness t for horned mammalian skulls. The inset shows the relation between diameter and thickness of mountain goat skulls, which display less scatter than the data for other horned mammalian skulls. The solid line indicates best fit $t = 0.0026L^{2.3}$ for all horned skulls and $t = 0.0019L^{2.6}$ for mountain goat skulls; dashed lines the 95% confidence intervals for this fit. Characteristic errors of measurement are shown.

Equation (8) successfully predicts the change of skull thickness with head height (see open symbols in Figure 4b). Juvenile giraffes have comparable heights (2 m) and skull dimensions (thickness 0.8–1.1 cm and length 12–15 cm) to their evolutionary predecessors, the okapi. As giraffes grow to their adult heights

of 5 m, their skulls broaden to $L \approx 17$–19 cm and thicken to $t \approx 2$–2.6 cm. According to (8), increasing an animal's height by a factor n and skull length by a factor m results in the skull thickening by a factor $p = n^{1/4}m$. Since giraffes increase in height by a factor of $n = 2.5$ and in skull length by a factor of $m = 1.1$–1.6, we predict that their skulls should thicken by a factor of $p = 1.4$–2.0. This predicted thickening is less than (but comparable to) the measured value $p = 1.8$–3.2. Thus, our model provides one reason for why giraffes have thicker skulls than okapi: the giraffe skull must grow thicker as the animal ages in order to absorb the shock of falling from a greater height.

Assuming that animals must at least survive falls from a stand yields that $H \sim L$. Therefore, (8) simplifies to $t \sim L^{1.25}$, which has an exponent close (1.25 versus 1.4) to the trend observed, $t = 0.018L^{1.4}$ with $R^2 = 0.93$ (Figure 4b). Thus, our model works well to predict skull thickness scaling exponents for non-ramming mammals.

4.3. *Ramming skulls.*

Some creatures must endure the impacts due to headbutting during mating rituals and self-defense, as is common in the family Bovidae (cows, sheep, rams, and bulls [Schaffer 1968; Lundrigan 1996]) as well as other mammals that are purported to ram underwater such as beaked and sperm whales [Carrier et al. 2002]. The skulls of such creatures must be able to survive the impact of a headbutt: the breaking force F must exceed the impact force $F_{\text{impact}} : F > F_{\text{impact}}$. The impact force results from the two skulls striking each other at relative speed $2U$. Since both animals are at a standstill after the headbutt, the total impact force is given by $F_{\text{impact}} = 2MU/\tau$, where M and U are the mass and speed of the animal. Kitchener [1988] claims that much of this impact energy is absorbed by the neck muscles of the animal. As a worst case scenario, we assume that all the kinetic energy of the running animals is transferred entirely into elastic deformation energy of the skull.

We now make a series of assumptions to simplify our relation for impact force. First, since (7) also holds for the impact of two identical spheres [Goldsmith 2001], we assume that the impact time again scales as L. Next, we can make some assumptions for running speed from the biology literature. The maximum speed of swimming animals is nearly constant at 1–2 m/s [Sato et al. 2007]. The maximum speed U of large terrestrial mammals [Iriarte-Díaz 2002] has been shown to scale as $U \sim L^{-0.5}$ where L is the skull size (assuming that animal skull size scales with body size). These assumptions yield that $F_{\text{impact}} \sim L^{1.5-2.0}$.

Proceeding similarly to the analysis in Sections 4.1 and 4.2, we predict that land-based and aquatic mammals should have a trend of $t \sim L^{0.75-1.0}$ in order to resist fracture by headbutting. However, for land-based mammals, we observed a trend of $t = 0.0026L^{2.3}$ with $R^2 = 0.65$, which exhibits a power exponent a more than double our predictions. Our model thus works rather poorly to predict the thickness of ramming animals. The R^2 coefficient indicates the high variability in skull thickness for this class of animals. We note that less variability is present among certain individual species, such as mountain goats, for which $t = 0.0019L^{2.6}$ with $R^2 = 0.96$.

Finally, while our model cannot account for the observed trends of ramming skull thicknesses, it is useful to investigate its predictive ability for an individual case. We consider the ramming of bighorn sheep. According to high-speed measurements [Schaffer 1968; Kitchener 1988], two bighorn sheep, each of mass $M = 100$ kg can run towards each other at a relative speed of $2U = 50$ mph$= 20$ m/s, striking with an impact time τ of 0.3 seconds. This yields an impact force of $2MU/\tau \approx 3000$–6000 N [Kitchener 1988]. Given a maximum tensile stress of $\sigma_f = 100$ MPa (given for bone in [Vogel 2003]), our

model predicts that a skull thickness of $t \sim (2MU/(\tau\sigma_f))^{0.5} = 0.5$–$0.7$ cm is needed to avoid fracture, which is less than (but of the same order of magnitude as) the skull thickness of 1.9 cm for bighorn sheep (Figure 4c). One reason for this discrepancy is that our model relies on an assumption of uniform shell thickness, whereas in our observations, sheep skulls had walls that were honeycombed; thus, while it worked well for other types of shells, it performs poorly here. We are unable to validate Hypothesis 3, that ramming skulls have thicknesses in order to absorb impact force by plastic deformation. Instead, it is likely that much of the energy of impact is absorbed by neck muscles [Kitchener 1988]. It is worthwhile to note, however, that the skulls of ramming animals must be stronger than those of non-rammers of the same size, as shown by the trends in thicknesses in Figure 1. While some portion of the impact energy may be absorbed by musculature, ramming animals still require skulls thicker than their non-ramming counterparts.

We apply our results to two other classes of animals, speculated to use ramming. Shown in Figure 1 are measurements of whale skull thickness, which are fitted by the trend $t = 0.12L^{1.1}$ with $R^2 = 0.66$ (see Table 1). Since this power-law exponent of 1.1 is much smaller than 2.4, the observed power law for ramming creatures, we conclude that whale skulls were not designed for ramming. Another animal once postulated to use ramming is the thick-headed dinosaur Pachycephalosaurus [Goodwin and Horner 2004]. Trends from previous measurements of 7 dinosaurs ($t = 0.3L^{1.2}$ with $R^2 = 0.94$) exhibit a power exponent much less than that of the rammers in this study, suggesting that Pachycephalosaurus' skull was also not designed for ramming.

5. Summary and conclusions

In this study, we used measurements of shell thickness to describe quantitatively how shell strength varied across turtles and mammals. The key results of this study include (1) clarifying the biomechanical rationale for why shell strength depends exclusively on thickness rather than on diameter and (2) using this result to conduct a structural classification of shells. Our scaling arguments were able to account for the geometries measured for turtle shells and hornless skulls, but not for horned skulls.

Our measurements indicate that eggs, turtle shells, and mammal skulls each exhibit distinct geometric trends. We showed this quantitatively by monitoring changes in thickness t according to shell size L. Specifically, we modeled change in shell shape using power laws, $t \sim bL^a$, where b is a scaling prefactor and the scaling exponent a indicates how the shell must change in thickness-to-length aspect ratio as the shell grows. For example, values of $a \approx 1$ indicate isometry, in which the organism's proportions are independent of size. Values of $a < 1$ indicate negative allometry, in which thickness-to-length ratio decreases with shell length. Conversely, values of $a > 1$ indicate positive allometry, in which thickness-to-length ratio increases with shell length; such organisms must devote relatively more resources into building up their shell thickness as they grow.

The exponent a can be used to compare how much energy it costs to bear the shell as the animal increases in size, a topic considered in [Zani and Claussen 1995; Miller and Birchard 2005]. The maximum force that animals can produce scales as their length squared [Alexander 1985]. The weight of the shells scales as $L^2 t \sim L^{2+a}$. Since all of the observed exponents a are greater than zero, larger animals will use a larger portion of their maximum load-bearing capacity than smaller animals. This means that larger animals will also use more energy to bear the shell during locomotion.

Eggshells exhibit a power law of $a \approx 1.5$ in order for eggs to support the gravitational loads of their mothers [Ar et al. 1979]. Our measurements indicated that $a \approx 0.8$ for turtles, $a \approx 1.4$ for non-ramming skulls, and $a \approx 2.4$ for ramming skulls. We hypothesized that turtle shells evolved to resist predator bites and mammal skulls evolved to resist the impact of accidental falls to the ground. Using simple scaling arguments for destructive force, we predicted scaling exponents consistent with those measured for turtles and non-ramming skulls, providing theoretical evidence for the validity of our hypotheses 1 and 2. We were unable to account for the scaling of ramming skulls. To further validate our hypotheses would require one to also predict the prefactors b and the factors of safety.

We now make a few comments on the measured prefactors b in our study (see Table 1). Predicting such prefactors is beyond the scope of this study, as it would require quantitative fracture experiments. However, such prefactors are important in developing factors of safety. A safety factor for a shell may be defined as the ratio of the maximum force to the typical force that may be resisted by the shell. The concept of safety factor is an important factor in device design and manufacturing. For instance, to design portable and safe helmets for use in sports and the military, one must first choose a particular function for the helmet, such as deflecting a bullet or resisting a fall, and then a factor of safety [Newman 2001]. With regards to natural shells, future workers may gain some insight on safety factors by conducting free-fall experiments. For example, reports by the CDC state that nearly 100% of human falls from six stories or higher are fatal, mainly due to head trauma, followed by abdominal hemorrhage [Stevens 2005]. In our theoretical section, we show that breaking force scales as falling height to the one-half power. Thus, if each story is approximately 2–3 human body lengths, and the skull is designed to survive falling from a single body length, the safety factor for the human skull (asterisk in Figure 3b) should be approximately $\sqrt{12}$–$\sqrt{18} \sim 3.5$–4.2. It would be interesting to examine safety factors for skulls among arboreal animals, in which the height fallen can greatly exceed body length.

In this study, we have focused on strength trends among adult animals. This was because juvenile skulls and shells were generally not readily available in museums. Some juvenile skulls were available for pigs and elephants as shown by the trends in Figure 4b. During growth, pig skulls increased in length by a factor of five, and elephant skulls by a factor of two. Trends in thickness among these two species indicates growth within these species at higher allometric rates ($a > 4$) than for hornless skulls in general. Our methods could not account for this large increase in thickness. Perhaps the thickening helps to offset decreases in bone density with age. For instance, falls by humans are the leading cause of death and injury for those over 65 years of age [Stevens 2005]. Other factors that may affect shell strength are the effect of environmental contaminants such as DDT in reducing shell density or thickness [Green 1998].

While here we examined how structural strength affects skull shape, the effect of hydrodynamic and aerodynamic forces remains unknown. For example, aquatic turtle shells have recently been found to be flattened compared to the land-dwelling turtles studied (Tristan Stayton, personal communication). Other superficial adaptations to the shell may also affect strength without accruing substantial weight; thus, for example, spines and ribs [Strathmann 1981] may deter predators or break a fall.

Appendix: Supplementary information

We describe the mechanics of a spherical shell loaded by a point or an area of pressure, as discussed by Steele [1989]. Consider a vertical point load F acting on a spherical dome of uniform thickness t,

diameter L composed of an isotropic, homogeneous material (see Figure 1). If the shell is sufficiently stiff, loading causes the cap to invert at an edge which lies at an angle $\alpha < 0.3$ with respect to the vertical. This observation has been confirmed qualitatively by Ar et al. [1979], who observed apex flattening of eggshells when loaded. The shells' greatest stresses lie at the edge of this shallow spherical cap, and will be estimated here. The elastic potential energy associated with this dimpled deformation, found using a linear expansion, is

$$U(\alpha) = -FL\frac{\alpha^2}{4} + 2\pi Etc^2\sqrt{\frac{L}{c}}\alpha^3, \tag{A.1}$$

where E is the Young's modulus of the material and c is the reduced thickness, $c = t/\sqrt{12(1 - \nu^2)}$. For a given force, the dimple forms at a position such that the potential energy is a minimum; this occurs at the angle

$$\alpha^* = \frac{FL}{12\pi Etc^2\sqrt{L/c}}. \tag{A.2}$$

As shown in [Steele 1989, Equations 5 and 7b], the bending moment per radius of the shell, M_s, and bending stress σ_b at the edge of this dimple can be expressed as

$$M_s = Etc\sqrt{\frac{4c}{L}}\alpha^*, \qquad \sigma_b = \frac{6M_s}{t^2} = \frac{F}{\pi t^2}. \tag{A.3}$$

Thus, the shell breaks when the stress at the edge exceeds the fracture stress σ_f; this occurs when the applied force exceeds the breaking force, $F = \pi\sigma_f t^2$.

Supplementary information

A table of lengths and thicknesses of skulls and turtle shells is available in the Electronic Supplement.

Acknowledgements

References

[Alexander 1985] R. M. Alexander, "The maximum forces exerted by animals", *J. Exp. Biol.* **115**:1 (1985), 231–238.

[Alexander 1996] R. M. Alexander, *Optima for animals*, Princeton University Press, Princeton, NJ, 1996.

[Alvarez 1990] F. Alvarez, "Horns and fighting in male Spanish ibex, *Capra pyrenaica*", *J. Mammal.* **71**:4 (1990), 608–616.

[Ar et al. 1979] A. Ar, H. Rahn, and C. V. Paganelli, "The avian egg: mass and strength", *Condor* **81**:4 (1979), 331–337.

[Biewener 1990] A. A. Biewener, "Biomechanics of mammalian terrestrial locomotion", *Science* **250**:4984 (1990), 1097–1103.

[Biewener 2003] A. A. Biewener, *Animal locomotion*, Cambridge University Press, Cambridge, 2003.

[Biggs et al. 1976] W. D. Biggs, J. D. Curry, and J. M. Gosline, *Mechanical design in organisms*, Wiley, New York, 1976.

[Boarman 2003] W. I. Boarman, "Managing a subsidized predator population: reducing common raven predation on desert tortoises", *Environ. Manag.* **32**:2 (2003), 205–217.

[Bramble 1974] D. M. Bramble, "Emydid shell kinesis: biomechanics and evolution", *Copeia* **1974**:3 (1974), 707–727.

[Carpenter and Lindsey 1980] K. Carpenter and D. Lindsey, "The dentary of *Brachychampsa montana* Gilmore (Alligatorinae; Crocodylidae), a late Cretaceous turtle-eating alligator", *J. Paleontol.* **54**:6 (1980), 1213–1217.

[Carrier et al. 2002] D. R. Carrier, S. M. Deban, and J. Otterstrom, "The face that sank the *Essex*: potential function of the spermaceti organ in aggression", *J. Exp. Biol.* **205**:12 (2002), 1755–1763.

[Chaudhri et al. 1981] M. M. Chaudhri, J. K. Wells, and A. Stephens, "Dynamic hardness, deformation and fracture of simple ionic crystals at very high rates of strain", *Philos. Mag. A* **43**:3 (1981), 643–664.

[Currey 1988] J. D. Currey, "Shell form and strength", pp. 183–210 in *The mollusca*, edited by E. R. Trueman and M. R. Clarke, Academic Press, San Diego, CA, 1988.

[Currey 2002] J. D. Currey, *Bones: structure and mechanics*, Princeton University Press, Princeton, NJ, 2002.

[Emerson and Bramble 1993] S. B. Emerson and D. M. Bramble, "Scaling, allometry and skull design", pp. 384–421 in *The skull*, vol. 3, edited by J. Hanken and B. K. Hall, University of Chicago Press, New York, 1993.

[Erickson et al. 2003] G. M. Erickson, A. K. Lappin, and K. A. Vliet, "The ontogeny of bite-force performance in American alligator (Alligator mississipiensis)", *J. Zool.* **260**:3 (2003), 317–327.

[Flügge 1973] W. Flügge, *Stresses in shells*, 2nd ed., Springer, New York, 1973.

[Gibbons 1987] J. W. Gibbons, "Why do turtles live so long?", *Biosci.* **37**:4 (1987), 262–269.

[Goldsmith 2001] W. Goldsmith, *Impact: the theory and physical behaviour of colliding solids*, Dover, Mineola, NY, 2001.

[Goodwin and Horner 2004] M. B. Goodwin and J. R. Horner, "Cranial histology of pachycephalosaurs (Ornithischia: Marginocephalia) reveals transitory structures inconsistent with head-butting behavior", *Paleobiol.* **30**:2 (2004), 253–267.

[Green 1998] R. E. Green, "Long-term decline in the thickness of eggshells of thrushes, Turdus spp., in Britain", *Proc. R. Soc. Lond. B* **265**:1397 (1998), 679–684.

[Heyman 1977] J. Heyman, *Equilibrium of shell structures*, Oxford University Press, Oxford, 1977.

[Heyman 1995] J. Heyman, *The stone skeleton: structural engineering of masonry architecture*, Cambridge University Press, Cambridge, 1995.

[Iriarte-Díaz 2002] J. Iriarte-Díaz, "Differential scaling of locomotor performance in small and large terrestrial mammals", *J. Exp. Biol.* **205**:18 (2002), 2897–2908.

[Iverson 1984] J. B. Iverson, "Proportional skeletal mass in turtles", *Fla. Sci.* **47** (1984), 1–11.

[Jackson et al. 1988] A. P. Jackson, J. F. V. Vincent, and R. M. Turner, "The mechanical design of nacre", *Proc. R. Soc. Lond. B* **234**:1277 (1988), 415–440.

[Jaslow and Biewener 1995] C. R. Jaslow and A. A. Biewener, "Strain patterns in the horncores, cranial bones and sutures of goats (*Capra hircus*) during impact loading", *J. Zool.* **235**:2 (1995), 193–210.

[Jennings and Macmillan 1986] J. S. Jennings and N. H. Macmillan, "A tough nut to crack", *J. Mater. Sci.* **21**:5 (1986), 1517–1524.

[Kitchener 1988] A. Kitchener, "An analysis of the forces of fighting of the blackbuck (*Antilope cervicapra*) and the bighorn sheep (*Ovis canadensis*) and the mechanical design of the horn of bovids", *J. Zool.* **214**:1 (1988), 1–20.

[Lundrigan 1996] B. Lundrigan, "Morphology of horns and fighting behavior in the family Bovidae", *J. Mammal.* **77**:2 (1996), 462–475.

[McMahon and Bonner 1985] T. A. McMahon and J. T. Bonner, *On size and life*, pp. 211, Scientific American Library, New York, 1985.

[Meers 2003] M. B. Meers, "Maximum bite force and prey size of *Tyrannosaurus rex* and their relationships to the inference of feeding behavior", *Hist. Biol.* **16**:1 (2003), 1–12.

[Menig et al. 2000] R. Menig, M. H. Meyers, M. A. Meyers, and K. S. Vecchio, "Quasi-static and dynamic mechanical response of *Haliotis rufescens* (abalone) shells", *Acta Mater.* **48**:9 (2000), 2383–2398.

[Miller and Birchard 2005] K. Miller and G. F. Birchard, "Influence of body size on shell mass in the ornate box turtle, *Terrapene Ornata*", *J. Herpetol.* **39**:1 (2005), 158–161.

[Newman 2001] J. A. Newman, "Biomechanics of head trauma: head protection", pp. 303–323 in *Accidental injury*, 2nd ed., edited by A. M. Nahum and J. Melvin, Springer, New York, 2001.

[Pérez-Higareda et al. 1989] G. Pérez-Higareda, A. Rangel-Rangel, H. M. Smith, and D. Chiszar, "Comments on the food and feeding habits of Morelet's crocodile", *Copeia* **1989**:4 (1989), 1039–1041.

[Pritchard 1993] W. G. Pritchard, "Scaling in the animal kingdom", *Bull. Math. Biol.* **55**:1 (1993), 111–129.

[Radinsky 1981] L. B. Radinsky, "Evolution of skull shape in carnivores, 1: Representative modern carnivores", *Biol J. Linn. Soc.* **15**:4 (1981), 369–388.

[Sato et al. 2007] K. Sato, Y. Watanuki, A. Takahashi, P. J. O. Miller, H. Tanaka, R. Kawabe, P. J. Ponganis, Y. Handrich, T. Akamatsu, Y. Watanabe, Y. Mitani, D. P. Costa, C.-A. Bost, K. Aoki, M. Amano, P. Trathan, A. Shapiro, and Y. Naito, "Stroke frequency, but not swimming speed, is related to body size in free-ranging seabirds, pinnipeds and cetaceans", *Proc. R. Soc. Lond. B* **274**:1609 (2007), 471–477.

[Schaffer 1968] W. M. Schaffer, "Intraspecific combat and the evolution of the Caprini", *Evol.* **22**:4 (1968), 817–825.

[Schönwetter 1960] M. Schönwetter, *Handbuch der Oologie*, vol. 1, Lief. 1–2, edited by W. Meise, Akademie Verlag, Berlin, 1960.

[Stancyk 1981] S. E. Stancyk, "Non-human predators of sea turtles and their control", pp. 139–152 in *Biology and conservation of sea turtles: proceedings of the World Conference on Sea Turtle Conservation* (Washington, DC, 1979), edited by K. A. Bjorndal, Smithsonian Institution Press, Washington, DC, 1981.

[Steele 1989] C. R. Steele, "Asymptotic analysis and computation for shells", pp. 3–31 in *Analytical and computation models of shells*, edited by A. K. Noor et al., ASME, New York, 1989.

[Stevens 2005] J. A. Stevens, "Falls among older adults: risk factors and prevention strategies", *J. Saf. Res.* **36**:4 (2005), 409–411.

[Strathmann 1981] R. R. Strathmann, "The role of spines in preventing structural damage to echinoid tests", *Paleobiol.* **7**:3 (1981), 400–406.

[Stronge and Stronge 2000] W. J. Stronge and W. J. Stronge, *Impact mechanics*, Cambridge University Press, Cambridge, 2000.

[Vogel 2003] S. Vogel, *Comparative biomechanics: life's physical world*, Princeton University Press, Princeton, NJ, 2003.

[Wroe et al. 2005] S. Wroe, C. McHenry, and J. Thomason, "Bite club: comparative bite force in big biting mammals and the prediction of predatory behaviour in fossil taxa", *Proc. R. Soc. Lond. B* **272**:1563 (2005), 619–625.

[Zangerl 1969] R. Zangerl, "The turtle shell", pp. 311–339 in *Biology of the reptilia*, edited by C. Gans, Academic Press, London, 1969.

[Zani and Claussen 1995] P. A. Zani and D. L. Claussen, "Effects of extrinsic load on locomotion in painted turtles (*Chrysemys picta*)", *Copeia* **1995**:3 (1995), 735–738.

[Zar 2007] J. H. Zar, *Biostatistical analysis*, Prentice-Hall, Upper Saddle River, NJ, 2007.

[Zuschin and Stanton 2001] M. Zuschin and R. J. Stanton, Jr., "Experimental measurement of shell strength and its taphonomic interpretation", *Palaios* **16**:2 (2001), 161–170.

DAVID L. HU: hu@me.gatech.edu
Schools of Mechanical Engineering and Biology, Georgia Institute of Technology, 801 Ferst Drive, Atlanta, GA 30332-0405, United States

and

Courant Institute of Mathematical Sciences, New York University, 251 Mercer Street, New York, NY 10012-1185, United States

KELLY SIELERT: kes335@nyu.edu
Courant Institute of Mathematical Sciences, New York University, 251 Mercer Street, New York, NY 10012-1185, United States

MICHAEL GORDON: meg320@nyu.edu
Courant Institute of Mathematical Sciences, New York University, 251 Mercer Street, New York, NY 10012-1185, United States

■■
■msp

LINEAR BUCKLING ANALYSIS OF CRACKED PLATES BY SFEM AND XFEM

PEDRO M. BAIZ, SUNDARARAJAN NATARAJAN,
STÉPHANE P. A. BORDAS, PIERRE KERFRIDEN AND TIMON RABCZUK

In this paper, the linear buckling problem for isotropic plates is studied using a quadrilateral element with smoothed curvatures and the extended finite element method. First, the curvature at each point is obtained by a nonlocal approximation via a smoothing function. This element is later coupled with partition of unity enrichment to simplify the simulation of cracks. The proposed formulation suppresses locking and yields elements which behave very well, even in the thin plate limit. The buckling coefficient and mode shapes of square and rectangular plates are computed as functions of crack length, crack location, and plate thickness. The effects of different boundary conditions are also studied.

1. Introduction

Plate-like structures (thin-walled structures) are one of the most widely used structural elements in advanced engineering design, particularly in the aerospace industry. In order to efficiently study such structures, different plate theories have been proposed during the years. In classical plate theory (also known as Kirchhoff) the shear deformation through the plate thickness is neglected because of the assumption that the normal to the middle surface remains normal after deformation. Although for most practical applications this theory is sufficient, it has been proved (see references [5] and [6] in [Reissner 1947]) that the Kirchhoff theory of thin plates is not in accordance with experimental results for problems with stress concentration — stresses at an edge of a hole when the hole diameter is of the same order of magnitude as the plate thickness — or in the case of composite plates, where the ratio of the Young's modulus to the shear modulus can be very large (low transverse shear modulus compared to isotropic materials). In shear deformable plate theory (also referred to as Mindlin or Reissner), it is assumed that the normal-to-the-middle surface will not necessarily remain perpendicular after deformation, adding rotations of the normal as extra unknowns into the partial differential equations, and therefore overcoming problems associated with the application of the classical theory.

A plate structure may lose its ability to withstand external loading when the stored compressive membrane strain energy reaches a critical level. This phenomenon, known as buckling, is characterised by sudden and disproportionate large displacements that could lead to structural failure. In the presence of flaws such as through-the-thickness cracks, critical buckling loads will decrease as a result of the local flexibility provided by the crack, severely affecting the performance of the plate structure. Buckling analysis of isotropic cracked panels has been conducted by researchers analytically and numerically. In

[Stahl and Keer 1972] homogeneous Fredholm integral equations of the second kind were used to solve the eigenvalue problem for cracked plates under compressive loading. Buckling of cracked elastic plates subjected to uniaxial tensile loads was presented in [Markström and Storåkers 1980]. More recently, in [Brighenti 2009] the effects of crack length and orientation on the buckling loads of rectangular elastic thin plates under different boundary conditions were shown, and similarly in [Alinia et al. 2007] for analysis of panels containing central or edge cracks under shear loading, both using the finite element method (FEM). Numerical approaches not based on FEM that address the eigenvalue problem of cracked plates under compressive loading include those of [Liu 2001] using the differential quadrature element method and [Purbolaksono and Aliabadi 2005] using the dual boundary element method. Other works dealing with buckling of cracked plates are [Sih and Lee 1986; Riks et al. 1992; Vafai et al. 2002].

Nowadays, it is well accepted that engineers need to resort to numerical approaches to solve a wider range of practical problems. FEM is the most widely used numerical technique in industry to solve structural problems and a wide range of commercially packages are currently available. Despite its robustness and versatility, FEM efficiency in modelling cracks, discontinuities, and areas of high stress concentration has always been considered an area for improvement since a very refined discretisation is typically necessary in order to obtain accurate solutions. If the discontinuity is moving or is located within a complex geometry, the task of obtaining an acceptable mesh could become very cumbersome and extremely time-consuming.

Extended FEM (XFEM) [Belytschko and Black 1999], which is based on a standard Galerkin procedure and employs the concept of partition of unity proposed in [Babuška et al. 1994], can accommodate the internal boundaries of a crack without regenerating the mesh around the discontinuity. The basic concept behind the method is the incorporation of special local enrichment functions into a standard FEM approximation. Recent areas of XFEM application cover a wide range of scientific and engineering problems, including fracture, dislocations, inclusions, grain boundaries, phase interfaces, multiscale, among others (see [Belytschko et al. 2009] for a recent review). In the particular case of plate bending, the first work on fracture of plates with XFEM was [Dolbow et al. 2000] while in [Areias and Belytschko 2005] a general nonlinear XFEM formulation for analysis of shells was presented. Wyart et al. [2007] presented a mixed-dimensional approach (shell/3D XFEM) for accurate analysis of cracks in thin-walled structures and Bordas et al. [2009] presented applications of strain smoothing in finite element problems with discontinuities and singularities for 2D, 3D, and plate/shell formulations (smoothed extended finite element method (SmXFEM)). In terms of eigenvalue problems, [Bachene et al. 2009; Natarajan et al. 2009b] presented an application of XFEM for the study of the linear vibration of cracked isotropic plates. Other recent works dealing with cracks in thin-walled structures are [Rabczuk and Areias 2006; Rabczuk et al. 2007; 2010].

The strain smoothing concept within FEM (SFEM) was recently proposed in [Liu et al. 2007a], and since then a series of publications addressing the properties and applications of the method in a variety of structural mechanics problems have been presented. Some of the recent papers on the area include: its mathematical foundations [Liu et al. 2007b; Nguyen-Xuan et al. 2008a; Bordas and Natarajan 2010], plate [Nguyen-Xuan et al. 2008b] and shell [Nguyen-Thanh et al. 2008] analyses, limit analysis [Le et al. 2010], and polygonal meshes [Dai et al. 2007]. The main idea behind SFEM is to split a finite element into subcells over which the gradients (strains) are smoothed. If a constant smoothing function is used over each subcell, the area integration can be recast into a line integration along its edges. This allows

for field gradients to be computed directly by only using the shape functions (no derivatives of shape functions are needed), which accordingly reduces the requirement on the smoothness of shape functions. Some of the major advantages of SFEM that have been shown in the literature include: insensitivity to mesh distortion, lower computational cost than FEM for the same accuracy level, flexibility (by offering elements ranging from the standard FEM to quasiequilibrium FEM), insensitivity to locking for low numbers of subcells, and the possibility of constructing arbitrary polygonal elements. This field of research has led to the development of related approaches such as node-based SFEM [Liu et al. 2009b] and edge-based smoothed FEM for 2D problems [Liu et al. 2009a] (called face-based smoothed FEM for 3D problems). Following all these new developments, very recently in [Liu 2010a; 2010b] a theoretical framework was presented to unify the formulation of element-based and mesh-free methods; it attempts to improve the accuracy and efficiency of numerical solutions by using incompatible formulations based on a weakened weak form.

All the above mentioned developments illustrate the great potential of XFEM, particularly when combined with strain smoothing techniques [Bordas et al. 2009]. Some of the areas of improvement that strain smoothing could provide for XFEM are simplifying integration of discontinuous functions by replacing domain integration by boundary integration (see also [Natarajan et al. 2009a; 2010] for techniques suppressing the need for subcells for the integration of discontinuous approximations) and increasing stress and stress intensity factor accuracy.

The present paper is inspired by recent developments that show how curvature smoothing coupled with partition of unity enrichment can produce a plate element capable of cracking which is significantly more accurate than formerly proposed elements [Bordas et al. 2009]. This work attempts specifically to investigate the possibilities of smoothed XFEM for linear plate buckling and the effect of using the smoothing operator for the higher-order terms in the plate buckling equation. First a recently developed curvature strain smoothing plate bending element [Nguyen-Xuan et al. 2008b] is used to study the linear plate buckling phenomena (eigenvalue problem). Then, XFEM is used to obtain critical buckling loads of cracked isotropic shear deformable plates. Finally, the SmXFEM [Bordas et al. 2009] approach is applied to the linear buckling problem of cracked Mindlin–Reissner plates. Some of these approaches have been previously introduced by the authors in the context of free vibration analysis of cracked plates [Natarajan et al. 2009b], but until now the application of SFEM, XFEM, and SmXFEM has not been attempted in the area of linear plate buckling.

2. Mindlin–Reissner plate buckling

2.1. *Basic problem formulation.* Let Ω be the domain of a flat isotropic homogeneous thick plate, Γ the boundary, and h the thickness. The midplane of the plate is taken as the reference plane, see Figure 1.

The basic assumption for displacements is

$$\left\{ \begin{array}{c} u(x, y, z) \\ v(x, y, z) \\ w(x, y, z) \end{array} \right\} = \left\{ \begin{array}{c} z\beta_x(x, y) \\ z\beta_y(x, y) \\ w(x, y) \end{array} \right\}, \tag{1}$$

where $u(x, y, z)$, $v(x, y, z)$, and $w(x, y, z)$ are the components of displacement at a general point in Ω on the x, y, and z axes, respectively; $w(x, y)$ represents the transverse deflection and $\beta_x(x, y)$ and
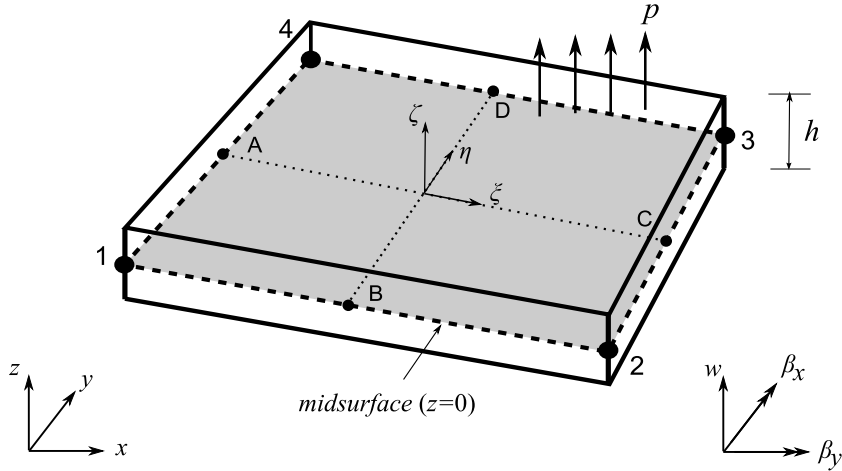
Figure 1. Quadrilateral shear deformable plate element.

$\beta_y(x, y)$ are the rotations in the x and y directions of the middle surface, respectively. The bending and shear strains for Mindlin–Reissner plate theory are given by

$$\kappa = \begin{bmatrix} \beta_{x,x} \\ \beta_{y,y} \\ \beta_{x,y} + \beta_{y,x} \end{bmatrix}, \quad \gamma = \begin{bmatrix} \beta_x + w_{,x} \\ \beta_y + w_{,y} \end{bmatrix}. \tag{2}$$

The total potential energy for a shear deformable plate subjected to in-plane prebuckling stresses ($\hat{\sigma}_0$), in the absence of other external forces and neglecting terms with third and higher powers, can be written as

$$\Pi = \frac{1}{2} \iiint_V \kappa^T Q_b \kappa \, dx \, dy \, dz + \frac{1}{2} \iiint_V \gamma^T Q_s \gamma \, dx \, dy \, dz + \iiint_V \sigma^0_{xx} \varepsilon^{NL}_{xx} \, dx \, dy \, dz$$

$$+ \iiint_V \sigma^0_{yy} \varepsilon^{NL}_{yy} \, dx \, dy \, dz + \iiint_V \sigma^0_{xy} \varepsilon^{NL}_{xy} \, dx \, dy \, dz, \tag{3}$$

where

$$\begin{Bmatrix} \varepsilon^{NL}_{xx} \\ \varepsilon^{NL}_{yy} \\ \varepsilon^{NL}_{xy} \end{Bmatrix} = \begin{Bmatrix} \frac{1}{2}\left((u_{,x})^2 + (v_{,x})^2 + (w_{,x})^2\right) \\ \frac{1}{2}\left((u_{,y})^2 + (v_{,y})^2 + (w_{,y})^2\right) \\ (u_{,x}u_{,y} + v_{,x}v_{,y} + w_{,x}w_{,y}) \end{Bmatrix}. \tag{4}$$

Combining (1)–(4) and integrating over the thickness (3), the total potential energy can be rewritten

$$\Pi = \frac{1}{2} \iint_\Omega \kappa^T D_b \kappa \, dx \, dy + \frac{1}{2} \iint_\Omega \gamma^T D_s \gamma \, dx \, dy + \frac{1}{2} \iint_\Omega [w_{,x} \ \ w_{,y}] \hat{\sigma}_0 \begin{Bmatrix} w_{,x} \\ w_{,y} \end{Bmatrix} h \, dx \, dy$$

$$+ \frac{1}{2} \iint_\Omega [\beta_{x,x} \ \ \beta_{x,y}] \hat{\sigma}_0 \begin{Bmatrix} \beta_{x,x} \\ \beta_{x,y} \end{Bmatrix} \frac{h^3}{12} \, dx \, dy + \frac{1}{2} \iint_\Omega [\beta_{y,x} \ \ \beta_{y,y}] \hat{\sigma}_0 \begin{Bmatrix} \beta_{y,x} \\ \beta_{y,y} \end{Bmatrix} \frac{h^3}{12} \, dx \, dy. \tag{5}$$

The coefficient matrices in (3) are defined as

$$\boldsymbol{D}_b = \frac{Eh^3}{12(1-\nu^2)} \begin{bmatrix} 1 & \nu & 0 \\ \nu & 1 & 0 \\ 0 & 0 & \frac{1}{2}(1-\nu) \end{bmatrix}, \quad \boldsymbol{D}_s = \frac{k_s Eh}{2(1+\nu)} \begin{bmatrix} 1 & 0 \\ 0 & 1 \end{bmatrix}, \tag{6}$$

$$\hat{\boldsymbol{\sigma}}_0 = \begin{bmatrix} \sigma_{xx}^0 & \sigma_{xy}^0 \\ \sigma_{yx}^0 & \sigma_{yy}^0 \end{bmatrix}, \tag{7}$$

where $\boldsymbol{D}_b$ is the bending stiffness matrix, $\boldsymbol{D}_s$ the shear stiffness matrix, E the Young's modulus, ν the Poisson ratio, and k_s the transverse shear correction factor (taken as $\frac{5}{6}$ in this work).

2.2. *Finite element implementation (Q4).* The problem domain Ω will be discretised into a finite number of quadrilateral isoparametric elements Ne:

$$\Omega \approx \Omega^h = \bigcup_{e=1}^{Ne} \Omega^e.$$

Using the shape functions of the quadrilateral element shown in Figure 1, lateral displacement and rotations can be expressed as

$$w = \sum_{i=1}^{4} N_i w_i, \quad \beta_x = \sum_{i=1}^{4} N_i \beta_{xi}, \quad \beta_y = \sum_{i=1}^{4} N_i \beta_{yi}, \tag{8}$$

where w_i, β_{xi}, and β_{yi} denote nodal displacements and rotations and N_i the vector of bilinear shape functions. Using the approximation in (8) the following expansions can be written:

$$\boldsymbol{\kappa} = \boldsymbol{B}_b \boldsymbol{q}, \quad \boldsymbol{\gamma} = \boldsymbol{B}_s \boldsymbol{q}, \tag{9}$$

$$\begin{Bmatrix} w_{,x} \\ w_{,y} \end{Bmatrix} = \boldsymbol{G}_b \boldsymbol{q}, \quad \begin{Bmatrix} \beta_{x,x} \\ \beta_{x,y} \end{Bmatrix} = \boldsymbol{G}_{s1} \boldsymbol{q}, \quad \begin{Bmatrix} \beta_{y,x} \\ \beta_{y,y} \end{Bmatrix} = \boldsymbol{G}_{s2} \boldsymbol{q}, \tag{10}$$

where

$$\boldsymbol{B}_{bi} = \begin{bmatrix} 0 & N_{i,x} & 0 \\ 0 & 0 & N_{i,y} \\ 0 & N_{i,y} & N_{i,x} \end{bmatrix}, \quad \boldsymbol{B}_{si} = \begin{bmatrix} N_{i,x} & N_i & 0 \\ N_{i,y} & 0 & N_i \end{bmatrix}, \quad \boldsymbol{q}_i = \begin{bmatrix} w_i \\ \beta_{xi} \\ \beta_{yi} \end{bmatrix}, \tag{11}$$

$$\boldsymbol{G}_{bi} = \begin{bmatrix} N_{i,x} & 0 & 0 \\ N_{i,y} & 0 & 0 \end{bmatrix}, \quad \boldsymbol{G}_{s1i} = \begin{bmatrix} 0 & N_{i,x} & 0 \\ 0 & N_{i,y} & 0 \end{bmatrix}, \quad \boldsymbol{G}_{s2i} = \begin{bmatrix} 0 & 0 & N_{i,x} \\ 0 & 0 & N_{i,y} \end{bmatrix}. \tag{12}$$

Using (8)–(12), the stationary form of the total potential energy expression (3) can be expressed as

$$(\boldsymbol{K} - \lambda \boldsymbol{K}_G)\boldsymbol{q}^m = 0, \quad m = 1, 2, \ldots \text{ degrees of freedom,}, \tag{13}$$

where $\boldsymbol{K}$ is the global stiffness matrix, $\boldsymbol{K}_G$ is the geometrical stiffness matrix, λ is a scalar by which the chosen in-plane loads must be multiplied in order to cause buckling, and vector $\boldsymbol{q}^m$ is the m-th buckling mode. The stiffness matrices in (13) can be explicitly written as

$$\boldsymbol{K} = \boldsymbol{K}_b + \boldsymbol{K}_s,$$

that is,

$$K = \int_{\Omega^e} B_b^T D_b B_b \, d\Omega^e + \int_{\Omega^e} B_s^T D_s B_s \, d\Omega^e \tag{14}$$

and $K_G K_{Gb} + K_{Gs}$, with

$$K_{Gb} = h \int_{\Omega^e} G_b^T \hat{\sigma}_0 G_b \, d\Omega^e, \tag{15}$$

$$K_{Gs} = \frac{h^3}{12} \int_{\Omega^e} G_{s1}^T \hat{\sigma}_0 G_{s1} \, d\Omega^e + \frac{h^3}{12} \int_{\Omega^e} G_{s2}^T \hat{\sigma}_0 G_{s2} \, d\Omega^e. \tag{16}$$

The shear contribution for the geometric stiffness matrix (K_{Gs}) is negligible for thin plates, but its effect becomes more significant as the plate thickness increases. Most of the available literature dealing with buckling of cracked plates does not consider the effect of (16); therefore, in order to establish meaningful comparisons with the reported literature [Stahl and Keer 1972; Liu 2001; Purbolaksono and Aliabadi 2005] this term could be included or neglected in the numerical solution (in the present work, all examples considered neglect this term).

2.3. *Shear locking.* It is well known that the bilinear element described above exhibits shear locking as the plate thickness approaches the Kirchhoff limit. This is due to the fact that when using the bilinear interpolation for displacements and rotations the transverse shear strains cannot vanish at all points in the element when subjected to a constant bending moment. To overcome this deficiency, various remedies such as reduced integration have been proposed. In the present work, classical reduced integration and MITC (mixed interpolation of tensorial components) [Bathe and Dvorkin 1985] approaches will be used to eliminate shear locking.

In the classical approach, the shear part of the stiffness matrix, K_s in (14), will be integrated using a 1×1 Gauss quadrature to avoid shear locking; this element will be referred to as Q4R.

In the approach proposed by [Bathe and Dvorkin 1985] displacement and rotations are interpolated as usual, but for the transverse shear strains, the covariant components measured in the natural coordinate system are interpolated. Following [Bathe and Dvorkin 1985] for the approximation of the shear strains, the second equation in (2) can be expressed as

$$\gamma = \begin{bmatrix} \gamma_x \\ \gamma_y \end{bmatrix} = J^{-1} \begin{bmatrix} \gamma_\xi \\ \gamma_\eta \end{bmatrix}, \tag{17}$$

with

$$\gamma_\xi = \tfrac{1}{2}[(1-\eta)\gamma_\xi^B + (1+\eta)\gamma_\xi^D], \tag{18}$$

$$\gamma_\eta = \tfrac{1}{2}[(1-\xi)\gamma_\eta^A + (1+\xi)\gamma_\eta^C], \tag{19}$$

where J is the Jacobian matrix and γ_η^A, γ_ξ^B, γ_η^C, and γ_ξ^D are the (physical) shear strains at the midside points A, B, C, and D, shown in Figure 1 together with the global (x, y, z) and local (ξ, η, ζ) coordinate systems. Using (17) and (19) and following the description in [Gruttmann and Wagner 2004], the shear part of the stiffness matrix, K_s in (14), can be rewritten as

$$\bar{B}_{si} = J^{-1} \begin{bmatrix} N_{i,\xi} & b_i^{11} N_{i,\xi} & b_i^{12} N_{i,\xi} \\ N_{i,\eta} & b_i^{21} N_{i,\eta} & b_i^{22} N_{i,\eta} \end{bmatrix}, \tag{20}$$

where

$$b_i^{11} = \xi_i x_{,\xi}^M, \quad b_i^{12} = \xi_i y_{,\xi}^M, \quad b_i^{21} = \eta_i x_{,\eta}^L, \quad b_i^{22} = \eta_i y_{,\eta}^L. \tag{21}$$

The coordinates of the unit square are $\xi_i \in \{-1, 1, 1, -1\}$, $\eta_i \in \{-1, -1, 1, 1\}$ and the allocation of the midside nodes to the corner nodes is given by $(i, M, L) \in \{(1, B, A); (2, B, C); (3, D, C); (4, D, A)\}$, see Figure 1. Using (20), now the shear part of the stiffness matrix (K_s) can be computed using full integration (2×2 Gauss quadrature); this element will be referred to as MITC.

3. Curvature strain smoothing

Strain smoothing has appeared in the finite element literature [Liu et al. 2007a; Nguyen-Xuan et al. 2008b] as an attractive option to obtain increased accuracy at a lower computational cost, deal with mesh distortion, and avoid locking, among other advantages. The idea behind the method is to express the strain field as a spatial average of the compatible strains and use this "smoothed strain" to obtain the element stiffness matrix.

Curvature strain smoothing for plate bending was first proposed in [Wang and Chen 2004] in meshfree methods and in [Nguyen-Xuan et al. 2008b] in a finite element framework. Following the derivation in [Nguyen-Xuan et al. 2008b], the smoothed bending strains for Mindlin–Reissner plates are given as

$$\tilde{\kappa} = \tilde{B}_b^C q, \tag{22}$$

and the corresponding smoothed element bending stiffness matrix is

$$\tilde{K}_b = \int_{\Omega^e} (\tilde{B}_b^C)^T D_b \tilde{B}_b^C \, d\Omega^e = \sum_{C=1}^{nc} \left(\tilde{B}_b^C(x_C) \right)^T D_b \tilde{B}_b^C(x_C) A_C, \tag{23}$$

where nc is the number of smoothing cells in the element. As described in [Nguyen-Xuan et al. 2008b], the integrands are constant over each smoothing cell domain (Ω_C^e) and the nonlocal curvature displacement matrix is given by

$$\tilde{B}_{bi}^C(x_C) = \frac{1}{A_C} \int_{\Gamma_C} \begin{pmatrix} 0 & N_i n_x & 0 \\ 0 & 0 & N_i n_y \\ 0 & N_i n_y & N_i n_x \end{pmatrix} d\Gamma_C. \tag{24}$$

This equation is evaluated using one Gauss point over each boundary cell segment Γ_C^m:

$$\tilde{B}_{bi}^C(x_C) = \frac{1}{A_C} \sum_{m=1}^{mt} \begin{pmatrix} 0 & N_i(x_m^G)n_x(x_m^G) & 0 \\ 0 & 0 & N_i(x_m^G)n_y(x_m^G) \\ 0 & N_i(x_m^G)n_y(x_m^G) & N_i(x_m^G)n_x(x_m^G) \end{pmatrix} l_m^C, \tag{25}$$

where x_m^G is the Gauss point (midpoint of segment m), l_m^C is the length of segment m, and mt is the total number of segments. The expression in (25) already includes the product of the Jacobian of transformation for a 1D 2-node element ($l_m^C/2$) and the Gauss quadrature weight (2). Combining the curvature strain smoothing and the mixed interpolation of tensorial components gives the following expression for

the stiffness matrix of a Mindlin–Reissner plate:

$$\tilde{\boldsymbol{K}} = \tilde{\boldsymbol{K}}_b + \bar{\boldsymbol{K}}_s, \tag{26}$$

$$\tilde{\boldsymbol{K}} = \sum_{C=1}^{nc} \left(\tilde{\boldsymbol{B}}_b^C(\boldsymbol{x}_C)\right)^T \boldsymbol{D}_b \tilde{\boldsymbol{B}}_b^C(\boldsymbol{x}_C) A_C + \int_{\Omega^e} \bar{\boldsymbol{B}}_s^T \boldsymbol{D}_s \bar{\boldsymbol{B}}_s \, d\Omega^e. \tag{27}$$

As mentioned in [Nguyen-Xuan et al. 2008b], this element will be referred to as MISC*k* (mixed interpolation and smoothed curvatures) with $k \in \{1, 2, 3, 4\}$ representing the number of smoothing cells (*nc*). These elements were shown to pass the patch test and to be slightly more accurate than the MITC for regular meshes. The most promising feature was their improved performance for irregular meshes and coarse meshes and their lower computational cost.

3.1. *Smoothing of bending geometric stiffness matrix.* Following a similar approach as the one presented by [Wang and Chen 2004; Nguyen-Xuan et al. 2008b] and shown above, the bending part of the geometric stiffness matrix given in (15) can be written as

$$\tilde{\boldsymbol{K}}_{Gb} = h \int_{\Omega^e} (\tilde{\boldsymbol{G}}_b^C)^T \hat{\boldsymbol{\sigma}}_0 \tilde{\boldsymbol{G}}_b^C \, d\Omega^e = h \sum_{C=1}^{nc} \left(\tilde{\boldsymbol{G}}_b^C(\boldsymbol{x}_C)\right)^T \hat{\boldsymbol{\sigma}}_0 \tilde{\boldsymbol{G}}_b^C(\boldsymbol{x}_C) A_C, \tag{28}$$

where

$$\tilde{\boldsymbol{G}}_{bi}^C(\boldsymbol{x}_C) = \frac{1}{A_C} \int_{\Gamma_C} \begin{pmatrix} N_i n_x & 0 & 0 \\ N_i n_y & 0 & 0 \end{pmatrix} d\Gamma_C. \tag{29}$$

Following the same numerical implementation used for (24), (29) will be evaluated using one Gauss point over each boundary cell segment Γ_C^m:

$$\tilde{\boldsymbol{G}}_{bi}^C(\boldsymbol{x}_C) = \frac{1}{A_C} \sum_{m=1}^{mt} \begin{pmatrix} N_i(\boldsymbol{x}_m^G) n_x(\boldsymbol{x}_m^G) & 0 & 0 \\ N_i(\boldsymbol{x}_m^G) n_y(\boldsymbol{x}_m^G) & 0 & 0 \end{pmatrix} l_m^C. \tag{30}$$

Using this expression in (28) corresponds to smoothing the higher-order bending terms given in (4). This case will be considered in the present work, in order to study the effect of smoothing higher-order terms within a shear deformable plate formulation. This element will be defined as MISC*k*_b (mixed interpolation and smoothed curvatures of global stiffness and geometric stiffness matrix). Similarly to MISC*k*, the number *k* in MISC*k*_b represents the number of smoothing cells in the element.

4. Extended finite element method for shear deformable plates

Following a similar enriched approximation for plate bending as presented in [Dolbow et al. 2000], deflection and rotations can be approximated as

$$\boldsymbol{w}^h(\boldsymbol{x}) = \sum_{i \in N^{\text{fem}}} N_i(\boldsymbol{x}) w_i + \sum_{j \in N^{\text{crack}}} N_j(\boldsymbol{x}) \bar{H}_j(\boldsymbol{x}) b_j^w + \sum_{k \in N^{\text{tip}}} N_k(\boldsymbol{x}) \left(\sum_{l=1}^{4} \bar{G}_{lk}(r, \theta) c_{kl}^w\right), \tag{31}$$

$$\boldsymbol{\beta}^h(\boldsymbol{x}) = \sum_{i \in N^{\text{fem}}} N_i(\boldsymbol{x}) \beta_i + \sum_{j \in N^{\text{crack}}} N_j(\boldsymbol{x}) \bar{H}_j(\boldsymbol{x}) b_j^\beta + \sum_{k \in N^{\text{tip}}} N_k(\boldsymbol{x}) \left(\sum_{l=1}^{4} \bar{F}_{lk}(r, \theta) c_{kl}^\beta\right), \tag{32}$$
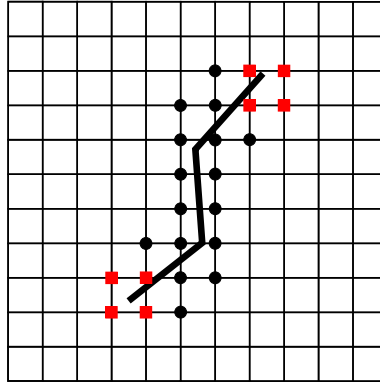
Figure 2. Crack on an uniform mesh of bilinear quadrilateral elements. Circle nodes are enriched by jump functions and square nodes by the asymptotic crack tip field.

where $N(\boldsymbol{x})$ denotes the standard bilinear shape functions, w_i and β_i the nodal unknowns associated with the continuous solution, b_j the nodal enriched degrees of freedom associated with the Heaviside function $\overline{H}_j(\boldsymbol{x})$, and c_{kl} the nodal enriched degrees of freedom associated with the elastic asymptotic crack tip functions $\overline{G}_{lk}(r, \theta)$ and $\overline{F}_{lk}(r, \theta)$. In (31) and (32) N^{fem} is the set of all nodes in the mesh, N^{crack} is the set of nodes whose shape function support is cut by the crack interior (circular nodes in Figure 2), and N^{tip} is the set of nodes whose shape function support is cut by the crack tip (square nodes in Figure 2).

4.1. *Enrichment functions.* The shifted enrichment functions in (31) and (32) are given by

$$\overline{H}_i(\boldsymbol{x}) = \big(H(\boldsymbol{x}) - H(\boldsymbol{x}_i)\big), \tag{33}$$

$$\overline{G}_{li}(\boldsymbol{x}) = \big(G_l(\boldsymbol{x}) - G_l(\boldsymbol{x}_i)\big), \quad \overline{F}_{li}(\boldsymbol{x}) = \big(F_l(\boldsymbol{x}) - F_l(\boldsymbol{x}_i)\big). \tag{34}$$

Shifting the enrichment functions is particularly useful because the influence of the enrichment on the displacement must vanish at the nodes for ease of applying boundary conditions.

The Heaviside enrichment function $H(\boldsymbol{x})$ in (33) is defined by

$$H(\boldsymbol{x}) = \begin{cases} +1 & \text{if the point is above the crack face,} \\ -1 & \text{if the point is below the crack face.} \end{cases} \tag{35}$$

Equation (35) is responsible for the description of the interior of the crack (jump in displacements).

The elastic crack tip enrichment functions in (34) are defined as (see [Dolbow et al. 2000; Bordas et al. 2009])

$$\{G_l(r, \theta)\} \equiv \left\{ r^{3/2} \sin\left(\frac{\theta}{2}\right), r^{3/2} \cos\left(\frac{\theta}{2}\right), r^{3/2} \sin\left(\frac{3\theta}{2}\right), r^{3/2} \cos\left(\frac{3\theta}{2}\right) \right\}, \tag{36}$$

$$\{F_l(r, \theta)\} \equiv \left\{ \sqrt{r} \sin\left(\frac{\theta}{2}\right), \sqrt{r} \cos\left(\frac{\theta}{2}\right), \sqrt{r} \sin\left(\frac{\theta}{2}\right) \sin(\theta), \sqrt{r} \cos\left(\frac{\theta}{2}\right) \sin(\theta) \right\}. \tag{37}$$

Here (r, θ) are polar coordinates with origin at the crack tip. These functions are not only responsible for closing the crack at the tip but they also introduce analytical information in the numerical approximation.

5. Smoothed extended finite element method

In [Bordas et al. 2009] it was shown how strain smoothing could be incorporated into XFEM formulations (including plate bending). In SmXFEM, smoothing must now be performed on discontinuous and nonpolynomial approximations. In the present case, curvature smoothing coupled with partition of unity enrichment can produce a plate element capable of cracking which is significantly more accurate than formerly proposed elements [Bordas et al. 2009].

5.1. *Summary of plate formulations.* As outlined in previous sections, four plate elements (enriched or standard) are considered in the present work:

- Q4R: This plate element uses the basic FE formulation for Mindlin–Reissner plate theory. It uses the standard gradient operators (plain shape function derivatives) for both bending and shear parts, and in order to avoid shear locking the shear part of the stiffness matrix, K_s in (14), will be integrated using a 1×1 Gauss quadrature.

- MITC: This element interpolates the out-of-plane shear stresses using collocation points at the element boundaries. It uses the standard gradient operators for the bending part (K_b), and the mixed interpolation of tensorial components [Bathe and Dvorkin 1985] for the shear part (K_s) of the stiffness matrix, (20).

- MISCk: This element, first introduced in [Nguyen-Xuan et al. 2008b], uses the curvature strain smoothing operator for the bending part given by (25), and the mixed interpolation of tensorial components [Bathe and Dvorkin 1985] for the shear part of the stiffness matrix given by (20), leading to the expression in (27).

- MISCk_b: This element is similar to MISCk but instead of using the standard operator for the bending part of the geometric matrix given by (15), it uses a smoothing operator for the higher-order terms given in (4). In other words, it uses the expression in (27) for the stiffness matrix (K) and the expression in (30) for the bending part of the geometric stiffness matrix (K_{Gb}).

5.2. *Strain smoothing in XFEM plate bending.* In this subsection, detailed description of the SmXFEM implementation for the buckling analysis of cracked Mindlin–Reissner plates is provided. For the sake of simplicity, only the expressions for the enriched MISCk element will be shown here. Enriched smoothed bending strain and enriched shear strain can be written as

$$\tilde{\kappa}^h = \sum_{i \in N^{\text{fem}}} \tilde{B}^C_{b_{\text{fem}}i} q_i + \sum_{j \in N^{\text{crack}}} \tilde{B}^C_{b_{\text{crack}}j} b_j + \sum_{k \in N^{\text{tip}}} \tilde{B}^C_{b_{\text{tip}}k} c_k, \tag{38}$$

$$\gamma^h = \sum_{i \in N^{\text{fem}}} \bar{B}_{s_{\text{fem}}i} q_i + \sum_{j \in N^{\text{crack}}} \bar{B}_{s_{\text{crack}}j} b_j + \sum_{k \in N^{\text{tip}}} \bar{B}_{s_{\text{tip}}k} c_k. \tag{39}$$

The enriched gradient operators in (38) and (39) can be explicitly written as

$$\tilde{B}^C_{b_{\text{crack}}j}(x_C) = \frac{1}{A_C} \sum_{m=1}^{mt} \begin{pmatrix} 0 & N_j(x_m^G)\bar{H}_j(x_m^G)n_x(x_m^G) & 0 \\ 0 & 0 & N_j(x_m^G)\bar{H}_j(x_m^G)n_y(x_m^G) \\ 0 & N_j(x_m^G)\bar{H}_j(x_m^G)n_y(x_m^G) & N_j(x_m^G)\bar{H}_j(x_m^G)n_x(x_m^G) \end{pmatrix} l_m^C, \tag{40}$$

$$\tilde{\boldsymbol{B}}^{C}_{b_{\text{tip}}k}(\boldsymbol{x}_C)\big|_{l=1,2,3,4} = \frac{1}{A_C} \sum_{m=1}^{mt} \begin{pmatrix} 0 & N_k(\boldsymbol{x}_m^G)\overline{F}_{lk}(\boldsymbol{x}_m^G)n_x(\boldsymbol{x}_m^G) & 0 \\ 0 & 0 & N_k(\boldsymbol{x}_m^G)\overline{F}_{lk}(\boldsymbol{x}_m^G)n_y(\boldsymbol{x}_m^G) \\ 0 & N_k(\boldsymbol{x}_m^G)\overline{F}_{lk}(\boldsymbol{x}_m^G)n_y(\boldsymbol{x}_m^G) & N_k(\boldsymbol{x}_m^G)\overline{F}_{lk}(\boldsymbol{x}_m^G)n_x(\boldsymbol{x}_m^G) \end{pmatrix} l_m^C \qquad (41)$$

and

$$\overline{\boldsymbol{B}}_{s_{\text{crack}}j} = \boldsymbol{J}^{-1} \begin{bmatrix} [N_j(\boldsymbol{x})\overline{H}_j(\boldsymbol{x})]_{,\xi} & b_j^{11}[N_j(\boldsymbol{x})\overline{H}_j(\boldsymbol{x})]_{,\xi} & b_j^{12}[N_j(\boldsymbol{x})\overline{H}_j(\boldsymbol{x})]_{,\xi} \\ [N_j(\boldsymbol{x})\overline{H}_j(\boldsymbol{x})]_{,\eta} & b_j^{21}[N_j(\boldsymbol{x})\overline{H}_j(\boldsymbol{x})]_{,\eta} & b_j^{22}[N_j(\boldsymbol{x})\overline{H}_j(\boldsymbol{x})]_{,\eta} \end{bmatrix}, \qquad (42)$$

$$\overline{\boldsymbol{B}}_{s_{\text{tip}}k}\big|_{l=1,2,3,4} = \boldsymbol{J}^{-1} \begin{bmatrix} [N_k(\boldsymbol{x})\overline{G}_{lk}(\boldsymbol{x})]_{,\xi} & b_i^{11}[N_k(\boldsymbol{x})\overline{F}_{lk}(\boldsymbol{x})]_{,\xi} & b_i^{12}[N_k(\boldsymbol{x})\overline{F}_{lk}(\boldsymbol{x})]_{,\xi} \\ [N_k(\boldsymbol{x})\overline{G}_{lk}(\boldsymbol{x})]_{,\eta} & b_i^{21}[N_k(\boldsymbol{x})\overline{F}_{lk}(\boldsymbol{x})]_{,\eta} & b_i^{22}[N_k(\boldsymbol{x})\overline{F}_{lk}(\boldsymbol{x})]_{,\eta} \end{bmatrix}. \qquad (43)$$

Similarly, for the bending and shear part of the geometric stiffness, the enriched gradient operators can be expressed as

$$\boldsymbol{G}_{b_{\text{crack}}j} = \begin{bmatrix} [N_j(\boldsymbol{x})\overline{H}_j(\boldsymbol{x})]_{,x} & 0 & 0 \\ [N_j(\boldsymbol{x})\overline{H}_j(\boldsymbol{x})]_{,y} & 0 & 0 \end{bmatrix}, \qquad \boldsymbol{G}_{b_{\text{tip}}k}\big|_{l=1,2,3,4} = \begin{bmatrix} [N_k(\boldsymbol{x})\overline{G}_{lk}(\boldsymbol{x})]_{,x} & 0 & 0 \\ [N_k(\boldsymbol{x})\overline{G}_{lk}(\boldsymbol{x})]_{,y} & 0 & 0 \end{bmatrix}, \qquad (44)$$

$$\boldsymbol{G}_{s1_{\text{crack}}j} = \begin{bmatrix} 0 & [N_j(\boldsymbol{x})\overline{H}_j(\boldsymbol{x})]_{,x} & 0 \\ 0 & [N_j(\boldsymbol{x})\overline{H}_j(\boldsymbol{x})]_{,y} & 0 \end{bmatrix}, \qquad \boldsymbol{G}_{s1_{\text{tip}}k}\big|_{l=1,2,3,4} = \begin{bmatrix} 0 & [N_k(\boldsymbol{x})\overline{F}_{lk}(\boldsymbol{x})]_{,x} & 0 \\ 0 & [N_k(\boldsymbol{x})\overline{F}_{lk}(\boldsymbol{x})]_{,y} & 0 \end{bmatrix}, \qquad (45)$$

$$\boldsymbol{G}_{s2_{\text{crack}}j} = \begin{bmatrix} 0 & 0 & [N_j(\boldsymbol{x})\overline{H}_j(\boldsymbol{x})]_{,x} \\ 0 & 0 & [N_j(\boldsymbol{x})\overline{H}_j(\boldsymbol{x})]_{,y} \end{bmatrix}, \qquad \boldsymbol{G}_{s2_{\text{tip}}k}\big|_{l=1,2,3,4} = \begin{bmatrix} 0 & 0 & [N_k(\boldsymbol{x})\overline{F}_{lk}(\boldsymbol{x})]_{,x} \\ 0 & 0 & [N_k(\boldsymbol{x})\overline{F}_{lk}(\boldsymbol{x})]_{,y} \end{bmatrix}. \qquad (46)$$

5.3. *Integration.* As mentioned, the integrations of the discretised terms presented in the previous sections are done using Gauss quadrature. In the present work boundary and domain integrals are evaluated for the MISCk and MISCk_b elements (the smoothed terms are evaluated using surface integrals, whereas the nonsmooth are obtained using domain integration) and only domain integrals for the classical Q4R and MITC elements.

The standard (nonenriched) domain integration uses 2×2 Gauss quadrature as it evaluates the bilinear shape functions sufficiently. The only exception to the standard (nonenriched) domain integration is with the shear part of the stiffness matrix, $\boldsymbol{K}_s$ in (14), which uses 1×1 Gauss quadrature.

For standard surface integration, terms in (25) and (30), two subcells with one Gauss point per boundary are used, as recommended in [Nguyen-Xuan et al. 2008b]; in this way computational efficiency and numerical stability are guaranteed. This implies that MISC2 and MISC2_b are the specific smoothed elements used in the present work.

For elements that are enriched the integration has to be adapted, so that the weak form on both sides of the crack contributes the correct enriched terms. The most common approach, which is also implemented here, is to subtriangulate the element (for example, Delaunay triangulation) in a way that the triangle edges conform with the discontinuity.

In the case of enriched elements using domain integration the following integration rules are used:

- Tip-blending elements: 16 Gauss points for the total element.
- Split-blending elements: 2 Gauss points for the total element.
- Split-tip-blending elements: 4 Gauss points for each triangular subelement.
- Split elements: 3 Gauss points for each triangular subelement.
- Tip elements: 13 Gauss points for each triangular subelement.

In the case of enriched elements using surface integration (smoothed enriched elements) the following integration rules are used:

- Tip-blending elements: 8 subcells with 1 Gauss points per edge.
- Split-blending elements: 2 subcells with 1 Gauss points per edge.
- Split-tip-blending elements: 4 subelements, each with 4 subcells with 1 Gauss points per edge.
- Split elements: 4 subelements, each with 2 subcells with 1 Gauss points per edge.
- Tip elements: 4 subelements, each with 8 subcells with 1 Gauss points per edge.

As in standard XFEM, there are 6 different types of elements:

- Tip elements are elements that contain the crack tip. All nodes belonging to a tip element are enriched with the near-tip fields ($\overline{G}_l(\boldsymbol{x})$ and $\overline{F}_l(\boldsymbol{x})$).
- Split elements are elements completely cut by the crack. Their nodes are enriched with the discontinuous function $\overline{H}(\boldsymbol{x})$.
- Tip-blending elements are elements neighbouring tip elements. They are such that some of their nodes are enriched with the near-tip fields ($\overline{G}_l(\boldsymbol{x})$ and $\overline{F}_l(\boldsymbol{x})$) and others are not enriched at all.
- Split-blending elements are elements neighbouring split elements. They are such that some of their nodes are enriched with the discontinuous function, $\overline{H}(\boldsymbol{x})$, and others are not enriched at all.
- Split-tip-blending elements are elements completely cut by the crack and neighbouring tip elements. They are such that all of their nodes are enriched with the discontinuous function, $\overline{H}(\boldsymbol{x})$, and some of their nodes are enriched with the near-tip fields ($\overline{G}_l(\boldsymbol{x})$ and $\overline{F}_l(\boldsymbol{x})$).
- Standard elements are elements that are in neither of the above categories. None of their nodes are enriched.

6. Numerical examples

In this section the formulation presented in the previous paragraphs is now applied to determine the normalised buckling coefficients for rectangular plates with different thicknesses (h/a), crack sizes (c/a), and boundary conditions. The plates have Young's modulus E, Poisson's ratio $\nu = 0.3$, length a (sides), and width b (ends). The compressive stress is applied in the longitudinal direction; see Figure 3. The results are compared with available analytical and numerical solutions when available. Due to the crack orientation considered in all examples (Figure 3) traction free boundary conditions (no contact between crack faces) can be assumed in all cases.

Normalised results are obtained using the classical plate buckling coefficient (K):

$$K = \frac{b^2}{\pi^2 D}\sigma_{\text{cr}} = \frac{12(1 - \nu^2)b^2}{\pi^2 E h^3}\lambda\sigma. \tag{47}$$

Plate boundary conditions are defined as follows:

$$\text{Simply supported:} \quad w = 0, \quad \beta_t = 0,$$

$$\text{Clamped:} \quad w = 0, \quad \beta_n = 0, \quad \beta_t = 0,$$

where n denotes normal and t tangential directions to the plate boundary.
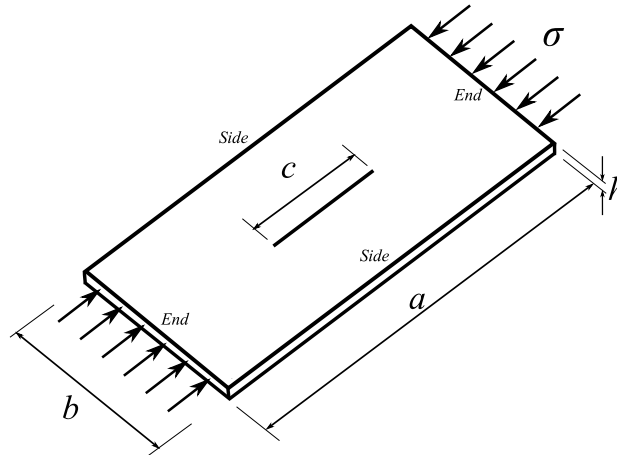
Figure 3. Centre crack plate geometry.

6.1. ***Buckling of simply supported plate (convergence).*** The first problem to be considered involves simply supported thin and thick square plates with no crack ($c/a = 0$). This example will illustrate the convergence performance of the recently developed MISC2 [Nguyen-Xuan et al. 2008b] and MISC2_b elements within the linear buckling problem (eigenvalue problem).

Six different uniform element distributions are considered in the convergence study (as shown in Tables 1 and 2). An analytical solution for linear buckling of Mindlin–Reissner plates was recently introduced

Mesh density	Q4R	MITC	MISC2	MISC2_b
11×11	4.0715 (1.79%)	4.0437 (1.09%)	4.0320 (0.80%)	4.0389 (0.97%)
15×15	4.0371 (0.93%)	4.0223 (0.56%)	4.0161 (0.40%)	4.0198 (0.49%)
19×19	4.0222 (0.55%)	4.013 (0.32%)	4.0092 (0.23%)	4.0115 (0.29%)
23×23	4.0144 (0.36%)	4.0082 (0.21%)	4.0055 (0.14%)	4.0071 (0.18%)
27×27	4.0098 (0.25%)	4.0053 (0.13%)	4.0034 (0.09%)	4.0045 (0.11%)
31×31	4.0069 (0.17%)	4.0035 (0.09%)	4.0020 (0.05%)	4.0029 (0.07%)

Table 1. Convergence of simply supported square plate with thickness ratio $h/a = 0.01$ (thin plate analytical solution $K = 4.000$).

Mesh density	Q4R	MITC	MISC2	MISC2_b
11×11	3.3127 (1.50%)	3.2943 (0.94%)	3.2865 (0.70%)	3.2922 (0.87%)
15×15	3.2899 (0.80%)	3.2801 (0.50%)	3.2760 (0.38%)	3.2790 (0.47%)
19×19	3.2800 (0.50%)	3.2739 (0.31%)	3.2713 (0.23%)	3.2732 (0.29%)
23×23	3.2748 (0.34%)	3.2707 (0.21%)	3.2689 (0.16%)	3.2702 (0.20%)
27×27	3.2718 (0.25%)	3.2688 (0.16%)	3.2675 (0.12%)	3.2684 (0.14%)
31×31	3.2698 (0.19%)	3.2676 (0.12%)	3.2666 (0.09%)	3.2673 (0.11%)

Table 2. Convergence of simply supported square plate with thickness ratio $h/a = 0.2$ (thick plate analytical solution $K = 3.2922$ [Hosseini-Hashemi et al. 2008]).
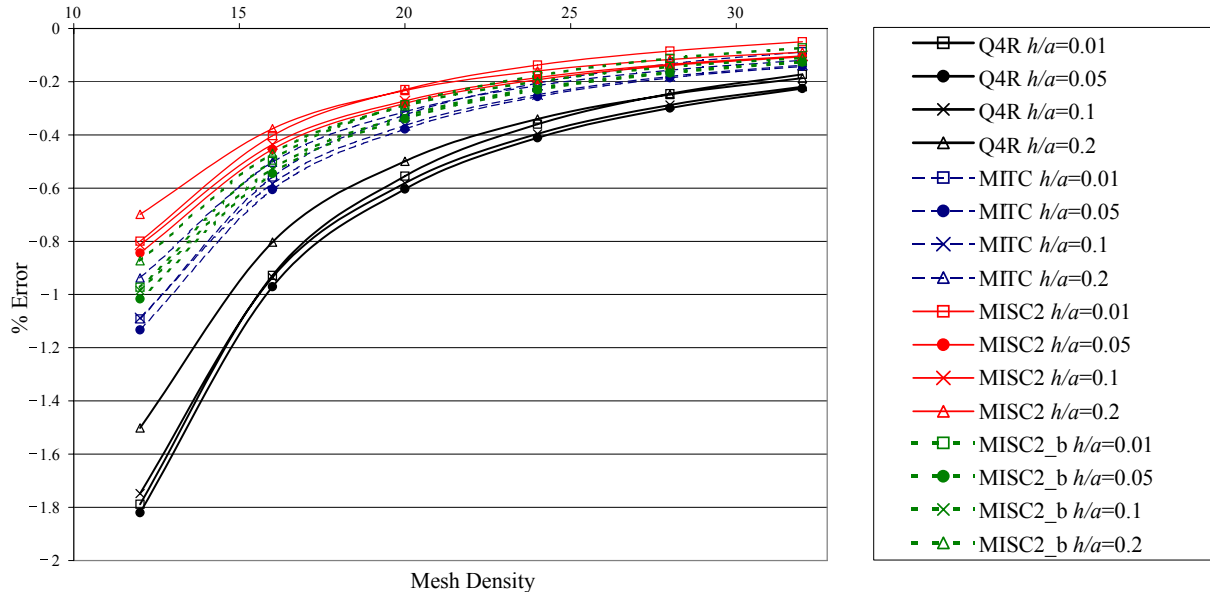
Figure 4. Convergence of normalised buckling coefficient for simply supported square $(a/b = 1)$ plates $(c/a = 0)$.

in [Hosseini-Hashemi et al. 2008] for a wide range of plate thicknesses that covers both thin and thick plates. Figure 4 presents an error comparison for each plate thickness ($h/a = 0.01, 0.05, 0.1, 0.2$) of all the elements considered in the present work. Additionally, Tables 1 and 2 present detailed results for only thin ($h/a = 0.01$) and very thick plates ($h/a = 0.2$), respectively.

As mentioned, the shear contribution for the geometric stiffness matrix ($\boldsymbol{K}_{Gs}$) is neglected in all cases in order to establish meaningful comparisons with the available analytical results [Stahl and Keer 1972; Liu 2001; Purbolaksono and Aliabadi 2005; Hosseini-Hashemi et al. 2008]. As can be seen from Figure 4, all results agree well with the analytical solution, with less than 2% difference for even the less refined mesh. The largest errors are obtained using the classical Q4R element while the smallest errors are obtained with the MISC2 element (always less than 1% error for even the less refined case). The MITC results are better than for the classical Q4R element but less accurate than the MISC2 and MISC2_b. Finally, it is possible to see from Figure 4 that the smoothed buckling element (MISC2_b) gives improved results over the MITC element but not better than the MISC2 element, implying that smoothing the higher powers of deformation given in (4) does not improve the element performance for regular meshes (not distorted).

Figure 5 shows the buckling modes for the coarsest mesh (11×11) used in the present example. The classical 1, 2, and 3 half ways expected for modes 1, 2, and 3 are clear in Figure 5.

6.2. *Sensitivity to mesh distortion of uncracked plates.* This second example will consider the effect of mesh distortion on the recently developed MISC2 [Nguyen-Xuan et al. 2008b] and MISC2_b elements within the linear buckling problem (eigenvalue problem). To study the effect of mesh distortion on the results, interior nodes are moved by an irregularity factor s. The coordinates of interior nodes are
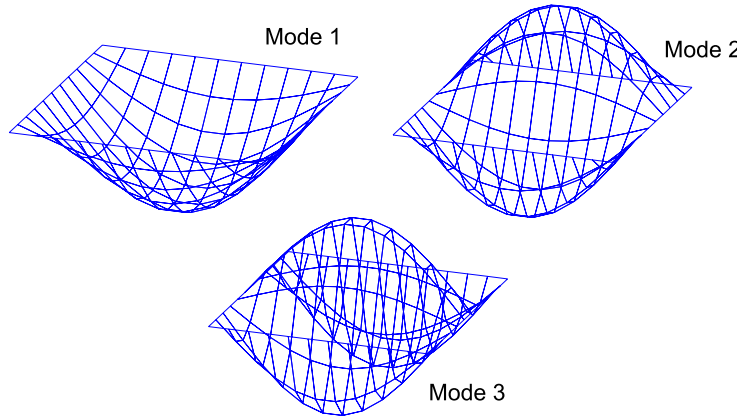
Figure 5. Buckling modes for simply supported square ($a/b = 1$) plate ($c/a = 0$).

obtained by the expressions [Liu et al. 2007a]

$$x' = x + sr_c\Delta x, \quad y' = y + sr_c\Delta y,$$

where r_c is a randomly generated number between -1.0 and 1.0, $s \in [0, 0.4]$ is used to control the degree of element distortion, and Δx and Δy are initial regular element sizes in the x and y directions, respectively.

Thin ($h/a = 0.01$) and thick ($h/a = 0.1$) simply supported square plates ($a/b = 1$) with no crack ($c/a = 0$) will be considered. The less refined mesh of the previous example (11×11 elements) will be used in all cases (see Figure 6).

Tables 3 and 4 provide the buckling coefficients for thin ($h/a = 0.01$) and thick plates ($h/a = 0.1$), respectively, and Figure 7 plots the normalised values for both cases. In the case of thin plates, the classical Q4R shows the largest errors while the newly presented MISC2_b (with smoothed bending part of the geometric stiffness matrix) provides the best results. A similar behaviour occurs for thick plates but with much less detrimental effects for the classical Q4R. This dependency of mesh distortion on plate thickness has been shown in previous works [Nguyen-Xuan et al. 2008b].
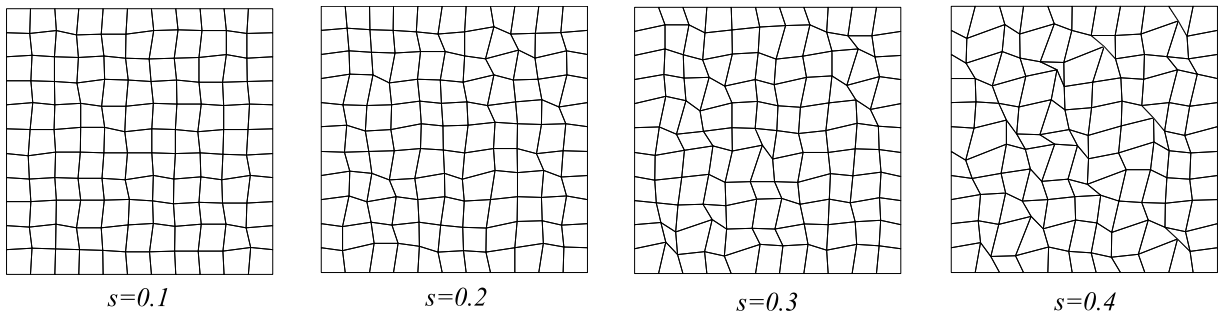

$s=0.1$ $s=0.2$ $s=0.3$ $s=0.4$

Figure 6. Effect of mesh distortion parameter in square plate with 11×11 elements.
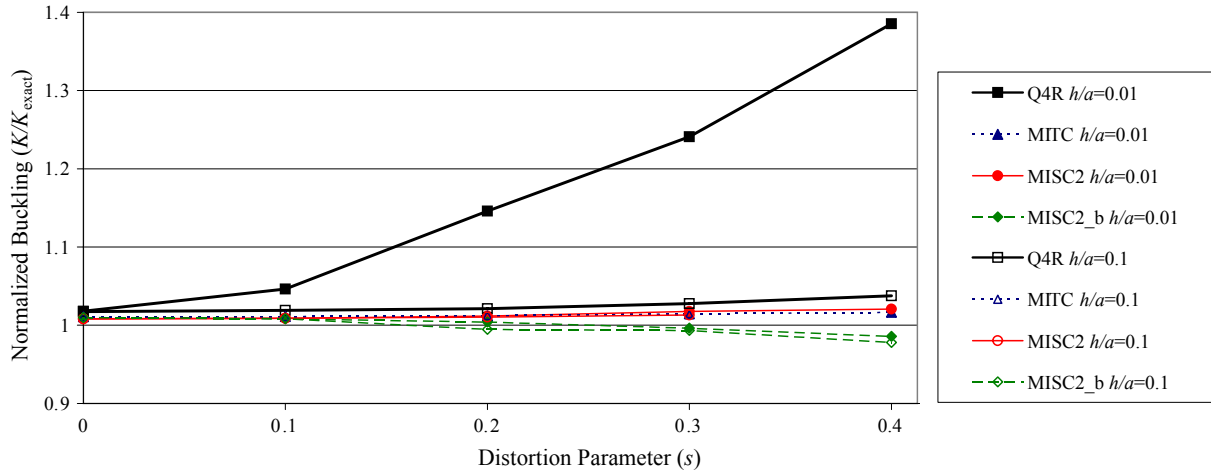
Figure 7. Influence of mesh distortion for buckling coefficient of simply supported square thin and thick plates.

From results in Tables 3 and 4 it is clear that although results for the smoothed buckling element (MISC2_b) give results that are not as accurate as the MISC2 element for regular meshes (no distortion), smoothing the higher powers of deformation given in (4) does improve the element performance for irregular meshes.

Mesh distortion	Q4R	MITC	MISC2	MISC2_b
0.0	4.0715 (1.79%)	4.0437 (1.09%)	4.0320 (0.80%)	4.0389 (0.97%)
0.1	4.1853 (4.63%)	4.0453 (1.13%)	4.0353 (0.88%)	4.0333 (0.83%)
0.2	4.5838 (14.6%)	4.0478 (1.19%)	4.0467 (1.17%)	4.0170 (0.43%)
0.3	4.9639 (24.1%)	4.0594 (1.48%)	4.0708 (1.77%)	3.9854 (0.37%)
0.4	5.5411 (38.5%)	4.0666 (1.66%)	4.0825 (2.06%)	3.9428 (1.43%)

Table 3. Effect of mesh distortion for simply supported square plate with thickness ratio $h/a = 0.01$ (thin plate analytical solution $K = 4.000$).

Mesh distortion	Q4R	MITC	MISC2	MISC2_b
0.0	3.8526 (1.75%)	3.8276 (1.09%)	3.8172 (0.81%)	3.8237 (0.99%)
0.1	3.8585 (1.90%)	3.8291 (1.13%)	3.8203 (0.89%)	3.8183 (0.84%)
0.2	3.8665 (2.12%)	3.8342 (1.26%)	3.8259 (1.04%)	3.7663 (0.53%)
0.3	3.8911 (2.76%)	3.8382 (1.37%)	3.8359 (1.31%)	3.7616 (0.65%)
0.4	3.9291 (3.77%)	–	–	3.7029 (2.20%)

Table 4. Effect of mesh distortion for simply supported square plate with thickness ratio $h/a = 0.1$ (thick plate analytical solution $K = 3.7864$ [Hosseini-Hashemi et al. 2008]).

6.3. *Sensitivity to mesh distortion of plates with a longitudinal centre crack.* This example extends on the previous example by including a longitudinal centre crack in the distorted mesh. Again, the same mesh density of the previous example will be used to obtain buckling coefficients of thin ($h/a = 0.01$) and thick ($h/a = 0.1$) simply supported square plates ($a/b = 1$) with a longitudinal centre crack ($c/a = 0.2$).

Tables 5 and 6 provide the buckling coefficients for thin ($h/a = 0.01$) and thick plates ($h/a = 0.1$), respectively; Figure 8 plots the normalised values for both cases. Table 5 shows why the classical Q4R is not used in XFEM plate formulations as it exhibits locking when modelling thin cracked plates (at least 50% error for regular meshes). The relatively large errors exhibited by other elements ($\sim$6%) is due to the coarse mesh size (11×11 elements) as will be shown in next examples.

6.4. *Rectangular plate with a longitudinal centre crack.* This example considers simply supported square and rectangular plates of different thickness ($h/a = 0.01, 0.1, 0.2$) with longitudinal centre cracks, as shown in Figure 3. All results were obtained with uniform meshes of 31×31 and 19×38 elements for the square and rectangular plates, respectively.

Figure 9 shows results for the square ($a/b = 1$) plates with Q4R-MITC and MISC2-MISC2_b elements, respectively. The classical Q4R element exhibits locking when modelling thin cracked plates ($h/a = 0.01$), and therefore are not shown in Figure 9. This is because when enriched elements are present in the model, a higher quadrature than 1×1 must be used (as mentioned in Section 5.3), leading to inaccurate results in the thin plate limit. All other elements exhibit an excellent performance for both thin and thick plates.

Mesh distortion	Q4R	MITC	MISC2	MISC2_b
0.0	5.8248 (52.2%)	4.0229 (5.15%)	4.0325 (5.40%)	4.0394 (5.58%)
0.1	6.1392 (60.5%)	4.0274 (5.27%)	4.0381 (5.55%)	4.0356 (5.48%)
0.2	6.5515 (71.2%)	4.0286 (5.30%)	4.0477 (5.80%)	3.9894 (4.27%)
0.3	7.2942 (90.7%)	4.0310 (5.36%)	4.0889 (6.87%)	3.9872 (4.21%)
0.4	–	–	–	3.9568 (3.42%)

Table 5. Effect of mesh distortion for simply supported square plate with thickness ratio $h/a = 0.01$ and longitudinal centre crack $c/a = 0.2$ (thin plate exact solution $K = 3.8259$ [Stahl and Keer 1972]).

Mesh distortion	Q4R	MITC	MISC2	MISC2_b
0.0	3.8235 (8.05%)	3.6606 (3.44%)	3.8170 (7.86%)	3.8236 (8.05%)
0.1	3.8158 (7.83%)	3.6569 (3.34%)	3.8185 (7.90%)	3.8142 (7.78%)
0.2	3.7931 (7.19%)	3.6497 (3.14%)	3.8256 (8.11%)	3.8003 (7.39%)
0.3	3.8800 (9.64%)	3.6931 (4.36%)	3.8474 (8.72%)	3.7538 (6.08%)
0.4	3.9557 (11.8%)	3.7160 (5.08%)	3.8553 (8.94%)	3.6420 (2.92%)

Table 6. Effect of mesh distortion for simply supported square plate with thickness ratio $h/a = 0.1$ and longitudinal centre crack $c/a = 0.2$ (thick plate solution $K = 3.53879$ [Liu 2001]).
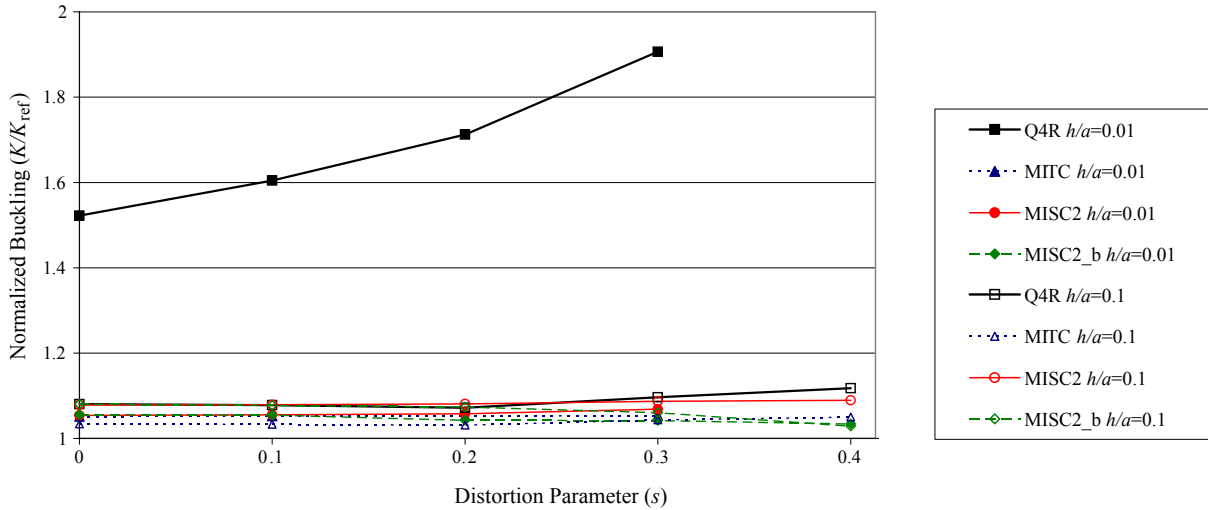
Figure 8. Influence of mesh distortion for buckling coefficient of simply supported square centre cracked ($c/a = 0.2$) thin and thick plates.
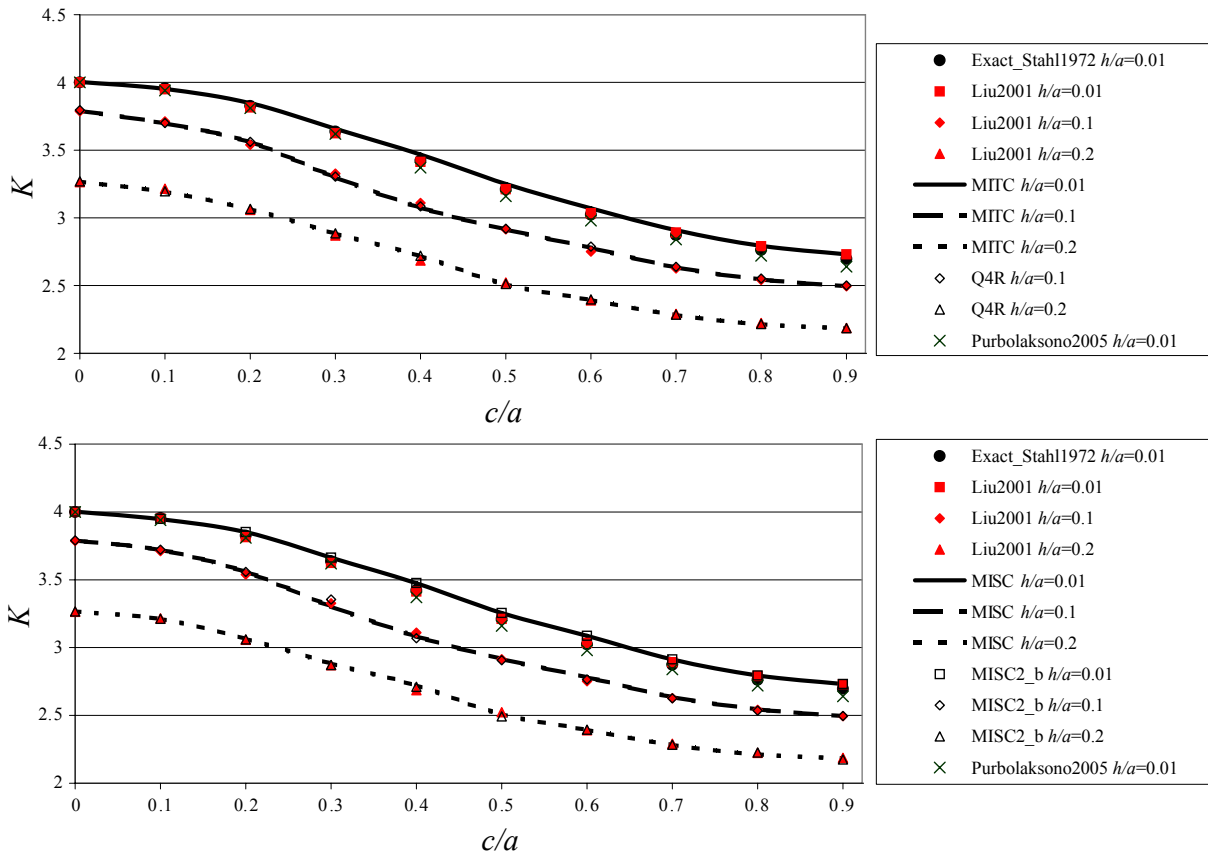

Figure 9. Buckling coefficients for square ($a/b = 1$) centre cracked plates. Top: Q4R and MITC. Bottom: MISC2 and MISC2_b.
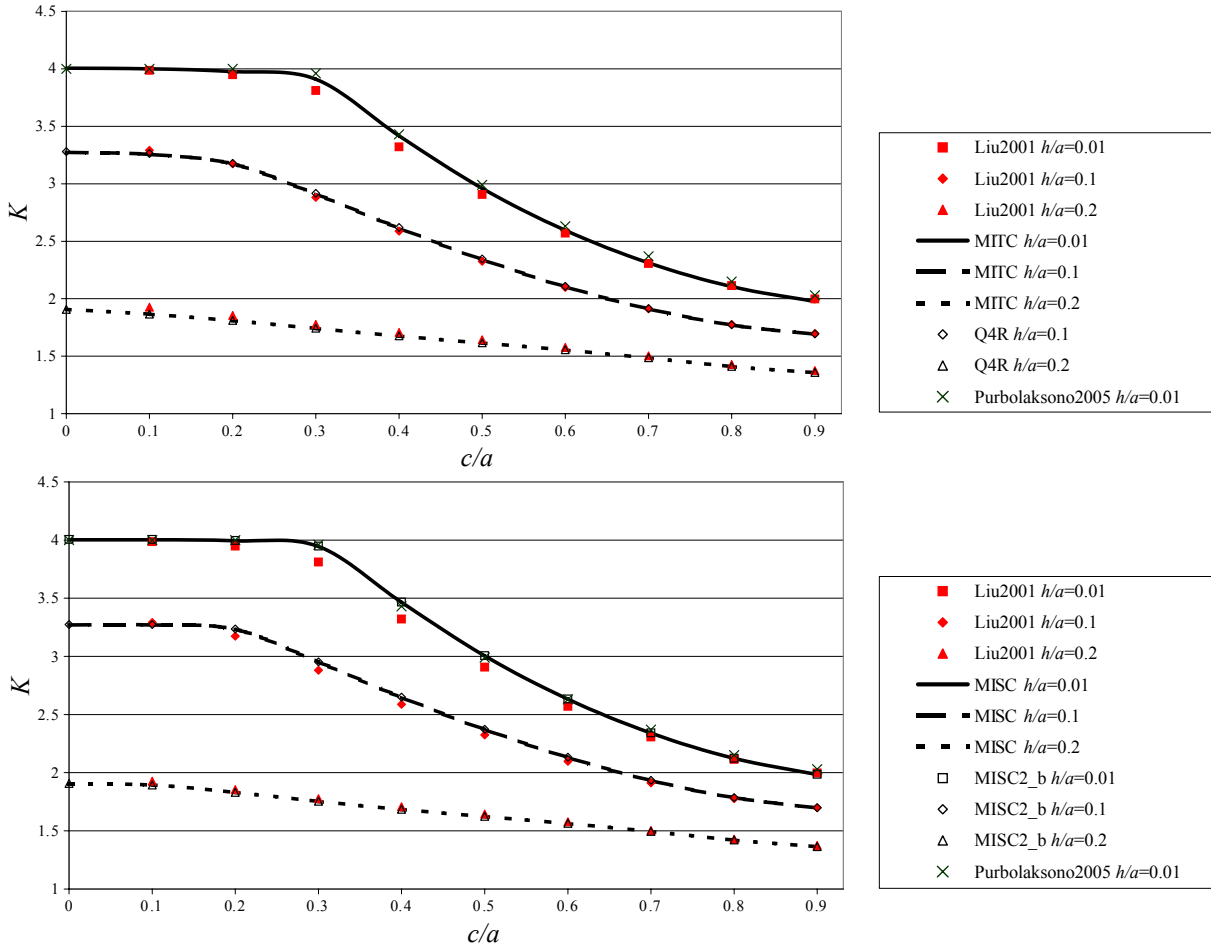
Figure 10. Buckling coefficients for rectangular ($a/b = 2$) centre cracked plates. Top: Q4R and MITC. Bottom: MISC2 and MISC2_b.

Figure 10 shows results for rectangular ($a/b = 2$) plates with Q4R-MITC and MISC2-MISC2_b elements, respectively. Again, results with the classical Q4R element are excluded for thin cracked plates ($h/a = 0.01$), due to locking.

As shown in Figures 9 and 10, an increase in crack length and thickness leads to a decrease on the critical buckling load. The 3 plate thicknesses ($h/a = 0.01, 0.1, 0.2$) and 10 crack sizes considered ($c/a = 0.0, 0.1, 0.2, 0.3, 0.4, 0.5, 0.6, 0.7, 0.8, 0.9$) give a clear picture of the behaviour of cracked thin and thick plates. In all cases results converge to the noncracked solution of thin and thick plates presented in the previous example.

In all cases good agreement is obtained with reported results (approximately 2% difference). The largest discrepancy (∼3%) between reported solutions occurs for short-medium crack sizes ($a/c = 0.2, 0.3, 0.4, 0.5$) in rectangular plates (Figure 10). In this area the present results agree more with the results in [Purbolaksono and Aliabadi 2005] than with [Liu 2001], particularly for the MISC2 and MISC2_b elements.
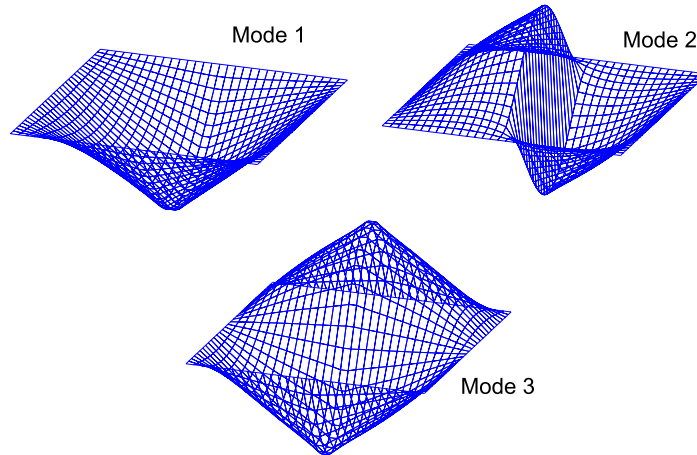
Figure 11. Buckling modes for simply supported centre cracked ($c/a = 0.9$) square plate ($a/b = 1$).
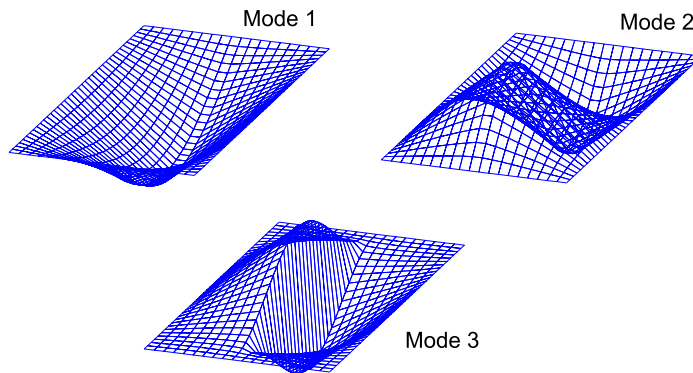

Figure 12. Buckling modes for simply supported centre cracked ($c/a = 0.9$) rectangular plate ($a/b = 2$).

Buckling modes for square and rectangular thin plates ($h/a = 0.01$) with the largest crack size ($a/c = 0.9$) are given in Figures 11 and 12, respectively. It is clear, by comparing Figures 5 and 11 that buckling modes change with the presence of the crack, in this case by adding a new mode (mode 2 in Figure 11) that replaces the classical second mode of 2 half waves (now mode 3 in Figure 11). Similarly, in the case of rectangular plates, instead of the classical 2 half waves for mode 1, now the presence of the crack leads to only 1 half waves mode (mode 1 in Figure 12).

6.5. *Rectangular plate with a longitudinal edge crack.* In this example, simply supported rectangular ($a/b = 2$) thin and thick plates with a transverse edge crack as shown in Figure 13 are analysed. Buckling coefficients for Q4R (except for the thin plate case $h/a = 0.01$) and MITC elements are given with respect to the normalised crack size in the top part of Figure 14. Similarly, the bottom part of the same figure shows buckling coefficients for MISC2 and MISC2_b elements. All results were obtained with an uniform mesh of 19×38 elements.
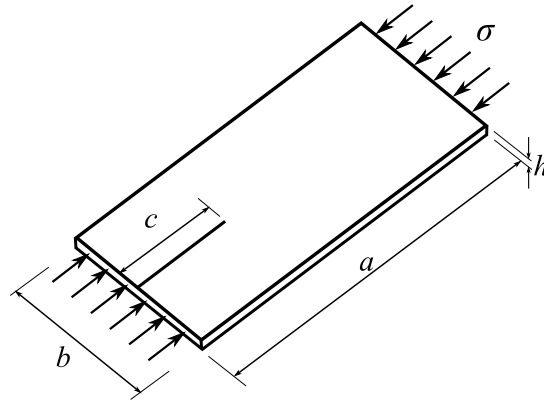
Figure 13. Edge crack plate geometry.
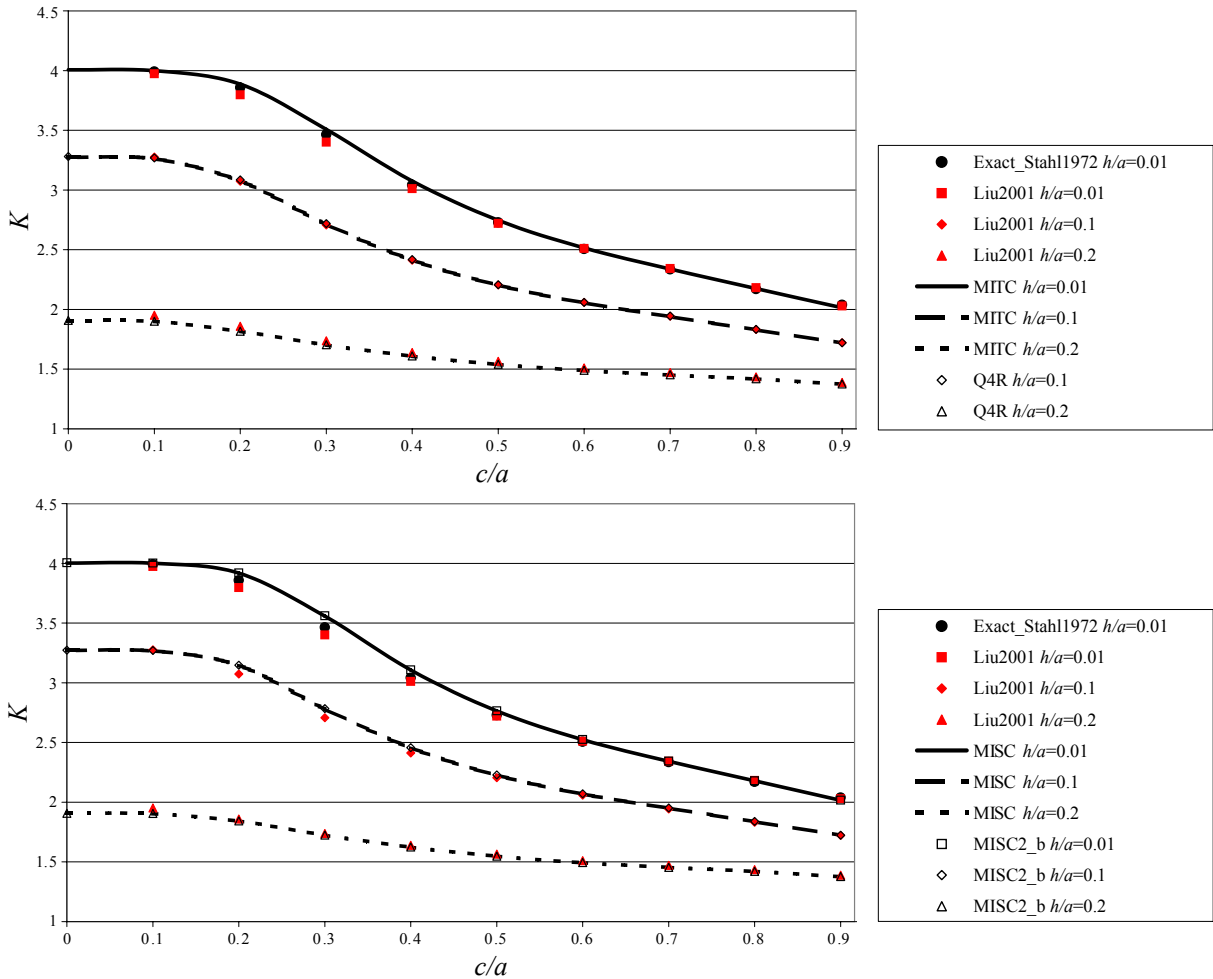
Figure 14. Buckling coefficients for rectangular ($a/b = 2$) edge cracked plates. Top: Q4R and MITC. Bottom: MISC2 and MISC2_b.
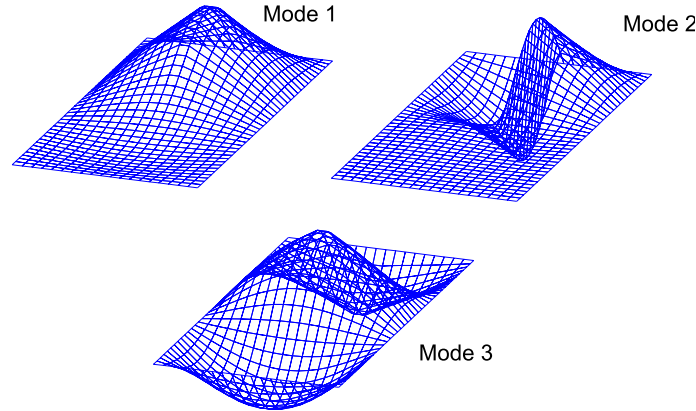
Figure 15. Buckling modes for simply supported edge cracked ($c/a = 0.5$) rectangular plate ($a/b = 2$).

Figure 14 also presents the analytical solution for thin cracked plates [Stahl and Keer 1972] and numerical solutions [Liu 2001]. In the majority of cases, very good agreement ($\sim 1\%$) was obtained with the reported results. The largest difference ($\sim 3\%$) with the reported data occurs for short-medium crack sizes ($a/c = 0.2, 0.3, 0.4, 0.5$), particularly for the MISC2 and MISC2_b elements. The first 3 buckling modes for a thin ($h/a = 0.01$) edge cracked ($c/a = 0.5$) rectangular plate ($a/b = 2$) are shown in Figure 15.
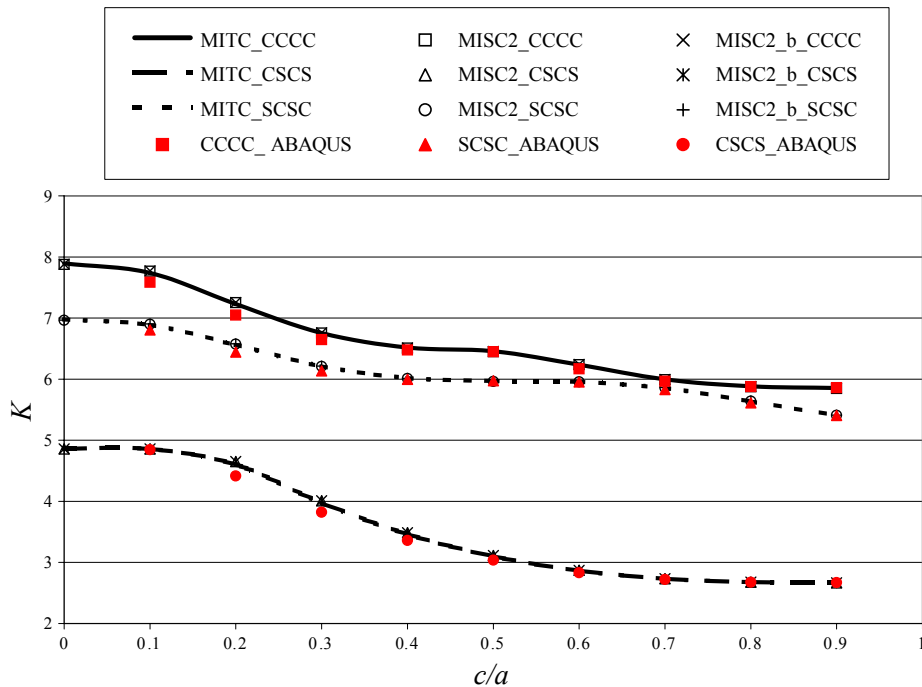
Figure 16. Buckling coefficients for rectangular ($a/b = 2$) centre cracked plates with different boundary conditions.

6.6. *Rectangular plate with a longitudinal centre crack under different boundary conditions.* This last example considers different boundary conditions in a rectangular centre cracked thin plate. The boundary conditions for each case are given as follows:

$$
\begin{array}{ll}
\text{CCCC}: & \text{Sides and ends clamped,} \\
\text{SCSC}: & \text{Sides clamped and ends simply supported,} \\
\text{CSCS}: & \text{Sides simply supported and ends clamped.}
\end{array}
$$

The aspect ratio of the plate is $a/b = 2$ and the plate thickness is $h/a = 0.01$, therefore only buckling coefficients for elements MITC, MISC2, and MISC2_b versus crack lengths (c/a) are presented in Figure 16 (as shown in the previous examples, element Q4R will exhibit locking under this condition). As expected each case of boundary conditions converges to the noncracked thin plate solutions ($c/a = 0$).

Figure 16 shows that as the crack size increases, buckling coefficients decrease for all the different boundary conditions. All the present results were obtained with an uniform mesh of 19×38 elements. In order to establish a comparison with standard FEM, symmetric ABAQUS models [ABAQUS 2009]
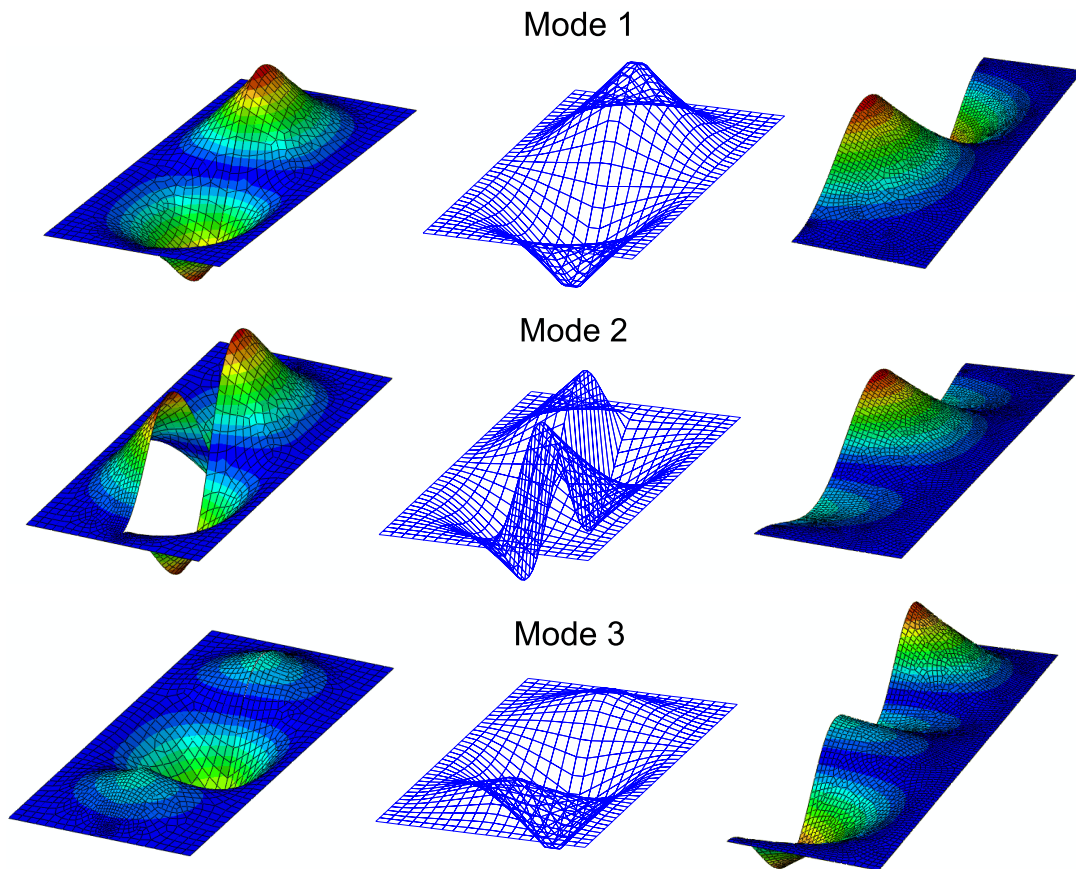

Figure 17. Buckling modes of clamped centre cracked ($c/a = 0.9$) rectangular plates ($a/b = 2$). Left: ABAQUS-seam model. Centre: XFEM model. Right: ABAQUS-symmetric model.

with an average of 4500 linear elements (S4R) are also plotted in Figure 16. Totally clamped cracked plates exhibit the highest buckling coefficient. SCSC, as expected, gives higher buckling coefficients than CSCS, as the simply supported condition along the sides (see Figure 3) in the CSCS case provides a weaker constraint than in the SCSC case.

Buckling modes for the largest crack size ($c/a = 0.9$) and totally clamped boundary conditions are presented in Figure 17. In this case, an additional ABAQUS model with a seam crack (ABAQUS-seam) is performed in order to compare buckling modes of full and symmetric models. It is clear from this figure the similarity in the first buckling mode for all cases. The second and third modes differ in the full and symmetric models as the antisymmetric opening mode (mode 2 in Figure 17) given by XFEM and ABAQUS-seam is not obtained in the symmetric ABAQUS model. Notice that the second mode in the ABAQUS symmetric solution corresponds to the third mode in the full models (XFEM and ABAQUS-seam).

7. Conclusions

In this paper, the smoothed extended finite element method was used to model the linear buckling response of uncracked and cracked isotropic shear deformable plates. Three different enriched elements were proposed: a stabilised MITC, a curvature smoothed MISC2, and a bending geometric stiffness matrix smoothed MISC2_b element. Each case corresponds to an extension of the previous. MISC2_b is an element only valid for linear plate buckling problems, and shows the influence of smoothing higher-order (nonlinear) terms. All enriched elements perform excellently (except for the Q4R element, which exhibits locking in the thin plate limit), with the MISC2 and MISC2_b elements providing slightly better results than the MITC element.

The effect of mesh distortion for uncracked and cracked plates was also considered, including the dependency on plate thickness. For distorted meshes, the classical Q4R element exhibits the worst performance, particularly for thin plates, while the newly proposed MISC2_b is shown to provide the most acceptable results for all cases (thin-thick and cracked-uncracked plates).

Two types of crack configurations have been considered in this study: a plate with a crack emanating from one edge, and a plate with a centrally located internal crack. Different plate thicknesses were considered, giving an overview of applications to thin and thick cracked plate buckling problems. It is seen that with increasing crack length and thickness, the buckling load decreases. Finally, different sets of boundary conditions were studied. It is worth noting that the present method greatly simplifies modelling of plate buckling with cracks, allowing us in some cases to provide antisymmetric crack opening modes that are not provided in classical symmetric FEM simulations, as shown with the totally clamped example.

References

[ABAQUS 2009] *ABAQUS user's manual*, Version 6.9.1, Hibbitt, Karlsson and Sorensen, Pawtucket, Rhode Island, 2009.

[Alinia et al. 2007] M. M. Alinia, S. A. A. Hosseinzadeh, and H. R. Habashi, "Numerical modelling for buckling analysis of cracked shear panels", *Thin-Walled Struct* **45**:12 (2007), 1058–1067.

[Areias and Belytschko 2005] P. M. A. Areias and T. Belytschko, "Non-linear analysis of shells with arbitrary evolving cracks using XFEM", *Int. J. Numer. Meth. Eng.* **62**:3 (2005), 384–415.

[Babuška et al. 1994] I. Babuška, G. Caloz, and J. E. Osborn, "Special finite element methods for a class of second order elliptic problems with rough coefficients", *SIAM J. Numer. Anal.* **31**:4 (1994), 945–981.

[Bachene et al. 2009] M. Bachene, R. Tiberkak, and S. Rechak, "Vibration analysis of cracked plates using the extended finite element method", *Arch. Appl. Mech.* **79**:3 (2009), 249–262.

[Bathe and Dvorkin 1985] K.-J. Bathe and E. N. Dvorkin, "A four-node plate bending element based on Mindlin/Reissner plate theory and a mixed interpolation", *Int. J. Numer. Meth. Eng.* **21** (1985), 367–383.

[Belytschko and Black 1999] T. Belytschko and T. Black, "Elastic crack growth in finite elements with minimal remeshing", *Int. J. Numer. Meth. Eng.* **45**:5 (1999), 601–620.

[Belytschko et al. 2009] T. Belytschko, R. Gracie, and G. Ventura, "A review of extended/generalized finite element methods for material modelling", *Model. Simul. Mater. Sci. Eng.* **17**:4 (2009), 1–31.

[Bordas and Natarajan 2010] S. P. A. Bordas and S. Natarajan, "On the approximation in the smoothed finite element method (SFEM)", *Int. J. Numer. Meth. Eng.* **81**:5 (2010), 660–670.

[Bordas et al. 2009] S. P. A. Bordas, T. Rabczuk, N. Hung, V. Nguyen, S. Natarajan, T. Bog, D. Quan, and N. Hiep, "Strain smoothing in FEM and XFEM", *Comput. Struct.* **88**:23-24 (2009), 1419–1443.

[Brighenti 2009] R. Brighenti, "Buckling sensitivity analysis of cracked thin plates under membrane tension or compression loading", *Nucl. Eng. Des.* **239**:6 (2009), 965–980.

[Dai et al. 2007] K. Y. Dai, G. R. Liu, and T. T. Nguyen, "An *n*-sided polygonal smoothed finite element method (*n*SFEM) for solid mechanics", *Finite Elem. Anal. Des.* **43**:11-12 (2007), 847–860.

[Dolbow et al. 2000] J. Dolbow, N. Moës, and T. Belytschko, "Modeling fracture in Mindlin–Reissner plates with the extended finite element method", *Int. J. Solids Struct.* **37**:48-50 (2000), 7161–7183.

[Gruttmann and Wagner 2004] F. Gruttmann and W. Wagner, "A stabilized one-point integrated quadrilateral Reissner–Mindlin plate element", *Int. J. Numer. Methods Eng.* **61**:13 (2004), 2273–2295.

[Hosseini-Hashemi et al. 2008] S. Hosseini-Hashemi, K. Khorshidi, and M. Amabili, "Exact solution for linear buckling of rectangular Mindlin plates", *J. Sound Vibration* **315**:1-2 (2008), 318–342.

[Le et al. 2010] C. V. Le, H. Nguyen-Xuan, H. Askes, S. P. A. Bordas, T. Rabczuk, and H. Nuguyen-Vinh, "A cell-based smoothed finite element method for kinematic limit analysis", *Int. J. Numer. Meth. Eng.* **83**:12 (2010), 1651–1674.

[Liu 2001] F. L. Liu, "Differential quadrature element method for buckling analysis of rectangular Mindlin plates having discontinuities", *Int. J. Solids Struct.* **38**:14 (2001), 2305–2321.

[Liu 2010a] G. R. Liu, "A G space theory and a weakened weak (W^2) form for a unified formulation of compatible and incompatible methods, I: Theory", *Int. J. Numer. Meth. Eng.* **81**:9 (2010), 1093–1126.

[Liu 2010b] G. R. Liu, "A G space theory and a weakened weak (W^2) form for a unified formulation of compatible and incompatible methods, II: Applications to solid mechanics problems", *Int. J. Numer. Meth. Eng.* **81**:9 (2010), 1127–1156.

[Liu et al. 2007a] G. R. Liu, K. Y. Dai, and T. T. Nguyen., "A smoothed finite element method for mechanics problems", *Comput. Mech.* **39**:6 (2007), 859–877.

[Liu et al. 2007b] G. R. Liu, T. T. Nguyen, K. Y. Dai, and K. Y. Lam, "Theoretical aspects of the smoothed finite element method (SFEM)", *Int. J. Numer. Meth. Eng.* **71**:8 (2007), 902–930.

[Liu et al. 2009a] G. R. Liu, T. Nguyen-Thoi, and K. Y. Lam, "An edge-based smoothed finite element method (ES-FEM) for static, free and forced vibration analyses of solids", *J. Sound Vibration* **320**:4-5 (2009), 1100–1130.

[Liu et al. 2009b] G. R. Liu, T. Nguyen-Thoi, H. Nguyen-Xuan, and K. Y. Lam, "A node-based smoothed finite element method (N-SFEM) for upper bound solutions to solid mechanics problems", *Comput. Struct.* **87**:1-2 (2009), 14–26.

[Markström and Storåkers 1980] K. Markström and B. Storåkers, "Buckling of cracked members under tension", *Int. J. Solids Struct.* **16**:3 (1980), 217–229.

[Natarajan et al. 2009a] S. Natarajan, S. Bordas, and D. R. Mahapatra, "Numerical integration over arbitrary polygonal domains based on Schwarz–Christoffel conformal mapping", *Int. J. Numer. Meth. Eng.* **80**:1 (2009), 103–134.

[Natarajan et al. 2009b] S. Natarajan, S. P. A. Bordas, and T. Rabczuk, "Linear free flexural vibration of cracked isotropic plates using the extended finite element method", preprint, 2009. Submitted to *Algorithms*.

[Natarajan et al. 2010] S. Natarajan, D. R. Mahapatra, and S. P. A. Bordas, "Integrating strong and weak discontinuities without integration subcells and example applications in an XFEM/GFEM framework", *Int. J. Numer. Meth. Eng.* **83**:3 (2010), 269–294.

[Nguyen-Thanh et al. 2008] N. Nguyen-Thanh, T. Rabczuk, H. Nguyen-Xuan, and S. P. A. Bordas, "A smoothed finite element method for shell analysis", *Comput. Methods Appl. Mech. Eng.* **198**:2 (2008), 165–177.

[Nguyen-Xuan et al. 2008a] H. Nguyen-Xuan, S. Bordas, and H. Nguyen-Dang, "Smooth finite element methods: convergence, accuracy and properties", *Int. J. Numer. Meth. Eng.* **74**:2 (2008), 175–208.

[Nguyen-Xuan et al. 2008b] H. Nguyen-Xuan, T. Rabczuk, S. Bordas, and J. F. Debongnie, "A smoothed finite element method for plate analysis", *Comput. Methods Appl. Mech. Eng.* **197**:13-16 (2008), 1184–1203.

[Purbolaksono and Aliabadi 2005] J. Purbolaksono and M. H. Aliabadi, "Dual boundary element method for instability analysis of cracked plates", *Comput. Model. Eng. Sci.* **8**:1 (2005), 73–90.

[Rabczuk and Areias 2006] T. Rabczuk and P. Areias, "A meshfree thin shell for arbitrary evolving cracks based on an extrinsic basis", *Comput. Model. Eng. Sci.* **16**:2 (2006), 115–130.

[Rabczuk et al. 2007] T. Rabczuk, P. M. A. Areias, and T. Belytschko, "A meshfree thin shell method for non-linear dynamic fracture", *Int. J. Numer. Meth. Eng.* **72**:5 (2007), 524–548.

[Rabczuk et al. 2010] T. Rabczuk, R. Gracie, J.-H. Song, and T. Belytschko, "Immersed particle method for fluid-structure interaction", *Int. J. Numer. Meth. Eng.* **81**:1 (2010), 48–71.

[Reissner 1947] E. Reissner, "On bending of elastic plates", *Quart. Appl. Math.* **5** (1947), 55–68.

[Riks et al. 1992] E. Riks, C. C. Rankin, and F. A. Brogan, "The buckling behavior of a central crack in a plate under tension", *Eng. Fract. Mech.* **43**:4 (1992), 529–548.

[Sih and Lee 1986] G. C. Sih and Y. D. Lee, "Tensile and compressive buckling of plates weakened by cracks", *Theor. Appl. Fract. Mech.* **6**:2 (1986), 129–138.

[Stahl and Keer 1972] B. Stahl and L. M. Keer, "Vibration and stability of cracked rectangular plates", *Int. J. Solids Struct.* **8** (1972), 69–91.

[Vafai et al. 2002] A. Vafai, M. Javidruzi, and H. E. Estekanchi, "Parametric instability of edge cracked plates", *Thin-Walled Struct.* **40**:1 (2002), 29–44.

[Wang and Chen 2004] D. Wang and J.-S. Chen, "Locking-free stabilized conforming nodal integration for meshfree Mindlin–Reissner plate formulation", *Comput. Methods Appl. Mech. Eng.* **193**:12-14 (2004), 1065–1083.

[Wyart et al. 2007] E. Wyart, D. Coulon, M. Duflot, T. Pardoen, J.-F. Remacle, and F. Lani, "A substructured FE-shell/XFE-3D method for crack analysis in thin-walled structures", *Int. J. Numer. Meth. Eng.* **72**:7 (2007), 757–779.

PEDRO M. BAIZ: p.m.baiz@imperial.ac.uk
Department of Aeronautics, Imperial College London, Prince Consort Road, London SW7 2AZ, United Kingdom

SUNDARARAJAN NATARAJAN: sundararajan.natarajan@gmail.com
School of Engineering, Cardiff University, Cardiff CF24 3AA, United Kingdom

STÉPHANE P. A. BORDAS: stephane.bordas@gmail.com
School of Engineering, Cardiff University, Cardiff CF24 3AA, United Kingdom

PIERRE KERFRIDEN: pierre.kerfriden@gmail.com
School of Engineering, Cardiff University, Cardiff CF24 3AA, United Kingdom

TIMON RABCZUK: timon.rabczuk@uni-weimar.de
Department of Civil Engineering, Bauhaus-Universität Weimar, 99421 Weimar, Germany

■msp

A FINITE ELEMENT FOR FORM-FINDING
AND STATIC ANALYSIS OF TENSEGRITY STRUCTURES

Dario Gasparini, Katalin K. Klinka and Vinicius F. Arcaro

This text describes a mathematical model for both form-finding and static analysis of tensegrity struc-
tures. A special line element that shows constant stress for any displacement of its nodes is used to
define a prestressed equilibrium configuration. The form-finding and static analysis are formulated as
an unconstrained nonlinear programming problem, where the objective function is the total potential
energy and the displacements of the nodal points are the unknowns. Analytical solutions for tensegrity
prisms are presented and compared with the numerical results of the proposed approach. A quasi-Newton
method is used, which avoids the evaluation of the tangent stiffness matrix. The source and executable
computer codes of the algorithm are available for download from the website of one of the authors.

1. Introduction

A review of the important literature related to form-finding methods for tensegrity structures is given
in [Tibert and Pellegrino 2003]. These methods can be classified into kinematical and statical methods.
This text concentrates on the total potential energy minimization method for both form-finding and static
analysis of tensegrity structures. A special line element that shows constant stress for any displacement
of its nodes is used to define a prestressed equilibrium configuration. The form-finding and static analysis
are formulated as an unconstrained nonlinear programming problem, where the objective function is the
total potential energy and the displacements of the nodal points are the unknowns. A quasi-Newton
method is used, which avoids the evaluation of the tangent stiffness matrix. There is an interesting
connection between minimizing the total potential energy, which is defined by an unconstrained nonlinear
programming problem, and the general method for form-finding first described in [Pellegrino 1986],
which is defined by a constrained nonlinear programming problem. The strain energy for a line element
can be interpreted as a penalty function, as it imposes resistance to changing the length of the element.
Minimization methods based on penalty functions were the first methods used for constrained nonlinear
programming. The total potential energy minimization method for the analysis of cable structures was
first described in [Pietrzak 1978]. The following conventions apply unless otherwise specified or made
clear by the context: a Greek letter expresses a scalar, and a lower-case letter represents a column vector.

2. Line element definition

Figure 1 shows the geometry of the element. The nodes are labeled 1 and 2. The nodal displacements
transform the element from its initial configuration to its final configuration. The strain is assumed
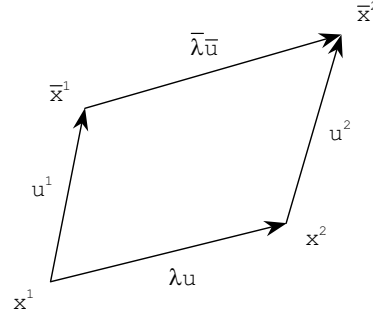constant along the element and the material homogeneous and isotropic.

Figure 1. Line element.

3. Deformed length

The vector u is a unit vector. Note that λ represents the distance between the nodes of the element in this initial configuration. However, this distance will not always represent the undeformed length of the element. The nodal displacements vectors are numbered according to its node numbers. The deformed length can be written as

$$\bar{\lambda} = \lambda\sqrt{1+\delta}, \tag{1}$$

where

$$\delta = 2u^T z + z^T z, \qquad z = \frac{u^2 - u^1}{\lambda}. \tag{2}$$

The unit vector parallel to the element in its deformed configuration can be written as

$$\bar{u} = \frac{u+z}{\sqrt{1+\delta}}. \tag{3}$$

4. State of constant cut

Consider an element with undeformed length less than the initial distance of its nodes. This situation can be pictured as an imaginary cut in the element's undeformed length. The element shows tension with zero nodal displacements. Considering μ as the value of the cut in the undeformed length, the strain-free length of the element can be written as

$$\rho = \frac{\mu}{\lambda}, \qquad \lambda_0 = \lambda(1-\rho). \tag{4}$$

The engineering strain can be written as

$$\varepsilon = \frac{\sqrt{1+\delta} - 1 + \rho}{1-\rho}. \tag{5}$$

Inaccuracy often results from the severe cancellation that occurs when nearly equal values are subtracted. In order to avoid it, the previous expression should be evaluated as

$$\varepsilon = \frac{\delta/(\sqrt{1+\delta} + 1) + \rho}{1-\rho}. \tag{6}$$

5. Potential strain energy

Considering σ as the conjugate stress to the engineering strain ε and α as the undeformed area of the element, the potential strain energy and its gradient with respect to the nodal displacements can be written as

$$\phi = \alpha\lambda_0 \int_0^\varepsilon \sigma(\xi)\,d\xi, \qquad \frac{\partial\varphi}{\partial u_i^1} = \alpha\lambda_0\sigma(\varepsilon)\frac{\partial\varepsilon}{\partial u_i^1}, \qquad \frac{\partial\varphi}{\partial u_i^1} = -\alpha\sigma(\varepsilon)\bar{u}_i, \tag{7}$$

$$\frac{\partial\varphi}{\partial u_i^2} = \alpha\lambda_0\sigma(\varepsilon)\frac{\partial\varepsilon}{\partial u_i^2}, \qquad \frac{\partial\varphi}{\partial u_i^2} = +\alpha\sigma(\varepsilon)\bar{u}_i. \tag{8}$$

Note that the conjugate stress to the engineering strain is not the Cauchy stress. However, for practical purposes where the strain is usually small, this stress can be taken as an approximation to the Cauchy stress.

6. Geometric interpretation

Figure 2 shows the geometric interpretation of the gradient of the potential strain energy as forces acting on nodes of the element. These forces are known as internal forces.
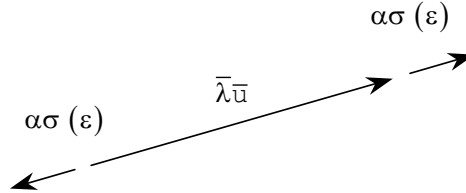
Figure 2. Geometric interpretation.

7. State of constant stress

Consider an element with strain-free length given by λ_0. The engineering strain can be written as

$$\varepsilon = \frac{\bar{\lambda} - \lambda_0}{\lambda_0}. \tag{9}$$

Supposing that the element shows constant stress σ, the potential strain energy can be written as

$$\varphi = \alpha\lambda_0 \int_0^\varepsilon \sigma\,d\xi = \alpha\sigma(\bar{\lambda} - \lambda_0). \tag{10}$$

The potential strain energy is equal to the force multiplied by the relative displacement between the nodes. In the expression for the strain energy, the strain-free length can be eliminated because it does not depend on the nodal displacements. Its permanence in the expression would only add constants, one for each element, to the total potential energy function. Minimizing a function plus a constant is equivalent to minimizing the function only. Therefore, the potential strain energy can be defined as

$$\varphi = \alpha\sigma\lambda\sqrt{1 + \delta}. \tag{11}$$

The gradient with respect to the nodal displacements can be written as

$$\frac{\partial \varphi}{\partial u_i^1} = -\alpha \sigma \bar{u}_i, \qquad \frac{\partial \varphi}{\partial u_i^2} = +\alpha \sigma \bar{u}_i. \tag{12}$$

The gradient can be interpreted as internal forces with constant modulus acting on nodes of the element. The element shows constant stress for any displacement of its nodes. A similar element was described in [Meek 1971]. The element was called a variable initial length element.

8. Internal forces equivalence

A cut value is equivalent to a stress value in the sense that they both produce the same internal forces. The following approach can be used when stress is a nonlinear invertible function of strain.

To find the cut value equivalent to the stress value, first find the strain:

$$\sigma(\varepsilon) = \sigma. \tag{13}$$

Then, find the cut value:

$$\mu = \frac{\lambda}{(1+\varepsilon)}\left(\varepsilon - \frac{\delta}{1+\sqrt{1+\delta}}\right). \tag{14}$$

To find the stress value equivalent to the cut value, first find the strain:

$$\varepsilon = \frac{\delta/(\sqrt{1+\delta}+1) + \rho}{1-\rho}. \tag{15}$$

Then, find the stress:

$$\sigma = \sigma(\varepsilon). \tag{16}$$

9. Stress and strain

For simplicity, consider a linear function with E as the modulus of elasticity. The potential strain energy can be written as

$$\sigma = E\varepsilon, \qquad \varphi = \tfrac{1}{2}\alpha\lambda_0 E\varepsilon^2. \tag{17}$$

In the case of a hyperelastic material, it is important to emphasize that the strain energy and its corresponding Cauchy stress can be written as functions of the nodal displacements. Therefore, this type of material can be considered without introducing any additional difficulty.

10. Analysis strategy

The initial configuration of a tensegrity structure is defined as the configuration of zero nodal displacements for all its nodes. An analysis strategy can be defined as follows: Select some elements and set them to the constant stress state by specifying a stress value. Find the prestressed equilibrium configuration. At this equilibrium configuration, change the elements from the constant stress state to its equivalent constant cut state. Note that the equilibrium configuration remains the same. Apply the loading and find the final equilibrium configuration.

11. Equilibrium configuration

Considering u as the vector of unknown displacements and f as the vector of applied nodal forces, the total potential energy function and its gradient can be written as

$$\pi(u) = \sum_{\text{elements}} \varphi(u) - f^T u, \qquad \nabla \pi(u) = \sum_{\text{elements}} \nabla \varphi(u) - f. \tag{18}$$

The stable equilibrium configurations correspond to local minimum points of the total potential energy function. In order to find the local minimum points of a nonlinear multivariate function, the general strategy that can be used is: Choose a starting point and move in a given direction such that the function decreases. Find the minimum point in this direction and use it as a new starting point. Continue this way until a local minimum point is reached. The problem of finding the minimum points of a nonlinear multivariate function is replaced by a sequence of subproblems, each one consisting of finding the minimum of a univariate nonlinear function. In the quasi-Newton methods, starting with the unit matrix, a positive-definite approximation to the inverse of the Hessian matrix is updated at each iteration. This update is made using only values of the gradient vector. A direction such that the function decreases is calculated as minus the product of this approximation of the inverse of the Hessian matrix and the gradient vector calculated at the starting point of each iteration. Consequently, it is not necessary to solve any system of equations. Moreover, analytical derivation of an expression for the Hessian matrix is not necessary. Note that by minimizing the total potential energy function it is almost impossible to find an unstable equilibrium configuration, which corresponds to a local maximum point. The only exception is that it is possible to find a saddle point, that is, a point the is a local minimum and also a local maximum. However, even in this improbable situation, a direction of negative curvature to continue toward a local minimum point can be found as described in [Gill and Murray 1974]. It is important to emphasize that minimizing total potential energy to find equilibrium configurations does not require support constraints to prevent rigid body motion. The computer code uses the limited-memory BFGS algorithm to tackle large-scale problems as described in [Nocedal and Wright 1999]. It also employs a line search procedure through cubic interpolation, as described in the same reference.

12. Geometrical shape minimization

Consider the following special case: A structure composed of elements in the state of constant stress with stress equal to one and elements in the state of constant cut with cut equal to zero. The area is equal to one for all elements. The vector of applied nodal forces is equal to zero. The stress-strain relationship is given by a linear function with E as the modulus of elasticity. The total potential energy can be written as

$$\pi(u) = \sum_{\text{stress}} \lambda \sqrt{1+\delta} + \frac{E}{2} \sum_{\text{cut}} \lambda \varepsilon^2. \tag{19}$$

The strain energy of an element in the state of constant stress is simply its final length. A high modulus of elasticity imposes resistance for changing the length of an element in the state of constant cut. The strain energy of an element in the state of constant cut can be interpreted as a penalty function. The problem can be interpreted as a constrained nonlinear programming problem of minimizing the sum of the lengths of the elements in the state of constant stress while keeping the lengths of the elements in the state of constant cut. This leads to an extension of the mathematical model of [Arcaro and Klinka 2009].

13. Analysis of a simple tensegrity

This problem and its relation to tensegrity structures was first described in [Calladine 1978]. Figure 3 shows a two-element truss with a vertical displacement on the center node.
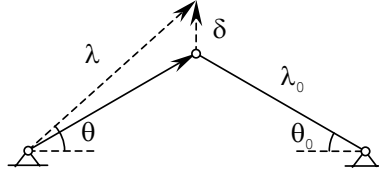

Figure 3. Two-element truss.

13.1. *Geometry.* From Figure 3 we can write

$$\lambda \cos \theta = \lambda_0 \cos \theta_0, \qquad \lambda \sin \theta = \lambda_0 \sin \theta_0 + \delta. \tag{20}$$

13.2. *Element length.* The element length as function of the rotation angle can be written as

$$\lambda(\theta) = \frac{\lambda_0 \cos \theta_0}{\cos \theta}. \tag{21}$$

The derivative of the rotation angle with respect to the vertical displacement can be written as

$$\frac{d\theta}{d\delta} = \frac{\cos^2 \theta}{\lambda_0 \cos \theta_0}. \tag{22}$$

13.3. *Equilibrium equation.* Considering α as the undeformed area of the elements, the total potential strain energy can be written as

$$\varphi = 2\alpha\lambda_\mu \int_0^\varepsilon \sigma(\xi) d\xi. \tag{23}$$

The derivative of the total potential strain energy with respect to the vertical displacement is equal to the force applied in the direction of this displacement (note that the force is positive upward):

$$f = \frac{d\varphi}{d\varepsilon} \frac{d\varepsilon}{d\theta} \frac{d\theta}{d\delta}, \qquad f = 2\alpha\sigma(\varepsilon) \frac{\cos^2 \theta}{\lambda_0 \cos \theta_0} \lambda'(\theta). \tag{24}$$

13.4. *Element strain.* Considering a cut μ in the initial length of the element, its undeformed length can be written as

$$\lambda_\mu = \lambda_0 - \mu. \tag{25}$$

The element strain can be written as

$$\varepsilon = \frac{\lambda(\theta)}{\lambda_\mu} - 1. \tag{26}$$

13.5. *Stress and strain.* The following approach can be used when stress is a nonlinear invertible function of strain. For simplicity, consider a linear function with E as the modulus of elasticity. By imposing a tension σ_μ on the elements at the prestressed configuration, its undeformed lengths can be written as

$$\lambda_\mu = \frac{\lambda_0 \cos \theta_0}{(1 + \sigma_\mu/E)}. \tag{27}$$

The cut in the initial length of the elements is given by

$$\mu = \lambda_0 - \lambda_\mu. \tag{28}$$

The equilibrium equation can be written as

$$\frac{f}{E\alpha} = 2 \sin \theta \left[\left(1 + \frac{\sigma_\mu}{E} \right) \frac{1}{\cos \theta} - 1 \right]. \tag{29}$$

Figure 4 shows the nondimensional force as a function of the rotation angle for $\sigma_\mu/E = 0.001$. The axial force on the elements can be written as

$$\alpha \sigma (\varepsilon) = \alpha E \left[\left(1 + \frac{\sigma_\mu}{E} \right) \frac{1}{\cos \theta} - 1 \right]. \tag{30}$$
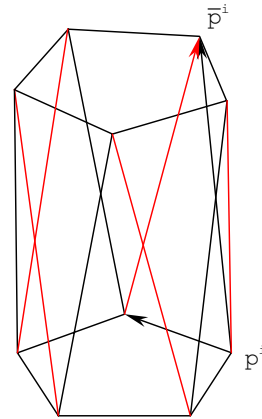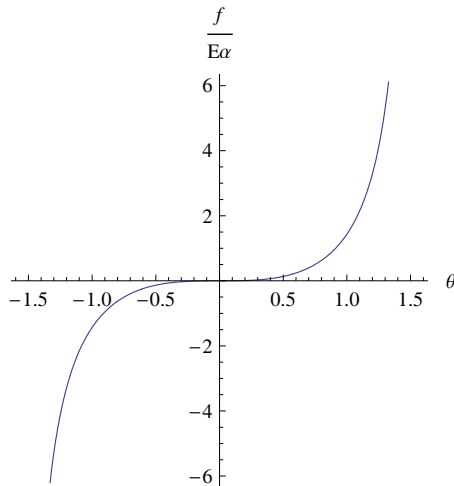
Figure 4. Nondimensional force versus rotation angle.   **Figure 5.** Straight tensegrity prism.

14. Analysis of tensegrity prisms

The analysis of [Oppenheim and Williams 2000] for a three-sided tensegrity prism is extended to a n-sided tensegrity prism. Figure 5 shows a straight tensegrity prism. The bottom and top regular polygons are inscribed in circles of equal radius. The sum of the lengths of the diagonal elements (shown in red) is minimized by rotating the top polygon counterclockwise with respect to the bottom polygon, while the lengths of the elements shown in black remain constant. The geometry defined by the final shape is also called a minimal tensegrity prism and can be used as a building block of complex tensegrity structures [Skelton and de Oliveira 2009].
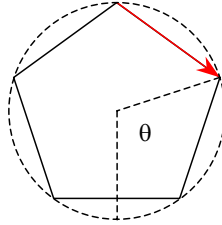
Figure 6. Top view of a straight tensegrity prism.

14.1. *Geometry.* For n-sided regular polygons, the coordinates of the vertices can be written as

$$\gamma = \frac{2\pi}{n}, \qquad p^i = \begin{bmatrix} \rho\cos(\gamma i) \\ \rho\sin(\gamma i) \\ 0 \end{bmatrix}, \qquad \bar{p}^i = \begin{bmatrix} \rho\cos(\theta + \gamma i) \\ \rho\sin(\theta + \gamma i) \\ \delta(\theta) \end{bmatrix}. \tag{31}$$

The following vectors are defined in terms of the coordinates of the vertices:

$$b^i = p^{i+1} - p^i, \qquad l^i = \bar{p}^i - p^{i+1}, \qquad v^i = \bar{p}^i - p^i. \tag{32}$$

14.2. *Interval for the rotation angle.* Figure 6 shows the top view of a straight tensegrity prism with one diagonal element shown in red.

The maximum clockwise rotation happens when a diagonal element intercepts the vertical axis on the center of the circle resulting in diagonal elements interference. This rotation angle is given by

$$\theta_{\min} = -(\pi - \gamma). \tag{33}$$

The maximum counterclockwise rotation happens when a vertical element (connects corresponding vertices of top and bottom polygons) intercepts the vertical axis on the center of the circle resulting in vertical elements interference. This rotation angle is given by

$$\theta_{\max} = \pi. \tag{34}$$

The interval for the rotation angle is

$$-(\pi - \gamma) \leqslant \theta \leqslant \pi. \tag{35}$$

14.3. *Height.* The square of the norm of vector v^i can be written as

$$\|v^i\|^2 = 2\rho^2(1 - \cos\theta) + \delta^2(\theta). \tag{36}$$

Considering v as the norm of vector v^i, which is constant, the expression for the height as function of rotation angle can be written as

$$\delta^2(\theta) = v^2 - 2\rho^2(1 - \cos\theta). \tag{37}$$

14.4. *Diagonal element length.* Considering λ as the norm of vector l^i, the square of the diagonal element length can be written as

$$\lambda^2(\theta) = v^2 + 2\rho^2[\cos\theta - \cos(\theta - \gamma)]. \tag{38}$$

14.5. _Minimum diagonal element length._ Due to symmetry, minimizing the sum of the diagonal element lengths is equivalent to minimizing the square of one diagonal element length.

$$\frac{\partial \lambda^2}{\partial \theta} = 0 \quad \Rightarrow \quad \tan \bar{\theta} = \frac{\sin \gamma}{\cos \gamma - 1}. \tag{39}$$

Notice that this expression is valid when the diagonal elements connect the corresponding bottom and top points in any symmetric way:

$$\bar{\theta} > 0 \quad \Rightarrow \quad \cos \bar{\theta} = \frac{\cos \gamma - 1}{\sqrt{2(1 - \cos \gamma)}}, \tag{40}$$

$$\bar{\theta} > 0 \quad \Rightarrow \quad \sin \bar{\theta} = \frac{\sin \gamma}{\sqrt{2(1 - \cos \gamma)}}. \tag{41}$$

14.6. _Element strain._ Considering a cut μ in the initial length of the diagonal element, its undeformed length can be written as

$$\lambda_\mu = \lambda(0) - \mu. \tag{42}$$

The element strain can be written as

$$\varepsilon = \frac{\lambda(\theta)}{\lambda_\mu} - 1. \tag{43}$$

14.7. _Equilibrium equation._ Considering α as the undeformed area of the diagonal elements, the total potential strain energy can be written as

$$\varphi = n\alpha\lambda_\mu \int_0^\varepsilon \sigma(\xi) \, d\xi. \tag{44}$$

The derivative of the total potential strain energy with respect to the vertical displacement is equal to the force applied in the direction of this displacement. This derivative is equal to the derivative with respect to the height (note that the force is positive upward when the vertical displacements of the bottom vertices are fixed):

$$f = \frac{d\varphi}{d\varepsilon} \frac{d\varepsilon}{d\theta} \frac{d\theta}{d\delta}, \qquad f = n\alpha\sigma(\varepsilon) \left[1 - \frac{\sin(\theta - \gamma)}{\sin \theta} \right] \frac{\delta(\theta)}{\lambda(\theta)}. \tag{45}$$

14.8. _Stress and strain._ The following approach can be used when stress is a nonlinear invertible function of strain. For simplicity, consider a linear function with E as the modulus of elasticity. By imposing a tension σ_μ on the diagonal elements at the prestressed configuration, its undeformed lengths can be written as

$$\lambda_\mu = \frac{\sqrt{v^2 - 2\rho^2 \sqrt{2(1 - \cos \gamma)}}}{(1 + \sigma_\mu / E)}. \tag{46}$$

The cut in the initial length of the diagonal elements can be written as

$$\mu = \lambda(0) - \lambda_\mu. \tag{47}$$

The equilibrium equation can be written as

$$\frac{f}{E\alpha} = n \left[\frac{1}{\lambda_\mu} - \frac{1}{\lambda(\theta)} \right] \left[1 - \frac{\sin(\theta - \gamma)}{\sin \theta} \right] \delta(\theta). \tag{48}$$
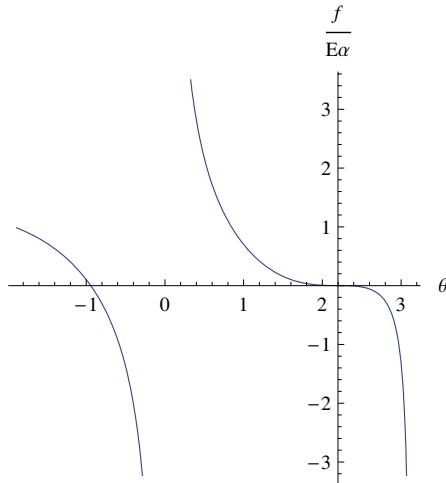
Figure 7. Nondimensional force versus rotation angle.

Figure 7 shows the nondimensional force as a function of the rotation angle for $n = 5$, $v/\rho = 3$, and $\sigma_\mu/E = 0.001$. Note that the vertical axis is placed on the position defined by the prestressed configuration.

The axial force on the diagonal elements can be written as $\alpha\sigma(\varepsilon) = \alpha E\left[\dfrac{\lambda(\theta)}{\lambda_\mu} - 1\right]$.

15. The stella octangula

Figure 8 shows the geometry of a sculpture called the stella octangula, which was proposed by the Hungarian architect, sculptor and author David Georges Emmerich. An extensive description of his works is given in [Chassagnoux 2006]. An analysis of this structure, using the dynamic relaxation method, was given in [Motro 2011].

Figure 8. The stella octangula.

The geometry is composed of 18 elements with length s and 6 diagonal elements with length $s\sqrt{3}$. The diagonal elements are connected as follows:

Element	Node	Node
3	4	11
6	5	10
9	6	12
12	7	1
15	8	3
18	9	2

Next we give the coordinates of the vertices, in terms of the parameters $r = s/\sqrt{3}$ and $h = s/\sqrt{6}$:

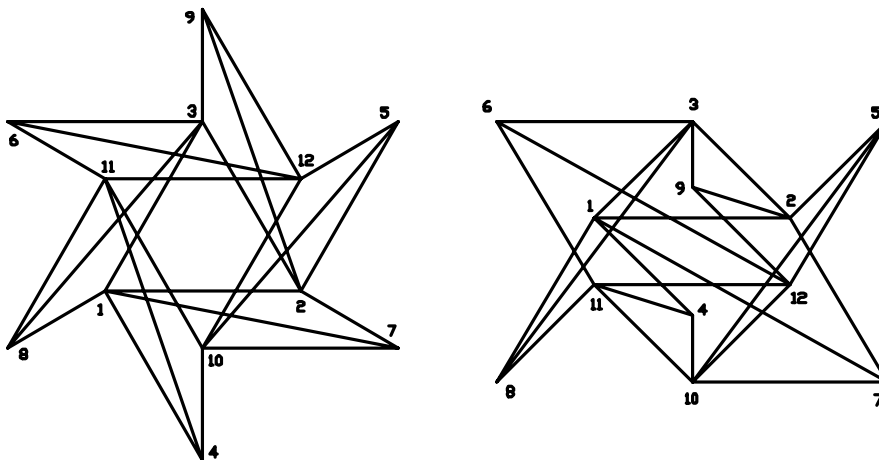| Node	X	Y	Z	Node	X	Y	Z
1	$-s/2$	$-r/2$	h	7	s	$-r$	$-h$
2	$s/2$	$-r/2$	h	8	$-s$	$-r$	$-h$
3	0	r	h	9	0	$2r$	$-h$
4	0	$-2r$	h	10	0	$-r$	$-h$
5	s	r	h	11	$-s/2$	$r/2$	$-h$
6	$-s$	r	h	12	$s/2$	$r/2$	$-h$

16. Examples

In the illustrations given in this section, elements shown in red are in compression; elements shown in blue are in tension; and elements in the initial configuration that start in the state of constant stress are shown in green.

Example 16.1 (A two-element truss with a vertical downward force applied on the center node). The force was calculated to make the element rotate -45 degrees from the prestressed configuration. The analytical expression for the equilibrium equation is presented in Section 12. The parameter values are

$$\theta_0 = 45 \text{ degrees}, \quad \lambda_0 = 1, \quad E = 1000, \quad \alpha = 1, \quad \sigma_\mu = 1, \quad f = -587.7864.$$

The value of the axial force found numerically coincides with the analytic one: 415.6278.

Here are the initial (left), prestressed (middle) configurations, and loaded (right) configurations:

Example 16.2 (A pentagonal prism with vertical forces applied on the top nodes). The bottom nodes are fixed only in the vertical direction. The analytical expression for the equilibrium equation is presented in Section 13. The parameter values are $n = 5$, $v = 3$, $\rho = 1$, $E = 1000$ for the diagonal elements, $E = 1000000$ to simulate the inextensible elements, $\alpha = 1$, and $\sigma_\mu = 1$.

Here are the initial (a) and the prestressed (b) configurations; the rotation angle from the initial configuration is equal to 126 degrees.

f	$+20.0$	-20.0
Analytical	30.72	19.83
Numerical	30.71	19.80
Error	-0.03%	-0.15%
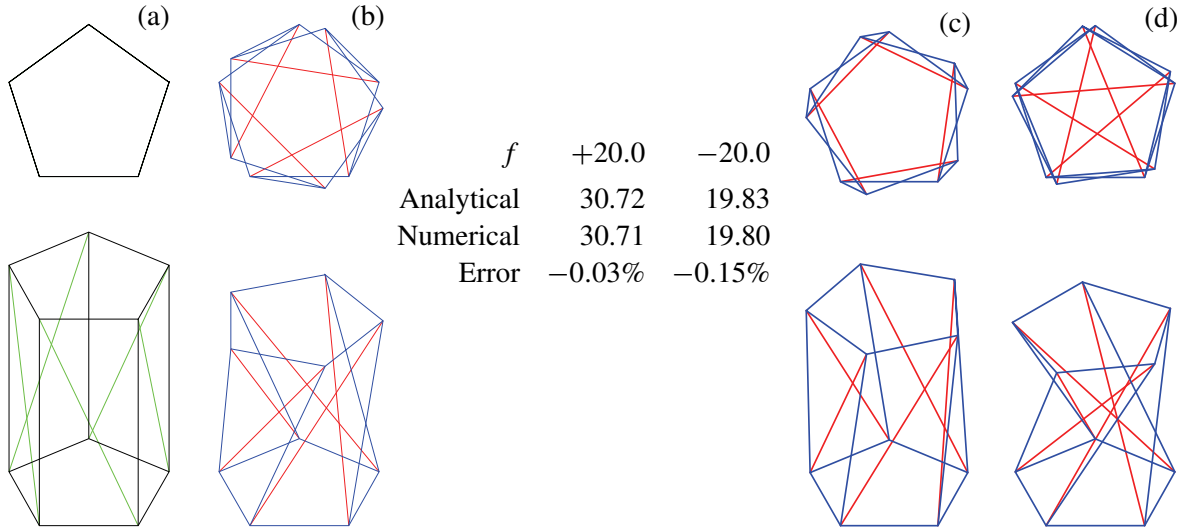
Also shown in (c) is the loaded configuration for $f = 20$ (rotation angle of about -34 degrees from the prestressed configuration), and in (d) the loaded configurations for $f = -20$ (rotation angle of about 27 degrees). The values for the axial force on the diagonal elements are given for these two cases.

Example 16.3. This is the same structure described in Example 16.2, except that $E = 1000$ for all elements. Here are the initial (a) and prestressed (b) configurations; the rotation angle from the initial configuration is 126 degrees.

f	$+20.0$	-20.0
Numerical	27.77	4.86
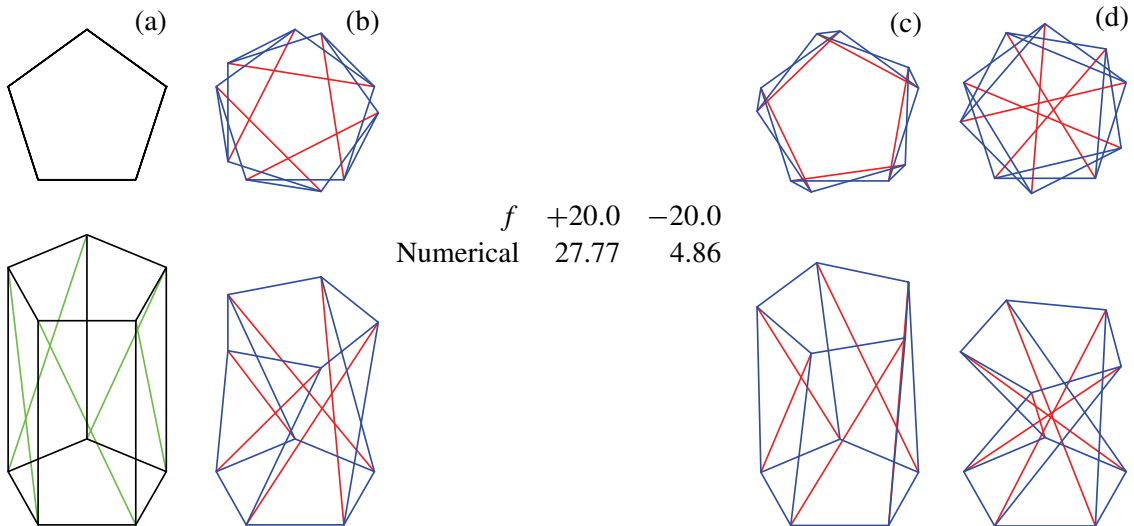
Also shown in (c) is the loaded configuration for $f = 20$ (rotation angle of about -38 degrees from the prestressed configuration), and in (d) the loaded configurations for $f = -20$ (rotation angle of about 45 degrees). The values for the axial force on the diagonal elements are given for these two cases.

Example 16.4 (A circular prism with axis on a circumference of radius 10). The section is defined by a regular triangle inscribed in a circle of radius 1. It is composed of 72 elements. The modulus of elasticity is 1000. The elements have area 1. Note that this is a nonplanar circular tensegrity that originates from connecting the ends of a straight prism tensegrity. This is a simple idea that can be used to define circular nonplanar tensegrities with any number of segments. A circular planar tensegrity was described recently in [Yuan et al. 2008]. Elements in the initial configuration that start in the state of constant stress are shown in green with stress of 5. There are no support constraints. The loading consists of self-equilibrated radial forces applied on the nodes of the exterior circumference.

Here are the initial (left), prestressed (middle), and loaded (right) configurations under the forces shown in the table.

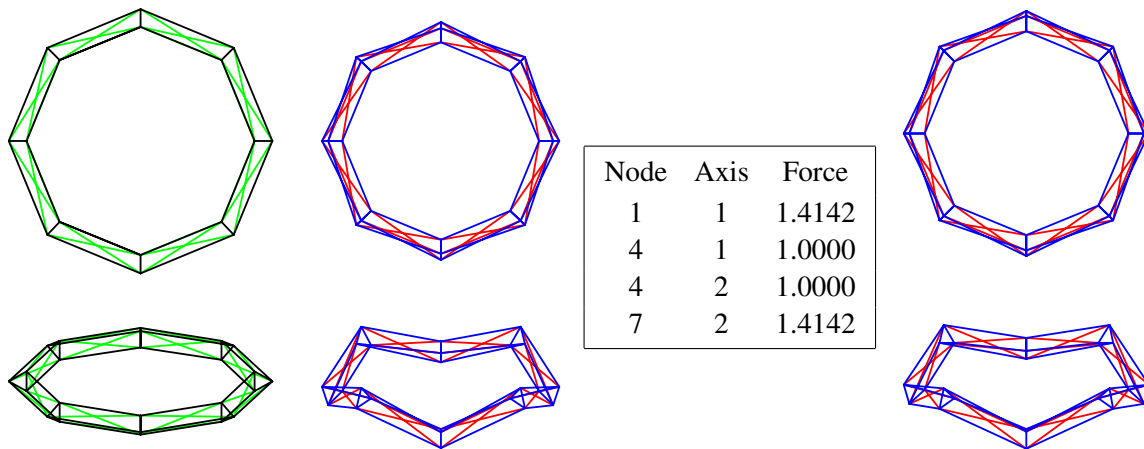| Node	Axis	Force
1	1	1.4142
4	1	1.0000
4	2	1.0000
7	2	1.4142

The elements are connected as follows:

Element	1	2	3	4	5	6	7	8	9	25	26	27	28	29	30	49	50	51	52	53	54
Node	1	2	3	4	5	6	7	8	9	1	2	3	5	6	4	2	3	1	4	5	6
Node	2	3	1	5	6	4	8	9	7	4	5	6	8	9	7	4	5	6	8	9	7

Here are the coordinates of the initial (left), prestressed (middle), and loaded (right) configurations. Due to symmetry, the tables show information for only one fourth of the structure.

Node	X	Y	Z	Node	X	Y	Z	Node	X	Y	Z
1	11.0000	0.0000	0.0000	1	9.3879	–0.0000	–2.1490	1	9.5010	–0.0000	–2.0677
2	9.5000	0.0000	0.8660	2	9.9007	0.0000	–0.4922	2	9.9371	0.0000	–0.3904
3	9.5000	0.0000	–0.8660	3	8.2098	0.0000	–0.8759	3	8.2630	0.0000	–0.8446
4	7.7782	7.7782	0.0000	4	6.6382	6.6382	2.1490	4	6.7182	6.7182	2.0677
5	6.7175	6.7175	0.8660	5	5.8052	5.8052	0.8759	5	5.8428	5.8428	0.8446
6	6.7175	6.7175	–0.8660	6	7.0009	7.0009	0.4922	6	7.0266	7.0266	0.3904
7	0.0000	11.0000	0.0000	7	0.0000	9.3879	–2.1490	7	0.0000	9.5010	–2.0677
8	0.0000	9.5000	0.8660	8	–0.0000	9.9007	–0.4922	8	–0.0000	9.9371	–0.3904
9	0.0000	9.5000	–0.8660	9	0.0000	8.2098	–0.8759	9	0.0000	8.2630	–0.8446

The next table shows the axial force for the prestressed and the loaded configurations:

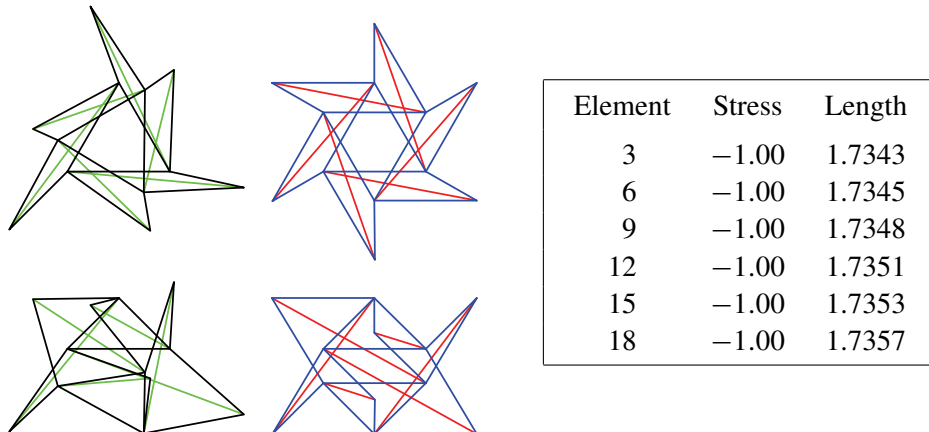| Element	1, 6, 7	2, 5, 8	3, 4, 9	25, 30	26, 27, 28, 29	49, 51, 52, 54	50, 53
Force	1.3113	1.0841	1.4375	−5.5232	−4.9454	5.0000	5.0000
Force	0.5762	1.5137	4.7852	−6.3702	−4.1728	3.7936	8.5064

Example 16.5 (A stella octangula with parameter $s = 1$). The modulus of elasticity is 1000. The elements have area 1. There are support constraints on nodes 1, 2, and 3 to prevent rigid body motion. A nonregular tensegrity can be generated by imposing different stress values for selected elements of a regular tensegrity. The regular tensegrity can be recovered by imposing equal stress values for the same selected elements on the previously generated nonregular tensegrity.

We illustrate here the initial configuration of the regular stella octangula and its prestressed configuration (nonregular stella octangula). The stress values for the diagonal elements of the initial configuration and the lengths of the diagonal elements of the prestressed configuration are also shown.

Element	Stress	Length
3	−1.25	1.4573
6	−1.50	1.5664
9	−1.75	1.6312
12	−2.00	1.8578
15	−2.25	1.8899
18	−2.50	1.8914
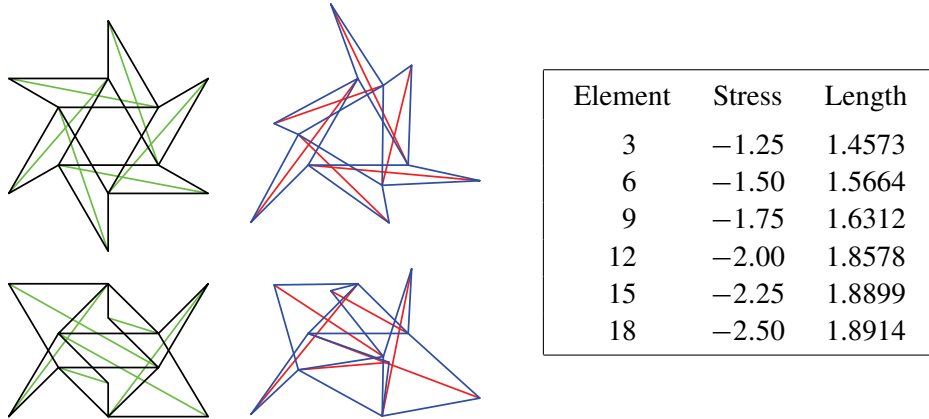
Finally, we illustrate the initial configuration of the nonregular stella octangula and its prestressed version, which is again a regular stella octangula. The stress values for the diagonal elements (initial configuration) and the lengths of the diagonal elements (prestressed configuration) are also shown.

Element	Stress	Length
3	−1.00	1.7343
6	−1.00	1.7345
9	−1.00	1.7348
12	−1.00	1.7351
15	−1.00	1.7353
18	−1.00	1.7357

17. Conclusions

A mathematical model is presented for form-finding and static analysis of tensegrity structures. The proposed model shows good agreement with analytical solutions for regular tensegrity structures. It can also handle nonregular tensegrity structures. The minimization of total potential energy has several advantages over solving the equilibrium equations in nonlinear mechanics: it allows solving for underconstrained structures. It is not necessary to derive the tangent stiffness matrix. It is not necessary to solve any system of equations. The model can handle large-scale problems.

References

[Arcaro and Klinka 2009] V. F. Arcaro and K. K. Klinka, "Finite element analysis for geometrical shape minimization", *J. Int. Assoc. Shell Spat. Struct.* **50**:2 (2009), 79–86.

[Calladine 1978] C. R. Calladine, "Buckminster Fuller's "Tensegrity" structures and Clerk Maxwell's rules for the construction of stiff frames", *Int. J. Solids Struct.* **14**:2 (1978), 161–172.

[Chassagnoux 2006] A. Chassagnoux, "David Georges Emmerich: Professor of morphology", *Int. J. Space Struct.* **21**:1 (2006), 59–71.

[Gill and Murray 1974] P. E. Gill and W. Murray, "Newton-type methods for unconstrained and linearly constrained optimization", *Math. Program.* **7**:1 (1974), 311–350.

[Meek 1971] J. L. Meek, *Matrix structural analysis*, McGraw-Hill, New York, 1971.

[Motro 2011] R. Motro, "Structural morphology of tensegrity systems", *Meccanica* **46**:1 (2011), 27–40.

[Nocedal and Wright 1999] J. Nocedal and S. J. Wright, *Numerical optimization*, Springer, New York, 1999.

[Oppenheim and Williams 2000] I. J. Oppenheim and W. O. Williams, "Geometric effects in an elastic tensegrity structure", *J. Elasticity* **59**:1-3 (2000), 51–65.

[Pellegrino 1986] S. Pellegrino, *Mechanics of kinematically indeterminate structures*, Ph.D. thesis, University of Cambridge, 1986.

[Pietrzak 1978] J. Pietrzak, "Matrix formulation of static analysis of cable structures", *Comput. Struct.* **9**:1 (1978), 39–42.

[Skelton and de Oliveira 2009] R. E. Skelton and M. C. de Oliveira, *Tensegrity systems*, Springer, New York, 2009.

[Tibert and Pellegrino 2003] A. G. Tibert and S. Pellegrino, "Review of form-finding methods for tensegrity structures", *Int. J. Space Struct.* **18**:4 (2003), 209–223.

[Yuan et al. 2008] X. Yuan, Z. Peng, S. Dong, and B. Zhao, "A new tensegrity module: "torus"", *Adv. Struct. Eng.* **11**:3 (2008), 243–251.

DARIO GASPARINI: dag6@cwru.edu
Civil Engineering Department, Case Western Reserve University, 2182 Adelbert Road, Cleveland, OH 44106-7201, United States

KATALIN K. KLINKA: katalin@klinka.hu
Department of Structural Engineering, Budapest University of Technology and Economics, 2 Bertalan Lajos, Budapest H-1111, Hungary

VINICIUS F. ARCARO: vinicius.arcaro@gmail.com
College of Civil Engineering, University of Campinas, Avenida Albert Einstein 951, Campinas, SP 13083-852, Brazil
http://www.arcaro.org

:::msp

STRUCTURAL DESIGN OF PYRAMIDAL TRUSS CORE SANDWICH BEAMS LOADED IN 3-POINT BENDING

MING LI, LINZHI WU, LI MA, BING WANG AND ZHENGXI GUAN

The dimensions of pyramidal lattice truss core sandwich beams loaded in 3-point bending are designed to achieve the most weight-efficient structure. The bending stiffness and strength of the sandwich beam is predicted theoretically, and the identified failure modes include core member buckling, core member crushing, face wrinkling, and face crushing. To predict the relevant limit loads of the four failure modes, a force analysis is carried out based on structural mechanics. The inclined angle of the core member is determined by maximizing the bending stiffness-to-weight ratio. The length and radius of the core member, the thickness of the face, and the length of the sandwich beam are determined by maximizing the bending strength-to-weight ratio for the given height of the core. The effectiveness of the design method is validated by experiments, and the specimen with optimal geometric parameters possesses the largest weight efficiency. The useful results are extended to give an available design tool for sandwich beam manufacturers.

1. Introduction

Sandwich structures are widely used in weight-sensitive structures where high stiffness-to-weight and strength-to-weight ratios are required [Vinson 2001]. The cores of sandwich structures are conventionally made of foams and honeycombs [Bitzer 1997; Gibson and Ashby 1997; He and Hu 2008]. Recent research has shown the higher weight efficiency of lattice structures compared to that of foams [Evans et al. 2001]. Numerous studies on metallic and polymer foams have shown that the strength of the foams is governed by cell wall bending (that is, bending-dominated materials) for all loading conditions and scales as $\bar{\rho}^{1.5}$, where $\bar{\rho}$ is the relative density of the foam [Chen et al. 1999; Ashby et al. 2000]. On the other hand, the strength of a structure that deforms by cell wall stretching (that is, strength-dominated materials) scales with $\bar{\rho}$. Deshpande et al. [2001] have analyzed the topological criteria for lattice structures to be stretching-dominated. They considered a periodic assembly of pin-jointed trusses with similarly situated nodes, and determined the degree of connectivity of bars per node in order to ensure stretching domination. For the case of a sandwich panel comprised of solid faces and a pin-jointed truss core, at least three core trusses per node are required for collapse to occur by truss stretching. Based on this criterion, numerous lattice topology structures have been proposed including those with tetrahedral [Deshpande et al. 2001; Deshpande and Fleck 2001; Wallach and Gibson 2001; Wicks and Hutchinson 2001; Chiras et al. 2002], pyramidal [Zok et al. 2004; Cote et al. 2007; Queheillalt and Wadley 2009], 3D-Kagome [Hyun et al. 2003; Wang et al. 2003; Lim and Kang 2006; Fan et al. 2007] structures, and so on. Besides the superior mechanical properties, truss core sandwich structures have additional potential by virtue of their open structure for multifunctional applications [Evans et al. 1998;

Lu et al. 2005; Wadley 2006]. For example, sandwich panels with solid faces and truss cores can serve as a heat transfer element simultaneously carrying loads. The cavity between the faces could be used for storage of a liquid in other applications.

For truss core sandwich structures, optimal design is an important problem that has attracted the attention of many researchers. The goal is to find the optimal geometric parameters that minimize the weight subject to a given load. Wicks and Hutchinson [2001] have studied the structural optimization of sandwich panels with octet truss cores and truss faces or solid faces in combinations of bending and transverse shear loads. Cote et al. [2007] have studied the minimum weight designs of pyramidal truss core sandwich columns in in-plane compression. It appears that only a few researchers have dealt with the optimal design of pyramidal truss core sandwich structures subject to 3-point bending loads. Zok et al. [2004], for example, investigated optimal design of pyramidal truss core sandwich panels in combinations of bending and transverse shear loads.

In the above-mentioned works, however, we cannot determine the thickness of the core, the thickness of the face, the radius of the core member, and the length of the sandwich structure simultaneously, and there is always a family of relationships among these variables. Thus, it is inconvenient for a structural designer. A simple and direct mathematical relation is preferable for a structural designer. Furthermore, for the lattice truss core sandwich beams, the common failure modes include face yielding, face buckling, core member yielding, and core member buckling [Wicks and Hutchinson 2001; Zok et al. 2004]. However, the four failure modes often can't converge at one point in the failure mechanism maps, and the optimal design is based on three failure modes: face yielding, face buckling, and core buckling (or face yielding, face buckling, and core yielding). Theoretically, the optimal design should be based on all four failure modes simultaneously. In the present paper, we consider a pyramidal truss core sandwich beam comprised of a pyramidal lattice truss core and two solid faces. When the sandwich beam is loaded in 3-point bending, the structural parameters are designed on the basis of optimal bending stiffness as well as bending strength, which is not according to the failure mechanism maps. Thus, all failure modes are active simultaneously. The present optimal design method offers a principle foundation for designing pyramidal truss core sandwich beams.

In this study, three assumptions are given, and then the bending stiffness and strength of a pyramidal truss core sandwich beam loaded in 3-point bending are predicted theoretically. To better understand the failure modes, force analysis of the pyramidal truss core sandwich beam is conducted. Based on the principle of minimizing the weight, the inclined angle, and the radius of the core member, the thickness of the face and the length of the sandwich beam are calculated. Experiments are carried out to validate the effectiveness of the structural design method on the specimen with optimal geometric parameters that possesses the largest weight efficiency. Several conclusions are given in the last section.

2. Predictions of the stiffness and strength of pyramidal truss core sandwich beams in 3-point bending

Consider a 3D sandwich beam with pyramidal truss cores and solid faces loaded in 3-point bending and with the geometry as shown in Figure 1. The loading is imposed on the center line of the top face. The sandwich beam is comprised of faces of thickness t_f and a square base pyramidal truss core with circular section of radius r and length l, and inclined at an angle ω with respect to the face. Thus, the height, H_c,
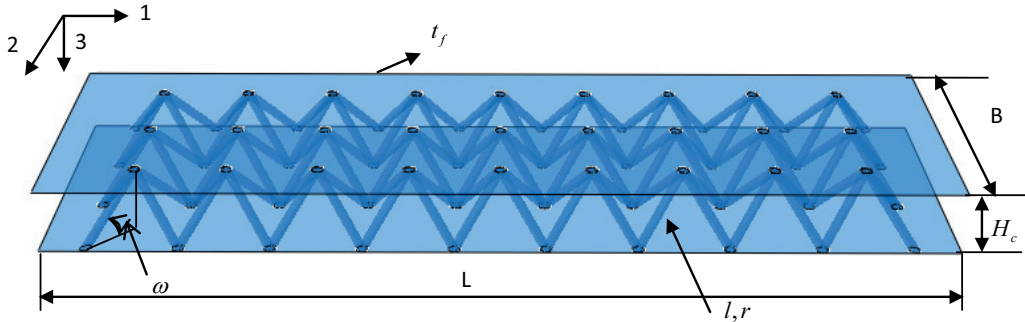
Figure 1. Geometry of the pyramidal truss core sandwich beam.

of the core is given by

$$H_c = l \sin \omega. \tag{1}$$

The span between the supports and the width of the sandwich beam are denoted by L and B, respectively. In the present paper, the span between the supports of the beam is almost equal to the length of the beam. Thus, L also represents the length of the beam in the following content. The relative density $\bar{\rho}$ of the core is given by

$$\bar{\rho} = \frac{2\pi r^2}{\sin \omega (l \cos \omega)^2}. \tag{2}$$

The underlying assumptions considered in the analytical predictions are:

- The faces are very thin compared with the total thickness of the sandwich beam.

- The macroscopic mechanical performance of the pyramidal truss core is too weak to provide a significant contribution to the bending rigidity of the sandwich beam.

- The nodes between the truss core and the faces are pin-joints offering no rotational restriction, and will not rupture in the loading process.

2.1. *Analytical predictions of the bending stiffness.* Referring to [Allen 1969, pp. 15–21], the deflection of a sandwich beam loaded in 3-point bending is the sum of the bending and shear deflections:

$$\delta = \frac{PL^3}{48(EI)_{\text{eq}}} + \frac{PL}{4(AG)_{\text{eq}}}, \tag{3}$$

where δ is the deflection at the beam's center due to P. The equivalent bending and shear stiffness are, respectively, given by

$$(EI)_{\text{eq}} \approx \tfrac{1}{2} E_f B t_f H_c^2, \qquad (AG)_{\text{eq}} = G_{13} B H_c. \tag{4}$$

E_f is the elastic modulus of the faces and G_{13} is the transverse shear modulus of the pyramidal truss core. According to assumptions (1) and (2), the core gives a negligible contribution to the overall bending stiffness and the faces give a negligible contribution to the overall transverse shear stiffness. The transverse shear modulus G_{13} is given by [Deshpande and Fleck 2001]

$$G_{13} = \tfrac{1}{8} \bar{\rho} E_c \sin^2(2\omega), \tag{5}$$

where E_c is the elastic modulus in the axial direction of the core member.

2.2. *Analytical predictions of the bending strength.* When a pyramidal truss core sandwich beam is loaded in 3-point bending, four main failure modes have been identified [Wicks and Hutchinson 2001]: core member buckling, core member crushing, face wrinkling, and face crushing. (If the material comprising the sandwich beam is elastic-brittle, such as a fiber reinforced composite, it will crush in a compression stress state; if the material is elastic-plastic, such as a metal, it will yield. We take crushing as the failure mode). To better understand the failure modes, it is essential to analyze the force distribution of a pyramidal truss core sandwich beam loaded in 3-point bending.

Force analysis based on structural mechanics. For simplicity, we initially consider a 2D sandwich structure with truss cores and truss faces subjected to a 3-point bending load, as sketched in Figure 2. The sandwich structure possesses m unit cells along the length direction, where the unit cell is represented by the gray area. The height of the core is also denoted as H_c and the inclined angle is denoted as θ. According to the foregoing pin-joint idealization of assumption (3), all members in the truss core sandwich beam are two-force rods which can only bear axial force. Based on the theory of structural mechanics, the forces in the face members and core members are shown in Figure 2. The maximum force in the face members is beneath the loading roller, which is $(m/2) P \cot \theta$. The span L of the sandwich is given by

$$L = 2m H_c \cot \theta, \tag{6}$$

and therefore the maximum force F_f in the face members is given by

$$F_f = \frac{m}{2} P \cot \theta = \frac{PL}{4H_c}. \tag{7}$$

The forces in all of the core members are identical, and are given by

$$F_c = \frac{P}{2 \sin \theta}. \tag{8}$$

Subsequently, consider a 3D sandwich beam with a pyramidal truss core and solid faces as shown in Figure 1. The sandwich beam is subjected to a 3-point bending load P along the whole width, so the load carried by a unit cell along the width direction is $P \sqrt{2} l \cos \omega / B$. The schematic illustration of the
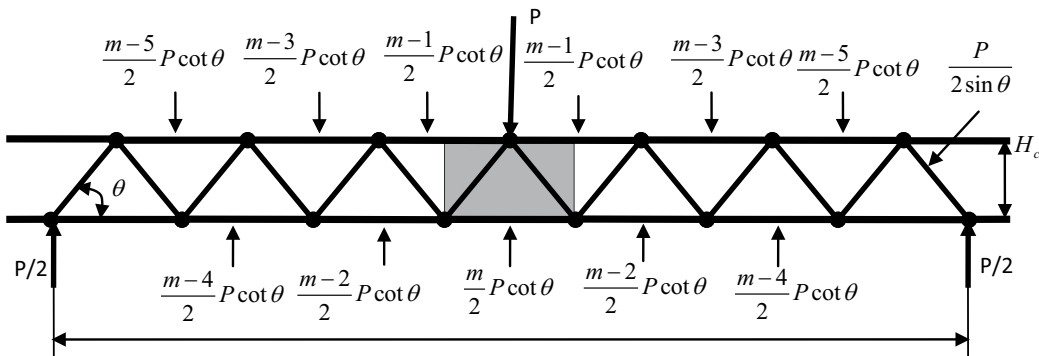

Figure 2. Force distribution of 2D sandwich beam with truss cores and truss faces.
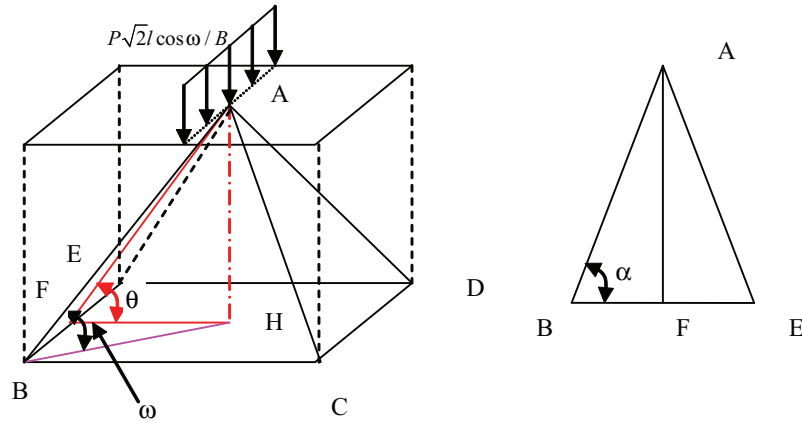
Figure 3. Force analysis and geometrical relations of a pyramidal unit cell.

force distribution of a unit cell is shown in Figure 3. From the above analysis, we have

$$F_{AF} = 2F_{AB} \sin \alpha = \frac{P\sqrt{2}l \cos \omega}{2B \sin \theta}. \tag{9}$$

According to the geometric relations, $\sin \alpha = AF/AB$, $\sin \theta = AH/AF$, and $\sin \omega = AH/AB$, we obtain

$$F_{AB} = \frac{P\sqrt{2}l \cos \omega}{4B \sin \alpha \sin \theta} = \frac{P\sqrt{2}l \cos \omega}{4B \sin \omega}. \tag{10}$$

So, the forces in the core members are

$$F_c = F_{AB} = \frac{P\sqrt{2}l \cos \omega}{4B \sin \omega}. \tag{11}$$

The maximum force in the faces of the 3D sandwich beam is also given by (7).

Failure modes: limit load calculations. According to (7) and (11), limit loads corresponding to the four failure modes are given by

$$P_{cb} = \frac{4B \sin \omega}{\sqrt{2}l \cos \omega} \sigma_{cb} \pi r^2 \quad \text{(core member buckling)}, \qquad P_{fw} = \frac{4H_c}{L} \sigma_{fw} B t_f \quad \text{(face wrinkling)},$$

$$P_{cc} = \frac{4B \sin \omega}{\sqrt{2}l \cos \omega} \sigma_{cc} \pi r^2 \quad \text{(core member crushing)}, \qquad P_{fc} = \frac{4H_c}{L} \sigma_{fc} B t_f \quad \text{(face crushing)}, \tag{12}$$

where σ_{cb} and σ_{cc} are the buckling and crushing strength of the core member, respectively, and σ_{fw} and σ_{fc} are the wrinkling and crushing strength of the faces, respectively. Core member buckling occurs between the two end joints of the truss loaded in a compressive stress state, and the buckling strength of the core member is given by

$$\sigma_{cb} = k_1^2 \pi^2 E_c \left(\frac{r}{2l}\right)^2, \tag{13}$$

where $k_1 = 1$ for a core member with simply supported ends, consistent with the pin-joint assumption. The upper face is subjected to compressive stress, and may fail by elastic buckling or crushing at the location on the face with maximum force (beneath the central roller). Face wrinkling occurs between

the adjacent nodes of attachment, which is known as intercellular buckling. The wrinkling strength of the faces is given by

$$\sigma_{fw} = \frac{k_2^2 \pi^2 E_f t_f^2}{12(\sqrt{2}l\cos\omega)^2}. \tag{14}$$

The rotational restraining effect of the truss core on the faces at the nodes of attachment is neglected, so $k_2 = 1$. The crushing strength of the core member σ_{cc} and the crushing strength of the face σ_{fc} can be measured experimentally.

3. Structural design of the pyramidal truss core sandwich beam

3.1. *Design of the inclined angle of the core member.* From (3), the overall bending stiffness-to-weight ratio will increase with the increase of the shear-modulus-to-weight ratio. The shear-modulus-to-weight ratio is given as

$$\frac{G_{13}}{\rho\bar{\rho}} = \frac{1}{8\rho} E_c \sin^2(2\omega), \tag{15}$$

where ρ is the density of the parent material. The shear-modulus-to-weight ratio reaches its maximum when the inclined angle, ω, equals $45°$; the overall bending stiffness-to-weight ratio also reaches its maximum here, while other geometric parameters remain constant. Thus, the inclined angle of the core member should be fixed at $45°$.

3.2. *Design of the radius of the core member.* For a core member loaded in axial compression loading, its weight efficiency will achieve its maximum value when core member crushing and buckling occur simultaneously. Based on this principle, we can obtain the optimal radius of the core member upon equating P_{cb} to P_{cc}, as follows:

$$r_{\rm cr} = H_c \frac{2}{k_1\pi\sin\omega}\sqrt{\frac{\sigma_{cc}}{E_c}}. \tag{16}$$

Then, take $\sigma_{c,\rm cr}$ as the failure strength of the core member, which is given by $\sigma_{c,\rm cr} = \sigma_{cc} = \sigma_{cb}$.

3.3. *Design of the thickness of the faces.* Based on the same principle used in Section 3.2, the weight efficiency of the face will achieve its maximum value when the face crushing and wrinkling occur simultaneously. The optimal thickness, $t_{f,\rm cr}$, of the faces can be obtained upon equating P_{fc} to P_{fw}:

$$t_{f,\rm cr} = H_c \frac{\cos\omega}{k_2\pi\sin\omega}\sqrt{\frac{24\sigma_{fc}}{E_f}}. \tag{17}$$

Then, take $\sigma_{f,\rm cr}$ as the failure strength of the faces, which is given by $\sigma_{f,\rm cr} = \sigma_{fc} = \sigma_{fw}$.

Design of the length of the sandwich beam. Using (12), the failure loads of the core member and faces are given as

$$P_{c,\rm cr} = \frac{4B\sin\omega}{\sqrt{2}l\cos\omega}\sigma_{c,\rm cr}\pi(r_{\rm cr})^2, \qquad P_{f,\rm cr} = \frac{4H_c}{L}\sigma_{f,\rm cr}Bt_{f,\rm cr}. \tag{18}$$

The weight efficiency of the whole sandwich structure achieves its maximum when every part fails simultaneously. So the faces and core members of the sandwich beam should fail simultaneously, which

means the failure load $P_{f,\mathrm{cr}}$ of the faces equates to the failure load $P_{c,\mathrm{cr}}$ of the core member, given as

$$\frac{4H_c}{L}\sigma_{f,\mathrm{cr}}Bt_{f,\mathrm{cr}} = \frac{4B\sin\omega}{\sqrt{2}l\cos\omega}\sigma_{c,\mathrm{cr}}\pi(r_{\mathrm{cr}})^2. \tag{19}$$

Substituting (1), (16), and (17) into (19), we obtain

$$L = H_c\frac{k_1^2}{k_2}\frac{(\cos\omega)^2}{\sin\omega}\frac{\sigma_{f,\mathrm{cr}}E_c}{\sigma_{c,\mathrm{cr}}^2}\sqrt{\frac{3\sigma_{f,\mathrm{cr}}}{E_f}}. \tag{20}$$

Hitherto, the design procedure can be summarized as follows:

- From (14), the inclined angle of the core member should be fixed at 45°.
- Given H_c, one can determine the length of the core member, the radius of the core member, the thickness of the faces and the length of the sandwich beam from (1), (16), (17), and (20), respectively.

4. Experiments and discussion

In order to validate the feasibility and effectiveness of the proposed structural design method, experiments are conducted.

4.1. *Fabrication of specimen.* The sandwich beam specimen is made of a carbon fiber reinforced composite T700/epoxy with a hot compression molding method. A set of molds with special structures are designed to fabricate the pyramidal truss core sandwich beam. The faces are comprised of a laminate of prepreg with the stack sequence $(0/90)_n$, where the number n can vary to gain a different face thickness. The core member is rolled into a circular cross section from two plies of prepreg with the stack sequence $(0/90)$. The preformed sandwich beam is cured at 125° C in an autoclave under a pressure of 0.5 MPa for an hour, and cools down to room temperature naturally. Then the specimen is taken out from the autoclave and removed from the molds. Because the sandwich beam specimen is fabricated with the same composite material and stack sequence, the equivalent elastic modulus and crushing strength of the face and core member are equal. Thus, $E_f = E_c = 60\,\mathrm{GPa}$ and $\sigma_{cc} = \sigma_{fc} = 329\,\mathrm{MPa}$. The density of the T700/epoxy composite is $\rho = 1500\,\mathrm{kg\,m^{-3}}$.

4.2. *Test protocol.* Ideally, the specimen geometries are designed to probe the different failure modes of face crushing, face wrinkling, core member crushing, and core member buckling. However, in the current study, it was not feasible to make a range of pyramidal truss core sandwich beams with different truss dimensions. From the above analysis, the optimal inclined angle of the core member is 45°, and thus the inclined angle of the specimen is fixed at 45° and the height of the core is 15 mm. The optimal radius of the core member is 1 mm. For the sandwich beam specimen, the radius of the core member is chosen as 1.25 mm, which is slightly lager than the optimal radius computed from (16). The reasons are as follows. First, it is difficult for fabrication if the truss radius is too small. Second, the material properties of the composite possess discreteness, so, we take a conservative value of the truss radius to prevent core member crushing from occurring prematurely. The optimal length of the sandwich beam and the thickness of the face are 248 mm and 1.73 mm, respectively. In order to find the largest weight efficiency, three types of specimens with face thicknesses 0.84 mm, 1.73 mm, and 2.6 mm are designed

and fabricated. The width of the specimen is 100 mm, and the span of the sandwich beam is taken as 248 mm, which is equal to the optimal value.

The weight of the sandwich beam is

$$W = \rho L B (\bar{\rho} H_c + 2 t_f). \tag{21}$$

The weight efficiency η is defined as

$$\eta = \frac{P_{cr}}{W}, \tag{22}$$

where P_{cr} is the failure load of the pyramidal lattice truss core sandwich beam loaded in 3-point bending.

The specimen is tested under 3-point bending using an Instron 5569 machine, applying loading through a 10 mm diameter cylindrical roller in accordance with ASTM standard C393 [ASTM 2006]. The load is applied at a rate of 1 mm min^{-1} and recorded with the load cell of the testing machine. A laser extensometer is used to measure the deflection, δ, of the specimen.

4.3. *Results and discussion.* The failure loads and weight efficiencies of the three types of specimens are listed in Table 1, and the corresponding bending responses are shown in Figure 4. From Table 1, good agreement is found between the measured and predicted failure loads, and the measured failure loads are somewhat lower than the predicted ones. These discrepancies are attributed to imperfections in the manufactured specimens, while the analytical predictions pertain to the idealized geometry. The predicted and measured weight efficiencies of the specimen with face thickness 1.73 mm are larger than those of the specimens with face thicknesses 0.84 mm and 2.6 mm, which validates the effectiveness of the structural design method.

The corresponding failure mode photographs are shown in Figures 5, 6, and 7. From Figure 5, it is found that the upper face of the specimen with face thickness 0.84 mm wrinkles like a sine wave in the compressive stress. For the specimen with face thickness 1.73 mm, it is found, from Figure 6, that the upper face and the core member crush simultaneously. From Figure 7, it is found that only core member

Predicted				
Thickness of face-sheet (mm)	Failure mode	Failure load (kN)	Weight (g)	Weight efficiency
0.84	FW	1.57	74.5	2107
1.73	FCC	13.73	151.9	9038
2.6	CC	13.78	227.6	6054
Measured				
Thickness of face-sheet (mm)	Failure mode	Failure load (kN)	Weight (g)	Weight efficiency
0.84	FW	1.55	85	1823
1.73	FCC	11.63	156	7455
2.6	CC	12.87	235	5476

Table 1. The predicted and measured failure loads and weight efficiencies. FW indicates face wrinkling, FCC face and core member crushing simultaneously, and CC core member crushing; for simplicity, the acceleration of gravity is taken as 10 N kg^{-1} in the computation of weight efficiency.
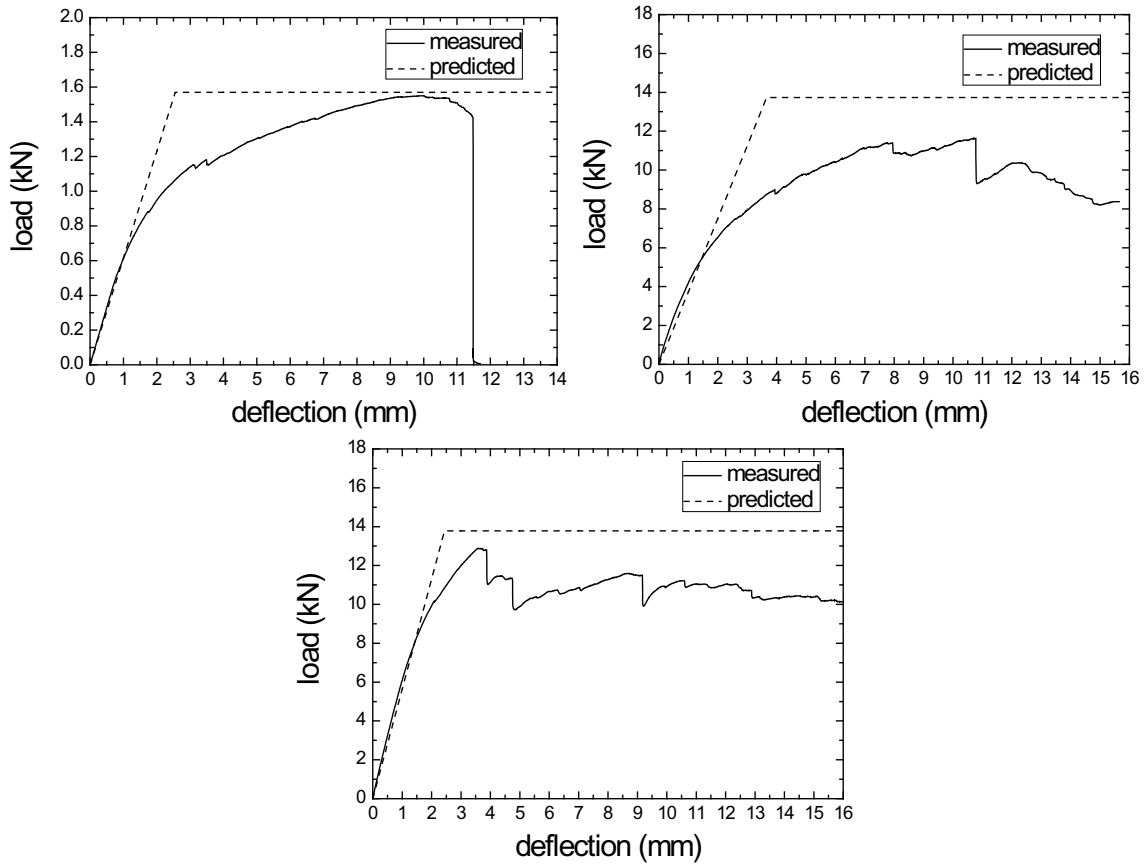
Figure 4. Bending response of sandwich structures with different face-sheet thicknesses: 0.84 mm (upper left), 1.73 mm (upper right), and 2.6 mm (lower).
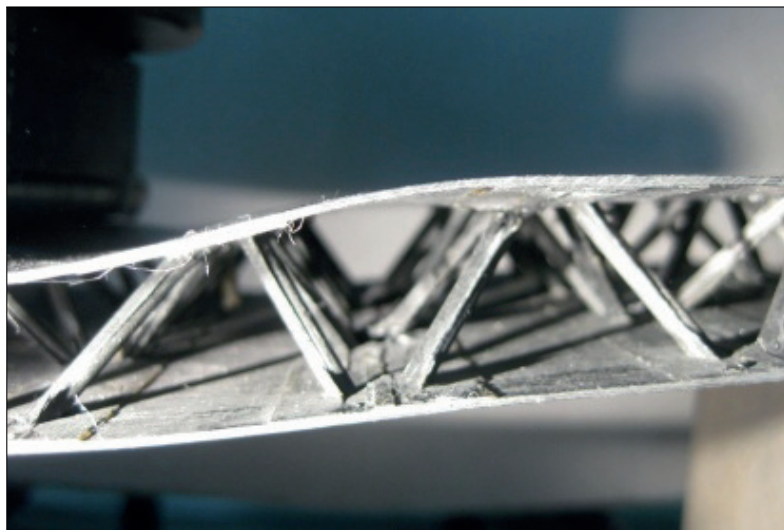

Figure 5. Face-sheet wrinkling of the specimen with face-sheet thickness 0.84 mm.
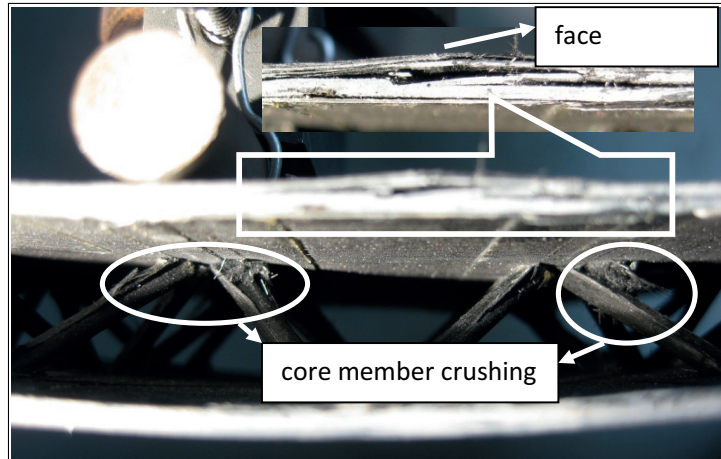
Figure 6. Face-sheet and core member crushing occur simultaneously for the specimen with face-sheet thickness 1.73 mm.
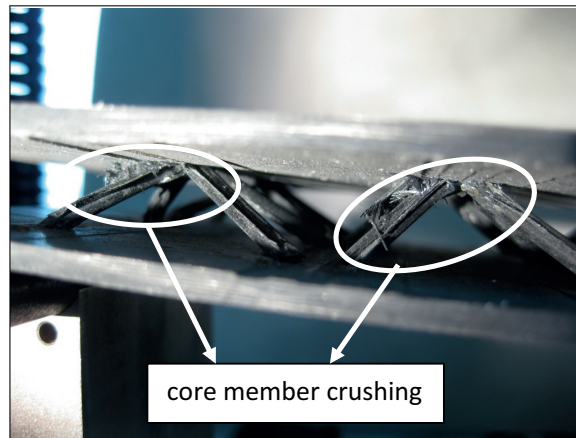

Figure 7. Core member crushing of the specimen with face-sheet thickness 2.6 mm.

crushing occurs for the specimen with face thickness 2.6 mm. All the failure modes observed above agree well with the predicted ones.

From Table 1, it is found that the ratio of the core thickness to the face thickness is about 9 at the condition of optimal geometric parameters. According to the quantitative definition of thin and thick face-sheets of sandwich structures given by [Allen 1969, pp. 15–21], the face can be treated as thin when the core thickness is lager than 5.77 times the face thickness. So, assumption (1) is reasonable. The length to the radius of the core member is about 20, which causes the transverse force of the core member to be rather smaller than the axial force, so the pin-joint idealization of assumption (2) is reasonable.

Generally, in actual loading conditions, the length of the beam is given. For example, for a bridge, the total span is directly given. Thus, in the geometric parameter optimization of a sandwich beam, the thickness of the core is considered as a design variable and the length of the sandwich beam is considered to be fixed. The thickness of the core can be determined from (20). Subsequently, the length of the core

member, the radius of the core member and the thickness of the face can be determined with (1), (16), and (17), respectively.

5. Conclusions

- Based on the pin-joint assumption, force analysis is implemented in a pyramidal truss core sandwich beam loaded in 3-point bending, and the limit load calculations are then conducted.

- The inclined angle of the core member should be fixed at 45° to maximize the overall bending stiffness-to-weight ratio.

- The length of the core member, the radius of the core member, the thickness of the face, and the length of the sandwich beam are all deduced with the condition of maximizing the bending strength-to-weight ratio.

- Experiments validate the feasibility and effectiveness of the proposed structural design method, and the specimen with optimal geometric parameters possesses the largest weight efficiency.

- In the present study, a simple and direct design procedure is developed, which is easy to implement for manufacturers.

Acknowledgement

References

[Allen 1969] H. G. Allen, *Analysis and design of structural sandwich panels*, Pergamon, Oxford, 1969.

[Ashby et al. 2000] M. F. Ashby, A. G. Evans, N. A. Fleck, L. J. Gibson, J. W. Hutchinson, and H. N. G. Wadley, *Metal foams: a design guide*, Butterworth Heinemann, Boston, 2000.

[ASTM 2006] "Standard test method for core shear properties of sandwich constructions by beam flexure", Technical report ASTM C393M-06, American Society for Testing and Materials International, West Conshohocken, PA, 2006.

[Bitzer 1997] T. Bitzer, *Honeycomb technology: materials, design, manufacturing, applications and testing*, Chapman & Hall, London, 1997.

[Chen et al. 1999] C. Chen, T. J. Lu, and N. A. Fleck, "Effect of imperfections on the yielding of two-dimensional foams", *J. Mech. Phys. Solids* **47**:11 (1999), 2235–2272.

[Chiras et al. 2002] S. Chiras, D. R. Mumm, A. G. Evans, N. Wicks, J. W. Hutchinson, K. Dharmasena, H. N. G. Wadley, and S. Fitchter, "The structural performance of near-optimized truss core panels", *Int. J. Solids Struct.* **39**:15 (2002), 4093–4115.

[Cote et al. 2007] F. Cote, R. Biagi, H. Bart-Smith, and V. S. Deshpande, "Structural response of pyramidal core sandwich columns", *Int. J. Solids Struct.* **44**:10 (2007), 3533–3556.

[Deshpande and Fleck 2001] V. S. Deshpande and N. A. Fleck, "Collapse of truss core sandwich beams in 3-point bending", *Int. J. Solids Struct.* **38**:36–37 (2001), 6275–6305.

[Deshpande et al. 2001] V. S. Deshpande, M. F. Ashby, and N. A. Fleck, "Foam topology bending versus stretching dominated architectures", *Acta Mater.* **49**:6 (2001), 1035–1040.

[Evans et al. 1998] A. G. Evans, J. W. Hutchinson, and M. F. Ashby, "Multifunctionality of cellular metal systems", *Prog. Mater. Sci.* **43**:3 (1998), 171–221.

[Evans et al. 2001] A. G. Evans, J. W. Hutchinson, N. A. Fleck, M. F. Ashby, and H. N. G. Wadley, "The topological design of multifunctional cellular metals", *Prog. Mater. Sci.* **46**:3–4 (2001), 309–327.

[Fan et al. 2007] H. L. Fan, F. H. Meng, and W. Yang, "Sandwich panels with Kagome lattice cores reinforced by carbon fibers", *Compos. Struct.* **81**:4 (2007), 533–539.

[Gibson and Ashby 1997] L. J. Gibson and M. F. Ashby, *Cellular solids: structure and properties*, 2nd ed., Cambridge University Press, Cambridge, 1997.

[He and Hu 2008] M. He and W. Hu, "A study on composite honeycomb sandwich panel structure", *Mater. Des.* **29**:3 (2008), 709–713.

[Hyun et al. 2003] S. Hyun, A. M. Karlsson, S. Torquato, and A. G. Evans, "Simulated properties of Kagomé and tetragonal truss core panels", *Int. J. Solids Struct.* **40**:25 (2003), 6989–6998.

[Lim and Kang 2006] J.-H. Lim and K.-J. Kang, "Mechanical behavior of sandwich panels with tetrahedral and Kagome truss cores fabricated from wires", *Int. J. Solids Struct.* **43**:17 (2006), 5228–5246.

[Lu et al. 2005] T. J. Lu, L. Valdevit, and A. G. Evans, "Active cooling by metallic sandwich structures with periodic cores", *Prog. Mater. Sci.* **50**:7 (2005), 789–815.

[Queheillalt and Wadley 2009] D. T. Queheillalt and H. N. G. Wadley, "Titanium alloy lattice truss structures", *Mater. Des.* **30**:6 (2009), 1966–1975.

[Vinson 2001] J. R. Vinson, "Sandwich structures", *Appl. Mech. Rev. (ASME)* **54**:3 (2001), 201–214.

[Wadley 2006] H. N. G. Wadley, "Multifunctional periodic cellular metals", *Phil. Trans. R. Soc. A* **364**:1838 (2006), 31–68.

[Wallach and Gibson 2001] J. C. Wallach and L. J. Gibson, "Mechanical behavior of a three-dimensional truss material", *Int. J. Solids Struct.* **38**:40–41 (2001), 7181–7196.

[Wang et al. 2003] J. Wang, A. G. Evans, K. Dharmasena, and H. N. G. Wadley, "On the performance of truss panels with Kagome cores", *Int. J. Solids Struct.* **40**:25 (2003), 6981–6988.

[Wicks and Hutchinson 2001] N. Wicks and J. W. Hutchinson, "Optimal truss plates", *Int. J. Solids Struct.* **38**:30–31 (2001), 5165–5183.

[Zok et al. 2004] F. W. Zok, S. A. Waltner, Z. Wei, H. J. Rathbun, R. M. McMeeking, and A. G. Evans, "A protocol for characterizing the structural performance of metallic sandwich panels: application to pyramidal truss cores", *Int. J. Solids Struct.* **41**:22–23 (2004), 6249–6271.

MING LI: lmrocket@163.com
Center for Composite Materials, Harbin Institute of Technology, Harbin 150001, China

LINZHI WU: wlz@hit.edu.cn
Center for Composite Materials, Harbin Institute of Technology, Harbin 150001, China

LI MA: mali@hit.edu.cn
Center for Composite Materials, Harbin Institute of Technology, Harbin 150001, China

BING WANG: wangbing86@hit.edu.cn
Center for Composite Materials, Harbin Institute of Technology, Harbin 150001, China

ZHENGXI GUAN: g185002@yahoo.com.cn
Xi'an Research Institute of High-tech, Xi'an 710025, China

▪msp

WAVE SCATTERING FROM A RECTANGULAR CRACK
IN AN ANISOTROPIC CLADDING

Per-Åke Jansson

Ultrasonic testing of a thick elastic plate with a crack in an anisotropic cladding is modeled analytically for a fully three-dimensional case. The model includes an ultrasonic transmitter and a receiver as well as wave scattering from a rectangular crack. The effect of a corrugated interface between the base component and the cladding is also taken into account. To solve the scattering problem the null field approach is employed to determine a Green's tensor for the same structure without a crack and the source point located in the cladding. Utilizing the Green's tensor an integral representation for the displacement field in the same structure with a crack and an incident field generated by an ultrasonic transducer may be derived. It is then straightforward to derive a hypersingular integral equation for the crack opening displacement, which can be used to determine the change in signal response due to the crack by Auld's reciprocity argument. Numerical results are given for a variety of cases illustrating the effects of size, position, and orientation of the crack and the properties of the corrugated interface.

Introduction

Ultrasonic nondestructive testing is frequently used to detect defects, e.g., in nuclear power plants. Even though the method has been in use for a considerable time and may be regarded as well-established, there is a need for modeling of the testing procedure. Such a model may be useful for planning of testing, for qualification of testing procedures, for interpretation of results, and for education purposes. Using a good mathematical model also has the benefit of being much cheaper than experimental methods, in particular when parameter studies are performed.

In the nuclear power industry it is common to use claddings, i.e., layers of austenitic steel, to prevent or reduce corrosion. A cladding may be applied to a thick plate or a thick-walled pipe by a manual or automated welding process. As a result of the fabrication process the interface between the base material and the cladding usually becomes corrugated, which is likely to affect the propagation of ultrasonic waves. Furthermore, the cladding material is normally anisotropic, which will also complicate the interpretation of test results. Thus, a numerical model for the testing procedure may be useful for understanding of the influence of the cladding on the signal response. An overview of ultrasonic testing of clad components is given in [Hudgell 1994].

Various wave propagation problems for a thick plate with a cladding with or without a crack have been studied previously. The 2D and 3D wave propagation problems for a structure without a crack have been investigated in [Krasnova et al. 2005; Krasnova 2005] using the null field approach, and in [Krasnova and Jansson 2006] using approximate boundary conditions at the interface. The 2D scalar scattering problem with a strip-like crack was solved in [Zagbai and Boström 2006], and the 2D P-SV

problem in [Jansson and Zagbai 2007]. In the present paper the analysis is generalized to the 3D case. A rudimentary version has previously been presented at a conference [Jansson 2010].

The aim of this paper is to develop a fully three-dimensional analytical model for a thick plate with a rectangular crack of arbitrary orientation in a cladding. Both materials are allowed to be anisotropic without any restrictions on symmetry or orientation of the crystal axes. In the numerical examples, however, only the case of an isotropic base material and a transversely isotropic cladding is studied. The effect of a one-dimensionally periodic interface between the base component and the cladding is also taken into account. Actually, real interfaces for welded claddings are more or less periodic. Besides, the analysis will be considerably simplified, since the periodicity can be utilized to discretize the problem. To solve the scattering problem a hypersingular integral equation technique is employed. The solution is exact in the sense that no restrictions are imposed on the frequency of the ultrasonic transmitter or the shape of the periodic interface, although numerical results are only given for a sinusoidal surface. In practice, however, the convergence will be poor for high frequencies and very rough interfaces. The results are believed to be valid, at least qualitatively, not only for a plate but also for components with curved surfaces, like pressure vessels and pipes, as long as the curvature is sufficiently small.

The integral equation method used in this paper is computationally efficient, but has the drawback that only defects of simple shapes can be handled. For more complex geometries it is necessary to rely on other methods, such as the finite element method. However, for 3D geometries and high frequencies a very large number of elements is needed, which may be a limitation. Other numerical methods include the strip element method of [Liu and Achenbach 1995], the elastodynamic finite integration technique, or EFIT [Langenberg et al. 2000], and the boundary element method (see [Wang et al. 1996], for example). Elastic wave scattering from periodic surfaces have previously been studied extensively for the case of isotropic media; see, e.g., [Fokkema and van den Berg 1977; Fokkema 1980; Lakhtakia et al. 1984].

1. Problem formulation

The geometry of the wave propagation problem is depicted in Figure 1. A thick plate is composed of two layers of different generally anisotropic materials in welded contact. The crystal axes may be arbitrarily
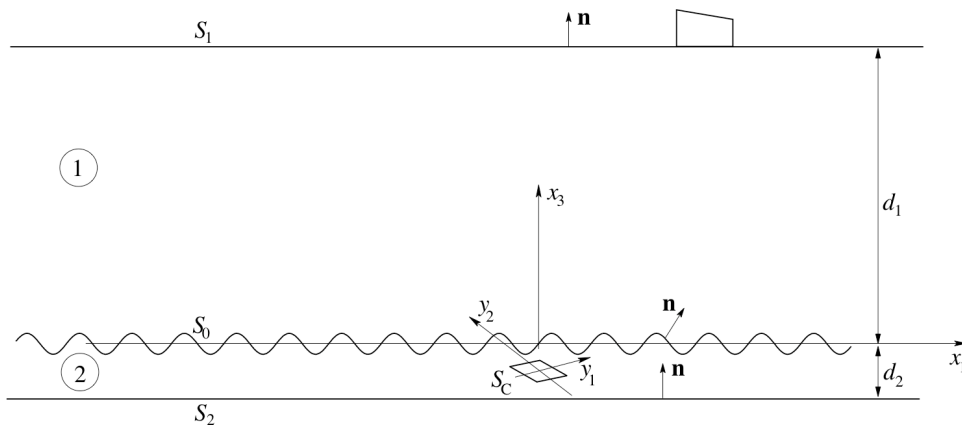

Figure 1. The geometry of a plate with a crack inside a cladding.

oriented. The interface S_0 is assumed to be periodic with a period a. This is believed to be a reasonable approximation, since real interfaces are more or less periodic. The layer of thickness d_1 is the base material. The cladding of thickness d_2 contains a rectangular crack

$$S_C \quad (|y_1| < c, \, |y_2| < d),$$

which may be tilted arbitrarily with respect to the back wall S_2. An ultrasonic transmitter is placed on the free surface S_1 of the base material. All numerical examples given here are for a transducer working in pulse-echo mode, even though the analysis is valid for the case of tandem inspection as well. Only the case of a transducer working at a fixed angular frequency ω will be considered, although it is straightforward, but somewhat time-consuming, to obtain results in the time domain.

For time-harmonic conditions the displacement fields u_j^i in the two materials $i = 1, 2$ satisfy

$$\frac{\partial}{\partial x_k} \sigma_{kj}^i + \rho^i \omega^2 u_j^i = 0, \tag{1}$$

where ρ^i is the corresponding density, and σ_{kj}^i is the stress tensor, which is related to the displacement by the constitutive relation

$$\sigma_{kj}^i = c_{kjk'j'}^i \frac{\partial}{\partial x_{j'}} u_{k'}^i, \tag{2}$$

where $c_{kjk'j'}^i$ are the stiffnesses of material i. Unless otherwise stated the summation convention is used throughout in the following.

The boundary conditions to be satisfied are

$$t_j = \sigma_{kj} n_k = 0$$

on S_1 (except directly below the transducer), S_2, and S_C. Furthermore, u_j and t_j are continuous on the interface S_0, where $x_3 = s(x_1)$. Here $s(x_1)$ is assumed to be a periodic function; in fact, it is taken as sinusoidal in the numerical examples:

$$s(x_1) = b \sin \frac{2\pi x_1}{a}. \tag{3}$$

There are two main reasons for this. Firstly, real interfaces are more or less sinusoidal. Secondly, certain integrals that will appear during the analysis can be evaluated analytically, which will speed up the computations considerably. It should be pointed out, however, that there is no fundamental difficulty in choosing some other periodic function, as long as it is differentiable. Finally, it is assumed that the radiation conditions are fulfilled, so that all waves are outgoing at infinity.

The first step in the solution is to determine a Green's tensor for the same structure without a crack. The source point is located in the cladding. This tensor is then used to derive an integral representation for the displacement field in the same structure with a crack and an incident field generated by an ultrasonic transducer. From the integral representation it is then possible to derive a hypersingular integral equation for the crack opening displacement. Once the crack opening displacement is known the change in signal response due to the crack can be determined using Auld's reciprocity argument [1979].

2. The Green's tensor for the structure without a crack

To determine the Green's tensor for the layered plate without a crack with a source in the cladding, i.e., the displacement field in both materials caused by a point force in material 2, the following integral representations are used:

$$\int_{S_1-S_0} \left[\Sigma_{kjj'}(\boldsymbol{x};\boldsymbol{x}')G^1_{jj''}(\boldsymbol{x};\boldsymbol{x}'') - G_{jj'}(\boldsymbol{x};\boldsymbol{x}')\Sigma^1_{kjj''}(\boldsymbol{x};\boldsymbol{x}'') \right] n_k \, dS$$
$$= \begin{cases} G_{j''j'}(\boldsymbol{x}'';\boldsymbol{x}') & (\boldsymbol{x}'' \text{ in material 1}), \\ 0 & (\boldsymbol{x}'' \text{ in material 2}); \end{cases} \quad (4)$$

$$\int_{S_0-S_2} \left[\Sigma_{kjj'}(\boldsymbol{x};\boldsymbol{x}')G^2_{jj''}(\boldsymbol{x};\boldsymbol{x}'') - G_{jj'}(\boldsymbol{x};\boldsymbol{x}')\Sigma^2_{kjj''}(\boldsymbol{x};\boldsymbol{x}'') \right] n_k \, dS$$
$$= \begin{cases} -G^2_{j''j'}(\boldsymbol{x}'';\boldsymbol{x}') & (\boldsymbol{x}'' \text{ in material 1}), \\ -G^2_{j''j'}(\boldsymbol{x}'';\boldsymbol{x}') + G_{j''j'}(\boldsymbol{x}'';\boldsymbol{x}'). & (\boldsymbol{x}'' \text{ in material 2}). \end{cases} \quad (5)$$

Here $G_{jj'}(\boldsymbol{x};\boldsymbol{x}')$ is the Green's tensor to be determined, and $G^i_{jj'}(\boldsymbol{x};\boldsymbol{x}')$ are half-space Green's tensors for material $i=1,2$. If the scattering properties of the interface are considered, $G^2_{j''j'}$ may be regarded as an incident field, $G_{j''j'}$ as the scattered field in material 1, and $G_{j''j'} - G^2_{j''j'}$ as the scattered field in material 2. The corresponding stress tensors $\Sigma^i_{kjj'}$ are related to the Green's tensors by

$$\Sigma^i_{kjj'}(\boldsymbol{x};\boldsymbol{x}') = c^i_{kjk'j''} \frac{\partial}{\partial x_{j''}} G^i_{k'j'}(\boldsymbol{x};\boldsymbol{x}'). \quad (6)$$

The half-space Green's tensors can be expressed as double Fourier transforms in x_1 and x_2:

$$G^2_{jj'}(\boldsymbol{x};\boldsymbol{x}') = \int_{-\infty}^{\infty} \int_{-\infty}^{\infty} \sum_{n=1}^{3} D^{2\pm}_n U^{2\pm}_{nj'} U^{2\pm}_{nj} \, e^{i(q(x_1-x_1')+p(x_2-x_2')+h^{2\pm}_n(x_3-x_3'))} \, dq \, dp$$

$$+ \int_{-\infty}^{\infty} \int_{-\infty}^{\infty} \sum_{n,n'=1}^{3} D^{2-}_n U^{2-}_{nj'} B^2_{nn'} U^{2+}_{n'j} \, e^{i(q(x_1-x_1')+p(x_2-x_2')+h^{2+}_{n'}(x_3+d_2)-h^{2-}_n(x_3'+d_2))} \, dq \, dp, \quad (7)$$

for $x_3 \gtrless x_3'$, and similarly for $G^1_{jj'}$; see Appendix A. Here $U^{2\pm}_{nj}$ are polarization vectors and $h^{2\pm}_n$ are the corresponding wavenumbers in the x_3-direction for plane wave solutions. These can be determined from a generalized eigenvalue problem derived from (1) and (2). The $+$ and $-$ signs refer to up- and downgoing waves, respectively. The coefficients $D^{2\pm}_n$ are determined from the jump condition at $x_3 = x_3'$, and $B^2_{nn'}$ is a reflection matrix determined from the condition of vanishing traction at the free surface S_2. The details are given in Appendix A.

The scattered field in material 2 may be expanded as

$$G_{jj'}(\boldsymbol{x};\boldsymbol{x}') - G^2_{jj'}(\boldsymbol{x};\boldsymbol{x}') = \int_{-\infty}^{\infty} \int_{-\infty}^{\infty} \sum_{n=1}^{3} f_{nj'}(q,p;x_1',x_2',x_3')[U^{2-}_{nj} e^{i(qx_1+px_2+h^{2-}_n x_3)}$$

$$+ \sum_{n,n'=1}^{3} B^2_{nn'} U^{2+}_{n'j} e^{i(qx_1+px_2+h^{3+}_{n'}(x_3+d_2)-h^{2-}_n d_2)}] \, dq \, dp. \quad (8)$$

The surface fields $G_{jj'}$ and $\Sigma_{kjj'}n_k$ at the interface can also be expanded as Fourier transforms:

$$G_{jj'}(x_1, x_2, s(x_1); \boldsymbol{x}') = \int_{-\infty}^{\infty} \int_{-\infty}^{\infty} \alpha_{jj'}(q', p'; \boldsymbol{x}') e^{i(q'x_1 + p'x_2)} \, dq' \, dp',$$

$$\Sigma_{kjj'}(x_1, x_2, s(x_1); \boldsymbol{x}')(1 + s'(x_1)^2)^{1/2} n_k = \int_{-\infty}^{\infty} \int_{-\infty}^{\infty} \beta_{jj'}(q', p'; \boldsymbol{x}') e^{i(q'x_1 + p'x_2)} \, dq' \, dp'. \tag{9}$$

The factor $(1 + s'^2)^{1/2}$ that appears in the integration measure is incorporated into the surface field for later convenience. To proceed the Fourier expansions for the Green's tensors and the surface fields are inserted into the integral representations (4)–(5), noting that $G_{jj'}(\boldsymbol{x}; \boldsymbol{x}') = G_{j'j}(\boldsymbol{x}'; \boldsymbol{x})$. Since the interface is periodic, the infinite integrals over the interface S_0 in (4) and (5) can be reduced to integrals over one period by using the identity

$$\int_{-\infty}^{\infty} g(x) e^{iqx} \, dx = \sum_{l=-\infty}^{\infty} \delta\left(\frac{qa}{2\pi} + l\right) \int_0^a g(x) e^{iqx} \, dx, \tag{10}$$

where $g(x)$ is periodic with period a; see [Richtmyer 1981], for instance.

After some tedious algebra a set of simultaneous equations for the Fourier coefficients is obtained:

$$0 = \sum_{l'=-\infty}^{\infty} \left(Q^1_{nlj'l'} \alpha_{j'jl'} + Q^2_{nlj'l'} \beta_{j'jl'} \right),$$

$$-\eta_{njl} = \sum_{l'=-\infty}^{\infty} \left(Q^3_{nlj'l'} \alpha_{j'jl'} + Q^4_{nlj'l'} \beta_{j'jl'} \right), \tag{11}$$

$$f_{njl} = \sum_{l'=-\infty}^{\infty} \left(P^3_{nlj'l'} \alpha_{j'jl'} + P^4_{nlj'l'} \beta_{j'jl'} \right),$$

together with an equation for the Fourier coefficients of the scattered field in material 1, that will not be needed in the following. Here

$$f_{njl}(q_0, p) = f_{nj}(q_0 + 2l\pi/a, p) = f_{nj}(q, p)$$

with $|q_0| < \pi/a$, etc. The coefficients η_{nj} are expansion coefficients for the incident field, i.e., for the half-space Green's tensor in material 2:

$$\eta_{nj}(q, p; \boldsymbol{x}') = D_n^{2+} U_{nj}^{2+} e^{-i(qx_1' + px_2' + h_n^{2+}x_3')} + \sum_{n'=1}^{3} D_{n'}^{2-} U_{n'j}^{2-} B_{n'n}^2 e^{-i(qx_1' + px_2' h_n^{2+}d_2 + h_{n'}^{2-}(x_3' + d_2))}. \tag{12}$$

Explicit expressions for the matrices P^i and Q^i are given in Appendix B for the case of a sinusoidal interface. From (11) it is now possible to solve for the coefficients f_{njl}, which means that the Green's tensor $G_{jj'}$ is determined in material 2. Introducing a matrix A such that

$$f_{njl} = \sum_{n'=1}^{3} \sum_{l'=-\infty}^{\infty} A_{nln'l'} \eta_{n'jl'}, \tag{13}$$

the explicit expression for the Green's tensor is

$$G_{jj'}(\boldsymbol{x}; \boldsymbol{x}') = G_{jj'}^2(\boldsymbol{x}; \boldsymbol{x}')$$

$$+ \sum_{l,l'=-\infty}^{\infty} \int_{-\pi/a}^{\pi/a} \int_{-\infty}^{\infty} \sum_{n=1}^{3} \Big[U_{njl}^{2-} e^{ih_{nl}^{2-} x_3} + \sum_{n'=1}^{3} B_{nn'l}^2 U_{n'jl}^{2+} e^{i[h_{n'l}^{2+}(x_3+d_2)-h_{nl}^{2-} d_2]} \Big] e^{i(q_l x_1 + p x_2)} \sum_{n''=1}^{3} A_{nln''l'}$$

$$\times \Big[D_{n''l'}^{2+} U_{n''j'l'}^{2+} e^{-ih_{n''l'}^{2+} x_3'} + \sum_{n'''=1}^{3} D_{n'''l'}^{2-} U_{n'''j'l'}^{2-} B_{n''n''l'}^2 e^{i(h_{n''l'}^{2+} d_2 - h_{n'''l'}^{2-}(x_3'+d_2))} \Big] \times e^{-i(q_{l'} x_1' + p x_2')} \, dq_0 \, dp, \quad (14)$$

where $q_l = q_0 + 2l\pi/a$.

3. The integral equation for the crack opening displacement

In order to derive an integral equation for the crack opening displacement it is convenient to first transform the Green's stress tensor derived in the previous section to the crack coordinate system $y_1 y_2 y_3$; see Figure 1. Denoting the coordinates of the center of the crack by $(a_c, 0, -d_c)$ and introducing a rotation matrix R, the coordinate transformation is

$$x_1 = R_{1j} y_j + a_c, \quad x_2 = R_{2j} y_j, \quad x_3 = R_{3j} y_j - d_c. \quad (15)$$

The transformed Green's tensor is

$$G_{jj'}^c(y_1, y_2, y_3; y_1', y_2', y_3')$$

$$= \int_{-\infty}^{\infty} \int_{-\infty}^{\infty} \sum_{n=1}^{3} D_n^{c\pm} U_{nj}^{c\pm} U_{nj'}^{c\pm} e^{i[q(y_1-y_1')+p(y_2-y_2')+h_n^{2+}(y_3-y_3')]} \, dq \, dp$$

$$+ \int_{-\infty}^{\infty} \int_{-\infty}^{\infty} \sum_{n=1}^{3} \sum_{n'=1}^{3} D_n^{2-} U_{nj'}^{2c-} B_{nn'}^2 U_{n'j}^{2c+} e^{i[\lambda_{kn'}^+ y_k - \lambda_{kn'}^- y_k' + (h_n^{2+} - h_n^{2-})(d_2-d_c)]} \, dq \, dp$$

$$+ \sum_{l,l'=-\infty}^{\infty} \int_{-\pi/a}^{\pi/a} \int_{-\infty}^{\infty} \sum_{n=1}^{3} \Big(U_{njl}^{2c-} e^{i(\lambda_{knl}^- y_k - h_{nl}^{2-} d_c)} + \sum_{n'=1}^{3} B_{nn'l}^{2c+} e^{i[\lambda_{kn'l}^+ y_k + h_{n'l}^{2+}(d_2-d_c) - h_{nl}^{2-} d_2]} \Big)$$

$$\times e^{iq_l a_c} \sum_{n''=1}^{3} A_{nln''l'} \Big(\sum_{n'''=1}^{3} D_{n''l'}^{2-} U_{n'''j'l'}^{2c-} B_{n''n''l'}^2 e^{-i[\lambda_{k'n''l'}^- y_{k'}' - h_{n''l'}^{2-} d_2 + h_{n'''l'}^{2-}(d_2-d_c)]}$$

$$+ D_{n''l'}^{2+} U_{n''j'l'}^{2c+} e^{-i(\lambda_{k'n''l'}^+ y_{k'}' - h_{n''l'}^{2+} d_c)} \Big) e^{-iq_{l'} a_c} \, dq_0 \, dp, \quad (16)$$

for $y_3 \gtrless y_3'$. Here

$$\lambda_{kn}^\pm = R_{1k} q + R_{2k} p + R_{3k} h_n^\pm, \quad (17)$$

$$U_{nj}^{2c\pm} = R_{jj'} U_{nj}^\pm. \quad (18)$$

Since the free space part of the Green's function has the same expression in both systems, $D_n^{c\pm}$ and $U_{nj}^{c\pm}$ are determined in the same way as the corresponding quantities in the $x_1 x_2 x_3$-system using the appropriate stiffnesses, see Appendix A.

The corresponding stress tensor $\Sigma^c_{kjj'}(\boldsymbol{x}; \boldsymbol{x}')$ is given by

$$\Sigma^c_{kjj'}(\boldsymbol{x}; \boldsymbol{x}') = c^{2c}_{kjk'j''} \frac{\partial}{\partial x_{j''}} G^c_{k'j'}(\boldsymbol{x}; \boldsymbol{x}'), \tag{19}$$

where $c^{2c}_{kjk'j''}$ are the stiffnesses of material 2 in the crack coordinate system.

Starting from the Green's tensor an integral representation for the crack opening displacement $\Delta u_j(\mathbf{x})$ can be derived:

$$\int_{S_c} \Delta u^c_j(\boldsymbol{x}) \Sigma^c_{kjj'}(\boldsymbol{x}; \boldsymbol{x}') n^c_k \mathrm{d}S_c = -u^{\mathrm{inc},2c}_{j'}(\boldsymbol{x}') + u^{2c}_{j'}(\boldsymbol{x}'). \tag{20}$$

Here superscript c denotes components in the crack system, and $u^{\mathrm{inc},2c}_{j'}(\boldsymbol{x}')$ is the displacement field that would have existed in material 2 if the crack had not been there. This field was determined in [Krasnova et al. 2005; Krasnova 2005] using a model for the ultrasonic transducer, where the stress below the transducer is prescribed; see next section.

Operating once more with the traction operator, this time with respect to the field point $\boldsymbol{x}'$ and taking the limit as y'_3 approaches zero yield an integral equation for the crack opening displacement:

$$\lim_{y'_3 \to 0^+} \int_{S_c} \Delta u_j(y_1, y_2) \tau_{jj'}(y_1, y_2, 0; y'_1, y'_2, y'_3) \, \mathrm{d}S_c = -\sigma^{\mathrm{inc},2c}_{3j'}(y'_1, y'_2, 0) \tag{21}$$

Here $\tau_{jj'}$ is the double Green's stress tensor, and $\sigma^{\mathrm{inc},2c}_{3j'}$ are stress components in the crack system due to the incident field. The explicit expression for $\tau_{jj'}$ is obtained by replacing $U^{c\pm}_{nj}$, $U^{2c\pm}_{nj}$, and $U^{2c\pm}_{njl}$ in (16) by $S^{\pm}_{nj}$, $S^{2c\pm}_{nj}$, and $S^{2c\pm}_{njl}$, respectively, where

$$S^{c\pm}_{nj} = \mathrm{i}(c^{2c}_{3j1j'}q + c^{2c}_{3j2j'}p + c^{2c}_{3j3j'}h^{2\pm}_n)U^{c\pm}_{nj'}, \tag{22}$$

$$S^{2c\pm}_{nj} = \mathrm{i}c^{2c}_{3jlj'}\lambda^{\pm}_{ln}U^{2c\pm}_{nj'}, \tag{23}$$

$$S^{2c\pm}_{njl} = \mathrm{i}c^{2c}_{3jkj'}\lambda^{\pm}_{knl}U^{2c\pm}_{nj'l}. \tag{24}$$

Equation (21) is hypersingular as a consequence of the twice differentiated Green's tensor. The limit in front cannot therefore be moved inside the integrand.

4. The incoming field

In the numerical examples only the case of an isotropic base material is studied. For this reason a transducer model developed in [Boström and Wirdelius 1995] is employed. In this model the stress at the interface between the transducer and the component is prescribed. It should be mentioned that there is no fundamental difficulty in treating an anisotropic base material, for instance by using the transducer model of [Niklasson 1998]. The explicit expression for the displacement field generated in an isotropic half-space is

$$u^t_j = \int_{-\infty}^{\infty} \int_{-\infty}^{\infty} \sum_{n=1}^{3} \xi_n(q, p) U^{1-}_{nj} \mathrm{e}^{\mathrm{i}[q(x_1-x_t)+p(x_2-y_t)+h^{1-}_n(x_3-d_1)]} \, \mathrm{d}q \, \mathrm{d}p. \tag{25}$$

Here (x_t, y_t, d_1) are the coordinates of the transmitter, and the coefficients ξ_n are given in [Boström and Wirdelius 1995] for various types of transmitters. The displacement field in a cladding without a crack is

$$u_j^{\text{inc}} = \sum_{l=-\infty}^{\infty} \sum_{n=1}^{3} \int_{-\pi/a}^{\pi/a} \int_{-\infty}^{\infty} g_{nl} \left(U_{njl}^{2-} e^{ih_{nl}^{2-}x_3} + \sum_{n'=1}^{3} B_{nn'l}^2 U_{n'jl}^{2+} e^{i[h_{n'l}^{2+}(x_3+d_3) - h_{nl}^{2-}d_2]} \right) e^{i(q_l x_1 + p x_2)} \, dq_0 \, dp, \quad (26)$$

according to [Krasnova et al. 2005; Krasnova 2005]. Here the coefficients g_{nl} are solutions to

$$
\begin{cases}
\displaystyle\sum_{l'=-\infty}^{\infty} \left(Q_{nljl'}^1 \alpha_{jl'} + Q_{nljl'}^2 \beta_{jl'} \right) = \xi_{nl} e^{-i(q_l x_t + p y_t + h_{nl}^{1-} d_1)}, \\
\displaystyle\sum_{l'=-\infty}^{\infty} \left(Q_{nljl'}^3 \alpha_{jl'} + Q_{nljl'}^4 \beta_{jl'} \right) = 0, \\
\displaystyle\sum_{l'=-\infty}^{\infty} \left(P_{nljl'}^3 \alpha_{jl'} + P_{nljl'}^4 \beta_{jl'} \right) = g_{nl}.
\end{cases}
\quad (27)
$$

Transforming to the crack coordinate system, and operating with the traction operator, the right hand side of (21) is obtained.

5. Solution to the integral equation

To discretize the integral equation, the crack opening displacement is expanded in Chebyshev functions ϕ_m according to

$$\Delta u_j(y_1, y_2) = \sum_{m,m'=1}^{\infty} \gamma_{jmm'} \phi_m(y_1/c) \phi_{m'}(y_2/d), \quad (28)$$

where c, d are half the sides of the crack, and the expansion functions are defined as

$$\phi_m(s) = \begin{cases} \dfrac{1}{\pi} \cos(m \arcsin s) & \text{for } m = 1, 3, \ldots, \\ \dfrac{i}{\pi} \sin(m \arcsin s) & \text{for } m = 2, 4, \ldots. \end{cases} \quad (29)$$

It is convenient to choose the Chebyshev functions, since they form a complete set that exhibits, like the displacement field, a square root behavior at the crack tips. Furthermore, the functions have the pleasant property that

$$\int_{-c}^{c} \phi_m(y_1/c) e^{iq y_1} \, dy_1 = (-1)^{m+1} m \frac{J_m(qc)}{q}. \quad (30)$$

Inserting the expression for Δu_j into (21) and projecting the result onto the Chebyshev functions yield a linear system of equations for the unknowns $\gamma_{jmm'}$:

$$\sum_{j'=1}^{3} \sum_{m''=1}^{\infty} \sum_{m'''=1}^{\infty} Z_{jmm'j'm''m'''} \gamma_{j'm''m'''} = M_{jmm'} \quad (31)$$

The explicit expressions for the matrices Z and M are given in Appendix C. It is now straightforward to solve for the coefficients $\gamma_{jmm'}$. Hence, the crack opening displacement is determined.

6. The signal response

Next, the reciprocity result of [Auld 1979] is used to relate the crack opening displacement (COD) to the output voltage from the receiving probe:

$$\delta\Gamma_1 = -\frac{i\omega}{4P} \int_{-c}^{c} \int_{-d}^{d} \Delta u_j(y_1, y_2) \sigma_{3j}^{re}(y_1, y_2) \, dy_1 \, dy_2, \tag{32}$$

where P is the incident electric power to the probe, Δu_j is the COD due to the incoming field, and σ_{2j}^{re} is the traction with the receiving probe acting as a transmitter in the absence of the crack. The quantity $\delta\Gamma_1$ denotes the extra electric reflection coefficient from the receiving probe due to the presence of the crack; this is essentially the quantity measured in practice.

Inserting the expansion (28) of the COD into (32) yields

$$\delta\Gamma_1 = \frac{i\omega}{4P} \sum_{j=1}^{3} \sum_{m=1}^{\infty} \sum_{m'=1}^{\infty} \gamma_{jmm'} M_{jmm'}^{re}, \tag{33}$$

where $M_{jmm'}^{re}$ is determined from the traction on the position of the crack with the receiver acting as a transmitter in the absence of a crack. For a transducer acting in pulse-echo mode it is, of course, not necessary to distinguish between the transmitter and the receiver.

Though the change in signal response due to the crack is the key quantity in a practical case, it may be of some interest to consider the effect of the interface separately. Using Auld's approach an expression for the difference in signal response between the structure without a crack and a half-space can be derived:

$$\delta\Gamma_2 = \frac{i\omega}{4P} (2\pi)^2 \sum_{l,l'=-\infty}^{\infty} \sum_{n=1}^{3} \int_{-\pi/a}^{\pi/a} \int_{-\infty}^{\infty} \xi_{nl}^{re} e^{-i[q_l(x_r+a_c)+py_r+h_{nl}^{1-}d_1]}$$

$$\times \left[\left(\frac{2\pi(l-l')}{ah_{nl}^{1-}} J_{l'-l}(h_{nl}^{1-}b) S_{n1jl}^{1-} + J_{l'-l}(h_{nl}^{1-}b) S_{n3jl}^{1-} \right) \alpha_j \left(-q_0 - l'\frac{2\pi}{a}, -p \right) \right.$$

$$\left. - U_{njl}^{1-} J_{l'-l}(h_{nl}^{1-}b) \beta_j \left(-q_0 - l'\frac{2\pi}{a}, -p \right) \right] dq_0 \, dp. \tag{34}$$

Here ξ_{nl}^{re} are the coefficients of (25) with the receiver acting as a transmitter, (x_r, y_r, d_1) are the coordinates of the receiver, and α_j, β_j are determined from (27).

7. Numerical results

There are numerous parameters that can be varied in this problem. Here some numerical results that illustrate the effect of the interface and the crack will be given. The base material 1 has a thickness $d_1 = 30$ mm and is regarded as an isotropic steel with density $\rho^1 = 8.40$ g/cm^3, and with longitudinal and transverse wave velocities 5.90 mm/μs and 3.20 mm/μs, respectively. The cladding has a thickness $d_2 = 5$ mm and is assumed to be a transversely isotropic steel with density $\rho^2 = 8.50$ g/cm^3 and stiffness constants (in GPa) $C_{11}^2 = 216$, $C_{22}^2 = C_{33}^2 = 250$, $C_{12}^2 = C_{13}^2 = 115$, and $C_{44}^2 = 100$, all in abbreviated notation. Only the case where the crystal axes coincide with the $x_1x_2x_3$-axes have been considered in the numerical examples. Damping in the materials is modeled by adding a small imaginary part, 2% of the real part, to all stiffnesses. It should be noted, however, that Auld's reciprocity relation is strictly

valid only for lossless media, which means that the present numerical results are approximate in that sense. The interface between the base material and the cladding is taken as sinusoidal according to (3) with $a = 5$ mm. Reflection from the scan surface $x_3 = d_1$ has been neglected in all numerical examples. The transmitter is of SV type working in pulse echo mode with an angle of 45°, and the size is 10 by 10 mm. Only the case of a fixed frequency, 1 or 2 MHz, has been studied. All results are calibrated with a side-drilled hole of diameter 3 mm and depth 33 mm.

When calculating the matrices Z and M from (52) and (53), it is necessary to truncate the infinite integrals. For the first two terms in matrix Z this has already been accomplished in [Boström et al. 2003], and the reader is referred to that paper for details. For the infinite integrals in the third term of Z and in M it was found that it is sufficient to evaluate the integrals from $-N$ to N, where $N = c_{s,cl}/2c_{s,b}$. Here $c_{s,cl} = \sqrt{C_{44}^2/\rho^2}$ is a typical shear wave velocity in the cladding, and $c_{s,b}$ is the shear wave velocity in the base material. Increasing N further above this value will not change the final result significantly. The sums over subscripts l and l' in the third term of matrix Z also need to be truncated. By experimenting numerically it has been found that the maximum value of l may be taken as $l_{\max} = \max(k_{s,cl}a - 3, 4)$, where $k_{s,cl} = 2\pi f/c_{s,cl}$ is the shear wave number in the cladding. In the same way it is necessary to truncate the summation over subscripts m and m' in (32). Using $m_{\max} = 2k_{s,cl}/3 + 4$ it is seen that the convergence will be sufficient. With the truncations chosen the accuracy is well below 0.1 dB, which corresponds to about 1 per cent in the amplitude of the signal measured. For comparison a difference of about 1-2 dB between simulations and experiments is normally considered as satisfactory in ultrasonic testing. To the author's knowledge there are neither results obtained by alternative methods nor experimental data to compare with for this particular problem.

Figure 2 shows the signal response for a few different sizes of the crack as a function of the position of a 2 MHz transmitter. The crack is "vertical", i.e., $y_1 = -x_3 + d_c$, $y_2 = x_2$, and $y_3 = x_1 - a_c$, and it is located below a valley of the interface ($a_c = 3.75$ mm). The amplitude of the interface is $b = 1$ mm.
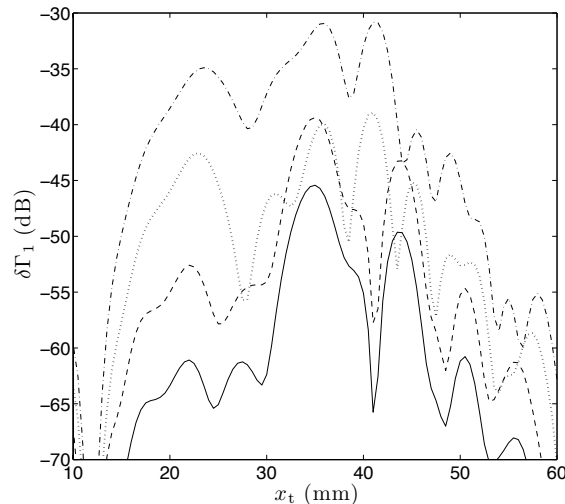

Figure 2. Signal response ($\delta\Gamma_1$) as a function of the position (x_t) of a 2 MHz transmitter for different sizes of the crack, 2×2 mm (solid), 2×4 mm (dashed), 3×3 mm (dotted), and 3×6 mm (dash-dotted).
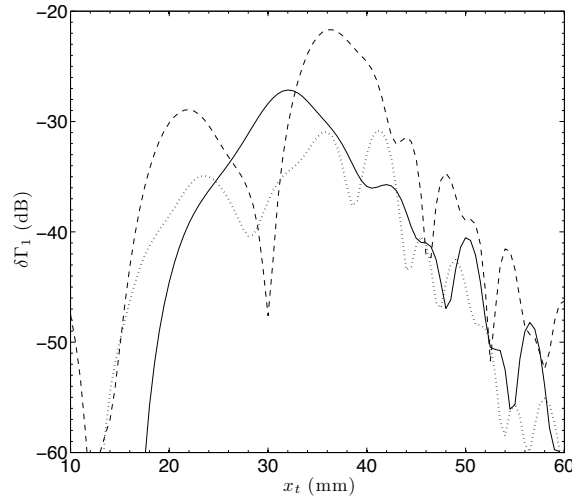
Figure 3. Signal response ($\delta\Gamma_1$) as a function of the position (x_t) of a 2 MHz transmitter for various values of the amplitude of the interface, $b = 0$ (solid), $b = 0.5$ mm (dashed), $b = 1$ mm (dotted).

Figure 3 shows the influence of the amplitude of the interface (b) for the 3×6 mm crack of Figure 2. The same 2 MHz transducer is used. Obviously the amplitude is very important for the signal response. Changing the b from 0.5 to 1 mm gives a decrease of about 9 dB for the maximum value. However, there does not seem to be any simple systematic relation between the amplitude b and the maximum signal response.

Figure 4 shows the effect of translating the crack with respect to the interface for the same transducer as in the previous examples. The positions chosen correspond to a crack centered directly below a top
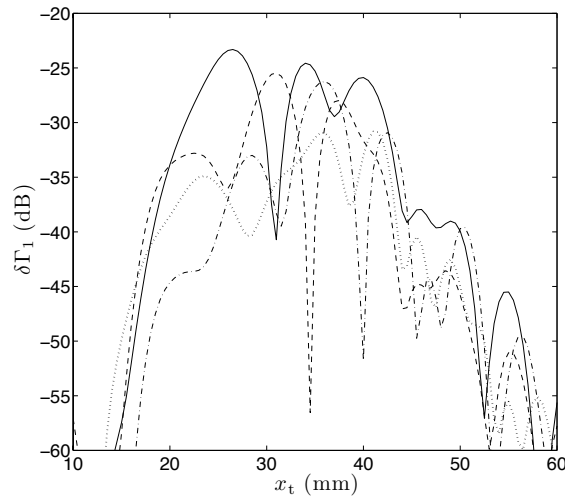

Figure 4. Signal response ($\delta\Gamma_1$) as a function of the position (x_t) of a 2 MHz transmitter for various values of the position of the crack relative to the corrugated interface, $a_c = 1.25$ mm (solid), $a_c = 2.5$ mm (dashed), $a_c = 3.75$ mm (dotted), $a_c = 0$ (dash-dotted).
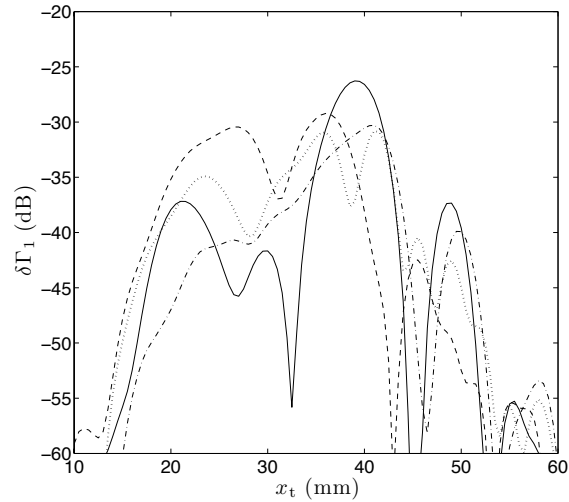
Figure 5. Signal response ($\delta\Gamma_1$) as a function of the position (x_t) of a 2 MHz transmitter for various values of the orientation of the crack, $\varphi = 0$ (horizontal crack, solid), $\varphi = 45°$ (dashed), $\varphi = 90°$ (vertical crack, dotted), $\varphi = 135°$ (dash-dotted).

or a valley of the interface, or in the middle of these two. There does not seem to be any systematic dependence on the position, but it is worth pointing out that there is a difference of about 8 dB between the maximum responses for a crack below a top ($a_c = 1.25$ mm) and a crack directly below a valley ($a_c = 3.75$ mm).

In Figure 5 the response from cracks with varying orientation is examined, still with a 2 MHz transducer. All cracks have a normal (y_3-axis) in the $x_1 x_3$-plane and are rotated an angle φ about the x_2-axis
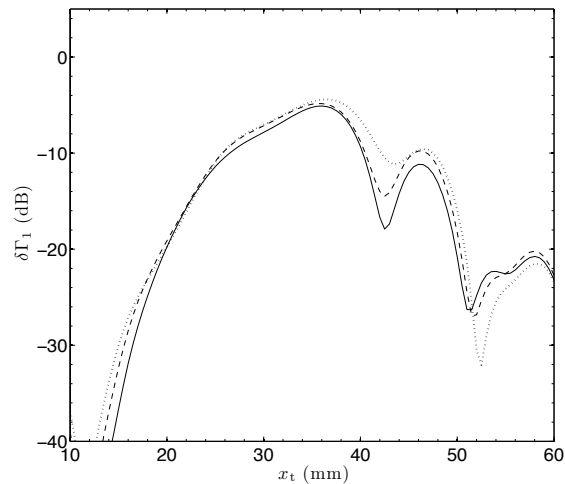

Figure 6. Signal response ($\delta\Gamma_1$) as a function of the position (x_t) of a 1 MHz transmitter for various values of the amplitude of the interface, $b = 0$ (solid), $b = 0.5$ mm (dashed), $b = 1$ mm (dotted).

with $\varphi = 0$ corresponding to the "horizontal" position, where the $y_1 y_2 y_3$-system is not rotated. The strongest echo is obtained from the horizontal crack, about 5 dB stronger than for the vertical crack.

Finally, in Figure 6 some results for a 1 MHz transducer are shown. Apart from the frequency, all parameters have the same values as in Figure 3. The obvious result is that at low frequencies the wavy interface only has a minor influence on the signal response. Similar results are obtained when the crack is translated sideways as in Figure 4. Tilting the crack, however, give results more in accordance with the 2 MHz case.

8. Concluding remarks

In this paper the effect of a two-dimensional periodic interface on three-dimensional wave scattering by a rectangular crack in a cladding has been investigated. A mathematical model has been developed, where the elastic wave propagation problem is solved exactly. It is seen that the properties of the wavy interface are of major importance for the signal response at higher frequencies. From systematic studies with varying values of the governing parameters it should possible to acquire a deeper understanding of the influence of the properties of the interface, the size, location, and orientation of the crack, the material parameters, etc. It is believed that the model will provide a useful tool for planning and qualification of ultrasonic testing procedures. For instance, it should be possible to judge whether a defect of a certain size, location, and orientation would be possible to detect using a certain method of inspection (transmitter type, frequency, search pattern).

Acknowledgments

Appendix A: The half-space Green's tensors

The half space Green's tensor expressed as a double Fourier transform has been derived in [Boström et al. 2003]. To do this plane wave solutions are determined by defining a vector $\boldsymbol{v}^i$ ($i = 1, 2$) as

$$\boldsymbol{v}^i = \left(\, u_1^i \ \ u_2^i \ \ u_3^i \ \ \sigma_{13}^i \ \ \sigma_{23}^i \ \ \sigma_{33}^i \, \right)^{\mathrm{T}}, \tag{35}$$

where all elements are assumed to have an $\exp(i(qx_1 + px_2 + h^i x_3))$ dependence, which is suppressed in the following. Substituting into (1) and (2) leads to a generalized eigenvalue problem

$$A^i \boldsymbol{v}^i = h^i C^i \boldsymbol{v}^i. \tag{36}$$

The explicit expressions for the matrices A^i and C^i are not given here. The reader is referred to [Boström et al. 2003] for details. Solving the eigenvalue problem gives six eigenvalues $h_n^{i\pm}$, $n = 1, 2, 3$, where the superscript indicates propagation in the positive or negative x_3-direction. The corresponding eigenvectors are denoted by

$$\boldsymbol{v}_n^{i\pm} = \left(\, U_{n1}^{i\pm} \ \ U_{n2}^{i\pm} \ \ U_{n3}^{i\pm} \ \ T_{n1}^{i\pm} \ \ T_{n2}^{i\pm} \ \ T_{n3}^{i\pm} \, \right)^{\mathrm{T}}. \tag{37}$$

The half-space Green's tensor can then be expressed as a double Fourier transform by adding the free space Green's tensor and a reflected part that is constructed so that the stress-free boundary condition on

the free surface is satisfied. For the base material ($i = 1$) the result is

$$G_{jj'}^1(\boldsymbol{x}; \boldsymbol{x}') = \int_{-\infty}^{\infty} \int_{-\infty}^{\infty} \sum_{n=1}^{3} D_n^{1\pm} U_{nj'}^{1\pm} U_{nj}^{1\pm}\, \mathrm{e}^{\mathrm{i}(q(x_1-x_1')+p(x_2-x_2')+h_n^{1\pm}(x_3-x_3'))}\, \mathrm{d}q\, \mathrm{d}p$$

$$+ \int_{-\infty}^{\infty} \int_{-\infty}^{\infty} \sum_{n,n'=1}^{3} D_n^{1+} U_{nj'}^{i+} B_{nn'}^1 U_{n'j}^{1-}\, \mathrm{e}^{\mathrm{i}(q(x_1-x_1')+p(x_2-x_2')+h_{n'}^{1-}(x_3-d_1)-h_n^{1+}(x_3'-d_1))}\, \mathrm{d}q\, \mathrm{d}p, \quad (38)$$

for $x_3 \gtrless x_3'$. The quantities $D_n^{i\pm}$ are determined by the jump condition for the free space Green's tensor at $x_3 = x_3'$. This leads to

$$\sum_{n=1}^{3} (D_n^{i+} U_{nj}^{i+} U_{nj'}^{i+} - D_n^{i-} U_{nj}^{i-} U_{nj'}^{i-}) = 0, \tag{39}$$

$$\sum_{n=1}^{3} (D_n^{i+} T_{nj}^{i+} U_{nj'}^{i+} - D_n^{i-} T_{nj}^{i-} U_{nj'}^{i-}) = -\delta_{jj'}/(2\pi)^2. \tag{40}$$

Obviously, there are 18 equations and 6 unknowns for each material. However, the equations are not linearly independent, since the symmetry properties of the Green's tensor have already been exploited. The reflection matrix B^i is determined from the condition that the traction vanishes on the free surface, which means that

$$T_{nj}^{1+} + \sum_{n'=1}^{3} B_{nn'}^1 T_{n'j}^{1-} = 0, \tag{41}$$

$$T_{nj}^{2-} + \sum_{n'=1}^{3} B_{nn'}^2 T_{n'j}^{2+} = 0, \tag{42}$$

for $n, j = 1, 2, 3$.

Appendix B: The matrices $\boldsymbol{Q}^i$ and $\boldsymbol{P}^i$

If reflection at the scan surface S_1 is neglected, and the interface is taken as sinusoidal,

$$s(x_1) = b \sin \frac{2\pi x_1}{a}, \tag{43}$$

then the explicit expressions for the matrices $Q^1, \ldots, Q^4, P^3, P^4$ are

$$Q_{nljl'}^1 = A_{nljl'}^{1-} \mathrm{e}^{\mathrm{i}h_{nl}^{1-} d_1}, \tag{44}$$

$$Q_{nljl'}^2 = C_{nljl'}^{1-} \mathrm{e}^{\mathrm{i}h_{nl}^{1-} d_1}, \tag{45}$$

$$Q_{nljl'}^3 = A_{nljl'}^{2+} + \sum_{n'=1}^{3} A_{n'ljl'}^{2-} B_{n'nl}^2 \mathrm{e}^{\mathrm{i}d_2(h_{nl}^{2+} - h_{n'l}^{2-})}, \tag{46}$$

$$Q_{nljl'}^4 = C_{nljl'}^{2+} + \sum_{n'=1}^{3} C_{n'ljl'}^{2-} B_{n'nl}^2 \mathrm{e}^{\mathrm{i}d_2(h_{nl}^{2+} - h_{n'l}^{2-})}, \tag{47}$$

$$P_{nljl'}^3 = A_{nljl'}^{2-}, \tag{48}$$

$$P_{nljl'}^4 = C_{nljl'}^{2-}, \tag{49}$$

where

$$A_{nkljl'}^{i\pm} = 2\pi \left(\frac{2\pi(l-l')}{h_{nl}^{i\pm}} S_{n1jl}^{i\pm} + a S_{n3jl}^{i\pm} \right) \mathrm{J}_{l'-l}(bh_{nl}^{i\pm}) D_{nl}^{i\pm}, \tag{50}$$

$$C_{nljl'}^{i\pm} = 2\pi a U_{njl}^{i\pm} \mathrm{J}_{l'-l}(bh_{nl}^{i\pm}) D_{nl}^{i\pm}. \tag{51}$$

Appendix C: The matrices Z and M

The explicit expressions for the matrices Z and M from (31) are

$$Z_{jmm'j'm''m'''}$$

$$= (-1)^{m''+m'''} mm'm''m''' \int_{-\infty}^{\infty} \int_{-\infty}^{\infty} \sum_{n=1}^{3} D_n^{c-} S_{nj}^{c-} S_{nj'}^{c-} \frac{\mathrm{J}_m(qc)\mathrm{J}_{m'}(pd)\mathrm{J}_{m''}(qc)\mathrm{J}_{m'''}(pd)}{q^2 p^2}\, dq\, dp$$

$$+ (-1)^{m''+m'''} mm'm''m''' \int_{-\infty}^{\infty} \int_{-\infty}^{\infty} \sum_{n,n'=1}^{3} D_n^{2-} S_{nj}^{2c-} B_{nn'}^2 S_{n'j'}^{2c+}$$

$$\times \frac{\mathrm{J}_m(\lambda_{1n}^- c)\mathrm{J}_{m'}(\lambda_{2n}^- d)\mathrm{J}_{m''}(\lambda_{1n'}^+ c)\mathrm{J}_{m'''}(\lambda_{2n'}^+ d)}{\lambda_{1n}^- \lambda_{2n}^- \lambda_{1n'}^+ \lambda_{2n'}^+} e^{i(h_{n'}^{2+}-h_n^{2-})(d_2-d_c)}\, dq\, dp$$

$$+ (-1)^{m''+m'''} mm'm''m''' \sum_{l,l'=-\infty}^{\infty} \int_{-\pi/a}^{\pi/a} \int_{-\infty}^{\infty} \sum_{n,n'=1}^{3} A_{nln'l'} \tag{52}$$

$$\times \left(S_{nj'l}^{2c-} \frac{\mathrm{J}_{m''}(\lambda_{1nl}^- c)\mathrm{J}_{m'''}(\lambda_{2nl}^- d)}{\lambda_{1nl}^- \lambda_{2nl}^-} e^{-ih_{nl}^{2-} d_c} + \sum_{n''=1}^{3} B_{nn''l}^2 S_{n''j'l}^{2c+} \frac{\mathrm{J}_{m''}(\lambda_{1n''l}^+ c)\mathrm{J}_{m'''}(\lambda_{2n''l}^+ d)}{\lambda_{1n''l}^+ \lambda_{2n''l}^+} e^{i[h_{n''l}^{2+}(d_2-d_c)-h_{nl}^{2-} d_2]} \right)$$

$$\times \left(D_{n'l'}^{2+} S_{n'jl'}^{2c+} \frac{\mathrm{J}_m(\lambda_{1n'l'}^+ c)\mathrm{J}_{m'}(\lambda_{2n'l'}^+ d)}{\lambda_{1n'l'}^+ \lambda_{2n'l'}^+} e^{ih_{n'l'}^{2+} d_c} \right.$$

$$\left. + \sum_{n'''=1}^{3} D_{n'''l'}^{2-} B_{n''n'l'}^2 S_{n'''j'l'}^{2c-} \frac{\mathrm{J}_m(\lambda_{1n'''l'}^- c)\mathrm{J}_{m'}(\lambda_{2n'''l'}^- d)}{\lambda_{1n'''l'}^- \lambda_{2n'''l'}^+} e^{i[-h_{n'''l'}^{2-}(d_2-d_c)+h_{n'l'}^{2+} d_2]} \right) e^{2\pi i(l-l')a_c/a}\, dq_0\, dp.$$

It should be noted that the first two terms in the matrix Z correspond to scattering from a rectangular crack in a homogeneous anisotropic medium, which is the problem solved in [Boström et al. 2003]. Thus, it is only the third term, describing the influence of the cladding, which needs to be calculated.

$$M_{jmm'} = (-1)^{(m+m')} mm' \sum_{n,n'=1}^{3} \sum_{l,l'=-\infty}^{\infty} \int_{-\pi/a}^{\pi/a} \int_{-\infty}^{\infty} g_{nl} e^{iq_l a_c}$$

$$\times \left(S_{njl}^{2c-} \frac{\mathrm{J}_m(\lambda_{1nl}^- c)\mathrm{J}_{m'}(\lambda_{2nl}^- d)}{\lambda_{1nl}^- \lambda_{2nl}^-} e^{-ih_{nl}^{2-} d_c} + \sum_{n'=1}^{3} B_{nn'l}^2 S_{n'jl}^{2c+} \frac{\mathrm{J}_m(\lambda_{1n'l}^+ c)\mathrm{J}_{m'}(\lambda_{2n'l}^+ d)}{\lambda_{1n'l}^+ \lambda_{2n'l}^+} e^{i[h_{n'l}^{2+}(d_2-d_c)-h_{nl}^{2-} d_2]} \right) dq_0\, dp. \tag{53}$$

References

[Auld 1979] B. A. Auld, "General electromechanical reciprocity relations applied to the calculation of elastic wave scattering coefficients", *Wave Motion* **1**:1 (1979), 3–10.

[Boström and Wirdelius 1995] A. Boström and H. Wirdelius, "Ultrasonic probe modeling and nondestructive crack detection", *J. Acoust. Soc. Am.* **97**:5 (1995), 2836–2848.

[Boström et al. 2003] A. Boström, T. Grahn, and A. J. Niklasson, "Scattering of elastic waves by a rectangular crack in an anisotropic half-space", *Wave Motion* **38**:2 (2003), 91–107.

[Fokkema 1980] J. T. Fokkema, "Reflection and transmission of elastic waves by the spatially periodic interface between two solids (theory of the integral-equation method)", *Wave Motion* **2**:4 (1980), 375–393.

[Fokkema and van den Berg 1977] J. T. Fokkema and P. M. van den Berg, "Elastodynamic diffraction by a periodic rough surface (stress-free boundary)", *J. Acoust. Soc. Am.* **62**:5 (1977), 1095–1101.

[Hudgell 1994] R. J. Hudgell, *Handbook on the ultrasonic examination of austenitic clad steel components*, EUR **15786**, Office for Official Publications of the European Communities, Luxembourg, 1994.

[Jansson 2010] P.-Å. Jansson, "Scattering from a rectangular crack in a cladding", pp. 383–388 in *IUTAM Symposium on Recent Advances of Acoustic Waves in Solids* (Taipei, 2009), edited by T.-T. Wu and C.-C. Ma, IUTAM Bookseries **26**, Springer, New York, 2010.

[Jansson and Zagbai 2007] P.-Å. Jansson and T. Zagbai, "2D P-SV wave scattering by a crack in a cladding", pp. 71–78 in *Review of progress in quantitative nondestructive evaluation* (Portland, OR, 2006), edited by D. O. Thompson and D. E. Chimenti, AIP Conference Proceedings **894**, American Institute of Physics, Melville, NY, 2007.

[Krasnova 2005] T. Krasnova, *Elastic wave scattering from corrugated surfaces in anisotropic media*, Ph.D. thesis, Chalmers University of Technology, Gothenburg, 2005.

[Krasnova and Jansson 2006] T. Krasnova and P.-Å. Jansson, "Wave scattering from a slightly wavy interface between two anisotropic media", *J. Nondestruct. Eval.* **25**:4 (2006), 155–164.

[Krasnova et al. 2005] T. Krasnova, P.-Å. Jansson, and A. Boström, "Ultrasonic wave propagation in an anisotropic cladding with a wavy interface", *Wave Motion* **41**:2 (2005), 163–177.

[Lakhtakia et al. 1984] A. Lakhtakia, V. K. Varadan, V. V. Varadan, and D. J. N. Wall, "The *T*-matrix approach for scattering by a traction-free periodic rough surface", *J. Acoust. Soc. Am.* **76**:6 (1984), 1839–1846.

[Langenberg et al. 2000] K. J. Langenberg, R. Hannemann, T. Kaczorowski, R. Marklein, B. Koehler, C. Schurig, and F. Walte, "Application of modeling techniques for ultrasonic austenitic weld inspection", *NDT & E Int.* **33**:7 (2000), 465–480.

[Liu and Achenbach 1995] G. R. Liu and J. D. Achenbach, "Strip element method to analyze wave scattering by cracks in anisotropic laminated plates", *J. Appl. Mech.* (*ASME*) **62**:3 (1995), 607–613.

[Niklasson 1998] A. J. Niklasson, "Ultrasonic three-dimensional probe modeling in anisotropic solids", *J. Acoust. Soc. Am.* **103**:5 (1998), 2432–2442.

[Richtmyer 1981] R. D. Richtmyer, *Principles of advanced mathematical physics*, vol. 1, Springer, New York, 1981.

[Wang et al. 1996] C.-Y. Wang, J. D. Achenbach, and S. Hirose, "Two-dimensional time domain BEM for scattering of elastic waves in solids of general anisotropy", *Int. J. Solids Struct.* **33**:26 (1996), 3843–3864.

[Zagbai and Boström 2006] T. Zagbai and A. Boström, "2D SH wave scattering by a crack in a cladding", pp. 81–88 in *Review of progress in quantitative nondestructive evaluation* (Brunswick, ME, 2005), edited by D. O. Thompson and D. E. Chimenti, AIP Conference Proceedings **820**, American Institute of Physics, Melville, NY, 2006.

PER-ÅKE JANSSON: per-ake.jansson@chalmers.se
Department of Applied Mechanics, Chalmers University of Technology, SE-412 96 Gothenburg, Sweden

■msp

EFFECT OF ADDING CRUMB TIRE RUBBER PARTICLES ON THE MECHANICAL PROPERTIES OF DCPD-MODIFIED SULFUR POLYMER MORTARS

HAMED MARAGHECHI, IMAN FOTOVAT AHMADI AND SIAMAK MOTAHARI

Sulfur polymer mortars are composite materials in which modified sulfur is the binder while sand and other fillers are used as aggregates. Sulfur-based composite materials are characterized by their high chemical and mechanical properties along with fast setting behavior. However, sulfur modification is essential in order to achieve sulfur mortars with enhanced characteristics. In this study, incorporation of crumb tire rubber in dicyclopentadiene-modified sulfur-based mortars, as some replacement of sand, is evaluated. Use of crumb tire rubber influences the compressive stress-strain behavior of the mortars significantly. While the compressive strength of the rubber-added mortars is reduced dramatically, the postpeak response of the mortars is of the great interest. Use of a reactive-mixing method improves the compressive strength of rubber-added sulfur polymer mortars up to approximately 25%. Scanning electron microscopy observations confirm better adhesion between the rubber particles and sulfur polymer matrix via reactive mixing. Furthermore, it is clarified that the crumb tire rubber type and presence of a curing agent during the mortar preparation process affect the mechanical properties of the sulfur mortar.

1. Introduction

Large amounts of sulfur are produced annually in some countries, from the mining of sulfur deposits and as a byproduct of oil and gas refining in the petroleum industry. Nowadays sulfur is known as a prominent candidate for certain applications in construction industries. As an alternative to cement concrete, sulfur concretes have found their way among other construction materials. Sulfur concrete is obtained by mixing modified sulfur melt as the binder and preheated stone, sand, and filler as aggregates. Solidification of the fresh mix occurs rapidly and the concrete gains its strength shortly. High mechanical strength, fast setting, low permeability, and high chemical resistance against strong acids and saline environments are some of the remarkable characteristics of sulfur concrete [Abdel-Jawad and Al-Qudah 1994]. In many specialized construction and transportation applications in which conventional materials like Portland cement are unable to endure the operational conditions, sulfur concretes would be an appropriate substituent option. These conditions could include pipes or tiles for handling acidic sewer waters, airfield runways and aircraft parking, flooring material for industrial plants, and tanks for holding corrosive substances [Yue et al. 2006; Mohamed and El Gamal 2007; 2009].

Sulfur concrete with unmodified sulfur binder lacks durability and stability. During solidification from melt, pure or unmodified sulfur crystallizes to the monoclinic allotrope (S_β), which is stable between the melting point of sulfur and 95°C. On further cooling to ambient temperature, the monoclinic allotrope reverts to the denser orthorhombic allotrope (S_α), which has a different crystalline structure. This transition takes approximately a day to complete. As a result of the distinct densities and structures

of these two allotropes, large shrinkage and residual internal stresses are induced within the bulk of the sulfur. In addition, when using unmodified sulfur as the binder in composite materials or concretes, microcrystals of orthorhombic sulfur start to grow and change into macrocrystals of orthorhombic sulfur. This makes the composite brittle and impractical for most applications, due to loss of durability. Chemical modification of sulfur overcomes these problems, particularly concerning the changes in crystallinity. Frequently, polysulfides, or some commercial materials such as SRX™ (Starcrete™ Technologies Inc.), are used in order to modify and control the crystallization of sulfur [Blight et al. 1978; Bordoloi and Pearce 1978]. Other chemicals, such as dicyclopentadiene (DCPD), its oligomers, and bitumen have also been employed [McBee and Sullivan 1982; Mohamed et al. 2006]. The reaction products of these components are mostly mixtures of various polysulfides and unreacted sulfur. The reactions of sulfur with dicyclopentadiene have been investigated by several researchers [Blight et al. 1978; Bordoloi and Pearce 1978; Mohamed and El Gamal 2007]. While sulfur-modified concrete is a promising alternative material in specialized applications, its high initial fabrication costs and relatively low melting temperature comparing to Portland cement restrict its utilization in large-scale ordinary constructions.

The increasing volume of used tires in landfills has caused serious environmental problems. Since waste rubber is not easily biodegradable even after a long period of landfill treatment, material and energy recovery are alternatives to disposal. Thus, many studies have been carried out in recent decades looking for applications of waste rubber in construction materials, especially in Portland cement concretes. Researchers have endeavored to enhance some mechanical properties of concrete, such as toughness and energy absorption, by incorporating scrap tire rubber of various shapes and sizes: crumb, milled tire rubber, slit, and shredded or chipped tires [Topçu and Avcular 1997; Khatib and Bayomy 1999; Segre and Joekes 2000; Bennazzouk et al. 2003; Albano et al. 2005; Bignozzi and Sandrolini 2006]. Tantala et al. [1996] examined the energy absorption capacity of rubberized Portland cement concrete (rubcrete) mixtures made by replacing 5% to 10% of coarse aggregate by volume with scrap rubber, and reported that the toughness of rubcretes is higher than that of the control concrete mixture. Low-density concrete mixtures, made using crumb rubber to replace up to 30% by weight of coarse and fine aggregate, have shown improved crack and chemical resistance [Sukontasukkul and Chaikaew 2006]. According to [Siddique and Naik 2004], on the use of scrap tire rubber in concrete, the compressive strengths of rubber modified concretes are less than those of unmodified concretes; however, toughness and impact strength improve. Moreover, it was observed that the use of coarse scrap tire rubber affects the properties more negatively than the use of fine particles [Eldin and Senouci 1993]. Analyzing the fracture mechanisms in rubber modified concretes indicated that the bonds between cement and rubber particles were weak. Bond strength augmentation between rubber and cement is the key parameter in overcoming the defects of rubber modified concrete [Topçu and Avcular 1997].

This paper presents the results of a study on the use of crumb tire rubber as a feasible toughness enhancer in sulfur polymer mortars. The effect of rubber content on stress-strain behavior, compressive strength, density, and elastic modulus is investigated and compared with Portland cement mortars. Furthermore, reactive mixing and ordinary mixing procedures and their influence on the compressive strength of the prepared samples are evaluated. As a result, the effect of the presence of crumb rubber particles during the copolymerization of sulfur with dicyclopentadiene (DCPD) is determined. Finally, the influence of rubber type — tread or sidewall tire rubber — and the availability of traditional rubber-curing agents during mortar mixing on the mechanical properties of the sulfur polymer mortar is studied.

2. Experimental

Materials. Elemental sulfur (99.9% purity) was obtained from the Tehran Refinery Complex, Iran. Dicyclopentadiene (DCPD) was supplied by Merck with 99.9% purity. Stearic acid, zinc oxide, and accelerator CZ (N-cyclohexyl benzothiazole-2-sulfenamide) were supplied by Issatiss (Yazd Tire Co.) and used as curing agents. Crumb tire rubber selected from tread and sidewall sections of car tires was supplied by Issatiss (Yazd Tire Co.), with maximum particle size of approximately 0.4 mm and densities of 1.15 ± 0.02 g/cm^3 and 1.09 ± 0.02 g/cm^3, respectively. The composition of tire tread and sidewall rubber are presented in Table 1. Ordinary Portland cement type II was provided by the Abeyek Company, Iran. Washed natural river sand with density of 2.60 g/cm^3 was used as fine aggregate in sulfur and Portland cement mortar mixtures. The sand was kept in a 140°C oven for twelve hours to dry and heat up. The maximum size of sand in sulfur-based mortars is 2.4 mm and the stone dust was used as filler. Cumulative grain size distribution of the crumb tire rubber and sand particles are shown in Figure 1.

Procedures. As a binder of mortars, modified sulfur was produced by a copolymerization reaction of sulfur melt with 10% (w/w) dicyclopentadiene uniformly mixed for three hours at 140°C using a mechanical stirrer. The progress of the reaction was followed carefully by temperature and viscosity variation.

Components	Tire tread	Tire sidewall
Natural rubber	50	50
Synthetic rubber	50 (SBR)	45 (BR)
Carbon black	45	50
Naphthenic oil	9	7
Zinc oxide	3	3
Sulfur	1.5	2

Table 1. Chemical compositions of tire tread and sidewall tire (parts per hundred of rubber).
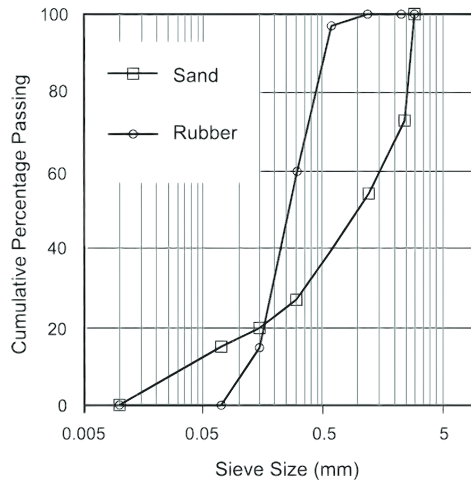
Figure 1. Cumulative grain-size distribution of crumb rubber and sand particles.

Components	P	S	MS0	MS5	MS10	MS15
Sulfur	0	35	0	0	0	0
Portland cement	35	0	0	0	0	0
Modified sulfur	0	0	35	35	35	35
Sand	55	55	55	50	45	40
Filler	10	10	10	10	10	10
Crumb rubber	0	0	0	5	10	15

Table 2. Mix design of Portland cement and sulfur polymer mortars with and without crumb tire rubber (volume %).

Since the reaction was exothermic, accurate temperature control was essential to make sure the reaction temperature did not exceed 145°C; otherwise the viscosity would rise abruptly and unstable sulfur would form. The reaction product, which hereafter is called modified sulfur binder, was a mixture of polysulfide and unreacted sulfur.

Portland cement and pristine and modified sulfur polymer mortar proportions are reported in Table 2, so that their characteristics can be assessed and compared with each other by performing the proposed analyses. The mixtures marked with "P" and "S" are the formulations in which Portland cement and pristine sulfur, respectively, are used as the binder. The symbol "MS" represents the mortars containing modified sulfur binder. MS0, MS5, MS10, and MS15 mixtures are those in which 0, 5, 10, and 15% (v/v) of sand are replaced by crumb tire rubber with identical particle size, respectively. Portland cement mortars were prepared by mixing the components shown in Table 1 with a water/cement ratio of 0.48. Specimens were cured at 20°C and 100% relative humidity for 28 days prior to testing. In order to make fresh sulfur polymer mortars comprising crumb tire rubber particles, initially prefabricated modified sulfur binder was melt mixed with the specified amounts of rubber particles for 5 minutes mechanically so that homogeneous mixtures in which modified sulfur binder wetted the rubber particles utterly were obtained. Subsequently, sand and filler particles that were preheated up to 140°C were added to the mixture according to their volume percentages in Table 2 under strict temperature control. After a homogeneous mixture was attained, prepared mortars were cast in cubic preheated steel molds (130°C) with dimensions of $50 \times 50 \times 50$ mm. They were then compacted by a vibrator for 30 s. The samples were permitted to cool down to ambient temperature and demolded after 24 hours. All tests were implemented one week after mixing.

In one set of experiments, in order to evaluate the increase in adhesion between rubber particles and sulfur polymer matrix, reactive mixing and ordinary mixing procedures were studied. In the former procedure, crumb rubber particles were added to the reaction mixture of sulfur/DCPD from the beginning of the copolymerization, while in latter the rubber particles were added after the copolymerization of sulfur with DCPD.

Testing techniques. Differential scanning calorimetry (DSC) was performed by Dupont 2000 V4.0B equipment to examine the influence of different DCPD percentages on the allotropic phase transformation of the sulfur as a result of thermal variation. Three different sulfur mixtures with 5, 8, and 10 wt% DCPD were analyzed after being stored for a week; the heating rate was 10°C/min.

Mechanical properties of the prepared samples were determined one week after molding as average value of three samples for each mixture by a Zwick 1494 (Germany) testing machine on $50 \times 50 \times 50$ mm cubic sulfur polymer mortar with a constant deflection rate of 5 mm/min.

In order to investigate the interface adhesion between the rubber particles and modified sulfur binder qualitatively, microstructure observations were carried out by scanning electron microscopy (CamScan, MV2300, operated at 20 kV) on the fracture surface resulting from compressive strength tests after samples were sputtered with silver layer.

3. Results and discussion

DSC characterization of modified sulfur. In order to be assured of the copolymerization reaction between the sulfur and the modifier, DSC diagrams for pure sulfur and sulfur with three different DCPD loading percentages are depicted in Figure 2. It was mentioned before that the advantage of sulfur modification is that the crystalline phase transformation during cooling down of the molten sulfur to ambient temperature would be retarded. Hence, less orthorhombic structures are formed due to the presence of polysulfides. Sulfur and modified sulfur samples prepared from the molten state were analyzed with DSC after proper storage time under ambient conditions. The storage period is to ensure enough time for the phase transformation from S_β to S_α to be complete. In the DSC heating diagram corresponding to pure sulfur (Figure 2a), two separated endothermic peaks are observed. The first peak at around 102°C is attributed to the crystalline phase transformation of orthorhombic (S_α) to monoclinic (S_β) structures during temperature increase. The second peak is associated with the melting of sulfur monoclinic structures
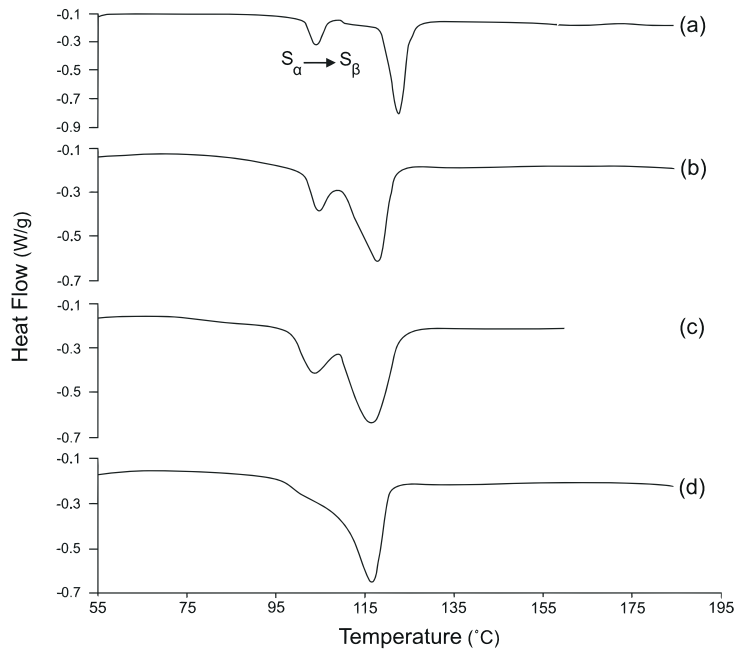

Figure 2. DSC diagrams of (a) pristine sulfur, (b) 5 wt% DCPD and sulfur, (c) 8 wt% DCPD and sulfur, and (d) 10 wt% DCPD and sulfur.

which obviously require more heating energy. However, it is observed that by addition of DCPD to pure sulfur the first peak gradually broadens and becomes the shoulder of the second peak as the percentage loading of the modifier increases (Figures 2b and 2c) and then when 10 wt% DCPD is used the second peak is mostly diminished (Figure 2d). A similar observation was reported in [Lui et al. 2008], a study on sulfur coated urea. The modified sulfur is a mixture of polysulfides and unreacted sulfur. In fact, polysulfides hinder the crystallization of free unreacted sulfur in the modified sulfur binder substantially. Thus, the unpleasant mechanical behavior of pristine sulfur concrete as well as its volume shrinkage is avoided via modification process since the modified sulfur does not undergo the allotropic transformation during thermal alteration.

Effect of the addition and replacement methods. The compressive strength of two sulfur polymer mortar mixtures, with the same formulation as MS10, yet prepared through different approaches — addition and replacement — was compared. In the addition method sand grains were replaced by rubber particles indiscriminately, while in the replacement method sand aggregates were replaced with crumb rubber tire of a similar grain size. The results indicate that using the replacement method the compressive strength grows by approximately %5, reaching 18.96 MPa, relative to 17.98 MPa for the sample prepared via the addition method. As a consequence of volumetric substitution of the similar size sand with crumb rubber particles in the replacement method, it is observed that sulfur polymer mortar with higher compressive strength and fluidity is achieved. This is mainly because in the addition method, sand particles are replaced by rubber grains with a larger total surface area for the same bulk volume. Thus the resulting mortar has a higher interface area between sulfur paste and rubber grains, relative to mortar prepared via the replacement method. Since the sulfur-rubber bond is weaker than the sulfur-sand bond, reduction in strength and workability is observed in the case of the addition method. Similarly, replacing the sand by rubber based on mass percentage would result in a severe slump and strength reduction. Therefore, all mortars in this study are prepared through the replacement method, in which sand particles are replaced by similar-sized rubber grains.

Effect of rubber particles on physical and mechanical properties of mortar. The physical and mechanical properties of the mortars described in Table 2 are listed in Table 3. Preliminary observations of all fresh mortars showed relatively good flowability, as a result of the high volume fraction of binder. During the preparation of the sulfur polymer mortars, it was observed that the workability of the fresh mixtures decreases with an increase in the rubber content. According to [Eldin and Senouci 1994], on

Composition	Hardened unit weight (g/cm^3)	Compressive strength (MPa)	Elastic modulus (GPa)	Failure strain (%)
P	2.45	32.48	–	–
S	2.43	39.54	18.34	0.221
MS0	2.40	48.87	21.68	0.229
MS5	2.34	31.62	17.36	0.242
MS10	2.25	18.96	9.31	0.254
MS15	2.19	15.51	6.86	0.313

Table 3. Physical and mechanical properties of the samples.

rubberized concrete, this observation is attributed to the interlocking structure of tire chips, which lessens the flowability of concrete. It is also claimed that this behavior could be related to the reduced density of the concrete as well as the high friction between the rubber particles and the mixture due to the rough surface of the rubber aggregate particles [Nehdi and Khan 2001; Cairns et al. 2004].

All prepared sulfur polymer mortars possess lower density than the Portland cement mortar. Logically, replacement of natural sand with rubber particles reduces the density of the sulfur polymer mortars, as a result of the inherent lower density of rubber particles compared to sand. Unit weight results indicate that increasing the crumb rubber content decreases the sulfur polymer mortar density, resulting in lighter mortars (Table 3). For instance, the MS15 sample exhibited lighter weight, with density decreased approximately 8.7% as compared to sulfur polymer mortar without rubber particles (MS0).

According to Table 3, the compressive strength of the pristine sulfur mortar (S) is almost 21% higher than that of Portland cement mortar. It is also observed that sulfur polymer mortar (MS0) has higher compressive strength and elastic modulus than pristine sulfur mortar. This is due to the fact that polysulfides retard the unfavorable crystallization transformation and thus less shrinkage occurs upon cooling and less residual stresses are developed within mortar. This leads to higher mechanical properties in comparison with unmodified mortar. Introduction of rubber particles in sulfur polymer mortars leads to a general decreasing of mechanical properties. Considerable reduction in compressive strength is observed for sulfur polymer mortars in which sand grains are replaced by rubber particles. The more sand grains substituted by rubber particles, the less the compressive strength of the mortar. In mortars with 5% rubber, a decrease of approximately 35% in compressive strength is observed in comparison with MS0, while the approximate reductions in compressive strength of the mortars with 10% and 15% rubber content are 61% and 68% respectively. That an increase in volume percentage of rubber particles in the mortar from 10 to 15% reduces the compressive strength at a slower rate has also been observed and reported by other authors [Eldin and Senouci 1994]. Reduction in compressive strength and modulus was anticipated because rubber particles have lower modulus and higher resiliency in comparison with sand grains. This results in the formation of cracks within the mortar, particularly along the boundary of separated phases, upon loading and also in failure of sulfur polymer mortar. In fact, weak adhesion between the surface of rubber particles and the modified sulfur binder causes the mortars to fail at lower stresses as a result of debonding between the rubber and the binder. Similar findings have been made by other researchers while using scrap tire rubber in Portland cement concretes. The reduction of the compressive strength is attributed to the weak rubber/binder adhesion [Eldin and Senouci 1994; Bignozzi and Sandrolini 2006]. It can also be assumed that since crumb rubber particles have a low elasticity modulus they act as void in concrete, and hence they are not able to withstand the applied external load. However, it is found that the enhancement of the adhesion between the rubber and binder through pretreatment of the rubber particles improves its ultimate mechanical strength [Nehdi and Khan 2001]. The comparison between the compressive strength of rubber-added sulfur polymer mortar and that of Portland cement mortar reveals that although with incorporation of crumb rubber in sulfur polymer mortar composition the mechanical strength is decreased, the obtained values may still be acceptable for some nonstructural applications.

Stress-strain curves for pristine sulfur mortar and sulfur polymer mortars, with and without rubber particles, are presented in Figure 3. As observed in the left part of the figure, pure sulfur mortar exhibits completely brittle behavior and after its peak stress, the mortar fractures and collapses abruptly. Modification of sulfur by DCPD has generated a binder system with slightly ductile characteristics;
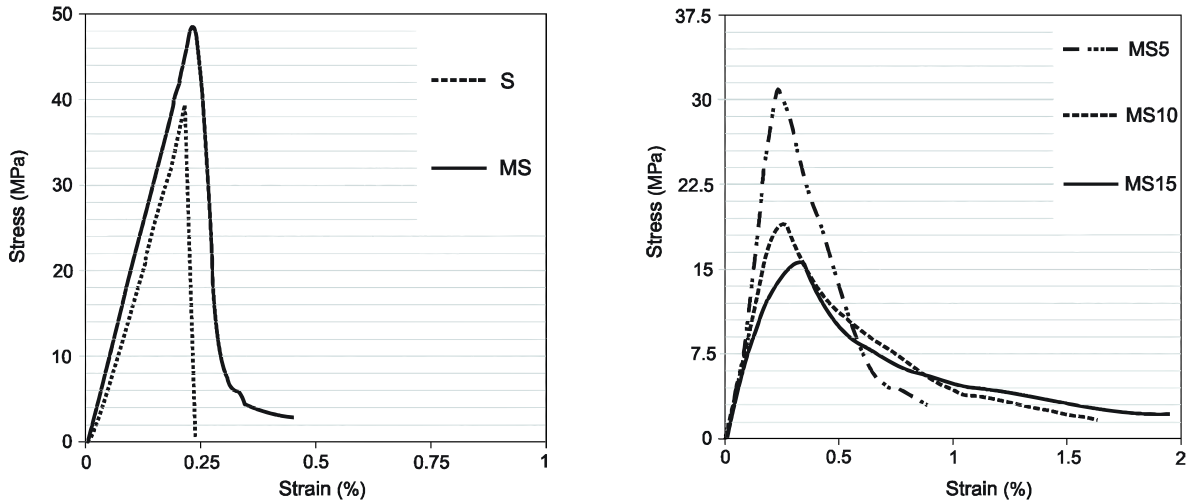
Figure 3. Left: Stress-strain curves for pristine sulfur mortar (S) and sulfur polymer mortar (MS0) samples. Right: Stress-strain curves for mortar samples containing different percentages of crumb rubber particles.

therefore the MS0 sample shows improved behavior in comparison with mortar S, resulting from the inhibition of allotrope conversion, as discussed before. Despite the unfavorable effect of rubber particles on compressive strength, the increase in rubber content improves postpeak response of the mortars. It can be inferred from Figure 3, right, that rubber-added sulfur polymer mortars sustain their integrity and withstand deformations better than mortars without rubber. As a matter of fact, various cracks are generated within samples under compression loads due to stress concentration on the interface of rubber particles and binder, which leads to failure of the sample; however, rubber particles lessen the crack propagation rate and hence delay the failure of samples containing crumb rubber tire. Figure 4 shows photographs of an MS15 sample during postpeak deformation and after its failure. The picture in part (a) is taken at a stress of 7 MPa and strain of 0.66%, and as it is seen the sample has withstood large plastic deformation without full disintegration and has kept its unity after undergoing remarkable displacement.
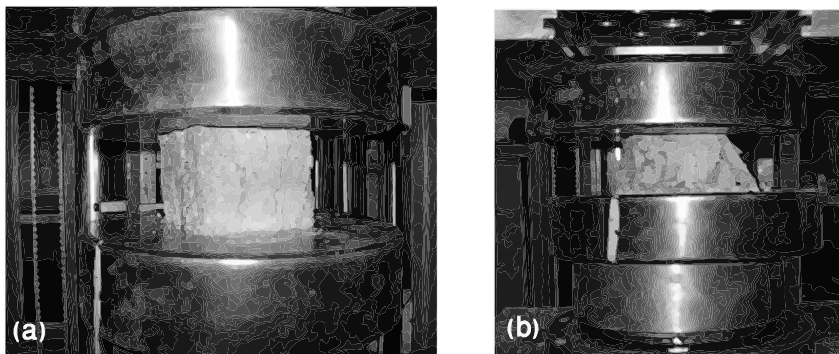

Figure 4. Behavior of MS15 mortar (a) during postpeak deformation and (b) after failure.

Such a behavior of the rubber-added mortars is not observed in mortars without rubber particles. With an increase in the rubber content, samples reveal more ductile behavior and the deformability of the sulfur polymer mortar is enhanced. The displacement of strain at peak toward higher values for rubber-added mortars confirms the above-mentioned behavior transition. Similar behavior was reported in [Yue et al. 2006] by increasing the rubber content in sulfur rubber concrete. This is mainly because rubber particles serve as crack stabilizers and toughness enhancers in sulfur polymer mortars. Moreover, it can be seen in Table 3 that the elastic modulus declines with increasing rubber content in sulfur polymer mortar, which is associated with the formation of a less rigid mortar.

Comparison of ordinary mixing and reactive mixing procedures. As mentioned before, the weak adhesion of the rubber and modified sulfur binder results in significant strength loss in rubber-added mortars. Hence, promoting affinity by means of chemical interaction between the rubber particles and the modified sulfur binder can improve the mechanical properties. To this end, favorable conditions for the reaction between the surface of the rubber particles and the modified sulfur binder are achieved through the inclusion of the rubber particles in the sulfur modification reactor during copolymerization by DCPD. This procedure is called reactive mixing, due to the simultaneous presence of DCPD, sulfur, and rubber particles in the reactor, while in the ordinary method rubber particles are added after the copolymerization of sulfur with DCPD. It is evident that the sulfur radicals serve to substitute allylic hydrogen sites present in elastomer chains to form crosslinked structures. Noting the possibility of the existence of double bonds on the surface of cured rubber particles, pristine sulfur or DCPD-modified sulfur could react with rubber unsaturated bonds at 140°C for 3 hours, and further vulcanization of rubber particles and interaction with the sulfur would form during reactive mixing. According to Table 4, the compressive strengths of the samples prepared through reactive mixing indicate more than 20% growth. Although increase in the rubber content decreases the compressive strength of sulfur polymer mortars, the growth rate of the compressive strength of the samples prepared via reactive mixing in comparison with that of samples prepared by the ordinary mixing method is enhanced with increase in rubber content. In other words, the compressive strength of MS5, MS10, and MS15 improve by approximately 21%, 24%, and 25%, respectively, which shows enhanced interactions between sulfur and rubber in the case of reactive mixing.

In order to visualize the enhanced interaction and adhesion between rubber and sulfur phases, SEM micrographs of the fracture surfaces of rubber-added sulfur polymer mortar (MS10) prepared by ordinary and reactive mixing procedures are presented in Figure 5. The images depict the interface of rubber particles and a bulk region of modified sulfur binder phases. Comparing the two micrographs, it is observed that the adhesion of rubber particles and modified sulfur binder is enhanced by the reactive mixing method

Compressive strength (MPa)			
Ordinary mixing		Reactive mixing	
MS5	31.62	RMS5	38.26
MS10	18.96	RMS10	23.51
MS15	15.51	RMS15	19.39

Table 4. Comparison of the compressive strengths of samples prepared via reactive mixing and ordinary mixing procedures.
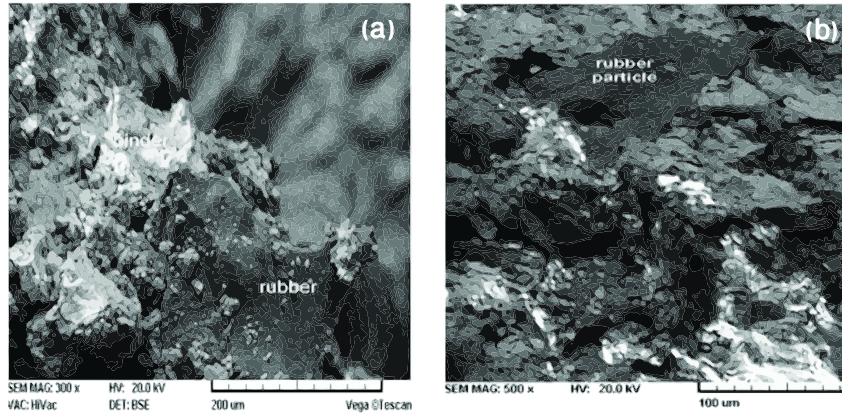
Figure 5. SEM micrographs of the sample prepared via (a) ordinary mixing and (b) reactive mixing procedures.

while relatively weaker bonding between components is obtained through ordinary mixing. Figure 5b shows a rubber particle well-adhered to the modified sulfur binder as a result of chemical interaction between them during reactive mixing. The increase in compressive strength of reactively mixed mortars further confirms the improved interactions between the sulfur binder and rubber particles.

Effect of rubber type and curing agent.   Finally, the effect of utilizing two different rubber types, selected from the treads and sidewalls of tires, on compressive strength of the sulfur polymer mortar is evaluated. The compressive strengths of the MS10 and MS15 formulations comprising the different rubber type are shown in Table 5. The increase in compressive strength as a result of using the sidewalls of tires in comparison with using the tread sections is due to the distinct composition of these sections. The fact that the properties and microstructure of the rubber employed in tread and sidewall sections of tire are different may lead to enhanced strength of sulfur polymer mortar to which sidewall rubber has been added. In the supplied sidewall sections of tires, good resistance against crack propagation and fatigue are the most desirable characteristics, which leads frequently to usage of polybutadiene and natural rubber in this part. On the other hand, styrene butadiene rubber (SBR) accompanied by natural rubber are used extensively in tread sections of supplied tires due to its great abrasion resistance, as presented in Table 1.

		Sulfur polymer mortar properties		
		Unit weight (g/cm^3)	Compressive strength (MPa)	Failure strain (%)
Tread rubber	MS10	2.27	18.96	0.254
	MS15	2.21	15.51	0.313
Sidewall rubber	MS10	2.25	19.87	0.221
	MS15	2.17	16.08	0.276

Table 5. Comparison of properties of sulfur polymer mortars containing rubber from tread and sidewall tire sections.

Therefore, the selection of appropriate rubber is a key parameter in achieving improved properties. In order to study the effect of conventional rubber-curing agents on improving the adhesion between sulfur and rubber, several agents were added to the sulfur polymer reactor in the reactive mixing procedure, 30 minutes before the end of the polymerization: namely, stearic acid, zinc oxide, and the accelerator known as CZ (*N*-cyclohexyl-2-benzothiazolesulfenamide). These compounds, which are well-known in rubber industry, are typically added to rubber to accelerate and improve vulcanization by sulfur. The mass ratio of stearic acid, zinc oxide, CZ and rubber was adjusted to 2:10:2:100. Through this approach, the compressive strength of a sulfur polymer mortar mixture including 10% rubber was increased by approximately 7%, which can be attributed to further vulcanization of the surface of rubber particles by sulfur.

4. Conclusions

The overall results in this work reveal that the incorporation of crumb tire rubber particles in sulfur polymer mortars results in a composite material with lower density and more ductile behavior, which maintains its consistency after failure to high strains. However, the lower strength of rubber particles and the poor adhesion between the surface of the rubber and the modified sulfur binder reduce the compressive strength of the mortars. Use of a reactive mixing method causes some chemical interactions between the surface of the rubber particles and the modified sulfur binder which finally improves the compressive strength of the rubber-added sulfur polymer mortars. Also, use of sidewall tire rubber results in a slight improvement in the compressive strength of mortars compared with the use of tread section tire rubber. Furthermore, it is observed that the presence of curing agents during the preparation process of the sulfur polymer mortars enhanced their mechanical properties due to the further vulcanization of the rubber particles. Although compressive strength reduction occurred due to the usage of rubber particles in the sulfur polymer mortar, these mortars still can be utilized in many applications thanks to their generally higher compressive strength as compared to Portland cement mortars, as well as the other features that have been described.

References

[Abdel-Jawad and Al-Qudah 1994] Y. Abdel-Jawad and M. Al-Qudah, "The combined effect of water and temperature on the strength of sulfur concrete", *Cem. Concr. Res.* **24**:1 (1994), 165–175.

[Albano et al. 2005] C. Albano, N. Camacho, J. Reyes, J. L. Feliu, and M. Hernández, "Influence of scrap rubber addition to Portland I concrete composites: destructive and non-destructive testing", *Compos. Struct.* **71**:3–4 (2005), 439–446.

[Bennazzouk et al. 2003] A. Bennazzouk, K. Mezreb, G. Doyen, A. Goullieux, and M. Quéneudec, "Effect of rubber aggregates on the physico-mechanical behaviour of cement-rubber composites-influence of the alveolar texture of rubber aggregates", *Cem. Concr. Res.* **25**:7 (2003), 711–720.

[Bignozzi and Sandrolini 2006] M. C. Bignozzi and F. Sandrolini, "Tyre rubber waste recycling in self-compacting concrete", *Cem. Concr. Res.* **36**:4 (2006), 735–739.

[Blight et al. 1978] L. Blight, B. R. Currell, B. J. Nash, R. A. M. Scott, and C. Stillo, "Preparation and properties of modified sulfur systems", Chapter 2, pp. 13–30 in *New uses of sulfur, II* (New Orleans, LA, 1977), edited by D. J. Bourne, Advances in Chemistry **165**, American Chemical Society, Washington, DC, 1978.

[Bordoloi and Pearce 1978] B. K. Bordoloi and E. M. Pearce, "Plastic sulfur stabilization by copolymerization of sulfur with dicyclopentadiene", Chapter 3, pp. 31–53 in *New uses of sulfur, II* (New Orleans, LA, 1977), edited by D. J. Bourne, Advances in Chemistry **165**, American Chemical Society, Washington, DC, 1978.

[Cairns et al. 2004] R. Cairns, H. Y. Kew, and M. J. Kenny, "The use of recycled rubber tyres in concrete construction", Technical report, University of Strathclyde, Glasgow, 2004, Available at http://tinyurl.com/Cairns-2004-Glasgow.

[Eldin and Senouci 1993] N. N. Eldin and A. B. Senouci, "Rubber-tire particles as concrete aggregate", *J. Mater. Civ. Eng. (ASCE)* **5**:4 (1993), 478–496.

[Eldin and Senouci 1994] N. N. Eldin and A. B. Senouci, "Measurement and prediction of the strength of rubberized concrete", *Cem. Concr. Compos.* **16**:4 (1994), 287–298.

[Khatib and Bayomy 1999] Z. K. Khatib and F. M. Bayomy, "Rubberized Portland cement concrete", *J. Mater. Civ. Eng. (ASCE)* **11**:3 (1999), 206–213.

[Lui et al. 2008] Y.-H. Lui, T.-J. Wang, L. Qin, and Y. Jin, "Urea particle coating for controlled release by using DCPD modified sulfur", *Powder Technol.* **183**:1 (2008), 88–93.

[McBee and Sullivan 1982] W. C. McBee and T. A. Sullivan, "Concrete formulation comprising polymeric reaction product of sulfur/cyclopentadiene oligomer/dicyclopentadiene", US Patent 4,348,313, September 7, 1982, Available at http://patft1.uspto.gov/netacgi/nph-Parser?patentnumber=4348313.

[Mohamed and El Gamal 2007] A.-M. O. Mohamed and M. El Gamal, "Sulfur based hazardous waste solidification", *Environ. Geol.* **53**:1 (2007), 159–175.

[Mohamed and El Gamal 2009] A.-M. O. Mohamed and M. El Gamal, "Hydro-mechanical behavior of a newly developed sulfur polymer concrete", *Cem. Concr. Compos.* **31**:3 (2009), 186–194.

[Mohamed et al. 2006] A.-M. O. Mohamed, M. El Gamal, and A. K. El Saiy, "Thermo-mechanical performance of the newly developed sulfur polymer concrete", pp. 15–26 in *Reclaiming the desert: towards a sustainable environment in arid lands* (Abu Dhabi, 2006), edited by A.-M. O. Mohamed, Developments in Arid Regions Research **3**, Taylor & Francis, London, 2006.

[Nehdi and Khan 2001] M. Nehdi and A. Khan, "Cementitious composites containing recycled tire rubber: an overview of engineering properties and potential applications", *Cem. Concr. Aggreg.* **23**:1 (2001), 3–10.

[Segre and Joekes 2000] N. Segre and I. Joekes, "Use of tire rubber particles as addition to cement paste", *Cem. Concr. Res.* **30**:9 (2000), 1421–1425.

[Siddique and Naik 2004] R. Siddique and T. R. Naik, "Properties of concrete containing scrap-tire rubber: an overview", *Waste Manag.* **24**:6 (2004), 563–569.

[Sukontasukkul and Chaikaew 2006] P. Sukontasukkul and C. Chaikaew, "Properties of concrete pedestrian block mixed with crumb rubber", *Constr. Build. Mater.* **20**:7 (2006), 450–457.

[Tantala et al. 1996] M. W. Tantala, J. A. Lepore, and I. Zandi, "Quasi-elastic behavior of rubber included concrete (RIC) using waste rubber tires", in *Proceedings of the 12th International Conference on Solid Waste Technology and Management* (Philadelphia, 1996), edited by I. Zandi, University of Pennsylvania, Chester, PA, 1996.

[Topçu and Avcular 1997] I. B. Topçu and N. Avcular, "Analysis of rubberized concrete as a composite material", *Cem. Concr. Res.* **27**:8 (1997), 1135–1139.

[Yue et al. 2006] L. Yue, J. Caiyun, and X. Yunping, "The properties of sulfur rubber concrete (SRC)", *J. Wuhan Univ. Technol. Mater. Sci.* **21**:1 (2006), 129–133.

HAMED MARAGHECHI: hym5061@psu.edu
Department of Civil and Environmental Engineering, Pennsylvania State University, 3127 Research Drive, State College, PA, 16803, United States

IMAN FOTOVAT AHMADI: imanfotovat@alumni.ut.ac.ir
Department of Chemical Engineering, College of Engineering, University of Tehran, P.O. Box 11365-4563, Tehran, Iran

SIAMAK MOTAHARI: smotahari@ut.ac.ir
Department of Chemical Engineering, College of Engineering, University of Tehran, P.O. Box 11365-4563, Tehran, Iran

msp

UNIQUENESS THEOREMS IN THE EQUILIBRIUM THEORY OF THERMOELASTICITY WITH MICROTEMPERATURES FOR MICROSTRETCH SOLIDS

ANTONIO SCALIA AND MERAB SVANADZE

In this paper the linear equilibrium theory of thermoelasticity with microtemperatures for isotropic microstretch solids is considered and some basic results of the classical theories of elasticity and thermoelasticity are generalized. Green's formulas in the theory are obtained. A wide class of internal and external boundary value problems are formulated, and uniqueness theorems are proved.

1. Introduction

In the last years the theory of thermoelasticity for bodies with microstructure has been intensively studied. A thermodynamic theory for elastic materials with inner structure whose particles, in addition to microdeformations, possess microtemperatures was proposed in [Grot 1969]. Riha [1975; 1976] developed a theory of micromorphic fluids with microtemperatures.

The linear theory of thermoelasticity with microtemperatures for materials with inner structure whose particles, in addition to the classical displacement and temperature fields, possess microtemperatures was presented in [Ieşan and Quintanilla 2000], where an existence theorem was proved and the continuous dependence of solutions of the initial data and body loads was established. The exponential stability of solutions of equations in this theory was established in [Casas and Quintanilla 2005]. The fundamental solutions of equations in the theory of thermoelasticity with microtemperatures were constructed in [Svanadze 2004b]. Representations of Galerkin type and general solutions of equations of dynamic and steady vibrations in this theory were obtained in [Scalia and Svanadze 2006]. In [Scalia and Svanadze 2009b; Svanadze 2003], the basic boundary value problems (BVPs) of steady vibrations were investigated using the potential method and the theory of singular integral equations. In [Scalia and Svanadze 2009a; Scalia et al. 2010; Ieşan and Scalia 2010], basic theorems in the equilibrium and steady vibrations theories of thermoelasticity with microtemperatures were proved.

The theory of micromorphic elastic solids with microtemperatures, in which microelements possess microtemperatures and can stretch and contract independently of their translations, was presented in [Ieşan 2001]. The fundamental solutions of equations in this theory were constructed in [Svanadze 2004a]. Uniqueness theorems in the dynamical theory thermoelasticity of porous media with microtemperatures were proved in [Quintanilla 2009]. The existence and uniqueness of solutions in the linear theory of heat conduction in micromorphic continua were established in [Ieşan 2002]. Recently, the representations of solutions in the theory of thermoelasticity with microtemperatures for microstretch solids were obtained in [Svanadze and Tracinà 2011].

The theory of micropolar thermoelasticity with microtemperatures was presented in [Ieşan 2007]. The existence and asymptotic behavior of the solutions in this theory were proved in [Aouadi 2008]. A linear theory of thermoelastic bodies with microstructure and microtemperatures which permits the transmission of heat as thermal waves at finite speed was constructed in [Ieşan and Quintanilla 2009], and existence and uniqueness results in the context of the dynamic theory were established. An extensive review and the basic results in the microcontinuum field theories are given in [Eringen 1999; Ieşan 2004].

In this paper the linear equilibrium theory of thermoelasticity with microtemperatures for isotropic microstretch solids [Ieşan 2001] is considered and some basic results of the classical theories of elasticity and thermoelasticity (see [Kupradze et al. 1979; Knops and Payne 1971]) are generalized. Green's formulae are obtained for the theory. A wide class of internal and external BVPs are formulated, and uniqueness theorems are proved.

2. Basic equations

We consider an isotropic elastic material with microstructure that occupies a region Ω of Euclidean three-dimensional space E^3. Let $\boldsymbol{x} = (x_1, x_2, x_3)$ be a point of E^3 and set $\boldsymbol{D_x} = (\partial/\partial x_1, \partial/\partial x_2, \partial/\partial x_3)$.

The fundamental system of field equations in the linear equilibrium theory of thermoelasticity with microtemperatures for isotropic microstretch solids consists of the equations of equilibrium [Ieşan 2001]

$$t_{jl,j} + \rho F_l^{(1)} = 0, \tag{2-1}$$

the first moment of energy

$$q_{jl,j} + q_l - Q_l + \rho F_l^{(2)} = 0, \tag{2-2}$$

the balance of energy

$$q_{l,l} + \rho s_1 = 0, \tag{2-3}$$

the balance of first stress moment

$$h_{l,l} - s + \rho\, s_2 = 0, \tag{2-4}$$

the constitutive equations

$$
\begin{aligned}
t_{jl} &= (\lambda\, e_{rr} - \beta\,\theta + b\,\varphi)\delta_{jl} + 2\mu e_{jl}, \\
q_l &= k\,\theta_{,l} + k_1\, w_l, \\
q_{jl} &= -k_4\, w_{r,r}\delta_{jl} - k_5\, w_{j,l} - k_6\, w_{l,j}, \\
Q_l &= (k_1 - k_2)w_l + (k - k_3)\,\theta_{,l}, \\
h_l &= \gamma\varphi_{,l} - d\, w_l, \\
s &= b\, e_{rr} - m\,\theta + \xi\,\varphi,
\end{aligned}
\tag{2-5}
$$

and the geometric equations

$$e_{lj} = \tfrac{1}{2}(u_{l,j} + u_{j,l}), \tag{2-6}$$

where $\boldsymbol{u} = (u_1, u_2, u_3)$ is the displacement vector, $\boldsymbol{w} = (w_1, w_2, w_3)$ is the microtemperature vector, θ is the temperature measured from the constant absolute temperature T_0 ($T_0 > 0$), φ is the microdilatation function, t_{jl} are the components of stress tensor, ρ is the reference mass density ($\rho > 0$), h_l is the microstretch, $\boldsymbol{F}^{(1)} = (F_1^{(1)}, F_2^{(1)}, F_3^{(1)})$ is the body force, $\boldsymbol{q} = (q_1, q_2, q_3)$ is the heat flux vector, s is the

intrinsic body load, s_1 is the heat supply, s_2 is the general external body load, q_{jl} are the components of first heat flux moment tensor, $\boldsymbol{Q} = (Q_1, Q_2, Q_3)$ is the mean heat flux vector, $\boldsymbol{F}^{(2)} = (F_1^{(2)}, F_2^{(2)}, F_3^{(2)})$ is first heat source moment vector, $\lambda, \mu, \beta, \gamma, \xi, b, d, m, k, k_1, k_2, \ldots, k_6$ are constitutive coefficients, δ_{lj} is the Kronecker delta, e_{lj} are the components of strain tensor, the subscripts preceded by a comma denote partial differentiation with respect to the corresponding Cartesian coordinate, $j, l = 1, 2, 3$, and repeated indices are summed over the range $\{1, 2, 3\}$.

By virtue of (2-5) and (2-6), the system (2-1)–(2-4) can be expressed in terms of the displacement vector $\boldsymbol{u}$, the microtemperature vector $\boldsymbol{w}$, the temperature θ and the microdilatation function φ. We obtain a system of eight partial differential equations of the linear equilibrium theory of thermoelasticity with microtemperatures for isotropic and homogeneous microstretch solids [Ieşan 2001]:

$$
\begin{aligned}
\mu \, \Delta \boldsymbol{u} + (\lambda + \mu) \operatorname{grad} \operatorname{div} \boldsymbol{u} - \beta \operatorname{grad} \theta + b \operatorname{grad} \varphi &= -\rho \, \boldsymbol{F}^{(1)}, \\
k_6 \, \Delta \boldsymbol{w} + (k_4 + k_5) \operatorname{grad} \operatorname{div} \boldsymbol{w} - k_3 \operatorname{grad} \boldsymbol{\theta} - k_2 \boldsymbol{w} &= \rho \, \boldsymbol{F}^{(2)}, \\
k \, \Delta \theta + k_1 \operatorname{div} \boldsymbol{w} &= -\rho \, s_1, \\
\gamma \, \Delta \varphi - b \operatorname{div} \boldsymbol{u} - d \operatorname{div} \boldsymbol{w} + m \, \theta - \xi \, \varphi &= -\rho \, s_2.
\end{aligned}
\tag{2-7}
$$

We introduce the matrix differential operator

$$
\boldsymbol{A}(\boldsymbol{D_x}) = \big(A_{pq}(\boldsymbol{D_x})\big)_{8 \times 8},
$$

where, for $j, l = 1, 2, 3$, we have

$$
A_{lj}(\boldsymbol{D_x}) = \mu \Delta \, \delta_{lj} + (\lambda + \mu) \frac{\partial^2}{\partial x_l \partial x_j}, \qquad A_{l7}(\boldsymbol{D_x}) = -\beta \frac{\partial}{\partial x_l}, \qquad A_{l8}(\boldsymbol{D_x}) = b \frac{\partial}{\partial x_l},
$$

$$
A_{l;j+3}(\boldsymbol{D_x}) = A_{l+3;j}(\boldsymbol{D_x}) = A_{l+3;8}(\boldsymbol{D_x}) = A_{7l}(\boldsymbol{D_x}) = A_{78}(\boldsymbol{D_x}) = 0,
$$

$$
A_{l+3;j+3}(\boldsymbol{D_x}) = (k_6 \Delta - k_2)\delta_{lj} + (k_4 + k_5) \frac{\partial^2}{\partial x_l \partial x_j}, \qquad A_{l+3;7}(\boldsymbol{D_x}) = -k_3 \frac{\partial}{\partial x_l}, \tag{2-8}
$$

$$
A_{7;l+3}(\boldsymbol{D_x}) = k_1 \frac{\partial}{\partial x_l}, \qquad A_{77}(\boldsymbol{D_x}) = k\Delta, \qquad A_{8l}(\boldsymbol{D_x}) = -b \frac{\partial}{\partial x_l},
$$

$$
A_{8;l+3}(\boldsymbol{D_x}) = -d \frac{\partial}{\partial x_l}, \qquad A_{87}(\boldsymbol{D_x}) = m, \qquad A_{88}(\boldsymbol{D_x}) = \gamma \Delta - \xi,
$$

Obviously, the system (2-7) can be written as

$$
\boldsymbol{A}(\boldsymbol{D_x})U(\boldsymbol{x}) = F(\boldsymbol{x}), \tag{2-9}
$$

where $U = (\boldsymbol{u}, \boldsymbol{w}, \theta, \varphi)$, $F = (-\rho \boldsymbol{F}^{(1)}, \rho \boldsymbol{F}^{(2)}, -\rho s_1, -\rho \, s_2)$, and $\boldsymbol{x} \in \Omega$.

3. Boundary value problems

In this section a wide class of BVPs of the linear equilibrium theory of thermoelasticity with microtemperatures for isotropic and homogeneous microstretch solids is formulated.

Let S be the closed surface surrounding the finite domain Ω^+ in E^3, $S \in C^{2,\alpha_1}$, $0 < \alpha_1 \le 1$, $\bar{\Omega}^+ = \Omega^+ \cup S$, $\Omega^- = E^3 \backslash \bar{\Omega}^+$, $\bar{\Omega}^- = \Omega^- \cup S$.

Definition 3.1. A vector function $U = (u, w, \theta, \varphi) = (U_1, U_2, \ldots, U_8)$ is called *regular* in Ω^- (or Ω^+) if

$$U_l \in C^2(\Omega^-) \cap C^1(\bar{\Omega}^-) \qquad (\text{or } U_l \in C^2(\Omega^+) \cap C^1(\bar{\Omega}^+))$$

and

$$U_l(x) = O(|x|^{-1}), \qquad \frac{\partial}{\partial x_j} U_l(x) = o(|x|^{-1}) \quad \text{for } |x| \gg 1, \tag{3-1}$$

where $j = 1, 2, 3$ and $l = 1, 2, \ldots, 8$.

We will use the matrix differential operators

$$P^{(m)}(D_x, n) = (P_{lj}^{(m)}(D_x, n))_{3\times 3} \quad \text{and} \quad P(D_x, n) = (P_{lj}(D_x, n))_{8\times 8},$$

where

$$
\begin{aligned}
P_{lj}^{(1)}(D_x, n) &= \mu\delta_{lj}\frac{\partial}{\partial n} + \mu n_j\frac{\partial}{\partial x_l} + \lambda n_l\frac{\partial}{\partial x_j} = \mu\delta_{lj}\frac{\partial}{\partial n} + (\lambda + \mu)n_l\frac{\partial}{\partial x_j} + \mu M_{lj}, \\
P_{lj}^{(2)}(D_x, n) &= k_6\delta_{lj}\frac{\partial}{\partial n} + k_5 n_j\frac{\partial}{\partial x_l} + k_4 n_l\frac{\partial}{\partial x_j} = k_6\delta_{lj}\frac{\partial}{\partial n} + (k_4 + k_5)n_l\frac{\partial}{\partial x_j} + k_5 M_{lj}
\end{aligned}
\tag{3-2}
$$

and, for $m = 1, 2$ and $j, l = 1, 2, 3$,

$$
\begin{aligned}
P_{lj}(D_x, n) &= P_{lj}^{(1)}(D_x, n), & P_{l7}(D_x, n) &= -\beta n_l, \\
P_{l+3;\,j+3}(D_x, n) &= P_{lj}^{(2)}(D_x, n), & P_{l8}(D_x, n) &= b\, n_l, \\
P_{7;\,l+3}(D_x, n) &= k_1\, n_l, & P_{77}(D_x, n) &= k\frac{\partial}{\partial n}, \\
P_{8;\,l+3}(D_x, n) &= -d\, n_l, & P_{88}(D_x, n) &= \gamma\frac{\partial}{\partial n}, \\
\end{aligned}
\tag{3-3}
$$
$$P_{l;\,j+3} = P_{l+3;\,j} = P_{l+3;\,7} = P_{l+3;\,8} = P_{7l} = P_{78} = P_{8l} = P_{87} = 0,$$

where $n = (n_1, n_2, n_3)$, $n(z)$ is the external unit normal vector to S at z, $\partial/\partial n$ is the derivative along the vector n, and

$$M_{lj} = n_j\frac{\partial}{\partial x_l} - n_l\frac{\partial}{\partial x_j}. \tag{3-4}$$

$P(D_x, n)$ and $P(D_x, n)U(x)$ are the stress operator and stress vector, respectively, in the linear theory of thermoelasticity with microtemperatures for microstretch solids; see [Ieşan 2001].

The internal BVPs of the linear equilibrium theory of thermoelasticity with microtemperatures for isotropic and homogeneous microstretch solids are formulated as follows:

Problem $(I)_{F,f}^+$**.** Find a regular (classical) solution to system (2-9) for $x \in \Omega^+$ satisfying the boundary conditions

$$\lim_{x \to z \in S} u(x) \equiv \{u(z)\}^+ = f^{(1)}(z), \tag{3-5}$$

$$\{w(z)\}^+ = f^{(2)}(z), \tag{3-6}$$

$$\{\theta(z)\}^+ = f_7(z), \tag{3-7}$$

$$\{\varphi(z)\}^+ = f_8(z) \tag{3-8}$$

with $\boldsymbol{f}^{(1)} = (f_1, f_2, f_3)$, $\boldsymbol{f}^{(2)} = (f_4, f_5, f_6)$; here $f_1, f_2, \ldots, f_8$ are known functions and $\boldsymbol{F}$ is a known eight-component vector function. Obviously, we can rewrite the boundary condition (3-5)–(3-8) in the form

$$\{\boldsymbol{U}(z)\}^+ = \boldsymbol{f}(z),$$

where $\boldsymbol{f} = (f_1, f_2, \ldots, f_8)$.

Problem $(II)_{\boldsymbol{F}, \boldsymbol{f}}^+$. Find a regular solution to system (2-9) for $\boldsymbol{x} \in \Omega^+$ satisfying the boundary conditions

$$\left\{ \boldsymbol{P}^{(1)}(\boldsymbol{D}_z, \boldsymbol{n}(z))\,\boldsymbol{u}(z) - \beta\,\theta(z)\,\boldsymbol{n}(z) + b\,\varphi(z)\,\boldsymbol{n}(z) \right\}^+ = \boldsymbol{f}^{(1)}(z), \tag{3-9}$$

$$\left\{ \boldsymbol{P}^{(2)}(\boldsymbol{D}_z, \boldsymbol{n}(z))\,\boldsymbol{w}(z) \right\}^+ = \boldsymbol{f}^{(2)}(z), \tag{3-10}$$

$$\left\{ k\frac{\partial\theta(z)}{\partial\boldsymbol{n}(z)} + k_1\,\boldsymbol{w}(z)\,\boldsymbol{n}(z) \right\}^+ = f_7(z), \tag{3-11}$$

$$\left\{ \gamma\frac{\partial\varphi(z)}{\partial\boldsymbol{n}(z)} - d\,\boldsymbol{w}(z)\,\boldsymbol{n}(z) \right\}^+ = f_8(z). \tag{3-12}$$

Obviously, by virtue of (3-3) we can rewrite the boundary conditions (3-9)–(3-12) in the form

$$\{\boldsymbol{P}(\boldsymbol{D}_z, \boldsymbol{n}(z))\,\boldsymbol{U}(z)\}^+ = \boldsymbol{f}(z).$$

Problem $(III)_{\boldsymbol{F}, \boldsymbol{f}}^+$. Find a regular solution to (2-9) for $\boldsymbol{x} \in \Omega^+$ satisfying (3-5), (3-10), (3-7), (3-8).

Problem $(IV)_{\boldsymbol{F}, \boldsymbol{f}}^+$. Find a regular solution to (2-9) for $\boldsymbol{x} \in \Omega^+$ satisfying (3-5), (3-6), (3-7), (3-12).

Problem $(V)_{\boldsymbol{F}, \boldsymbol{f}}^+$. Find a regular solution to (2-9) for $\boldsymbol{x} \in \Omega^+$ satisfying (3-5), (3-10), (3-7), (3-12).

Problem $(VI)_{\boldsymbol{F}, \boldsymbol{f}}^+$. Find a regular solution to (2-9) for $\boldsymbol{x} \in \Omega^+$ satisfying (3-9), (3-6), (3-7), (3-8).

Problem $(VII)_{\boldsymbol{F}, \boldsymbol{f}}^+$. Find a regular solution to (2-9) for $\boldsymbol{x} \in \Omega^+$ satisfying (3-9), (3-10), (3-7), (3-8).

Problem $(VIII)_{\boldsymbol{F}, \boldsymbol{f}}^+$. Find a regular solution to (2-9) for $\boldsymbol{x} \in \Omega^+$ satisfying (3-9), (3-6), (3-7), (3-12).

Problem $(IX)_{\boldsymbol{F}, \boldsymbol{f}}^+$. Find a regular solution to (2-9) for $\boldsymbol{x} \in \Omega^+$ satisfying (3-9), (3-10), (3-7), (3-12).

Problem $(X)_{\boldsymbol{F}, \boldsymbol{f}}^+$. Find a regular solution to (2-9) for $\boldsymbol{x} \in \Omega^+$ satisfying (3-9), (3-6), (3-11), (3-12).

Problem $(XI)_{\boldsymbol{F}, \boldsymbol{f}}^+$. Find a regular solution to (2-9) for $\boldsymbol{x} \in \Omega^+$ satisfying (3-5), (3-6), (3-11), (3-12).

Problem $(XII)_{\boldsymbol{F}, \boldsymbol{f}}^+$. Find a regular solution to (2-9) for $\boldsymbol{x} \in \Omega^+$ satisfying (3-5), (3-10), (3-11), (3-12).

We now turn to the external BVPs, spelling out only the first two (the external BVPs $(III)_{\boldsymbol{F}, \boldsymbol{f}}^-$ through $(XII)_{\boldsymbol{F}, \boldsymbol{f}}^-$ are formulated similarly).

Problem $(I)_{\boldsymbol{F}, \boldsymbol{f}}^-$. Find a regular solution to system (2-9) for $\boldsymbol{x} \in \Omega^-$ satisfying the boundary condition

$$\lim_{\boldsymbol{x} \to z \in S} \boldsymbol{U}(\boldsymbol{x}) \equiv \{\boldsymbol{U}(z)\}^- = \boldsymbol{f}(z),$$

where $\boldsymbol{F}$ and $\boldsymbol{f}$ are known eight-component vector functions, and supp $\boldsymbol{F}$ is a finite domain in Ω^-.

Problem $(II)_{\boldsymbol{F}, \boldsymbol{f}}^-$. Find a regular solution to system (2-9) for $\boldsymbol{x} \in \Omega^-$ satisfying the boundary condition

$$\{\boldsymbol{P}(\boldsymbol{D}_z, \boldsymbol{n}(z))\,\boldsymbol{U}(z)\}^- = \boldsymbol{f}(z).$$

4. Green's formulae

In this section the Green's formulae in the linear equilibrium theory of thermoelasticity with microtemperatures for isotropic and homogeneous microstretch solids are obtained.

We introduce the notation

$$W(U, U') = W^{(1)}(u, u') + W^{(2)}(w, w') + (b\,\varphi - \beta\,\theta)\,\text{div}\,u' + (k_2 w + k_3\,\text{grad}\,\theta)\,w'$$
$$+ (k_1\,w + k\,\text{grad}\,\theta)\,\text{grad}\,\theta' + (\gamma\,\text{grad}\,\varphi - d\,w)\,\text{grad}\,\varphi' + (b\,\text{div}\,u - m\,\theta + \xi\,\varphi)\,\varphi', \quad (4\text{-}1)$$

where $u' = (u'_1, u'_2, u'_3)$ and $w' = (w'_1, w'_2, w'_3)$ are three-component vector functions, θ' and φ' are scalar functions, $U' = (u', w', \theta', \varphi')$ and

$$W^{(1)}(u, u') = \tfrac{1}{3}(3\lambda + 2\mu)\,\text{div}\,u\,\text{div}\,u'$$

$$+ \mu\left[\frac{1}{2}\sum_{\substack{l,j=1\\l\neq j}}^{3}\left(\frac{\partial u_j}{\partial x_l} + \frac{\partial u_l}{\partial x_j}\right)\left(\frac{\partial u'_j}{\partial x_l} + \frac{\partial u'_l}{\partial x_j}\right) + \frac{1}{3}\sum_{l,j=1}^{3}\left(\frac{\partial u_l}{\partial x_l} - \frac{\partial u_j}{\partial x_j}\right)\left(\frac{\partial u'_l}{\partial x_l} - \frac{\partial u'_j}{\partial x_j}\right)\right],$$

$$W^{(2)}(w, w') = \tfrac{1}{3}(3k_4 + k_5 + k_6)\,\text{div}\,w\,\text{div}\,w' + \tfrac{1}{2}(k_6 - k_5)\,\text{curl}\,w\,\text{curl}\,w'$$

$$+ \frac{k_6 + k_5}{2}\left[\frac{1}{2}\sum_{\substack{l,j=1\\l\neq j}}^{3}\left(\frac{\partial w_j}{\partial x_l} + \frac{\partial w_l}{\partial x_j}\right)\left(\frac{\partial w'_j}{\partial x_l} + \frac{\partial w'_l}{\partial x_j}\right) + \frac{1}{3}\sum_{l,j=1}^{3}\left(\frac{\partial w_l}{\partial x_l} - \frac{\partial w_j}{\partial x_j}\right)\left(\frac{\partial w'_l}{\partial x_l} - \frac{\partial w'_j}{\partial x_j}\right)\right]. \quad (4\text{-}2)$$

We are now in a position to prove Green's theorem in the linear equilibrium theory of thermoelasticity with microtemperatures for the domains Ω^+ and Ω^-.

Theorem 4.1. *If $U = (u, w, \theta)$ is a regular vector field in Ω^+ and $U' = (u', w', \theta') \in C^1(\Omega^+)$, then*

$$\int_{\Omega^+}\left[A(D_x)\,U(x)\,U'(x) + W(U, U')\right]dx = \int_S P(D_z, n(z))\,U(z)\,U'(z)\,d_z S, \quad (4\text{-}3)$$

where $A(D_x)$ and $P(D_z, n(z))$ are the operators defined by (2-8) and (3-3), respectively.

Proof. We introduce the matrix differential operators

$$A^{(1)}(D_x) = \left(A^{(1)}_{lj}(D_x)\right)_{3\times 3}, \quad A^{(1)}_{lj}(D_x) = A_{lj}(D_x),$$
$$A^{(2)}(D_x) = \left(A^{(2)}_{lj}(D_x)\right)_{3\times 3}, \quad A^{(2)}_{lj}(D_x) = A_{l+3;\,j+3}(D_x).$$

From Green's formula in the classical theory of elasticity, expressed as

$$\int_{\Omega^+}\left[A^{(1)}(D_x)\,u\,u' + W^{(1)}(u, u')\right]dx = \int_S P^{(1)}(D_z(n, z))\,u(z)\,u'(z)\,d_z S$$

(see [Kupradze et al. 1979]), we have

$$\int_{\Omega^+}\left[(A^{(1)}\,u - \beta\,\text{grad}\,\theta + b\,\text{grad}\,\varphi)u' + W^{(1)}(u, u') + (\beta\,\text{grad}\,\theta - b\,\text{grad}\,\varphi)\,u'\right]dx$$
$$= \int_S P^{(1)}(D_z, n(z))\,u(z)\,u'(z)\,d_z S. \quad (4\text{-}4)$$

On account of the identity $\int_{\Omega^+} (\text{grad } \theta \, \boldsymbol{u}' + \theta \, \text{div } \boldsymbol{u}') \, d\boldsymbol{x} = \int_S \theta \, \boldsymbol{n} \, \boldsymbol{u}' \, d_z S$ (see [Kupradze et al. 1979]), it follows from (4-4) that

$$\int_{\Omega^+} \left[(\boldsymbol{A}^{(1)} \, \boldsymbol{u} - \beta \, \text{grad } \theta + b \, \text{grad } \varphi) \boldsymbol{u}' + W^{(1)}(\boldsymbol{u}, \boldsymbol{u}') + (b \, \varphi - \beta \, \theta) \, \text{div } \boldsymbol{u}' \right] d\boldsymbol{x}$$
$$= \int_S \boldsymbol{R}(\boldsymbol{D}_z, \boldsymbol{n}(z)) \boldsymbol{v}(z) \boldsymbol{u}'(z) \, d_z S, \quad (4\text{-}5)$$

where $\boldsymbol{v} = (\boldsymbol{u}, \theta, \varphi)$ is a five-component vector and

$$\boldsymbol{R}(\boldsymbol{D}_x, \boldsymbol{n}) = (R_{lj}(\boldsymbol{D}_x, \boldsymbol{n}))_{3 \times 5}, \quad R_{lj}(\boldsymbol{D}_x, \boldsymbol{n}) = P_{lj}(\boldsymbol{D}_x, \boldsymbol{n}), \quad R_{l4}(\boldsymbol{D}_x, \boldsymbol{n}) = -\beta \, n_l, \quad R_{l5}(\boldsymbol{D}_x, \boldsymbol{n}) = b \, n_l,$$

for $l, j = 1, 2, 3$. It may be shown similarly that Green's formula [Kupradze et al. 1979]

$$\int_{\Omega^+} \left[A^{(2)}(\boldsymbol{D}_x) \, \boldsymbol{w} \, \boldsymbol{w}' + W^{(2)}(\boldsymbol{w}, \boldsymbol{w}') \right] d\boldsymbol{x} = \int_S P^{(2)}(\boldsymbol{D}_z(\boldsymbol{n}, z)) \, \boldsymbol{w}(z) \, \boldsymbol{w}'(z) \, d_z S$$

may be rewritten as

$$\int_{\Omega^+} \left[(A^{(2)}(\boldsymbol{D}_x) \, \boldsymbol{w} - k_2 \boldsymbol{w} - k_3 \, \text{grad } \theta) \, \boldsymbol{w}' + W^{(2)}(\boldsymbol{w}, \boldsymbol{w}') + (k_2 \boldsymbol{w} + k_3 \, \text{grad } \theta) \, \boldsymbol{w}' \right] d\boldsymbol{x}$$
$$= \int_S P^{(2)}(\boldsymbol{D}_z(\boldsymbol{n}, z)) \, \boldsymbol{w}(z) \, \boldsymbol{w}'(z) \, d_z S. \quad (4\text{-}6)$$

By virtue of the identities [Kupradze et al. 1979]

$$\int_{\Omega^+} \left(\Delta \, \theta \, \theta' + \text{grad } \theta \, \text{grad } \theta' \right) d\boldsymbol{x} = \int_S \frac{\partial \theta(z)}{\partial \boldsymbol{n}(z)} \, \theta'(z) \, d_z S,$$
$$\int_{\Omega^+} \left(\text{div} \boldsymbol{w} \, \theta' + \boldsymbol{w} \, \text{grad } \theta' \right) d\boldsymbol{x} = \int_S \boldsymbol{w} \, \boldsymbol{n} \, \theta' d_z S,$$

we have

$$\int_{\Omega^+} \left[(k \Delta \, \theta + k_1 \, \text{div } \boldsymbol{w}) \theta' + (k \, \text{grad } \theta + k_1 \boldsymbol{w}) \, \text{grad } \theta' \right] d\boldsymbol{x} = \int_S \left(k \frac{\partial \theta}{\partial \boldsymbol{n}} + k_1 \boldsymbol{w} \, \boldsymbol{n} \right) \theta' d_z S. \quad (4\text{-}7)$$

It may be shown similarly that

$$\int_{\Omega^+} \left[(\gamma \Delta \, \varphi - b \, \text{div } \boldsymbol{u} - d \, \text{div } \boldsymbol{w} + m \, \theta - \xi \, \varphi) \, \varphi' + (\gamma \, \text{grad } \varphi - d \, \boldsymbol{w}) \, \text{grad } \varphi' + (b \, \text{div } \boldsymbol{u} - m \, \theta + \xi \, \varphi) \, \varphi' \right] d\boldsymbol{x}$$
$$= \int_S \left(\gamma \frac{\partial \varphi}{\partial \boldsymbol{n}} - d \, \boldsymbol{w} \, \boldsymbol{n} \right) \varphi' d_z S. \quad (4\text{-}8)$$

Keeping (4-1) in mind, (4-5)–(4-8) yield (4-3), and the theorem is proved. $\qquad \square$

The following theorem holds for an infinite domain Ω^-.

Theorem 4.2. *Let* $\boldsymbol{U} = (\boldsymbol{u}, \boldsymbol{w}, \theta, \varphi)$ *be a regular vector field in* Ω^-. *Let* $\boldsymbol{U}' = (\boldsymbol{u}', \boldsymbol{w}', \theta', \varphi') \in C^1(\Omega^-)$ *satisfy*

$$\boldsymbol{U}'(\boldsymbol{x}) = O(|\boldsymbol{x}|^{-1}) \quad and \quad \frac{\partial}{\partial x_j} \boldsymbol{U}'(\boldsymbol{x}) = o(|\boldsymbol{x}|^{-1}) \quad for \; |\boldsymbol{x}| \gg 1, \; j = 1, 2, 3. \quad (4\text{-}9)$$

Then

$$\int_{\Omega^-} \left[\boldsymbol{A}(\boldsymbol{D}_x) \, \boldsymbol{U}(\boldsymbol{x}) \, \boldsymbol{U}'(\boldsymbol{x}) + W(\boldsymbol{U}, \boldsymbol{U}') \right] d\boldsymbol{x} = - \int_S \boldsymbol{P}(\boldsymbol{D}_z, \boldsymbol{n}(z)) \, \boldsymbol{U}(z) \, \boldsymbol{U}'(z) \, d_z S. \quad (4\text{-}10)$$

Proof. Let Ω_r be a sphere of sufficiently large radius r so that $\bar{\Omega}^+ \subset \Omega_r$, S_r is the boundary of the sphere Ω_r. The theorem is proved by applying Green's formula (4-3) to the finite domain $\Omega_r^- = \Omega^- \cap \Omega_r$. The positive normal to the boundary Ω_r^- is the inward one. Hence, we obtain

$$\int_{\Omega_r^-} \left[A(D_x) U(x) U'(x) + W(U, U') \right] dx$$
$$= - \int_S P(D_z, n(z)) U(z) U'(z) d_z S - \int_{S_r} P(D_z, n(z)) U(z) U'(z) d_z S. \quad (4\text{-}11)$$

In view of (3-1) and (4-9), the integral over S_r tends to zero when $r \to \infty$. Therefore, the limit of the right-hand side and hence the limit of the left-hand side of (4-11) exist and are equal. From (4-4) we obtain (4-10) and the theorem is proved. $\qquad \square$

In the classical theory of elasticity one considers the *generalized stress operator* [Kupradze et al. 1979, Chapter I]. We denote this operator by $P_{(\tau_1)}^{(1)}(D_x, n)$ and we have (*ibid.*)

$$P_{(\tau_1)}^{(1)}(D_x, n) = \left(P_{(\tau_1)lj}^{(1)}(D_x, n) \right)_{3 \times 3},$$
$$P_{(\tau_1)lj}^{(1)}(D_x, n) = \mu \delta_{lj} \frac{\partial}{\partial n} + (\lambda + \mu) n_l \frac{\partial}{\partial x_j} + \tau_1 M_{lj}, \quad (4\text{-}12)$$

where τ_1 is an arbitrary number and M_{lj} is defined by (3-4). Obviously, the operator $P^{(1)}$ is obtained from the operator $P_{(\tau_1)}^{(1)}$ if we set $\tau_1 = \mu$, i.e., $P_{(\mu)}^{(1)} = P^{(1)}$.

In the sequel we use the matrix differential operator [Scalia et al. 2010]

$$P_{(\tau_2)}^{(2)}(D_x, n) = \left(P_{(\tau_2)lj}^{(2)}(D_x, n) \right)_{3 \times 3},$$
$$P_{(\tau_2)lj}^{(2)}(D_x, n) = k_6 \delta_{lj} \frac{\partial}{\partial n} + (k_4 + k_5) n_l \frac{\partial}{\partial x_j} + \tau_2 M_{lj}, \quad (4\text{-}13)$$

where τ_2 is an arbitrary number. Obviously, the operator $P^{(2)}$ is obtained from operator $P_{(\tau_2)}^{(2)}$ if we set $\tau_2 = k_5$, i.e., $P_{(k_5)}^{(2)} = P^{(2)}$.

We introduce the notation

$$W_{(\tau)}(U, U') = W_{(\tau_1)}^{(1)}(u, u') + W_{(\tau_2)}^{(2)}(w, w') + (b \varphi - \beta \theta) \operatorname{div} u' + (k_2 w + k_3 \operatorname{grad} \theta) w'$$
$$+ (k_1 w + k \operatorname{grad} \theta) \operatorname{grad} \theta' + (\gamma \operatorname{grad} \varphi - d w) \operatorname{grad} \varphi' + (b \operatorname{div} u - m \theta + \xi \varphi) \varphi', \quad (4\text{-}14)$$

where $\tau = (\tau_1, \tau_2)$ and

$$W_{(\tau_1)}^{(1)}(u, u') = \tfrac{1}{3}(3\lambda + 4\mu - 2\tau_1) \operatorname{div} u \operatorname{div} u' + \tfrac{1}{2}(\mu - \tau_1) \operatorname{curl} u \operatorname{curl} u'$$

$$+ \frac{1}{2}(\mu + \tau_1) \left[\frac{1}{2} \sum_{l,j=1; l \neq j}^{3} \left(\frac{\partial u_j}{\partial x_l} + \frac{\partial u_l}{\partial x_j} \right) \left(\frac{\partial u'_j}{\partial x_l} + \frac{\partial u'_l}{\partial x_j} \right) + \frac{1}{3} \sum_{l,j=1}^{3} \left(\frac{\partial u_l}{\partial x_l} - \frac{\partial u_j}{\partial x_j} \right) \left(\frac{\partial u'_l}{\partial x_l} - \frac{\partial u'_j}{\partial x_j} \right) \right],$$

$$W_{(\tau_2)}^{(2)}(w, w') = \tfrac{1}{3}(3k_4 + 3k_5 + k_6 - 2\tau_2) \operatorname{div} w \operatorname{div} w' + \tfrac{1}{2}(k_6 - \tau_2) \operatorname{curl} w \operatorname{curl} w'$$

$$+ \frac{1}{2}(k_6 + \tau_2) \left[\frac{1}{2} \sum_{l,j=1; l \neq j}^{3} \left(\frac{\partial w_j}{\partial x_l} + \frac{\partial w_l}{\partial x_j} \right) \left(\frac{\partial w'_j}{\partial x_l} + \frac{\partial w'_l}{\partial x_j} \right) + \frac{1}{3} \sum_{l,j=1}^{3} \left(\frac{\partial w_l}{\partial x_l} - \frac{\partial w_j}{\partial x_j} \right) \left(\frac{\partial w'_l}{\partial x_l} - \frac{\partial w'_j}{\partial x_j} \right) \right]. \quad (4\text{-}15)$$

It is easy to see that $W_{(\mu)}^{(1)} = W^{(1)}$ and $W_{(k_5)}^{(2)} = W^{(2)}$.

Equations (4-5), (4-6), (4-12)–(4-15) and Theorems 4.1 and 4.2 have the following consequences.

Theorem 4.3. *Let $U = (u, w, \theta, \varphi)$ be a regular vector field in Ω^+ and let $U' = (u', w', \theta', \varphi') \in C^1(\Omega^+)$. Suppose $\tau = (\tau_1, \tau_2)$ is an arbitrary vector and set, for $l, j = 1, 2, 3$,*

$$R_{(\tau_1)}(D_x, n) = \left(R_{(\tau_1) lj}(D_x, n)\right)_{3\times 5}, \quad R_{(\tau_1) l4}(D_x, n) = -\beta\, n_l,$$

$$R_{(\tau_1) lj}(D_x, n) = P^{(1)}_{(\tau_1) lj}(D_x, n), \qquad R_{(\tau_1) l5}(D_x, n) = b\, n_l.$$

Then

$$\int_{\Omega^+} \left[(A^{(1)} u - \beta \operatorname{grad} \theta + b \operatorname{grad} \varphi)u' + W^{(1)}_{(\tau_1)}(u, u') + (b\,\varphi - \beta\,\theta) \operatorname{div} u'\right] dx$$
$$= \int_S R_{(\tau_1)}(D_z(n, z))\, v(z)\, u'(z)\, d_z S,$$

$$\int_{\Omega^+} \left[(A^{(2)}(D_x)\, w - k_2 w - k_3 \operatorname{grad} \theta)\, w' + W^{(2)}_{(\tau_2)}(w, w') + (k_2 w + k_3 \operatorname{grad} \theta)\, w'\right] dx$$
$$= \int_S P^{(2)}_{(\tau_2)}(D_z, n(z))w(z)w'(z)\, d_z S. \quad (4\text{-}16)$$

Theorem 4.4. *Let $U = (u, w, \theta, \varphi)$ be a regular vector field in Ω^- and let $U' = (u', w', \theta', \varphi') \in C^1(\Omega^-)$ satisfy (4-9). Then, for $\tau = (\tau_1, \tau_2)$ is an arbitrary vector, we have*

$$\int_{\Omega^-} \left[(A^{(1)} u - \beta \operatorname{grad} \theta + b \operatorname{grad} \varphi)u' + W^{(1)}_{(\tau_1)}(u, u') + (b\,\varphi - \beta\,\theta) \operatorname{div} u'\right] dx$$
$$= -\int_S R_{(\tau_1)}(D_z(n, z))\, v(z)\, u'(z)\, d_z S,$$

$$\int_{\Omega^-} \left[(A^{(2)}(D_x)\, w - k_2 w - k_3 \operatorname{grad} \theta)\, w' + W^{(2)}_{(\tau_2)}(w, w') + (k_2 w + k_3 \operatorname{grad} \theta)\, w'\right] dx$$
$$= -\int_S P^{(2)}_{(\tau_2)}(D_z(n, z))w(z)w'(z)\, d_z S,$$

$$\int_{\Omega^-} \left[(k\Delta\theta + k_1 \operatorname{div} w)\theta' + (k \operatorname{grad} \theta + k_1 w) \operatorname{grad} \theta'\right] dx = -\int_S \left(k\frac{\partial\theta}{\partial n} + k_1 w\, n\right)\theta' d_z S,$$

$$\int_{\Omega^-} \left[(\gamma \Delta \varphi - b \operatorname{div} u - d\ \operatorname{div} w + m\,\theta - \xi\,\varphi)\, \varphi' + (\gamma \operatorname{grad} \varphi - d\, w) \operatorname{grad} \varphi' + (b \operatorname{div} u - m\,\theta + \xi\,\varphi)\, \varphi'\right] dx$$
$$= -\int_S \left(\gamma\frac{\partial\varphi}{\partial n} - d\, w\, n\right)\varphi' d_z S, \quad (4\text{-}17)$$

Theorem 4.5. *Let $U = (u, w, \theta, \varphi)$ be a regular vector field in Ω^+ and let $U' = (u', w', \theta', \varphi') \in C^1(\Omega^+)$. Let $\tau = (\tau_1, \tau_2)$ be an arbitrary vector and set, for $l, j = 1, 2, 3$,*

$$P_{(\tau)}(D_x, n) = \left(P_{(\tau) lj}(D_x, n)\right)_{8\times 8}, \qquad P_{(\tau) lj}(D_x, n) = P^{(1)}_{(\tau_1) lj}(D_x, n),$$

$$P_{(\tau) l+3; j+3}(D_x, n) = P^{(2)}_{(\tau_2) lj}(D_x, n), \qquad P_{(\tau) l7}(D_x, n) = -\beta n_l, \qquad P_{(\tau) l8}(D_x, n) = b\, n_l,$$

$$P_{(\tau) 7; l+3}(D_x, n) = k_1 n_l, \quad P_{(\tau) 77}(D_x, n) = k\frac{\partial}{\partial n}, \quad P_{(\tau) 88}(D_x, n) = \gamma\frac{\partial}{\partial n}, \quad P_{(\tau) 8; l+3}(D_x, n) = -d\, n_l,$$

$$P_{(\tau) l; j+3} = P_{(\tau) l+3; j} = P_{(\tau) l+3; 7} = P_{(\tau) l+3; 8} = P_{(\tau) 7l} = P_{(\tau) 78} = P_{(\tau) 8l} = P_{(\tau) 87} = 0. \quad (4\text{-}18)$$

Then

$$\int_{\Omega^+} \left[A(D_x)\, U(x)\, U'(x) + W_{(\tau)}(U, U') \right] dx = \int_S P_{(\tau)}(D_z, n(z)) U(z) U'(z)\, d_z S.$$

Theorem 4.6. *Let $U = (u, w, \theta, \varphi)$ be a regular vector field in Ω^- and let $U' = (u', w', \theta', \varphi') \in C^1(\Omega^-)$ and U' satisfy (4-9). Then*

$$\int_{\Omega^-} \left[A(D_x)\, U(x)\, U'(x) + W_{(\tau)}(U, U') \right] dx = - \int_S P_{(\tau)}(D_z, n(z))\, U(z)\, U'(z) d_z S,$$

where $\tau = (\tau_1, \tau_2)$ is an arbitrary vector.

In the sequel we use the following two values $\tau^{(1)}$ and $\tau^{(2)}$ of the vector τ:

$$\tau^{(1)} = (\mu, k_5), \qquad \tau^{(2)} = (-\mu, -k_6). \tag{4-19}$$

By virtue of (3-2), (3-3), (4-1), (4-2), it follows from (4-14) and (4-18) that $P_{(\tau^{(1)})} = P$ and $W_{(\tau^{(1)})} = W$.

The operator $P_{(\tau)}(D_z, n)$ will be called *the generalized stress operator* in the linear theory of thermoelasticity with microtemperatures for microstretch solids.

5. Uniqueness theorems

In this section we prove the uniqueness theorems for the internal and external BVPs $(K)_{F,f}^+$ and $(K)_{F,f}^-$, where $K = I, II, \ldots, XII$.

Theorem 5.1. *If the conditions*

$$\mu > 0, \quad 3\lambda + 2\mu > 0, \quad \gamma > 0, \quad (3\lambda + 2\mu)\,\xi > 3b^2, \tag{5-1}$$

$$k > 0, \quad k_6 + k_5 > 0 \quad k_6 - k_5 > 0, \quad 3k_4 + k_5 + k_6 > 0, \quad (k_1 + T_0\, k_3)^2 < 4T_0\, k\, k_2 \tag{5-2}$$

are satisfied, the internal BVP $(K)_{F,f}^+$ admits at most one regular solution, where $K = I, III, IV, V$.

Proof. Suppose that there are two regular solutions of the internal BVP $(K)_{F,f}^+$. Then their difference U corresponds to zero data ($F = f = 0$), i.e., U is a regular solution of problem $(K)_{0,0}^+$, where $K = I, III, IV, V$. If $U = U'$, we obtain from (4-5)–(4-8)

$$\int_{\Omega^+} \left[W^{(1)}(u, u) + (b\,\varphi - \beta\,\theta)\,\mathrm{div}\,u \right] dx = 0, \tag{5-3}$$

$$\int_{\Omega^+} \left[W^{(2)}(w, w) + (k_2 w + k_3\,\mathrm{grad}\,\theta)\,w \right] dx = 0, \tag{5-4}$$

$$\int_{\Omega^+} (k\,\mathrm{grad}\,\theta + k_1 w)\,\mathrm{grad}\,\theta\, dx = 0, \tag{5-5}$$

$$\int_{\Omega^+} \left[(\gamma\,\mathrm{grad}\,\varphi - d\,w)\,\mathrm{grad}\,\varphi + (b\,\mathrm{div}\,u - m\,\theta + \xi\,\varphi)\,\varphi \right] dx = 0. \tag{5-6}$$

Equations (5-4) and (5-5) imply

$$\int_{\Omega^+} \left[T_0\, W^{(2)}(w, w) + \left(T_0\, k_2 |w|^2 + (k_1 + T_0\, k_3) w\,\mathrm{grad}\,\theta + k\,|\mathrm{grad}\,\theta|^2 \right) \right] dx = 0. \tag{5-7}$$

Keeping (5-2) in mind, (4-2) yields

$$W^{(2)}(\boldsymbol{w}, \boldsymbol{w}) \geq 0, \quad T_0\, k_2 |\boldsymbol{w}|^2 + (k_1 + T_0\, k_3)\boldsymbol{w}\, \text{grad}\, \theta + k\, |\text{grad}\, \theta|^2 \geq 0. \tag{5-8}$$

On the basis of (5-8) we obtain from (5-7) $\boldsymbol{w}(\boldsymbol{x}) = \boldsymbol{0}$ and $\theta(\boldsymbol{x}) = \text{const}$, for $\boldsymbol{x} \in \Omega^+$. In view of homogeneous boundary condition $\{\theta(\boldsymbol{z})\}^+ = 0$ it follows that

$$\boldsymbol{w}(\boldsymbol{x}) = \boldsymbol{0} \quad \text{and} \quad \theta(\boldsymbol{x}) = 0 \quad \text{for } \boldsymbol{x} \in \Omega^+. \tag{5-9}$$

By virtue of (5-9) from (5-3) and (5-6) we obtain

$$\int_{\Omega^+} \left[W^{(1)}(\boldsymbol{u}, \boldsymbol{u}) + 2b\, \varphi \, \text{div}\, \boldsymbol{u} + \xi\, |\varphi|^2 + \gamma |\text{grad}\, \varphi|^2\right] d\boldsymbol{x} = 0, \tag{5-10}$$

Keeping (4-2) and (5-1) in mind, (5-10) gives

$$\varphi(\boldsymbol{x}) = 0, \tag{5-11}$$

$$W^{(1)}(\boldsymbol{u}, \boldsymbol{u}) = 0 \quad \text{for } \boldsymbol{x} \in \Omega^+. \tag{5-12}$$

Equations (5-1) and (5-12) show that $\boldsymbol{u}$ is the rigid displacement vector [Ieşan 2004], having the form

$$\boldsymbol{u}(\boldsymbol{x}) = \boldsymbol{a}' + [\boldsymbol{a}'' \times \boldsymbol{x}], \tag{5-13}$$

where $\boldsymbol{a}'$ and $\boldsymbol{a}''$ are arbitrary real constant three-component vectors and $[\boldsymbol{a}'' \times \boldsymbol{x}]$ is the vector product of $\boldsymbol{a}''$ and $\boldsymbol{x}$. Keeping in mind the homogeneous boundary condition $\{\boldsymbol{u}(\boldsymbol{z})\}^+ = \boldsymbol{0}$ from (5-13) we have $\boldsymbol{u}(\boldsymbol{x}) = \boldsymbol{0}$ for $\boldsymbol{x} \in \Omega^+$. In view of (5-9) and (5-11) we get $\boldsymbol{U}(\boldsymbol{x}) = \boldsymbol{0}$ for $\boldsymbol{x} \in \Omega^+$. Hence, the uniqueness of the solution of BVP $(K)^+_{F,f}$ is proved, where $K = I, III, IV, V$. $\qquad\square$

Theorem 5.1 leads to:

Theorem 5.2. *If the conditions* (5-1) *and* (5-2) *are satisfied, then any two regular solutions of the BVP* $(K)^+_{F,f}$, $K = VI, VII, VIII, IX$, *differ only by an additive vector* $\boldsymbol{U} = (\boldsymbol{u}, \boldsymbol{w}, \theta, \varphi)$, *where*

$$\boldsymbol{u}(\boldsymbol{x}) = \boldsymbol{a}' + [\boldsymbol{a}'' \times \boldsymbol{x}], \quad \boldsymbol{w}(\boldsymbol{x}) = \boldsymbol{0}, \quad \theta(\boldsymbol{x}) = \varphi(\boldsymbol{x}) = 0 \quad \text{for } \boldsymbol{x} \in \Omega^+,$$

$\boldsymbol{a}'$ *and* $\boldsymbol{a}''$ *being arbitrary real constant three-component vectors.*

Theorem 5.3. *If the conditions* (5-1) *and* (5-2) *are satisfied, then any two regular solutions of the BVP* $(K)^+_{F,f}$, $K = II, X$, *differ only by an additive vector* $\boldsymbol{U} = (\boldsymbol{u}, \boldsymbol{w}, \theta, \varphi)$, *where*

$$\boldsymbol{u}(\boldsymbol{x}) = \boldsymbol{a}' + [\boldsymbol{a}'' \times \boldsymbol{x}] + d_1 \boldsymbol{x}, \quad \boldsymbol{w}(\boldsymbol{x}) = \boldsymbol{0}, \quad \theta(\boldsymbol{x}) = c_1, \quad \varphi(\boldsymbol{x}) = d_2 \quad \text{for } \boldsymbol{x} \in \Omega^+, \tag{5-14}$$

$\boldsymbol{a}'$ *and* $\boldsymbol{a}''$ *being arbitrary real constant three-component vectors,* c_1 *an arbitrary real constant,*

$$d_1 = \frac{\beta\, \xi - b\, m}{(3\lambda + 2\mu)\xi - 3b^2}\, c_1, \quad \text{and} \quad d_2 = \frac{(3\lambda + 2\mu)m - 3b\beta}{(3\lambda + 2\mu)\xi - 3b^2}\, c_1.$$

Proof. The difference $\boldsymbol{U}$ between two regular solutions of the BVP $(K)^+_{F,f}$ is a regular solution of the homogeneous BVP $(K)^+_{0,0}$, where $K = II, X$. It may be shown similarly that

$$\boldsymbol{w}(\boldsymbol{x}) = \boldsymbol{0}, \quad \theta(\boldsymbol{x}) = c_1, \quad \text{for } \boldsymbol{x} \in \Omega^+, \tag{5-15}$$

where c_1 is an arbitrary real constant. On the basis of (5-16) the vector $(\boldsymbol{u}, \varphi)$ is a regular solution in Ω^+ of the nonhomogeneous system

$$
\begin{aligned}
\mu \, \Delta \boldsymbol{u} + (\lambda + \mu) \operatorname{grad} \operatorname{div} \boldsymbol{u} + b \operatorname{grad} \varphi &= \boldsymbol{0}, \\
(\gamma \Delta - \xi) \, \varphi - b \operatorname{div} \boldsymbol{u} &= -m \, c_1,
\end{aligned}
\tag{5-16}
$$

satisfying the nonhomogeneous boundary condition

$$
\left\{ \boldsymbol{P}^{(1)}(\boldsymbol{D}_z, \boldsymbol{n}) \boldsymbol{u}(z) + b \varphi \, \boldsymbol{n} \right\}^+ = c_1 \beta \, \boldsymbol{n}(z), \quad \left\{ \frac{\partial \varphi(z)}{\partial \boldsymbol{n}(z)} \right\}^+ = 0 \qquad \text{for } z \in S. \tag{5-17}
$$

We introduce the notation

$$
\tilde{\boldsymbol{u}}(\boldsymbol{x}) = \boldsymbol{u}(\boldsymbol{x}) - d_1 \, \boldsymbol{x}, \quad \tilde{\varphi}(\boldsymbol{x}) = \varphi(\boldsymbol{x}) - d_2. \tag{5-18}
$$

Thanks to (5-17), (5-18), and the equalities $3b \, d_1 + \xi \, d_2 = m c_1$, $(3\lambda + 2\mu) \, d_1 + b \, d_2 = \beta \, c_1$, the vector $(\tilde{\boldsymbol{u}}, \tilde{\varphi})$ is the regular solution of the homogeneous BVP

$$
\begin{aligned}
\mu \, \Delta \tilde{\boldsymbol{u}}(\boldsymbol{x}) + (\lambda + \mu) \operatorname{grad} \operatorname{div} \tilde{\boldsymbol{u}}(\boldsymbol{x}) + b \operatorname{grad} \tilde{\varphi}(\boldsymbol{x}) &= \boldsymbol{0}, \\
(\gamma \Delta - \xi) \, \tilde{\varphi}(\boldsymbol{x}) - b \operatorname{div} \tilde{\boldsymbol{u}}(\boldsymbol{x}) &= 0, \\
\left\{ \boldsymbol{P}^{(1)}(\boldsymbol{D}_z, \boldsymbol{n}) \tilde{\boldsymbol{u}}(z) + b \, \tilde{\varphi} \, \boldsymbol{n} \right\}^+ = \boldsymbol{0}, \quad \left\{ \frac{\partial \tilde{\varphi}(z)}{\partial \boldsymbol{n}(z)} \right\}^+ &= 0
\end{aligned}
\tag{5-19}
$$

for $\boldsymbol{x} \in \Omega^+$ and $z \in S$. It is easily to see that the Green's formulae for $\tilde{\boldsymbol{u}}$ and $\tilde{\varphi}$ have the form

$$
\begin{aligned}
\int_{\Omega^+} \left[(A^{(1)} \, \tilde{\boldsymbol{u}} + b \operatorname{grad} \tilde{\varphi}) \tilde{\boldsymbol{u}} + W^{(1)}(\tilde{\boldsymbol{u}}, \tilde{\boldsymbol{u}}) + b \, \tilde{\varphi} \operatorname{div} \tilde{\boldsymbol{u}} \right] d\boldsymbol{x} &= \int_S \left[\boldsymbol{P}^{(1)}(\boldsymbol{D}_z, \boldsymbol{n}) + b \tilde{\varphi} \, \boldsymbol{n} \right] \tilde{\boldsymbol{u}} \, d_z S, \\
\int_{\Omega^+} \left[\left((\gamma \Delta - \xi) \, \tilde{\varphi} - b \operatorname{div} \tilde{\boldsymbol{u}} \right) \tilde{\varphi} + \left(\gamma \, |\operatorname{grad} \tilde{\varphi}|^2 + \xi \, |\tilde{\varphi}|^2 + b \, \tilde{\varphi} \operatorname{div} \tilde{\boldsymbol{u}} \right) \right] d\boldsymbol{x} &= \gamma \int_S \frac{\partial \tilde{\varphi}}{\partial \boldsymbol{n}} \, \tilde{\varphi} \, d_z S.
\end{aligned}
\tag{5-20}
$$

Keeping in mind (5-19) from (5-20) we obtain

$$
\int_{\Omega^+} \left[W^{(1)}(\tilde{\boldsymbol{u}}, \tilde{\boldsymbol{u}}) + 2 \, b \, \tilde{\varphi} \operatorname{div} \tilde{\boldsymbol{u}} + \xi \, |\tilde{\varphi}|^2 + \gamma \, |\operatorname{grad} \tilde{\varphi}|^2 \right] d\boldsymbol{x} = 0. \tag{5-21}
$$

On account of (5-1) from (5-21) it follows that

$$
\tilde{\boldsymbol{u}}(\boldsymbol{x}) = \boldsymbol{a}' + [\boldsymbol{a}'' \times \boldsymbol{x}] \quad \text{and} \quad \tilde{\varphi}(\boldsymbol{x}) = 0 \quad \text{for } \boldsymbol{x} \in \Omega^+, \tag{5-22}
$$

where $\boldsymbol{a}'$ and $\boldsymbol{a}''$ are arbitrary real constant three-component vectors. Using (5-15), (5-18) and (5-22) we get (5-14). Hence, the theorem is proved. $\qquad \square$

Theorem 5.3 leads to:

Theorem 5.4. *If the conditions* (5-1) *and* (5-2) *are satisfied, any two regular solutions of the BVP* $(K)_{F,f}^+$, $K = XI, XII$, *differ only by additive vector* $\boldsymbol{U} = (\boldsymbol{u}, \boldsymbol{w}, \theta, \varphi)$, *where*

$$
\boldsymbol{u}(\boldsymbol{x}) = \boldsymbol{w}(\boldsymbol{x}) = \boldsymbol{0}, \quad \theta(\boldsymbol{x}) = c_1, \quad \varphi(\boldsymbol{x}) = d_3 \qquad \text{for } \boldsymbol{x} \in \Omega^+, \tag{5-23}
$$

c_1 *is an arbitrary real constant, and* $d_3 = m \, c_1 / \xi$.

Now let us establish the uniqueness of regular solutions of the external BVPs.

Theorem 5.5. *If conditions* (5-1) *and* (5-2) *are satisfied, then the external BVP* $(K)_{F,f}^-$ *admits at most one regular solution, where* $K = I, II, \ldots, XII.$

Proof. Suppose that there are two regular solutions of the external BVP $(K)_{F,f}^-$, where $K = I, II, \ldots, XII.$ Then their difference U corresponds to zero data ($F = f = 0$), i.e., U is a regular solution of problem $(K)_{0,0}^-$.

In a similar way as in the proof of Theorem 4.4 we obtain

$$\int_{\Omega^-} \left[W^{(1)}(u, u) + (b\,\varphi - \beta\,\theta)\,\mathrm{div}\,u \right] dx = 0, \tag{5-24}$$

$$\int_{\Omega^-} \left[W^{(2)}(w, w) + (k_2 w + k_3\,\mathrm{grad}\,\theta)\,w \right] dx = 0, \tag{5-25}$$

$$\int_{\Omega^-} (k\,\mathrm{grad}\,\theta + k_1 w)\,\mathrm{grad}\,\theta\,dx = 0, \tag{5-26}$$

$$\int_{\Omega^-} \left[(\gamma\,\mathrm{grad}\,\varphi - d\,w)\,\mathrm{grad}\,\varphi + (b\,\mathrm{div}\,u - m\,\theta + \xi\,\varphi)\,\varphi \right] dx = 0. \tag{5-27}$$

Equations (5-25) and (5-26) imply $w(x) = 0$ and $\theta(x) = \mathrm{const}$, for $x \in \Omega^-$. In view of condition (3-1) we get $\theta(x) = 0$ for $x \in \Omega^-$; hence,

$$w(x) = 0 \quad \text{and} \quad \theta(x) = 0 \qquad \text{for } x \in \Omega^-. \tag{5-28}$$

Taking (5-28) into account, (5-24) and (5-27) yield

$$\int_{\Omega^-} \left[W^{(1)}(u, u) + 2b\,\varphi\,\mathrm{div}\,u + \xi\,|\varphi|^2 + \gamma|\mathrm{grad}\,\varphi|^2 \right] dx = 0. \tag{5-29}$$

Keeping in mind (3-1) and (5-1) from Eq. (5-29) we have

$$u(x) = 0 \quad \text{and} \quad \varphi(x) = 0 \qquad \text{for } x \in \Omega^-, \tag{5-30}$$

and in view of (5-28) we get $U(x) = 0$ for $x \in \Omega^-$, as desired. $\qquad\square$

6. Uniqueness theorems under weak conditions

In this section we use Theorems 4.3 and 4.4 to prove the uniqueness of regular solutions of the problems $(I)_{F,f}^+$ and $(I)_{F,f}^-$ under weaker conditions that (5-1) and (5-2).

Theorem 6.1. *If the conditions*

$$\mu > 0, \quad \lambda + 2\mu > 0, \quad \gamma > 0, \quad (\lambda + 2\mu)\,\xi > b^2, \tag{6-1}$$

$$k > 0, \quad k_6 > 0, \quad k_7 > 0, \quad (k_1 + T_0 k_3)^2 < 4T_0 k k_2 \tag{6-2}$$

are satisfied, the internal BVP $(K)_{F,f}^+$ *admits at most one regular solution, where* $k_7 = k_4 + k_5 + k_6$ *and* $K = I, IV.$

Proof. Suppose that there are two regular solutions of problem $(K)_{F,f}^+$. Their difference U is a regular solution of problem $(K)_{0,0}^+$, where $K = I, IV$. If $U = U'$ and $\tau = \tau^{(2)}$ (see (4-19)), it follows from (4-7),

(4-8), (4-15), and (4-16) that

$$\int_{\Omega^+} \left[W^{(1)}_{(-\mu)}(\boldsymbol{u}, \boldsymbol{u}) + (b\,\varphi - \beta\,\theta)\,\mathrm{div}\,\boldsymbol{u} \right] d\boldsymbol{x} = 0, \tag{6-3}$$

$$\int_{\Omega^+} \left[W^{(2)}_{(-k_6)}(\boldsymbol{w}, \boldsymbol{w}) + (k_2 \boldsymbol{w} + k_3 \mathrm{grad}\,\theta)\ \boldsymbol{w} \right] d\boldsymbol{x} = 0, \tag{6-4}$$

$$\int_{\Omega^+} \left[k\,|\mathrm{grad}\,\theta|^2 + k_1 \boldsymbol{w}\,\mathrm{grad}\,\theta \right] d\boldsymbol{x} = 0, \tag{6-5}$$

$$\int_{\Omega^+} \left[\gamma\,|\mathrm{grad}\,\varphi|^2 - d\,\boldsymbol{w}\mathrm{grad}\,\varphi + b\,\varphi\,\mathrm{div}\,\boldsymbol{u} - m\,\theta\,\varphi + \xi\,|\varphi|^2 \right] d\boldsymbol{x} = 0, \tag{6-6}$$

where

$$W^{(1)}_{(-\mu)}(\boldsymbol{u}, \boldsymbol{u}) = (\lambda + 2\mu)\,|\mathrm{div}\,\boldsymbol{u}|^2 + \mu\,|\mathrm{curl}\,\boldsymbol{u}|^2, \quad W^{(2)}_{(-k_6)}(\boldsymbol{w}, \boldsymbol{w}) = k_7\,|\mathrm{div}\,\boldsymbol{w}|^2 + k_6\,|\mathrm{curl}\,\boldsymbol{w}|^2.$$

From (6-4) and (6-5) it follows that

$$\int_{\Omega^+} \left[T_0\,W^{(2)}_{(-k_6)}(\boldsymbol{w}, \boldsymbol{w}) + \left(T_0\,k_2|\boldsymbol{w}|^2 + (k_1 + T_0\,k_3)\boldsymbol{w}\,\mathrm{grad}\,\theta\ + k\,|\mathrm{grad}\,\theta|^2 \right) \right] d\boldsymbol{x} = 0. \tag{6-7}$$

Keeping in mind (6-2), we have from (6-7)

$$\boldsymbol{w}(\boldsymbol{x}) = \boldsymbol{0}, \quad \theta(\boldsymbol{x}) = \mathrm{const} \quad \text{for } \boldsymbol{x} \in \Omega^+.$$

By the homogeneous boundary condition we get $\theta(\boldsymbol{x}) = 0$ for $\boldsymbol{x} \in \Omega^+$, and from (6-3) and (6-6) we get

$$\int_{\Omega^+} \left[\mu\,|\mathrm{curl}\,\boldsymbol{u}|^2 + (\lambda + 2\mu)\,|\mathrm{div}\,\boldsymbol{u}|^2 + 2b\,\varphi\,\mathrm{div}\,\boldsymbol{u} + \xi\,|\varphi|^2 + \gamma\,|\mathrm{grad}\,\varphi|^2 \right] d\boldsymbol{x} = 0. \tag{6-8}$$

By (6-1) from (6-8) we obtain $\varphi(\boldsymbol{x}) = 0$, $\mathrm{div}\,\boldsymbol{u}(\boldsymbol{x}) = 0$, $\mathrm{curl}\,\boldsymbol{u}(\boldsymbol{x}) = \boldsymbol{0}$ for $\boldsymbol{x} \in \Omega^+$. Hence, $\boldsymbol{u}$ is a regular solution of the BVP

$$\Delta\,\boldsymbol{u}(\boldsymbol{x}) = \boldsymbol{0}, \quad \{\boldsymbol{u}(\boldsymbol{z})\}^+ = \boldsymbol{0} \quad \text{for } \boldsymbol{x} \in \Omega^+,\ \boldsymbol{z} \in S. \tag{6-9}$$

This implies $\boldsymbol{u}(\boldsymbol{x}) = \boldsymbol{0}$ for $\boldsymbol{x} \in \Omega^+$, as needed. $\qquad\square$

Theorem 6.2. *If the conditions* (6-1) *and* (6-2) *are satisfied, any two regular solutions of the BVP* $(XI)^+_{F,f}$ *may differ only by an additive vector* $\boldsymbol{U} = (\boldsymbol{u}, \boldsymbol{w}, \theta, \varphi)$, *where* $\boldsymbol{U}$ *is given by* (5-23), c_1 *is an arbitrary real constant and* d_3 *is defined in Theorem 5.4.*

Proof. The difference $\boldsymbol{U}$ between two regular solutions of the BVP $(XI)^+_{F,f}$ is a regular solution of the homogeneous BVP $(XI)^+_{0,0}$. Using Green's formula (4-16) and (6-2), we can show as above that

$$\boldsymbol{w}(\boldsymbol{x}) = \boldsymbol{0} \quad \text{and} \quad \theta(\boldsymbol{x}) = c_1 \qquad \text{for } \boldsymbol{x} \in \Omega^+,$$

and the vector function $\boldsymbol{u}$ and function φ from a regular solution in Ω^+ of the nonhomogeneous system

$$\mu\,\Delta\boldsymbol{u} + (\lambda + \mu)\,\mathrm{grad}\,\mathrm{div}\,\boldsymbol{u} + b\,\mathrm{grad}\,\varphi = \boldsymbol{0},$$

$$(\gamma\,\Delta - \xi)\,\varphi - b\,\mathrm{div}\,\boldsymbol{u} = -m\,c_1,$$

satisfying the homogeneous boundary condition

$$\{\boldsymbol{u}(\boldsymbol{z})\}^+ = 0, \quad \left\{ \frac{\partial\,\varphi(\boldsymbol{z})}{\partial\,\boldsymbol{n}(\boldsymbol{z})} \right\}^+ = 0 \qquad \text{for } \boldsymbol{z} \in S,$$

where c_1 is an arbitrary real constant. If we introduce

$$\tilde{\varphi}(x) = \varphi(x) - d_3, \tag{6-10}$$

the vector $(u, \tilde{\varphi})$ is then a regular solution of the homogeneous BVP

$$\mu \, \Delta u(x) + (\lambda + \mu) \operatorname{grad} \operatorname{div} u(x) + b \operatorname{grad} \tilde{\varphi}(x) = \mathbf{0},$$

$$(\gamma \Delta - \xi) \, \tilde{\varphi}(x) - b \operatorname{div} u(x) = 0, \quad \{u(z)\}^{+} = \mathbf{0}, \quad \left\{ \frac{\partial \tilde{\varphi}(z)}{\partial n(z)} \right\}^{+} = 0 \tag{6-11}$$

for $x \in \Omega^{+}$ and $z \in S$. It is easily to see that by virtue of (6-11) the Green's formulas (4-8) and (4-16) for u and $\tilde{\varphi}$ take on the form

$$\int_{\Omega^{+}} \left[W^{(1)}_{(-\mu)}(u, u) + b \, \tilde{\varphi} \operatorname{div} u \right] dx = 0, \quad \int_{\Omega^{+}} \left[\left(\gamma |\operatorname{grad} \tilde{\varphi}|^{2} + \xi \, |\tilde{\varphi}|^{2} + b \, \tilde{\varphi} \operatorname{div} u \right) \right] dx = 0, \tag{6-12}$$

and on the basis of (6-7) we obtain from (6-12)

$$\int_{\Omega^{+}} \left[(\lambda + 2\mu) \, |\operatorname{div} u|^{2} + 2 \, b \, \tilde{\varphi} \operatorname{div} u + \xi \, |\tilde{\varphi}|^{2} + \mu \, |\operatorname{curl} u|^{2} + \gamma |\operatorname{grad} \tilde{\varphi}|^{2} \right] dx = 0. \tag{6-13}$$

Taking (6-1) into account, (6-13) implies that

$$u(x) = a' + [a'' \times x] \quad \text{and} \quad \tilde{\varphi}(x) = 0 \qquad \text{for } x \in \Omega^{+}, \tag{6-14}$$

where a' and a'' are arbitrary real constant three-component vectors. Using the homogeneous boundary condition (6-11), we obtain from (6-14) that $u(x) = \mathbf{0}$ for $x \in \Omega^{+}$, and using (6-14) we get from (6-10) that $\varphi(x) = d_3$ for $x \in \Omega^{+}$, as needed. $\square$

Theorem 6.3. *If conditions* (6-1) *and* (6-2) *are satisfied, the external BVP* $(K)^{-}_{F,f}$ *admit at most one regular solution, where* $K = I, II, XI$.

Proof. Suppose that there are two regular solutions of problem $(K)^{-}_{F,f}$. Their difference U is a regular solution of problem $(K)^{-}_{0,0}$, where $K = I, II, XI$. If $U = U'$ and $\tau = \tau^{(2)}$, we have from (4-17) and (4-19)

$$\int_{\Omega^{-}} \left[W^{(1)}_{(-\mu)}(u, u) + (b \, \varphi - \beta \, \theta) \operatorname{div} u \right] dx = 0,$$

$$\int_{\Omega^{-}} \left[T_0 \, W^{(2)}_{(-k_6)}(w, w) + \left(T_0 \, k_2 |w|^{2} + (k_1 + T_0 \, k_3) w \operatorname{grad} \theta \ + k \, |\operatorname{grad} \theta|^{2} \right) \right] dx = 0, \tag{6-15}$$

$$\int_{\Omega^{-}} \left[\gamma |\operatorname{grad} \varphi|^{2} - d \, w \operatorname{grad} \varphi + b \, \varphi \operatorname{div} u - m \, \theta \, \varphi + \xi \, |\varphi|^{2} \right] dx = 0.$$

Similarly, taking (3-1), (6-1), and (6-2) into account, we obtain from (6-15) that $w(x) = \mathbf{0}$, $\theta(x) = \varphi(x) = 0$, $\operatorname{div} u(x) = 0$, and $\operatorname{curl} u(x) = \mathbf{0}$ for $x \in \Omega^{-}$. Hence, u is regular solution of the BVP

$$\Delta \, u(x) = \mathbf{0}, \quad \{u(z)\}^{-} = \mathbf{0} \qquad \text{for } x \in \Omega^{-}, \, z \in S. \tag{6-16}$$

Therefore (6-16) shows that $u(x) = \mathbf{0}$ for $x \in \Omega^{-}$. $\square$

Remark 6.4. From (5-1) and (5-2) we have (6-1) and (6-2), respectively. Indeed, (5-1) and (5-2) imply

$$\lambda + 2\mu = \tfrac{1}{3} \big((3\lambda + 2\mu) + 4\mu \big) > 0, \quad k_6 = \tfrac{1}{2} \big((k_6 + k_5) + (k_6 - k_5) \big) > 0, \quad k_7 = \tfrac{1}{3} \big((3k_4 + k_5 + k_6) + 2(k_6 + k_5) \big) > 0.$$

7. Concluding remarks

(1) In [Knops and Payne 1971], the uniqueness theorems of the first BVP (on the boundary given the displacement vector) and the second BVP (on the boundary given the stress vector) in the classical theory of elasticity are proved under the conditions $\mu > 0$, $\lambda + 2\mu > 0$ and $\mu > 0$, $3\lambda + 2\mu > 0$, respectively.

(2) Using the uniqueness Theorems 5.1–5.4 and 6.1–6.3 it is possible to prove the existence theorems in the equilibrium theory of thermoelasticity with microtemperatures for microstretch solids by means of the potential method and the theory of singular integral equations.

(3) The conditions (5-1), (5-2) and (6-1), (6-2) are sufficient for the uniqueness of solutions of BVPs in the theory of equilibrium thermoelasticity with microtemperatures for microstretch solids occupying arbitrary 3D domains with a smooth surface. Establishing necessary conditions for the uniqueness of solutions is an open problem in the classical theory of thermoelasticity [Kupradze et al. 1979], the theory of thermoelasticity with microtemperatures [Ieşan and Quintanilla 2000], the micropolar theory of thermoelasticity, theories of micromorphic elasticity and thermomicrostretch elastic solid [Eringen 1999], and in the theory of thermoelasticity with microtemperatures for microstretch solids [Ieşan 2001]. The necessary condition for uniqueness of solutions have been established only in the classical theory of elasticity (see [Knops and Payne 1971; Fosdick et al. 2007], for details).

References

[Aouadi 2008] M. Aouadi, "Some theorems in the isotropic theory of microstretch thermoelasticity with microtemperatures", *J. Thermal Stresses* **31**:7 (2008), 649–662.

[Casas and Quintanilla 2005] P. S. Casas and R. Quintanilla, "Exponential stability in thermoelasticity with microtemperatures", *Internat. J. Engrg. Sci.* **43**:1-2 (2005), 33–47.

[Eringen 1999] A. C. Eringen, *Microcontinuum field theories, I: Foundations and solids*, Springer, New York, 1999.

[Fosdick et al. 2007] R. Fosdick, M. D. Piccioni, and G. Puglisi, "A note on uniqueness in linear elastostatics", *J. Elasticity* **88**:1 (2007), 79–86.

[Grot 1969] R. Grot, "Thermodynamics of a continuum with microstructure", *Int. J. Eng. Sci.* **7**:8 (1969), 801–814.

[Ieşan 2007] D. Ieşan, "Thermoelasticity of bodies with microstructure and microtemperatures", *Int. J. Solids Struc.* **44**:25-26 (2007), 8648–8662.

[Ieşan and Quintanilla 2000] D. Ieşan and R. Quintanilla, "On a theory of thermoelasticity with microtemperatures", *J. Thermal Stresses* **23**:3 (2000), 199–215.

[Ieşan and Scalia 2010] D. Ieşan and A. Scalia, "Plane deformation of elastic bodies with microtemperatures", *Mech. Res. Commun.* **37**:7 (2010), 617–621.

[Ieşan 2001] D. Ieşan, "On a theory of micromorphic elastic solids with microtemperatures", *J. Thermal Stresses* **24**:8 (2001), 737–752.

[Ieşan 2002] D. Ieşan, "On the theory of heat conduction in micromorphic continua", *Internat. J. Engrg. Sci.* **40**:16 (2002), 1859–1878.

[Ieşan 2004] D. Ieşan, *Thermoelastic models of continua*, Solid Mechanics and its Applications **118**, Kluwer, Dordrecht, 2004.

[Ieşan and Quintanilla 2009] D. Ieşan and R. Quintanilla, "On thermoelastic bodies with inner structure and microtemperatures", *J. Math. Anal. Appl.* **354**:1 (2009), 12–23.

[Knops and Payne 1971] R. J. Knops and L. E. Payne, *Uniqueness theorems in linear elasticity*, Springer Tracts in Natural Philosophy **19**, Springer, New York, 1971.

[Kupradze et al. 1979] V. D. Kupradze, T. G. Gegelia, M. O. Basheleĭshvili, and T. V. Burchuladze, *Three-dimensional problems of the mathematical theory of elasticity and thermoelasticity*, Applied Mathematics and Mechanics **25**, North-Holland, Amsterdam, 1979.

[Quintanilla 2009] R. Quintanilla, "Uniqueness in thermoelasticity of porous media with microtemperatures", *Arch. Mech. (Arch. Mech. Stos.)* **61**:5 (2009), 371–382.

[Riha 1975] P. Riha, "On the theory of heat-conducting micropolar fluids with microtemperatures", *Acta Mech.* **23**:1-2 (1975), 1–8.

[Riha 1976] P. Riha, "On the microcontinuum model of heat conduction in materials with inner structure", *Int. J. Eng. Sci.* **14**:6 (1976), 529–535.

[Scalia and Svanadze 2006] A. Scalia and M. Svanadze, "On the representations of solutions of the theory of thermoelasticity with microtemperatures", *J. Thermal Stresses* **29**:9 (2006), 849–863.

[Scalia and Svanadze 2009a] A. Scalia and M. Svanadze, "On the linear theory of thermoelasticity with microtemperatures", pp. 465–468 in *Proc. 8th Internat. Congress on Thermal Stresses*, vol. II, 2009.

[Scalia and Svanadze 2009b] A. Scalia and M. Svanadze, "Potential method in the linear theory of thermoelasticity with microtemperatures", *J. Thermal Stresses* **32**:10 (2009), 1024–1042.

[Scalia et al. 2010] A. Scalia, M. Svanadze, and R. Tracinà, "Basic theorems in the equilibrium theory of thermoelasticity with microtemperatures", *J. Thermal Stresses* **33**:8 (2010), 721–753.

[Svanadze 2003] M. Svanadze, "Boundary value problems of the theory of thermoelasticity with microtemperatures", *Proc. Appl. Math. Mech.* **3**:1 (2003), 188–189.

[Svanadze 2004a] M. Svanadze, "Fundamental solutions in the theory of micromorphic elastic solids with microtemperatures", *J. Thermal Stresses* **27**:4 (2004), 345–366.

[Svanadze 2004b] M. Svanadze, "Fundamental solutions of the equations of the theory of thermoelasticity with microtemperatures", *J. Thermal Stresses* **27**:2 (2004), 151–170.

[Svanadze and Tracinà 2011] M. Svanadze and R. Tracinà, "Representations of solutions in the theory of thermoelasticity with microtemperatures for microstretch solids", *J. Thermal Stresses* **34**:2 (2011), 161–178.

ANTONIO SCALIA: scalia@dmi.unict.it
Dipartimento di Matematica e Informatica, Università di Catania, Viale Andrea Doria 6, I-95125 Catania, Italy

MERAB SVANADZE: svanadze@iliauni.edu.ge
Institute for Fundamental and Interdisciplinary Mathematics Research, Ilia State University, K. Cholokashvili Ave. 3/5, 0162 Tbilisi, Georgia

∎msp

IMPLICATIONS OF SHAKEDOWN FOR DESIGN OF ACTIVELY COOLED THERMOSTRUCTURAL PANELS

Natasha Vermaak, Lorenzo Valdevit, Anthony G. Evans,
Frank W. Zok and Robert M. McMeeking

Propulsion systems in future hypersonic vehicles will require use of actively cooled structures that can withstand extreme thermomechanical loads. Candidate designs and materials for such structures have previously been identified through conventional yield-based design principles. The present article outlines an approach that utilizes concepts of localized plasticity and shakedown under cyclic loading in the design process. For this purpose, an established computational technique is used to determine shakedown limits for prototypical cooled structures. The results are employed in a design sensitivity study. The study demonstrates that, by allowing for shakedown, structures with areal densities significantly lower than those obtained from yield-limited design can be obtained. The magnitude of the benefits depends on the specific geometry of interest, the thermomechanical boundary conditions and the constraints placed on the design.

1. Introduction

The operating conditions of scramjet engines require use of lightweight materials that can withstand extreme heat fluxes and structural loads. They also demand designs that incorporate active cooling by the fuel. Previous studies on the design of thermostructural panels for scramjet engine liners have been based on established yield-limited design principles, i.e., with allowable stresses up to (but not exceeding) that required for yielding at the most critically stressed point in the structure [Heiser and Pratt 1994; Buchmann 1979; Scotti et al. 1988; Youn and Mills 1995; Flieder et al. 1971; Valdevit et al. 2008]. Building upon this body of work, the present study integrates concepts of local plasticity and thermomechanical shakedown into the design strategy. The objective is to reduce the structural weight. The rationale is that allowing the stresses to locally exceed the yield strength of the material upon the first few cycles, with fully elastic response thereafter (shakedown), can result in substantially lighter designs. For this purpose, a simplified technique [Abdalla et al. 2007] is used to conduct numerical Bree-like analysis [Bree 1967] of prospective geometries and determine shakedown limits, defined by critical combinations of thermal and mechanical stresses. The geometries selected for numerical analysis are obtained from previous optimizations based on yield-limited design [Valdevit et al. 2008]. The numerical analysis is used in combination with analytical models for stress and temperature predictions to identify designs that yield structures that are lighter than those found by yield-limited optimization yet lie within the shakedown regime.

Figure 1, left, depicts the notional combustor liner of present interest. The liner consists of four panels, three of which are shown in a rectangular configuration in the figure; each panel has rectangular cooling
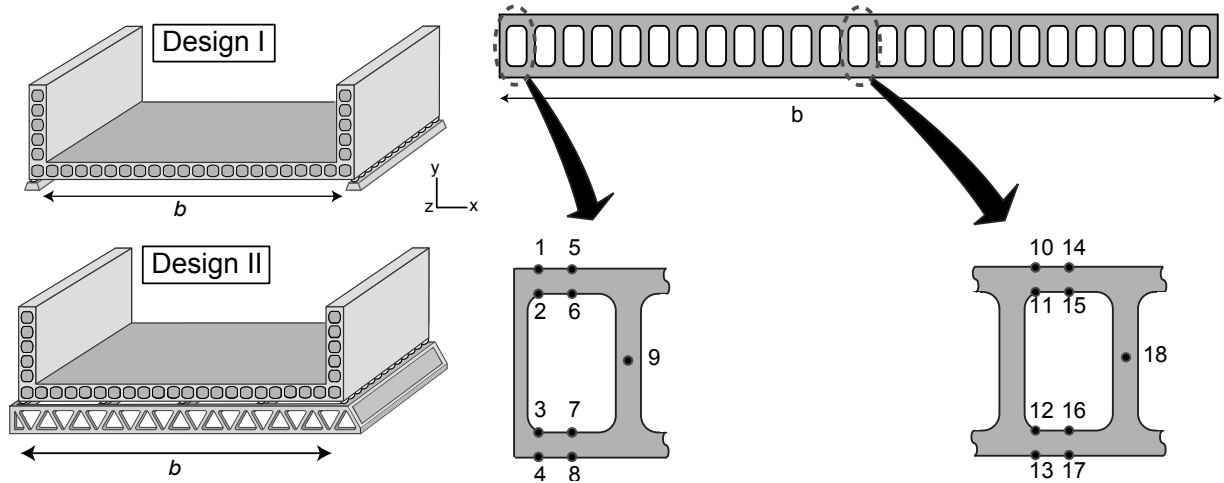
Figure 1. Left: notional design of scramjet engine liner. The two designs are distinguished by the nature of the underlying structure: either periodic linear supports or continuous panel. Both are assumed to be connected to the liner via rollers, thereby allowing unconstrained lateral thermal expansion. Right: cross-section through the liner and the locations of the 18 points most susceptible to yielding and monitored in the optimization code.

channels. The principal mechanical loads are those due to the internal pressure of the cooling fuel and the external pressure from the combustion gas. The dominant thermal loads arise from temperature gradients across the panel, subject to mechanical constraints imposed by the external boundaries (detailed in Section 3.) [Vermaak et al. 2010]. These loads and the pertinent structural dimensions are summarized in Figure 2.
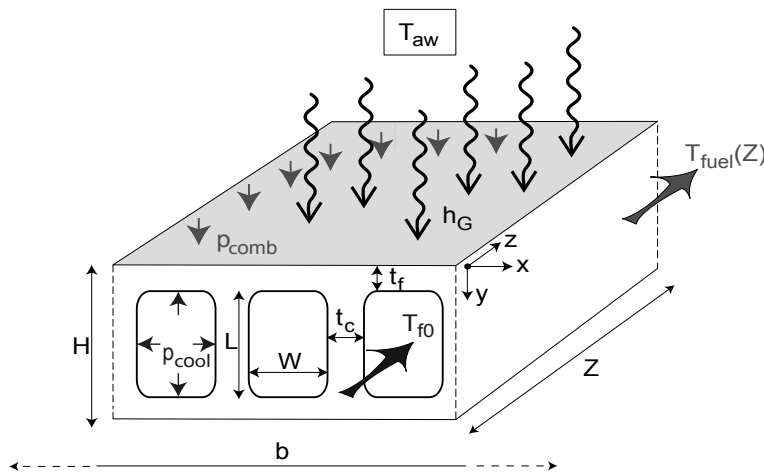

Figure 2. Schematic defining the geometry of the actively cooled panel, the pertinent dimensions, and the thermal and mechanical loads.

The article is organized as follows. First, the technique used to numerically determine shakedown limits is presented. Next, the use of the technique in the construction of a Bree diagram for a prototypical geometry is demonstrated. The results of a series of such computations are then used to identify optimal designs (with minimum mass) and their mass compared with those obtained through yield-limited optimizations. The weight benefits imparted by extending the design from yield-limited to shakedown-limited are computed for two types of external boundary conditions on the panel.

2. Construction of Bree diagrams

The classic problem. Bree diagrams [Bree 1967] have been used extensively in the nuclear pressure vessel industry to delineate the boundaries between various elastoplastic regimes. In the classic Bree problem, a thin-walled cylinder of an elastic, perfectly plastic material (see inset in Figure 3) is subjected to a fixed internal pressure, P, and a cyclic radial temperature difference ΔT between the inside and
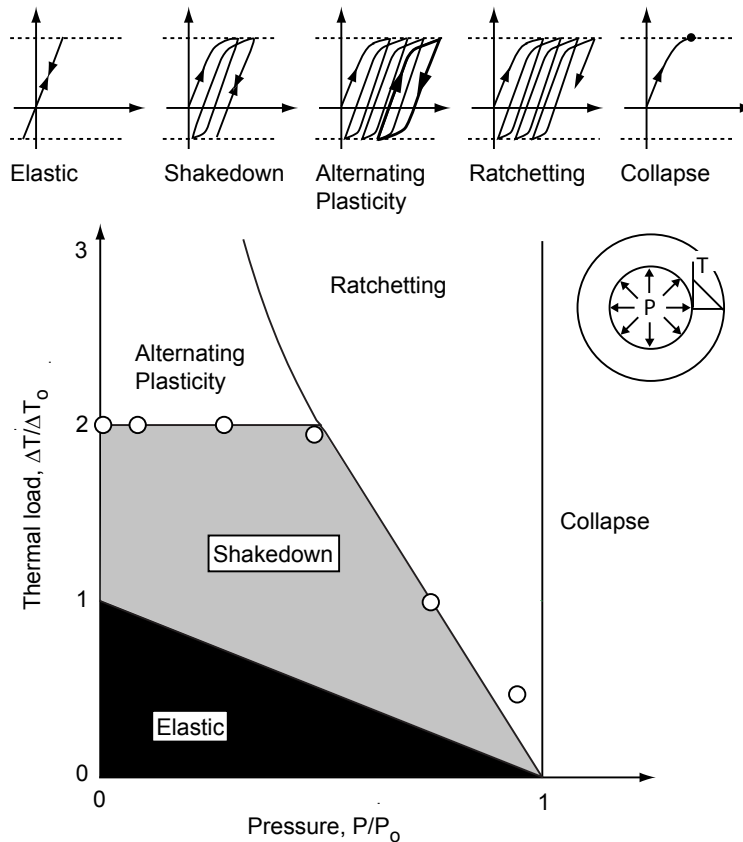

Figure 3. Top: prototypical stress-strain behaviors for an elastic-plastic material in the classic Bree problem. Bottom: the corresponding analytic Bree diagram. The fuel can is modeled as a cylindrical pressure vessel subject to constant internal pressure and a cyclic thermal gradient through the wall thickness. Data points represent FE calculations of the shakedown limit reported in [Abdalla et al. 2007].

outside walls.[1] The resulting Bree diagram is shown in Figure 3, bottom. The ordinate is $\Delta T/\Delta T_0$, where ΔT_0 is the temperature difference required for yield initiation in the absence of a mechanical load; the abscissa is P/P_0 with P_0 being the pressure that causes yielding in the absence of a temperature gradient.

For this configuration, the elastic domain is defined by $P/P_0 + \Delta T/\Delta T_0 < 1$. At one extreme, where $P/P_0 > 1$, *plastic collapse* occurs on the first load cycle. For intermediate combinations of P and ΔT, one of three behaviors is obtained (Figure 3) [Abdel-Karim 2005].

(1) In the *shakedown* regime, localized plastic deformation that occurs in the early stages of cycling gives rise to residual stresses that stabilize the plastic deformation. The consequence is purely elastic behavior during further loading cycles.

(2) *Alternating plasticity* occurs by loading beyond the shakedown limit. Here the plastic strain increment obtained during the first half of each loading cycle is followed by a plastic strain increment of equal magnitude but opposite sign during the second half. No net strain accrues during each cycle but the structure ultimately fails by low-cycle fatigue.

(3) *Ratcheting* refers to the condition in which a net increment of plastic strain accumulates during each cycle, eventually causing plastic collapse.

Computational approach. Although Bree diagrams can be constructed for simple geometries and loading conditions using analytical models [Bree 1967], numerical techniques are generally required [Abdel-Karim 2005]. In the present study, finite element analysis (FEA) is used to apply a methodology initially reported in [Abdalla et al. 2007]. The approach yields an estimate of the shakedown limit in accordance with Melan's lower bound theorem[2]. The theorem states that a structure will shakedown if a time-independent residual stress field can be found which satisfies mechanical equilibrium and the boundary conditions and the combined residual and elastic stresses do not exceed yield at any time during the loading cycle [König 1987; Bower 2009].

For implementation, the methodology requires two sets of computations for each geometry. In the first, the stresses caused by the cyclic load in an *elastic* structure are computed. This analysis is performed only once and its output stored. The second is an elastic-plastic analysis, assuming perfectly plastic behavior beyond yield, incorporating both the time-invariant and the cyclic loads in consecutive steps. The time-invariant load is applied first to a specified level and a half cycle of the varying load is then applied to its specified level. Each is incremented monotonically from zero to its peak value while an elastic-plastic analysis is carried out. Residual stresses are then calculated at every material point in accordance with

$$\sigma_{r,n} = \sigma_{\text{EP},n} - \sigma_E \frac{\Delta C_n}{\Delta C_{\text{ref}}}, \tag{1}$$

where σ_E and ΔC_{ref} are the stress tensor and cyclic load amplitude for the elastic analysis and $\sigma_{\text{EP},n}$ and ΔC_n are the corresponding values for the stress tensor and cyclic load amplitude resulting from the n-th trial calculation in the elastic-plastic analysis [Abdalla et al. 2007]. If the effective (von Mises) residual

---

[1]Subsequently, the effects of alternative loading sequences (e.g., in-phase versus out-of-phase) were also investigated [Ng and Moreton 1983].

[2]The Melan theorem and all analyses presented herein assume elastic perfectly plastic material behavior.

stresses lie inside the yield surface at every point in the structure, the n-th combination of time-invariant and cyclic loads constitute a lower bound to the shakedown limit. The process is repeated for progressively increasing time-invariant and cyclic loads until yield is just reached by the resulting effective residual stress. The associated combination of time-invariant and cyclic loads represents one point on the shakedown curve on the Bree diagram. The computations are repeated for other load combinations until the full shakedown boundary is obtained over the domain of interest. Results obtained in [Abdalla et al. 2007] for the classic Bree problem are reported in Figure 3.

Implementation for actively cooled combustor liner. The Bree diagram for a representative unit cell of an actively cooled panel was constructed in accordance with the preceding prescription. The cell geometry and dimensions (depicted in Figure 4) were obtained from a yield-limited optimization analysis reported in an earlier study [Valdevit et al. 2008]. Here the internal pressure within the channels is assumed to be time-invariant. The thermal load (assumed cyclic) consists of a uniform temperature difference between the two faces (denoted "hot" and "cold"). Uniform thermal expansion in the lateral (x_1) direction (without bending) is permitted. The selection of the internal pressure as the time-invariant load and the temperature difference as the cyclic load is consistent with Bree's original analysis.

All computations were performed using the ABAQUS$^{©}$ finite element code. The mesh consisted of biquadratic generalized plane strain elements with reduced integration and hybrid formulation (CPEG8RH). The radius of the corner fillet in the finite element analysis was taken to be 0.1 mm, representative of that obtained through electrical discharge machining (EDM) when a nominally square corner is prescribed. (The resulting radius is dictated largely by the diameter of the EDM wire.) This fillet value also represents the most conservative design as smaller fillets are not feasible by EDM (or any other reasonable
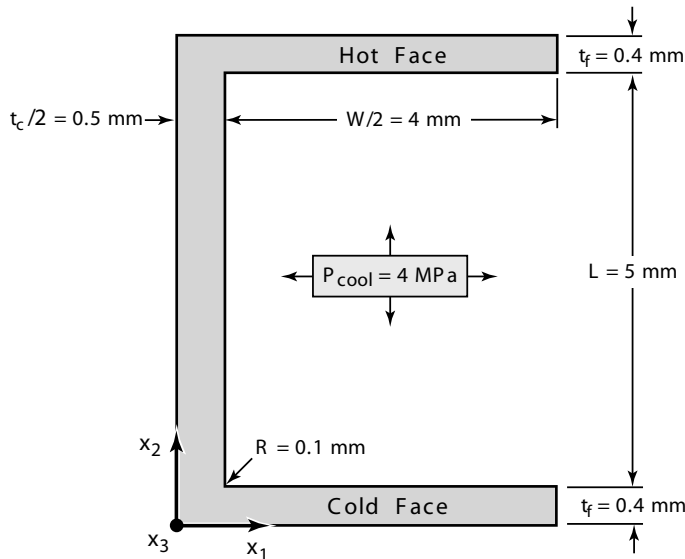

Figure 4. The half unit cell used in the finite element computations for construction of the Bree diagram in Figure 5. This particular geometry emerged as being nearly optimal for a yield-limited design. The boundary conditions are defined by: $u_1 = 0$ along $x_1 = 0$, $u_2 = 0$ along $x_2 = 0$, and $u_1 = $ constant along $x_1 = (W + t_c)/2$ (u being displacement).

	Inconel X-750	C-SiC
Upper use temperature, T^* (K)	1100	1810
Yield strength, σ_0 (at T^*) (MPa)	527	400
Temperature dependence of strength, $d\sigma_0/dT$ (MPa/K)	-0.4	—
Young's modulus, E (GPa)	130	140
Thermal expansion coefficient, α ($10^{-6}\,\mathrm{K}^{-1}$)	16	2
Thermal conductivity, k (W/mK)	23	15 (in-plane) 5 (through-thickness)
Density, ρ (kg/m^3)	8280	2000

Table 1. Thermomechanical properties of candidate materials.

manufacturing approach) and larger fillets will relax stress concentrations. The material properties were selected to be representative of Inconel X-750 (Table 1).

Elastic-plastic computations were performed for coolant pressures P ranging from zero to that needed to exceed the shakedown boundary in the absence of a thermal load. For presentation on a Bree diagram, the pressure was normalized by the *nominal* value P_0 required for first yield, obtained by modeling the face-sheet as a uniformly loaded edge-clamped plate under plane strain conditions. The result is (see [Valdevit et al. 2008; Beer and Johnston 1981])

$$P_0 = \frac{4}{\sqrt{3}}\sigma_0\left(\frac{t_f}{W}\right)^2, \tag{2}$$

where W is the channel width and t_f the face-sheet thickness (Figure 4). The value of P_0 obtained from the finite element analysis is somewhat lower than that calculated from (2), by about 30%. The nonconservative nature of the analytical prediction is due to the stress concentrations that arise at the corners in the finite element analysis but are neglected in the plate model.

At each pressure level, the temperature difference ΔT between the faces was incremented to ascertain both the first yield and the shakedown boundaries.[3] (No attempt was made to differentiate the elasto-plastic deformation modes beyond the shakedown limit, as they would all be equally unacceptable for the application under consideration.) This temperature difference was normalized by the critical value needed for yield initiation, calculated using the analytical solution presented in the Appendix.

The resulting Bree diagram is shown in Figure 5. It exhibits elastic and shakedown boundaries that are qualitatively similar to those in Figure 3 (though without the specific plasticity modes beyond the shakedown limit). While the classic Bree diagram for the thin-walled *cylindrical* pressure vessel is universally applicable to all such vessels subjected to the same sequence of loading conditions, the *rectangular* geometry of the present combustor panels precludes interpretation of Figure 5 as a similarly universal result. That is, the Melan theorem requirements are not automatically satisfied when the unit-cell geometry of the combustor panel is changed. Consequently, the Bree diagram in Figure 5 is specific

---

[3]In the FEA, conditions are checked at integration stations of the elements and the component is deemed to shakedown if all integration stations pass the test of not violating yield.
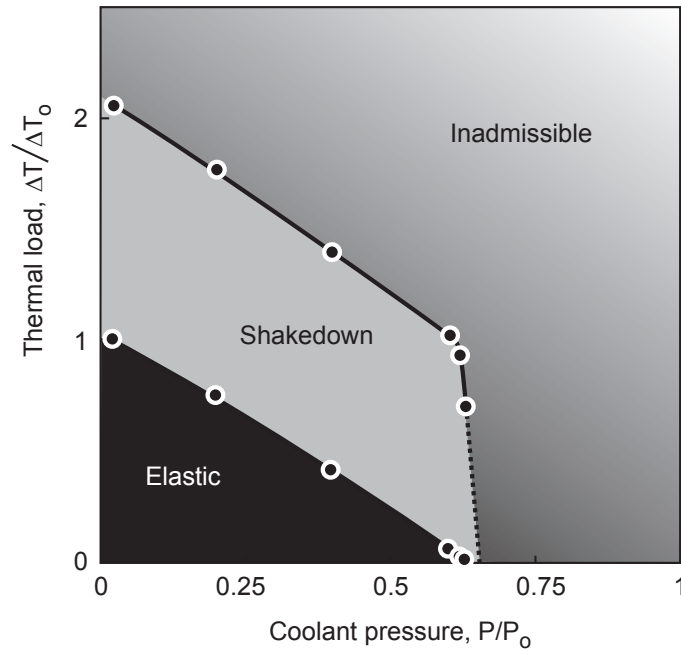
Figure 5. The Bree diagram for the combustor panel, based on analyses of the unit cell in Figure 4. Elastoplastic behaviors beyond shakedown (ratcheting, cyclic plasticity and plastic collapse) are considered inadmissible.

to the geometry depicted in Figure 4. Strictly, in order to utilize such results in an optimization code, computations of this kind would need to be performed for all possible geometries. The computational effort for this task would be prohibitive.

In light of these limitations, the shakedown concept was employed in the optimization in the following way. First, the dimensions of the optimal yield-limited design were obtained using the algorithm presented in [Valdevit et al. 2008] and summarized in Section 3. Then, the dimensions were incrementally varied in a manner that yielded a mass reduction and the shakedown limit was numerically computed. The process was repeated until the resulting structure was no longer within the shakedown limit. Comparisons of the mass of the penultimate structure with that of the yield-limited design were used to assess the benefits of extending the design into the shakedown domain. The following section describes the protocol used to determine optimal yield-limited designs. It also describes how these designs were varied in a sensitivity study to find lighter weight solutions subject to the shakedown limit.

3. Sensitivity study procedure

The reference [Valdevit et al. 2008] may be consulted for details not given in this section.

Optimal yield-or-fracture-limited designs. The optimization protocol was applied to two representative combustor panel support conditions (Figure 1). In Design I, periodic line supports are placed along the panel base. Panel-level bending stresses ensue between the supports due to the combustion pressure. In Design II, a supporting panel is attached to the base, preventing panel-level bending. Isotropic thermal

expansion is permitted in both designs. The essential difference between the designs is that, in Design II, the combustion pressure is rendered inconsequential, reducing the dominant loads to two: the coolant pressure and the panel level thermal gradient. In contrast, three loads remain for Design I.

The optimization protocol consists of the following steps. The values of heat load and fuel flow rate are identified for the specified vehicle Mach number, assumed to be 7. The heat load is characterized by the temperature difference between the combustion gas (specifically, the adiabatic wall temperature, $T_{aw} = 3050\,\text{K}$) and the hot surface (evaluated analytically) and the corresponding heat transfer coefficient, h_G. The latter was computed assuming steady-state combustion conditions, yielding $h_G = 445\,\text{W/m}^2\text{K}$. The fuel flow rate through the cooling channels was taken to be that for stoichiometric combustion of the fuel with the available oxygen in the flowpath. The (internal) pressure in the cooling channels is set by injection requirements ($p_{cool} = 4\,\text{MPa}$ for a prototypical vehicle), and the (external) combustion chamber pressure is obtained by the flow conditions in the combustor ($p_{comb} = 0.16\,\text{MPa}$ for Mach 7 conditions). The design parameters are incrementally varied over a prescribed range and the pertinent stresses and temperatures were computed. (In principle, the heat transfer coefficient can be increased to reflect local heat spikes due to nonuniform combustion and the flow rate varied relative to the stoichiometric value. Variations in these parameters were not considered in the present study.)

Temperature distributions were obtained by means of a thermal network model. The stresses due to both the coolant pressure and the temperature gradients were obtained at critical locations using standard thermoelastic plate analysis. A synopsis of the models for the temperature and stress distributions is presented in the Appendix. Upon comparison of the computed stresses and temperatures with the corresponding material and coolant properties, the viability of the design is ascertained.

Specifically, for viability in the case of metallic candidates that are *yield-limited*, the effective (von Mises) stress must not exceed the yield stress anywhere in the structure. Similarly, for ceramic matrix composite (CMC) candidates such as C/SiC, *fracture-limited* design is determined by ensuring that the maximum and minimum principal stresses in the structure remain below/above critical values ($\pm 400\,\text{MPa}$ for C/SiC).

Additionally, for all candidates the fuel temperature must not exceed that for coking (975 K for JP-7) and the maximum material temperature must not exceed its upper use (softening) temperature (1100 K for Inconel X-750). If solutions exist, the design is optimized for minimum mass, Additionally, to ensure realistic designs, constraints based on panel manufacturability and fuel pressure drop were also prescribed. For instance, to enable manufacturing of the panels by conventional means, minimum values were prescribed for the face and core member thicknesses (0.4 mm), the channel height (5 mm) and the channel width (2 mm). Numerical optimizations were performed using the quadratic optimizer MINCON in MATLAB. The process was repeated using several different randomly generated initial guesses to ensure the optimized solutions were not in local minima.

Probing benefits of shakedown. Two slightly different schemes were employed to calculate the operational conditions associated with the two sets of boundary conditions (defined by Designs I and II) and assess whether they reside within the shakedown limit. The scheme for Design II is straightforward. The internal pressure is selected to be 4 MPa and the operational temperature difference, ΔT_{panel}, is calculated from the thermal network model (Appendix). Comparisons of ΔT_{panel} with the shakedown value (calculated by FEA) determine the viability of the structure.

For Design I, an additional calculation is required to account for the combustion pressure in the Bree analysis. Since the panel acts essentially as a clamped plate that bends between the supports, the combustion pressure produces uniform tensile or compressive stresses in the face sheets normal to the direction of the underlying supports. These uniform stresses are of the same form as those arising from the thermal load. Additionally, both are operative at the same time, i.e., during combustion. Consequently, from a mathematical viewpoint, the two loads can be represented by an effective (fictitious) temperature change, ΔT_{eff}, that produces the same stresses in the face sheets. The stresses are obtained in the following way.

From an analysis of a plate under generalized plane strain conditions, the stresses induced by the *real* temperature difference ΔT_{panel} are given by

$$
\sigma_{xx}^{\Delta T_{\text{panel}}} = \begin{cases} -\dfrac{E\alpha\Delta T_{\text{panel}}}{2(1-\nu)} & \text{in the hot face,} \\[2ex] \dfrac{E\alpha\Delta T_{\text{panel}}}{2(1-\nu)} & \text{in the cold face,} \end{cases}
$$

$$
\sigma_{zz}^{\Delta T_{\text{panel}}} = \begin{cases} \left[\dfrac{-E\alpha\Delta T_{\text{panel}}}{2(1-\nu)}\right]\left[\dfrac{(2-\nu)Lt_c + 2t_f(W+t_c)}{Lt_c + 2t_f(W+t_c)}\right] & \text{in the hot face,} \\[2ex] \left[\dfrac{E\alpha\Delta T_{\text{panel}}}{2(1-\nu)}\right]\left[\dfrac{\nu Lt_c + 2t_f(W+t_c)}{Lt_c + 2t_f(W+t_c)}\right] & \text{in the cold face.} \end{cases}
\tag{3}
$$

From an analogous plate bending analysis, the stresses caused by the combustion pressure are

$$
\sigma_{xx}^{p_{\text{comb}}} = \begin{cases} p_{\text{comb}}\dfrac{1}{12}\dfrac{b^2}{(L+t_f)t_f} & \text{at points 1, 2, 5, 6,} \\[2ex] -p_{\text{comb}}\dfrac{1}{12}\dfrac{b^2}{(L+t_f)t_f} & \text{at points 3, 4, 7, 8,} \\[2ex] p_{\text{comb}}\dfrac{1}{24}\dfrac{b^2}{(L+t_f)t_f} & \text{at points 12, 13, 16, 17,} \\[2ex] -p_{\text{comb}}\dfrac{1}{24}\dfrac{b^2}{(L+t_f)t_f} & \text{at points 10, 11, 14, 15,} \end{cases}
\tag{4}
$$

$$
\sigma_{zz}^{p_{\text{comb}}} = \nu\sigma_{xx}^{p_{\text{comb}}} \quad \text{at all points.}
$$

where b is the distance between supports (assumed to be 0.5 m) and the points 1–17, defined on Figure 1, right, represent critical locations where stress combinations are most severe. The stress components in (3) and (4) are added at every point and the von Mises stress $\bar{\sigma}(\Delta T_{\text{panel}}, p_{\text{comb}})$ obtained in the usual manner:

$$
\bar{\sigma}(\Delta T_{\text{panel}}, p_{\text{comb}}) = \sqrt{\tfrac{1}{2}\left(\sigma_{xx}^2 + \sigma_{zz}^2 + (\sigma_{xx} - \sigma_{zz})^2\right)}.
\tag{5}
$$

The stresses produced by the *effective* temperature difference are of similar form to those in (3), with ΔT_{panel} replaced by ΔT_{eff}, yielding

$$
\sigma_{xx}^{\Delta T_{\text{eff}}} = \begin{cases} -\dfrac{E\alpha\Delta T_{\text{eff}}}{2(1-\nu)} & \text{in the hot face,} \\[2ex] \dfrac{E\alpha\Delta T_{\text{eff}}}{2(1-\nu)} & \text{in the cold face,} \end{cases}
\tag{6a}
$$

$$\sigma_{zz}^{\Delta T_{\text{eff}}} = \begin{cases} \left[\dfrac{-E\alpha\Delta T_{\text{eff}}}{2(1-\nu)}\right]\left[\dfrac{(2-\nu)Lt_c + 2t_f(W+t_c)}{Lt_c + 2t_f(W+t_c)}\right] & \text{in the hot face,} \\[12pt] \left[\dfrac{E\alpha\Delta T_{\text{eff}}}{2(1-\nu)}\right]\left[\dfrac{\nu Lt_c + 2t_f(W+t_c)}{Lt_c + 2t_f(W+t_c)}\right] & \text{in the cold face.} \end{cases} \tag{6b}$$

The corresponding effective stress is

$$\bar{\sigma}(\Delta T_{\text{eff}}) = \sqrt{\tfrac{1}{2}\left[\left(\sigma_{xx}^{\Delta T_{\text{eff}}}\right)^2 + (\sigma_{zz}^{\Delta T_{\text{eff}}})^2 + (\sigma_{xx}^{\Delta T_{\text{eff}}} - \sigma_{zz}^{\Delta T_{\text{eff}}})^2\right]}. \tag{7}$$

The effective temperature difference is obtained by setting $\bar{\sigma}(\Delta T_{\text{panel}}, p_{\text{comb}}) = \bar{\sigma}(\Delta T_{\text{eff}})$ — see Equations (5) and (7) — and numerically inverting the result to obtain $\Delta T_{\text{eff}}(\Delta T_{\text{panel}}, p_{\text{comb}})$. The viability of a design is ascertained by comparing ΔT_{eff} with the shakedown limit computed by FEA.

4. Designs allowing shakedown

The key results of the sensitivity study are summarized in Figure 6 for Designs I and II. The figure illustrates the benefits associated with designing to shakedown, characterized by the ratio of minimum panel masses. Also shown in Figure 6 is the panel mass for an optimized C/SiC composite. (This result is based on a fracture-limited design, using criteria based on critical values of the maximum and minimum principal stresses. Shakedown is not considered in this case since the underlying plasticity mechanisms
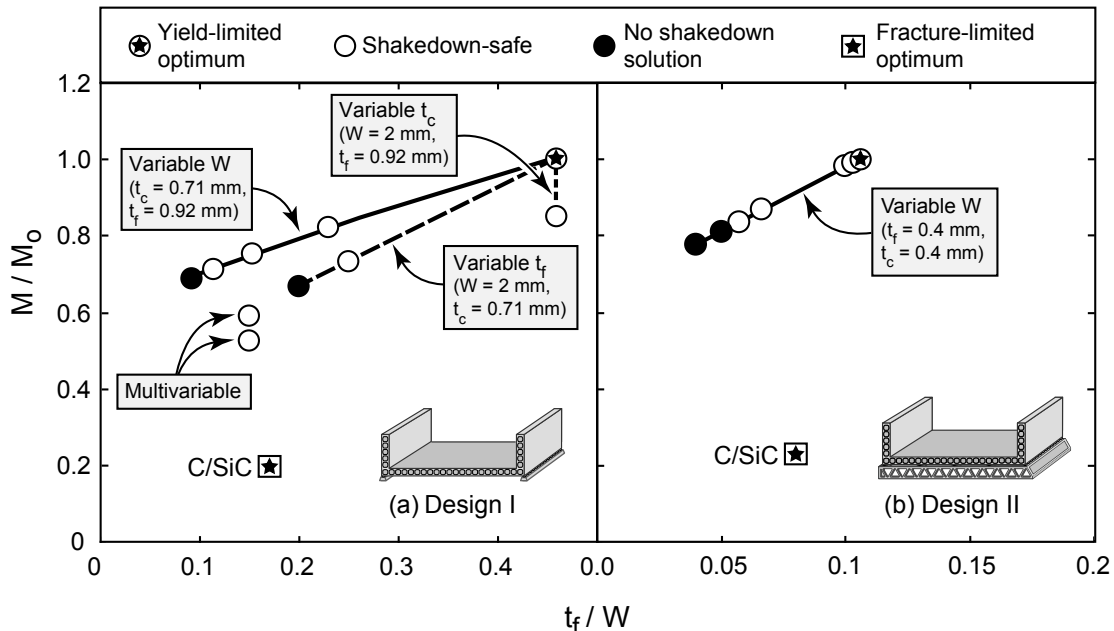

Figure 6. Benefits of shakedown-limited design in the minimum mass of an actively cooled Inconel X-750 panel under the two design scenarios. Here M_0 is the mass of the optimal yield-limited design. For all Inconel solutions, channel height, L, is at the minimum value (5 mm). Also shown for comparison are the results for the fracture-limited optimum for a C/SiC composite.

	Design I												Design II						
	C/SiC	Inconel X-750											C/SiC	Inconel X-750					
L	10.71	5	5	5	5	5	5	5	5	5	5	5	5	5	5	5	5	5	5
W	5.11	2	2	2	4	6	8	10	2	4	4	4	4.97	3.77	4	6	7	8	10
t_f	0.87	0.92	0.5	0.4	0.92	0.92	0.92	0.92	0.92	0.6	0.6	0.4	0.4	0.4	0.4	0.4	0.4	0.4	0.4
t_c	0.4	0.71	0.71	0.71	0.71	0.71	0.71	0.71	0.4	0.6	0.4	0.4	0.4	0.4	0.4	0.4	0.4	0.4	0.4
M/M_0	0.2	1	0.73	—	0.82	0.75	0.71	—	0.85	0.59	0.53	—	0.22	1	0.98	0.87	0.84	—	—
	FL	YL	SL	—	SL	SL	SL	—	SL	SL	SL	—	FL	YL	SL	SL	SL	—	—

Table 2. Geometries for design optimization and shakedown analyses. Abbreviations on the last row stand for fracture-limited (FY), yield-limited (YL), and shakedown-limited (SL). A dash on the last two rows indicates no solution. The geometric parameters L, W, t_f, and t_c are given in units of mm.

are not operative in these materials at the temperatures of interest.) For consistency, the C/SiC panel mass is also normalized by that of the optimized Inconel X-750 structure. Previous optimization studies have revealed C/SiC to yield the lightest structure and it is thus used as a benchmark against which the metallic designs are assessed.

Evidently the benefits of incorporating shakedown depend sensitively on the boundary conditions. For instance, for Design II, the optimal face sheet and core member thicknesses as well as channel height are already at their minimum allowable values in the yield-limited design (Table 2). Consequently, they cannot be reduced further to take advantage of the shakedown phenomenon. The only available avenue for weight reduction is to increase the channel width, W, from its optimal value of 3.8 mm. The results from a number of FEA computations for several values of W are summarized in Table 2 and plotted on Figure 6. In this case, the shakedown limit is breached when W exceeds 7 mm. The resulting weight reduction is modest (about 16%).

For Design I, incorporating shakedown yields greater benefits in mass reduction. In this case, among the free geometric variables, only the channel height, L, is at its minimum allowable value for the optimal yield-limited design. Consequently, computations were performed for lower values of face sheet and core member thicknesses as well as higher values of channel width. The results in Figure 6(a) are labeled accordingly. While each of these changes results in some mass reduction, the magnitudes of the contributions differ. For example, decreasing t_c from 0.71 mm to its minimum allowable value (0.4 mm) while maintaining all other parameters fixed yields a mass reduction of 15%. Mass reductions of 27% and 29% are obtained for reduced values of t_f (from 0.92 mm to 0.5 mm) and elevated values of W (from 2 mm to 8 mm), respectively. The greatest benefits are obtained by varying the three dimensions simultaneously. Among the cases considered here (Table 2), the best one produces a nearly 50% reduction in mass.

Even exploiting shakedown in the design of the Inconel X-750 structure, its mass is still about 2.7 times that of the optimized C/SiC structure. But, because of the relative ease of manufacturing metallic

components along with their superior structural robustness, the metallic alloy may prove to be preferable to the ceramic composite for the present application.

While the present shakedown analysis demonstrates potential weight savings, additional research is required to provide more insight into the physical behavior of such structures. Particularly, their response in competition with creep environments is of interest. The computational approach presented provides a working limit for shakedown that motivates the development of complementary models of material behavior during structural shakedown.

5. Conclusions

Incorporating shakedown into the design of actively cooled thermostructural panels can enable significant weight reduction. The magnitude of the benefit depends on the component of interest, the boundary conditions and the specific constraints placed on the design. For the component considered here — a liner for a scramjet engine operating at stoichiometric fuel flow rates under steady-state combustion conditions for Mach 7 flight — significant benefits accrue only when the liner is weakly supported by an external structure. Otherwise, when the support structure provides a more substantial constraint on deformation, the design is influenced more heavily by the material softening temperature and the secondary constraints derived from manufacturing limitations than by the thermomechanical loads. In such cases, the more aggressive design strategy, exploiting shakedown, is of minimal benefit.

Appendix: Synopsis of analytical models

Temperature distributions. Analytical expressions for the temperatures at critical locations in the panel have been obtained via a thermal network approach, subject to four simplifying assumptions:

(1) T_{aw} and h_G are uniform along the hot face;

(2) all heat is removed by forced convection in the cooling channels;

(3) longitudinal panel conduction is negligible so that the gradient of hot surface temperature in the fuel flow direction is due only to cooling into the fuel channel; and

(4) the coolant temperature, due to turbulent mixing, is uniform across the channel cross-section.

Based on the thermal network in Figure 7, the temperature in the fluid is:

$$T_f = T_{\text{aw}} - (T_{\text{aw}} - T_f^0) \cdot \exp(-\beta z) \tag{A.1}$$

and the temperature distributions at the 18 locations depicted in Figure 1 are:

$$T^{(i)} = T_{\text{aw}} - (T_{\text{aw}} - T_f^0) \cdot F^{(i)} \exp(-\beta z) \tag{A.2}$$

where $F^{(i)}$ and β depend on: the geometry of the panel (W, L, t_f, t_c); the thermal conductivity of the material, k_s; the thermal conductivity, k_f, kinematic viscosity, ν_f, and volumetric specific heat, $\rho_f c_{p,f}$, of the fuel; the heat transfer coefficient on the hot side, h_G; and the volumetric fuel flow rate, $\dot{V}$ (see [Valdevit et al. 2008] for details). Importantly, these functional dependencies are intertwined, thus precluding straightforward interpretation of the effect of each quantity on the temperature distribution.
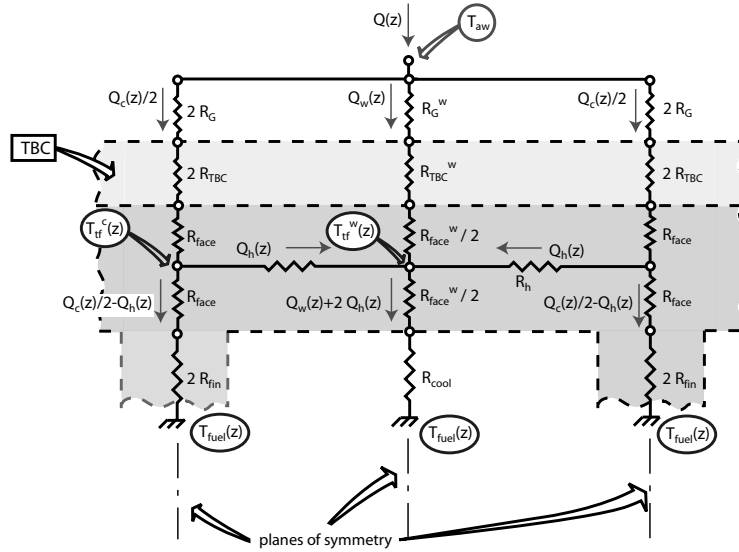
OVER THE WEB	$R_G = \dfrac{1}{h_G\, t_c}$	$R_{TBC} = \dfrac{t_{TBC}}{k_{TBC}^{\perp}\, t_c}$	$R_{face} = \dfrac{t_f}{k_s^{\perp}\, t_c}$	$R_{fin} = \dfrac{\tanh^{-1}\sqrt{2h_c/k_s^{\parallel}t_c}\,L}{\sqrt{2h_c/k_s^{\parallel}t_c}\,k_s^{\parallel}t_c}$		$R_h = \dfrac{W - t_c/2}{4\,k_s^{\parallel}t_f}$
BETWEEN WEBS	$R_G^w = \dfrac{t_c}{W}\,R_G$	$R_{TBC}^w = \dfrac{t_c}{W}\,R_{TBC}$	$R_{face}^w = \dfrac{t_c}{W}\,R_{face}$	$R_{cool} = \dfrac{1}{h_c\,W}$		

Figure 7. Thermal resistance network used to determine temperature distributions, along with expressions for all relevant thermal resistances.

The dominant thermal stresses in the panel depend on the temperature difference between the two faces $\Delta T_{\text{panel}}(z)$. For simplicity, this difference is averaged in the x-direction, and can be expressed as:

$$\Delta T_{\text{panel}}(z) = (T_{\text{aw}} - T_f^0) \cdot G_1 \cdot \exp(-\beta z) \tag{A.3}$$

where G_1 depends on the same quantities as $F^{(i)}$.

The accuracy of this analytical model has been verified with a number of selected computational fluid dynamics and FEA computations; the temperature distributions are generally captured by (A.2) to within $\sim 1\%$ and the temperature gradient captured by (A.3) to within $\sim 8\%$ [Valdevit et al. 2008].

Stress distributions. The dominant stresses are induced by the combustion chamber pressure, p_{comb}, on the hot side of the panel, the fuel pressure, p_{cool}, inside the cooling channels, and the temperature difference, ΔT_{panel}, between the hot and cold faces. Assuming generalized plane strain conditions (with no rotation about the x and y axes), the mechanical stresses (membrane plus bending) at each of the 18 locations depicted in Figure 1 are given by

$$\sigma_{m,x}^{(i)} = A^{(i)} p_{\text{cool}} + B^{(i)} p_{\text{comb}}, \quad \sigma_{m,z}^{(i)} = \nu \sigma_{m,x}^{(i)} \tag{A.4}$$

where the functions $A^{(i)}$, $B^{(i)}$ depend on panel geometry and support conditions and ν is Poisson's ratio. Similarly, the dominant thermal stresses can be expressed as:

$$\sigma_{T,x}^{(i)} = \frac{E\alpha}{1-\nu}(D_x^{(i)}\Delta T_{\text{panel}}^{(i)}), \quad \sigma_{T,z}^{(i)} = \frac{E\alpha}{1-\nu}(D_z^{(i)}\Delta T_{\text{panel}}^{(i)}), \tag{A.5}$$

where E and α are the Young's modulus and the coefficient of thermal expansion, respectively. The quantities $D_x^{(i)}$ and $D_z^{(i)}$ are functions of geometry only. Additional details are presented in [Valdevit et al. 2008]. The accuracy of this model has been verified with FEA. Its accuracy is better than $\sim 10\%$ on the top face and $\sim 20\%$ on the bottom face (*loc. cit.*).

Acknowledgements

References

[Abdalla et al. 2007] H. F. Abdalla, M. M. Megahed, and M. Y. A. Younan, "A simplified technique for shakedown limit load determination", *Nucl. Eng. Des.* **237**:12–13 (2007), 1231–1240.

[Abdel-Karim 2005] M. Abdel-Karim, "Shakedown of complex structures according to various hardening rules", *Int. J. Press. Vessels Pip.* **82**:6 (2005), 427–458.

[Beer and Johnston 1981] F. P. Beer and E. R. Johnston, *Mechanics of materials*, Chapter 7, McGraw-Hill, New York, 1981.

[Bower 2009] A. F. Bower, *Applied mechanics of solids*, Chapter 6, pp. 381–422, CRC Press, Boca Raton, FL, 2009, Available at http://www.solidmechanics.org.

[Bree 1967] J. Bree, "Elastic-plastic behaviour of thin tubes subjected to internal pressure and intermittent high-heat fluxes with application to fast-nuclear-reactor fuel elements", *J. Strain Anal. Eng. Des.* **2**:3 (1967), 226–238.

[Buchmann 1979] O. A. Buchmann, "Thermal-structural design study of an airframe-integrated scramjet", Contractor report NASA CR-3141, NASA, Washington, DC, 1979, Available at http://www.tinyurl.com/NASA-CR-3141.

[Flieder et al. 1971] W. C. Flieder, C. E. Richard, O. A. Buchmann, and F. M. Walters, "An analytical study of hydrogen cooled panels for application to hypersonic aircraft", Contractor report NASA CR-1650, NASA, Washington, DC, 1971, Available at http://www.tinyurl.com/NASA-CR-1650.

[Heiser and Pratt 1994] W. H. Heiser and D. T. Pratt, *Hypersonic airbreathing propulsion*, AIAA, Washington, DC, 1994.

[König 1987] J. A. König, *Shakedown of elastic-plastic structures*, Chapter 4, Fundamental Studies in Engineering **7**, Elsevier, Amsterdam, 1987.

[Ng and Moreton 1983] H. W. Ng and D. N. Moreton, "Bree diagrams for alternative loading sequences", pp. 279–312 in *Engineering approaches to high temperature design*, edited by B. Wilshire and D. R. J. Owen, Recent Advances in Creep and Fracture of Engineering Materials and Structures **2**, Pineridge Press, Swansea, 1983.

[Scotti et al. 1988] S. J. Scotti, C. J. Martin, and S. H. Lucas, "Active cooling design for scramjet engines using optimization methods", Technical memorandum NASA TM-100581, NASA Langley Research Center, Hampton, VA, 1988, Available at http://www.tinyurl.com/NASA-TM-100581.

[Valdevit et al. 2008] L. Valdevit, N. Vermaak, F. W. Zok, and A. G. Evans, "A materials selection protocol for lightweight actively cooled panels", *J. Appl. Mech.* (*ASME*) **75**:6 (2008), 061022.

[Vermaak et al. 2010] N. Vermaak, L. Valdevit, and A. G. Evans, "Influence of configuration on materials selection for actively cooled combustors", *J. Propuls. Power* **26**:2 (2010), 295–302.

[Youn and Mills 1995] B. Youn and A. F. Mills, "Cooling panel optimization for the active cooling system of a hypersonic aircraft", *J. Thermophys. Heat Transf.* **9**:1 (1995), 136–143.

NATASHA VERMAAK: natasha@engineering.ucsb.edu
Materials Department, University of California, Santa Barbara, CA 93106-5050, United States

LORENZO VALDEVIT: valdevit@uci.edu
Department of Mechanical and Aerospace Engineering and Department of Chemical Engineering and Materials Science, University of California, Irvine, CA 92697-3975, United States

ANTHONY G. EVANS: agevans@engineering.ucsb.edu
Materials Department, University of California, Santa Barbara, CA 93106-5050, United States
http://www.me.ucsb.edu/dept_site/people/evans_page.html

FRANK W. ZOK: zok@engineering.ucsb.edu
Materials Department, University of California, Santa Barbara, CA 93106-5050, United States
http://engineering.ucsb.edu/~zok/zok.html

ROBERT M. MCMEEKING: rmcm@engineering.ucsb.edu
Materials and Mechanical Engineering Departments, University of California, Santa Barbara, CA 93106-5050, United States

SUBMISSION GUIDELINES

ORIGINALITY

Authors may submit manuscripts in PDF format online at the Submissions page. Submission of a manuscript acknowledges that the manuscript is original and has neither previously, nor simultaneously, in whole or in part, been submitted elsewhere. Information regarding the preparation of manuscripts is provided below. Correspondence by email is requested for convenience and speed. For further information, write to one of the Chief Editors:

Davide Bigoni	bigoni@ing.unitn.it
Iwona Jasiuk	ijasiuk@me.concordia.ca
Yasuhide Shindo	shindo@material.tohoku.ac.jp

LANGUAGE

Manuscripts must be in English. A brief abstract of about 150 words or less must be included. The abstract should be self-contained and not make any reference to the bibliography. Also required are keywords and subject classification for the article, and, for each author, postal address, affiliation (if appropriate), and email address if available. A home-page URL is optional.

FORMAT

Authors can use their preferred manuscript-preparation software, including for example Microsoft Word or any variant of TeX. The journal itself is produced in LaTeX, so accepted articles prepared using other software will be converted to LaTeX at production time. Authors wishing to prepare their document in LaTeX can follow the example file at www.jomms.org (but the use of other class files is acceptable). At submission time only a PDF file is required. After acceptance, authors must submit all source material (see especially Figures below).

REFERENCES

Bibliographical references should be complete, including article titles and page ranges. All references in the bibliography should be cited in the text. The use of BibTeX is preferred but not required. Tags will be converted to the house format (see a current issue for examples); however, for submission you may use the format of your choice. Links will be provided to all literature with known web locations; authors can supply their own links in addition to those provided by the editorial process.

FIGURES

Figures must be of publication quality. After acceptance, you will need to submit the original source files in vector format for all diagrams and graphs in your manuscript: vector EPS or vector PDF files are the most useful. (EPS stands for Encapsulated PostScript.)

Most drawing and graphing packages—Mathematica, Adobe Illustrator, Corel Draw, MATLAB, etc.—allow the user to save files in one of these formats. Make sure that what you're saving is vector graphics and not a bitmap. If you need help, please write to graphics@mathscipub.org with as many details as you can about how your graphics were generated.

Please also include the original data for any plots. This is particularly important if you are unable to save Excel-generated plots in vector format. Saving them as bitmaps is not useful; please send the Excel (.xls) spreadsheets instead. Bundle your figure files into a single archive (using zip, tar, rar or other format of your choice) and upload on the link you been given at acceptance time.

Each figure should be captioned and numbered so that it can float. Small figures occupying no more than three lines of vertical space can be kept in the text ("the curve looks like this:"). It is acceptable to submit a manuscript with all figures at the end, if their placement is specified in the text by means of comments such as "Place Figure 1 here". The same considerations apply to tables.

WHITE SPACE

Forced line breaks or page breaks should not be inserted in the document. There is no point in your trying to optimize line and page breaks in the original manuscript. The manuscript will be reformatted to use the journal's preferred fonts and layout.

PROOFS

Page proofs will be made available to authors (or to the designated corresponding author) at a Web site in PDF format. Failure to acknowledge the receipt of proofs or to return corrections within the requested deadline may cause publication to be postponed.